Springer Theses
Recognizing Outstanding Ph.D. Research

Nicholas Chamberlain Stone

The Tidal Disruption of Stars by Supermassive Black Holes

An Analytic Approach

Springer

Springer Theses

Recognizing Outstanding Ph.D. Research

Aims and Scope

The series "Springer Theses" brings together a selection of the very best Ph.D. theses from around the world and across the physical sciences. Nominated and endorsed by two recognized specialists, each published volume has been selected for its scientific excellence and the high impact of its contents for the pertinent field of research. For greater accessibility to non-specialists, the published versions include an extended introduction, as well as a foreword by the student's supervisor explaining the special relevance of the work for the field. As a whole, the series will provide a valuable resource both for newcomers to the research fields described, and for other scientists seeking detailed background information on special questions. Finally, it provides an accredited documentation of the valuable contributions made by today's younger generation of scientists.

Theses are accepted into the series by invited nomination only and must fulfill all of the following criteria

- They must be written in good English.
- The topic should fall within the confines of Chemistry, Physics, EarthSciences, Engineering and related interdisciplinary fields such as Materials, Nanoscience, Chemical Engineering, Complex Systems and Biophysics.
- The work reported in the thesis must represent a significant scientific advance.
- If the thesis includes previously published material, permission to reproduce this must be gained from the respective copyright holder.
- They must have been examined and passed during the 12 months prior to nomination.
- Each thesis should include a foreword by the supervisor outlining the significance of its content.
- The theses should have a clearly defined structure including an introduction accessible to scientists not expert in that particular field.

More information about this series at http://www.springer.com/series/8790

Nicholas Chamberlain Stone

The Tidal Disruption of Stars by Supermassive Black Holes

An Analytic Approach

Doctoral Thesis accepted by Harvard University, USA

Springer

Nicholas Chamberlain Stone
Columbia Astrophysics Laboratory
Columbia University
New York, NY
USA

ISSN 2190-5053 ISSN 2190-5061 (electronic)
Springer Theses
ISBN 978-3-319-12675-3 ISBN 978-3-319-12676-0 (eBook)
DOI 10.1007/978-3-319-12676-0

Library of Congress Control Number: 2013955487

Springer Cham Heidelberg New York Dordrecht London

Printed on acid-free paper

Springer is part of Springer Science+Business Media (www.springer.com)

To my parents, Eve and Peter

Supervisor's Foreword

This impressive PhD thesis focuses on the rich physics associated with the tidal disruption of stars by supermassive black holes. In exploring various aspects of this astrophysical frontier, the author, Dr. Nicholas Stone, mastered advanced topics in theoretical hydrodynamics, general relativity, and stellar dynamics. The thesis shows unusual levels of creativity and physical insights. Let me illustrate these qualities with two examples.

Dr. Stone suggests that the tidal disruption rate of stars will be enhanced around a black hole that forms out of a merger between two progenitor black holes, and which then recoils as a result of anisotropic emission of gravitational waves. The standard disruption event rate is limited by the frequency at which new stars are gravitationally scattered into highly radial orbits, namely the rate at which the "loss cone" of disrupted stars is re-populated. Dr. Stone realized that if the black hole suddenly recoils relative to the background stars, then there is no need to re-populate the loss cone through relaxation processes, because the black hole encounters a fresh supply of stars along its new orbit. Dr. Stone demonstrated that the resulting rate of tidal disruption events could reach values of one per several decades, allowing the detection of multiple events per galaxy within an astronomer's lifetime.

Subsequently, Dr. Stone realized that Lense-Thirring precession due to black hole spin will lead to precession of accretion disks formed in tidal disruption events, periodic modulation of disk luminosity, and possible precession of associated jets. In 2011, the Swift satellite discovered an intense, transient gamma- and X-ray flare from a galactic nucleus at a redshift of 0.35. This flare has been explained as jet emission from a tidal disruption event aligned with our line of sight, offering a chance to probe an open question in accretion physics: which way will jets point in tilted accretion flows? Dr. Stone showed that the persistence of jetted X-ray emission in the Swift J164449.3+573451 flare over a timescale of weeks suggests that the jet aligned with the steady spin axis of the black hole (rather than the variable disk axis) during this event.

I have benefited greatly from Dr. Stone's insights during our collaboration, and I hope you will share my experience after reading this book.

Cambridge, MA, USA Avi Loeb
September 2014

Preface

This book presents a theoretical treatment of an exciting problem in astrophysics: the tidal disruption of stars by supermassive black holes (SMBHs). The multiwavelength flares produced by tidal disruption events (TDEs) have supernova-like luminosities, and their associated relativistic jets are visible to cosmological distances. TDEs probe the demography of quiescent SMBHs, and are natural laboratories for jet launching mechanisms and super-Eddington accretion. Although for many years this was an area of purely theoretical research, the first observations of TDEs began in the mid-1990s, and since then the sample of TDE candidates has grown rapidly. Many of the newest observations do not fit easily into the predictions of past TDE models, highlighting the need for renewed theoretical work on the subject.

Much state-of-the-art TDE research is done using numerical simulations, but the large hierarchy of mass, distance, time, and energy scales in tidal disruption means that analytic techniques are in many cases applicable, and often necessary. This book evolved out of my PhD thesis on stellar tidal disruption, and has retained as its central focus the study of TDEs through analytic methods. A majority of the chapters in this book represent my original research on TDEs, and they are interspersed with shorter chapters reviewing general results from the greater literature. These general chapters aim to provide a useful introduction for those new to the field, and to place the results of my thesis work in a greater context. The originality of the work presented in each chapter is covered here, and is also clearly labeled at the start of each chapter.

The first chapter broadly surveys TDE physics, and will be of the most interest to non-experts looking for a general introduction. The second chapter reviews existing literature on TDE rates to provide a formalism for calculating these rates in standard galactic nuclei. This rate calculation sets the stage for two chapters of original research; in the third and fourth chapters, we estimate the TDE rate following gravitational wave (GW) recoil of a SMBH (after a SMBH binary merger). Immediately after GW recoil, the TDE rate increases, sometimes to $\sim 10^{-1}$ TDEs per year. This "burst" of TDE flares can provide an electromagnetic counterpart to low frequency GW signals, localizing sources and measuring cosmological parameters. Millions of years later, recoiled SMBHs wandering through their host galaxies will produce spatially offset TDEs at a rate which is likely detectable with the *LSST*; this is the subject of the fourth chapter.

In the fifth chapter, we present another original research paper, showing that standard estimates for $\Delta\epsilon$, the energy spread of TDE debris, are wrong, sometimes by orders of magnitude. Correcting this error reduces the observability of many TDEs. We introduce a new analytic model for tidal disruption, calculate the dependence of $\Delta\epsilon$ on stellar spin, estimate general relativistic corrections to $\Delta\epsilon$, and quantify the GW signal generated from tidal compression.

The seventh chapter surveys past work on the importance of general relativistic effects for TDEs, describing the ways in which general relativity can modify TDE rates, the tidal disruption process, and the formation of accretion disks. Although this chapter primarily summarizes past research in the literature, it concludes with a brief summary of original, numerical research on how relativity can mediate debris circularization. The eighth chapter introduces the final original work of my thesis. In it we show that TDE light curves can constrain or measure SMBH spins, as Lense-Thirring torques produce quasiperiodic variability in disk emission. Precession of a relativistic jet could also measure SMBH spin, and we apply our model to the relativistic Swift J1644+57 TDE.

Finally, the ninth chapter offers concluding remarks, and thoughts on future directions for theoretical and observational development of this exciting subject.

Acknowledgments

This thesis would not have been possible without help from the many fantastic people who gave me the academic, technical, and personal support I needed during my 5 years at Harvard University. I will do my best to offer some much deserved thanks in this space.

I owe an immense debt to my family; to my parents most of all. From as early as I can remember, my parents kept me supplied with a continuous stream of science (and, perhaps more importantly, science fiction[1]) books. Later in life, they helped and encouraged me to succeed academically, but with a light enough touch that I always felt supported, not pressured. My sisters, too, have always been an important part of my life, and as an older brother it's been a pleasure to watch their successes—Madeleine, with her writing, and Jasmine, with her languages—during my intermittent struggles in graduate school. I am sure there will be many more of these moments in the future.

At Harvard, my thesis advisor Avi Loeb played the greatest role in my development as a scientist. I owe Avi a huge debt of gratitude for his mentorship and collaboration during the course of my PhD. One great thing about working with Avi is his openness to new ideas—our first project together was based on a question I nervously asked at his group meeting during my first semester at Harvard. Whenever I found myself stuck on a research project, Avi always made the time to help out. Since he generally has a fresh way of looking at a problem (or connecting it to another topic you're not previously aware of), these meetings usually cleared up my problems quickly. Most of what I know about being an actual, practicing scientist I have learned from Avi.

My other collaborators in research have also been great mentors and sources of inspiration. I wish to thank Re'em Sari for suggesting new ways to look at subjects I had thought I was already familiar with. Re'em's physical insights resolved many questions I couldn't find other ways to answer. Edo Berger has been a great collaborator, and also a fantastic connection to the world of observational astronomy.

[1] Although the tidal disruption of stars by black holes—the subject of this thesis—may seem like an esoteric topic, it's actually one I first read about at age 13 in a science fiction book my mother checked out of the library.

My collaborator Kimitake Hayasaki has brought reliable numerical expertise to our work, which is a great complement to my typically more analytical research. Since leaving Harvard, I have started many new research partnerships at Columbia University: Brian Metzger, Jeremiah Ostriker, Zoltan Haiman, and Aleksey Generozov have all been a pleasure to work with here. I would also like to thank my PhD thesis committee, which was chaired by Alicia Soderberg, contained Josh Grindlay, Ramesh Narayan, Avi Loeb, and Enrico Ramirez-Ruiz, and gave me many useful suggestions on an earlier version of this dissertation.

Last but not least, I owe many thanks to my friends from Cambridge, both in and out of astronomy, who made the potentially strenuous years of my PhD such a joy. In particular, I would like to thank Tarek Anous, Sarah Ballard, Zack Berta, Jon Bittner, Laura Blecha, Liz Brown, Ethan Butler, Sophie Guelff, Wen-fai Fong, Robert Harris, Michal Kolesar, Ben Kraft, Charles Krohn, Bianca Levy, Gongjie Li, Maggie McLean, Diego Munoz, Ryan O'Leary, Tony Pan, Bob Penna, Jon Rhinesmith, Sarah Rugheimer, Peter Russo, Greg Snyder, Nell Stevens, Paul Torrey, and especially Alicia Breakey.

Contents

Chapter 1
Introduction

1.1 SMBHs in Our Universe

From an observational perspective, supermassive black holes (SMBHs) are nearly ubiquitous in nearby galactic nuclei. These massive objects ($\sim 10^{5-10} M_{\odot}$) generally reside at the center of their host galaxy's stellar bulge, and can be observed either through the luminous accretion of gas, or via gravitational interactions with surrounding stellar populations. In this thesis, we focus on strong, disruptive tidal encounters between SMBHs and nearby stars, but SMBHs themselves are objects of much intrinsic interest, as we outline in this introductory section.

Mathematically, black holes are very simple objects, characterized by a mere three numbers (Wald 1984, Sect. 12.3): mass, spin, and charge[1]. For this reason, measuring the demographics of black holes is appealingly straightforward at a conceptual level - but the devil lies in the details. Although a variety of techniques can be used to measure the masses of SMBHs, the only effective approaches at large distances involve the luminous accretion flows present around a small minority of SMBHs. This introduces a potentially serious bias into SMBH mass measurements. Such bias is more pronounced for spin measurements, which for even the nearest SMBHs can only be performed by taking advantage of surrounding accretion flows. Probing the universe's "silent majority" of quiescent SMBHs is an inherently difficult task, but the many scientific motivations for studying SMBHs should encourage us to find ways to do this.

The most fundamental motivation for studying SMBHs is that as strongly relativistic objects, they offer a laboratory to probe and test general relativity (GR). Observations of Sgr A*, the SMBH in the center of the Milky Way, have provided some of the strongest evidence to date for the existence of event horizons (Broderick et al. 2009). Future observations of SgrA* (and M87's SMBH) with Very Long Baseline Interferometry will likely provide direct imaging of event horizons and the gas flows around them (Broderick and Loeb 2005; Doeleman et al. 2009; Broderick and Loeb 2009). Measurements of SMBH spin in distant galaxies using relativistically

[1] However, electric charge is expected to be negligibly small for any astrophysical black hole.

N. C. Stone, *The Tidal Disruption of Stars by Supermassive Black Holes,*
Springer Theses, DOI 10.1007/978-3-319-12676-0_1

broadened iron lines (Reynolds et al. 1999; Reynolds 2013) provide a zeroth-order check on the cosmic censorship hypothesis[2], and perhaps a more detailed test of the no-hair theorem as well (Johannsen and Psaltis 2012). Future detections of stellar motion in our own Galactic Center may enable a direct test of GR by measuring the mass, spin, and quadrupole moment[3] of Sgr A* (Merritt et al. 2010). Such a test could be facilitated by the discovery of a pulsar in the Galactic Center (Pfahl and Loeb 2004). SMBHs can also be used to probe other questions in fundamental physics; for example, general relativistic Kerr black holes are believed to possess a semiclassical instability to scalar fields in specific (low) energy ranges. The existence of spinning SMBHs in the universe places valuable constraints on massive photons (Pani et al. 2012) and other exotic light particles.

SMBHs also seem to play an integral role in the growth and evolution of galaxies. Specifically, the coevolution of galaxies and their central SMBHs has been observationally established by scaling relations linking the SMBH mass to a variety of galaxy parameters (Kormendy and Richstone 1995; Ferrarese and Merritt 2000; Ferrarese 2002; Tremaine et al. 2002; Bandara et al. 2009; Burkert and Tremaine 2010). These relationships are sometimes disputed (Kormendy and Bender 2011, for example) and are somewhat surprising, given that the SMBH mass is typically $\sim 1/500$ the total stellar mass of the bulge it resides in (Marconi and Hunt 2003). The standard explanation, at least for the well-known $M_{\rm BH} - \sigma$ relation, is that the gas accretion processes which grow a SMBH will also drive strong outflows that can self-regulate star formation through energy or momentum deposition (Silk and Rees 1998; Wyithe and Loeb 2003; Di Matteo et al. 2005; Hopkins et al. 2006). Alternative explanations, such as the central limit theorem (Peng 2007; Jahnke and Macciò 2011), exist as well, however. If there is a causal link between SMBH accretion and star formation, understanding the demographics and growth history of SMBHs becomes a crucially important step in understanding many other aspects of astrophysics.

The extreme accretion environments surrounding a minority of SMBHs are also sites of intrinsic astrophysical interest. These active galactic nuclei (AGN) are important targets for observations at all electromagnetic wavelengths. Although a full review of AGN phenomenology and accretion physics is well beyond the scope of this paper—indeed, it is the subject of many books, such as Krolik (1999) and Beckmann and Shrader (2012)—we do wish to mention a few points of interest. Because of their extreme luminosities, AGN are some of the most distant objects observed in the universe (Fan et al. 2003; Mortlock et al. 2011). Relativistic jets launched by AGN are also a possible source for observed ultra high energy cosmic rays (Biermann and Strittmatter 1987; Pierre Auger Collaboration et al. 2008; Farrar and Gruzinov 2009), whose origin is an important open question in particle astrophysics.

As a result of their compactness, large masses, and abundance (Volonteri et al. 2003), SMBH binaries (SMBHBs) are key sources for gravitational wave (GW)

[2] Which would be falsified by the discovery of a single SMBH with super-extremal spin.

[3] The black hole quadrupole moment is uniquely determined by mass and spin in GR, but not in many alternative theories of gravity (Johannsen and Psaltis 2010).

astronomy, detectable both by space-based, low frequency GW interferometers (Jennrich 2009; Amaro-Seoane et al. 2012b), and by pulsar timing arrays (Sazhin 1978; Jenet et al. 2004; Sesana et al. 2009). The coalescence of a SMBHB is an extremely energetic event, as numerical relativity simulations indicate that up to $\sim$10% of the binary rest mass energy can be radiated in GWs during the final orbits and plunge (Pretorius 2005). Small anisotropies in this final burst of gravitational radiation give a recoil kick to the merged SMBH, typically $\sim$100 km s^{-1} (Lousto et al. 2010a), but up to $\approx$5000 km s^{-1} (Campanelli et al. 2007; Lousto and Zlochower 2011; Lousto and Zlochower 2012). The instantaneous GW luminosity of such a merger can exceed the electromagnetic luminosity of the entire observable universe (Schnittman 2011), and in the right mass range ($\sim 10^{5-6} M_{\odot}$) would be detectable by a *LISA*-like instrument to any realistic redshift (Amaro-Seoane et al. 2012b, Fig. 3).

The detection of *LISA*-band GWs would lead to many scientific opportunities. By observing mergers of SMBHBs across cosmic time, SMBH demography could be studied in ways that lack the biases of AGN observations. The spins and redshifted masses of the merging SMBHs could be measured to high precision, with errors $\lesssim$1% (Klein et al. 2009; Amaro-Seoane et al. 2012b); if the merger is accompanied by an electromagnetic counterpart (to break the GW degeneracy between redshift and luminosity distance), these "standard sirens" would measure cosmological parameters independent of the standard cosmic distance ladder (Schutz 1986; Holz and Hughes 2005). Alternatively, if a low frequency GW observatory measures the GW-driven inspiral of a stellar mass compact object into a SMBH, the SMBH's Kerr spacetime could be mapped out in high precision (Ryan 1995). This would both measure the SMBH mass and spin, and test extensions of GR (Amaro-Seoane et al. 2007; Sopuerta 2010).

To summarize, both electromagnetic and GW observations of SMBHs offer immense scientific value. SMBHs are probes of strong-field GR, and also objects that play an important role in many different areas of astrophysics. In the next subsection, we briefly outline the most prominent of the many techniques used today to directly identify and measure SMBHs in our universe.

1.1.1 Observed SMBHs

The nearest SMBH, Sgr A*, resides in the center of the Milky Way. The advent of adaptive optics technology has allowed all six orbital elements to be measured for an entire population of stars, the S stars, on tight orbits around Sgr A* (Ghez et al. 2005; Gillessen et al. 2009). Until recently, the most tightly bound S-star known was S0-2 (Schödel et al. 2002), which orbited with a period of 16 years. Very recently, the much dimmer star S0-102 has been discovered to lie on an 11.5 year orbit (Meyer et al. 2012). The measurement of S star orbital properties has allowed the mass and distance of Sgr A* to be measured with high precision (Ghez et al. 2008)—although much closer S stars will need to be found in order to observe relativistic precession effects, let alone test GR (Merritt et al. 2010).

Although Sgr A* is the nearest SMBH, its extremely underluminous nature (Baganoff et al. 2003) prevented it from being the first detected by astronomers. The first strong evidence for astrophysical black holes was inferred by Lynden-Bell (1969), following earlier work by Hoyle and Fowler (1963) and Salpeter (1964). These theoretical papers were written in response to the first discoveries of quasars (Hazard et al. 1963; Schmidt 1963), which are found in much larger numbers today. AGN observations can provide SMBH mass estimates through photoionization modeling (Wandel et al. 1999) or reverberation mapping (Kaspi et al. 2000) of broad emission line regions, among other methods. As mentioned previously, observations of AGN can also measure SMBH spin through relativistically broadened iron lines (Reynolds 2013), whose profiles depend sensitively on the location of the innermost stable circular orbit (ISCO).

In the nearest galaxies, SMBH masses can be measured dynamically (albeit not as directly as for Sgr A*). This is generally accomplished using integrated stellar kinematic data (Gebhardt et al. 2000, for example) and comparing to three-integral dynamical models (Schwarzschild 1979) with ranges of SMBH masses. A different dynamical technique uses stimulated emission from water masers in SMBH accretion disks, which can provide both distance (Herrnstein et al. 1999) and mass (Greenhill et al. 1997) estimates for extragalactic SMBHs; other gas dynamical mass estimates can be used as well.

Taken together, the above techniques have taught us that SMBHs are nearly ubiquitous in nearby galactic nuclei (Kormendy and Richstone 1995; Ferrarese and Ford 2005). The SMBH mass function has been characterized using combinations of these methods, as well as host galaxy scaling relations (Franceschini et al. 1998; Shankar et al. 2004; Hopkins et al. 2007; Greene and Ho 2007). Its $z = 0$ peak is near $M_{\rm BH} \sim 10^6 - 10^7 M_\odot$, with a gradual decline at higher and perhaps lower masses (the low mass end is limited by small sample sizes and observational selection effects). The SMBH spin function seems to indicate a bias towards rapidly spinning SMBHs, but is limited by small number statistics (with roughly 20 measurements so far), strong selection effects, and a lack of independent checks on relativistic line broadening, the primary method of measurement (Reynolds 2013).

1.1.2 SMBH Formation and Growth

Despite the wealth of observational data on nearby SMBHs, and distant AGN, the origin of massive black holes in the universe is far from clear. Studying their growth and accretion history offers a few basic constraints. Soltan's argument (Soltan 1982; Yu and Tremaine 2002) indicates that typical SMBHs grow primarily through radiatively efficient accretion of gaseous matter (rather than through mergers with other SMBHs, or through the capture of stellar mass compact objects). However, the discovery of extreme quasars at high redshift (Mortlock et al. 2011, for example) suggests that at least some SMBHs were capable of reaching enormous sizes ($\gtrsim 10^9 M_\odot$) in the first Gyr of the universe. If their growth occurred due to Eddington-limited gas accretion

capable of spinning up the SMBHs, the seed black hole mass they grew from must have been quite large, in the range of $\gtrsim 10^4 M_\odot$ (Volonteri and Rees 2006). Ejection of SMBHs via GW recoil makes the observed high-z sample even more challenging to explain, although the problem can be ameliorated by invoking super-Eddington accretion (Alexander and Natarajan 2014), "chaotic accretion" of randomly aligned gas, or radiatively inefficient accretion flows (Volonteri and Rees 2006). Many different mechanisms have been proposed for the formation of SMBH seeds (Sesana 2012), of which three stand out as particularly promising:

- **Population III stellar remnants**: the first generation of stars have traditionally been estimated to reach sizable masses, hundreds of times as large as the Sun. The lack of metal line opacity in their atmospheres would limit mass loss in line driven winds, allowing for extreme supernovae that can produce black holes with $M_{\rm BH} \gtrsim 10^2 M_\odot$ (Madau and Rees 2001; Volonteri et al. 2003). Although the production of these SMBH seeds is likely more reliable than the other mechanisms listed here, the black holes produced from Population III stars are relatively small, and might have problems growing into observed high-z SMBHs assuming Eddington-limited accretion. Recent theoretical work indicating that Population III stars can fragment during formation into lower mass objects may worsen this problem (Stacy et al. 2010).
- **Star cluster instabilities**: at extreme densities, a population of stars or compact remnants can begin undergoing runaway collisions, culminating in the direct production of an intermediate mass black hole (IMBH), the ejection of all massive compact remnants, or the formation of a supermassive star. If the latter object forms, its lifetime is limited by both its available fuel and general relativistic instability, leading to slightly delayed IMBH formation. The densities required to begin this collisional runaway arise from the Spitzer instability (Spitzer 1987): the negative heat capacity of stellar systems means that the heaviest stars will sink to the center and become more tightly bound in a "core collapse" process. If the core collapse timescale is less than the lifetime of the most massive stars, the collisional runaway will begin and form a supermassive star (Devecchi and Volonteri 2009; Devecchi et al. 2010, 2012). IMBHs formed in this way will have masses $M_{\rm BH} \sim 10^3 M_\odot$, somewhat larger than in the prior scenario. Alternatively, if the core collapse timescale is longer than the relevant stellar lifetimes, then the cluster's densest central regions will be composed of stellar mass black holes. These black holes will typically eject themselves from the cluster (through strong scatterings and post-merger GW recoil), preventing IMBH formation. However, collisions in a cluster of stellar mass black holes can still produce an IMBH if their core collapse is mediated by a large-scale gas inflow that deepens the cluster potential (Davies et al. 2011). An IMBH produced in this way could possess an initial mass $M_{\rm BH} \sim 10^5 M_\odot$.
- **Direct collapse**: at high redshifts, primordial gas can collapse into a large SMBH seed, either directly (Loeb and Rasio 1994; Bromm and Loeb 2003; Mayer et al. 2010) or through a short-lived, intermediate "quasistar" phase (Begelman et al. 2006, 2008). This mechanism produces the largest SMBH seeds, generally

with $M_{\rm BH} \gtrsim 10^5 M_\odot$ - but see Begelman et al. (2008) for a scenario in which $M_{\rm BH}$ is limited to $\sim 10^3 - 10^4 M_\odot$. However, direct collapse requires somewhat delicate conditions to operate: if the dense gas is able to cool through molecular (H_2) or metal line emission, it will fragment into stars instead. Even slight metal enrichment from Population III stars could suffice to deactivate this channel of black hole formation (Volonteri et al. 2008).

Although demographics seem like the best tool to distinguish between these hypotheses, current observations of SMBHs do not yet strongly discriminate between SMBH formation mechanisms or patterns of growth. As our sample of SMBH spin measurements expands, we will increasingly be able to distinguish between growth mechanisms for SMBHs (Volonteri et al. 2005; Berti and Volonteri 2008). Spin measurements can also strengthen or relax the constraints that the present day SMBH mass function places on black hole seed masses. However, the limitations of current observational techniques will contribute significant uncertainty to any inferences drawn from SMBH demographic data. In particular, our measurements of SMBH masses and spins are biased towards the largest AGN; most SMBHs in the universe are smaller, and undergoing much weaker accretion.

More exotic future efforts could improve our understanding of SMBH demographics. In particular, low frequency GW astronomy will let us measure masses and spins of quiescent SMBHs out to large redshifts. Unfortunately, the funding situation for *LISA*-like instruments is quite uncertain, and pulsar timing arrays are unlikely to resolve any but the most massive SMBH binaries.

1.1.3 Stellar Tidal Disruption

There is one technique accessible to today's observers which enables the demographics of quiescent SMBHs to be measured. Over long timescales, stellar dynamics in galactic nuclei are collisional: the orbital parameters of individual stars change due to perturbations from other stars, compact stellar remnants, or more massive objects. Infrequently, a star can be perturbed onto an almost radial trajectory, and pass so close to the central SMBH that it is shredded by tidal forces (Hills 1975; Lidskii and Ozernoi 1979; Rees 1988). The fallback of stellar debris onto the SMBH will create a transient accretion disk, which in turn powers a luminous high-energy flare.

Roughly twenty of these tidal disruption events (TDEs) have been seen over the last two decades, and our theoretical picture of them is steadily improving. This thesis describes our work to better understand TDEs: their rates (Stone and Loeb 2011; Stone and Loeb 2012b), their dynamics (Hayasaki et al. 2013; Stone et al. 2013b), and their radiative emission (Stone and Loeb 2012a)[4]. The remainder of

[4] We also have examined an analogous scenario, in which a neutron star is tidally disrupted by a stellar mass black hole, producing a short gamma ray burst (Stone et al. 2013a). However, that type of tidal disruption is beyond the scope of this book.

this introduction will outline the current understanding of stellar tidal disruption, from both theoretical and observational perspectives. The study of TDEs is rapidly accelerating due to the wealth of new and unexpected observations over the last few years. However, if the potential of TDEs to trace SMBH demography in a less (or differently) biased way than AGN-based techniques is to be realized, much theoretical progress remains to be made. In the following introductory sections, we place special emphasis on the many important open questions which await solution.

1.2 Tidal Disruption Basics

1.2.1 The Newtonian Picture

Unlucky stars in galactic nuclei are occasionally perturbed onto nearly radial orbits. Although these trajectories are doomed by their interaction with the (strongly relativistic) central SMBH, much of the relevant physics can be derived in a Newtonian framework, which we employ here. If a star of mass M_* and radius R_* orbits a black hole of mass $M_{\rm BH}$ with orbital pericenter, $R_{\rm p}$, less than the tidal radius

$$R_{\rm t} = R_*(M_{\rm BH}/M_*)^{1/3}, \tag{1.1}$$

the star will be tidally disrupted (Hills, 1975). To within a factor of order unity, this is the same as the Roche radius or Hill radius seen in other areas of astrophysics. The strength of the disruption event can be measured by a dimensionless inverse impact parameter,

$$\beta = R_{\rm t}/R_{\rm p}, \tag{1.2}$$

which measures the strength of the tidal encounter (alternatively, some papers in the literature parametrize the strength of tidal encounters with $\eta_{\rm tidal} = \beta^{-3/2}$). Because the horizon of a black hole grows linearly with $M_{\rm BH}$, i.e.

$$R_{\rm s} = \frac{2GM_{\rm BH}}{c^2} \tag{1.3}$$

for a non-spinning hole, while the tidal radius only grows as $M_{\rm BH}^{1/3}$, above a critical mass (known as the Hills mass)

$$M_{\rm Hills} = 1.1 \times 10^8\ M_\odot\ r_*^{3/2} m_*^{-1/2}, \tag{1.4}$$

stars will be swallowed by the horizon prior to tidal disruption, making such events uninteresting from an electromagnetic point of view—although gravitational wave (GW) signals can still be emitted. In this and subsequent formulae, $r_* = R_*/R_\odot$ and $m_* = M_*/M_\odot$. We illustrate the region of parameter space accessible to TDEs in Fig. 1.1.

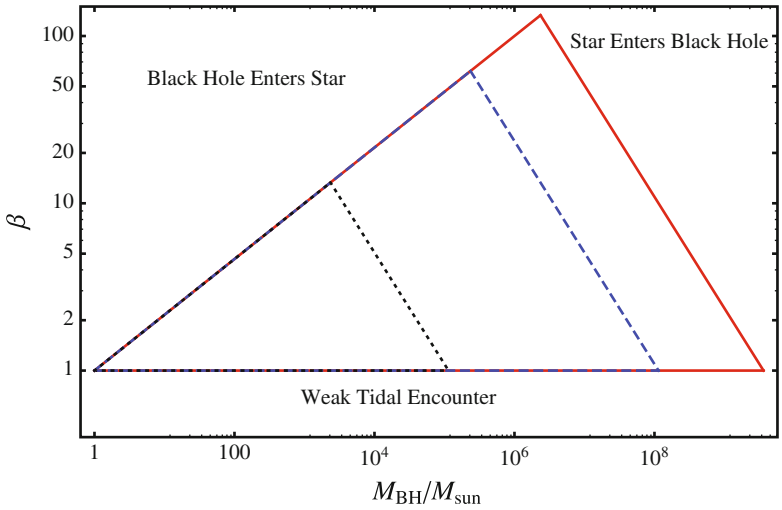

Fig. 1.1 The parameter space of tidal disruption: only a star within its respective triangle can be tidally disrupted by a black hole (Luminet and Pichon 1989). The three triangles are calculated for solar-type stars (*blue, dashed*), red giants with $M_* = M_\odot$, $R_* = 10R_\odot$ (*red, solid*), and white dwarfs with $M_* = M_\odot$, $R_* = 10^{-2}R_\odot$ (*black, dotted*). Below the triangles, $\beta < 1$ and tidal encounters are not fully disruptive. In the upper left of the diagram, $R_* > R_\mathrm{p}$ and deeply plunging orbits around small black holes lead to engulfment of the black holes by the stars. In the upper right of the diagram, the stars encounter a black hole past their Hills mass limit and are swallowed whole. Using these approximate formulae, white dwarfs, solar type stars and red giants can reach maximum β values of 13, 62, and 133, respectively

When a star is tidally disrupted, its constituent gas begins moving on roughly ballistic trajectories, with a spread of specific orbital energies that (approximately) "freezes in" at the moment of disruption, i.e. when the orbital radius $R = R_\mathrm{t}$. This spread in orbital energies arises because at the moment of disruption, leading portions of the star sit deeper in the SMBH potential well than the trailing portions, which are in shallower regions of the SMBH potential. Taking the Taylor expansion of the SMBH's potential at the star's position gives the approximate spread in debris specific energy (Rees 1988),

$$\Delta\epsilon = \frac{GM_\mathrm{BH}R_*}{R_\mathrm{t}^2}. \tag{1.5}$$

In much past literature this was incorrectly written as $GM_\mathrm{BH}R_*/R_\mathrm{p}^2$; Chapter 5 goes into significantly more detail on this disagreement. Tidal compression of the star orthogonal to the orbital plane (Carter and Luminet 1982; Carter and Luminet 1983) redistributes energies of individual fluid elements, but likely does not change the overall spread (Stone et al. 2013b; Guillochon and Ramirez-Ruiz 2013).

Most stars tidally disrupted in realistic galactic nuclei approach the SMBH on nearly parabolic, zero energy orbits whose apocenters lie at parsec scales (Magorrian

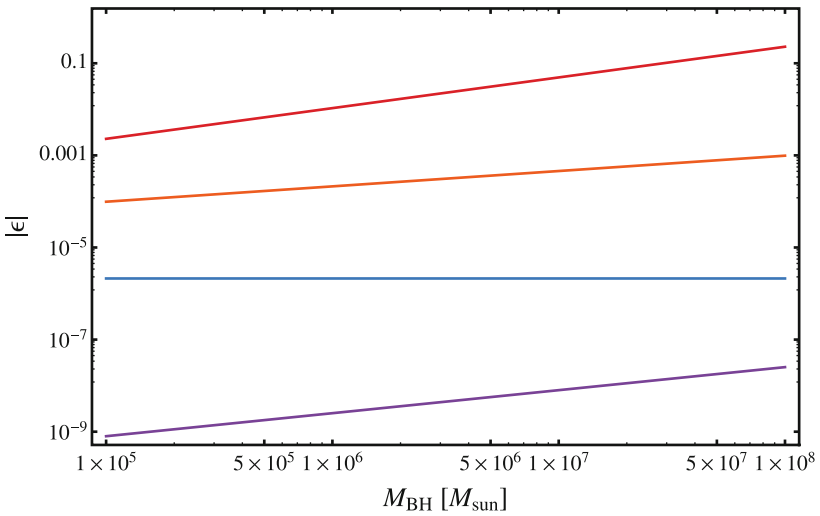

Fig. 1.2 The hierarchy of specific energy scales in stellar tidal disruption, plotted in units of c^2. The red curve shows the specific energy of circularization, $\epsilon_{\rm circ}$; the orange curve shows the frozen-in tidal energy spread $\Delta\epsilon$; the blue curve shows the star's specific binding energy, ϵ_*, and the purple curve shows the center of mass orbital specific energy for stars scattered in from the SMBH influence radius. For simplicity, we approximate the influence radius as 3 pc $(M_{\rm BH}/10^6 M_\odot)^{1/2}$. The absolute values of all energies are taken

and Tremaine 1999; Wang and Merritt 2004). We can therefore write a hierarchy of relevant specific energies, with the center of mass orbital specific energy $|\epsilon_{\rm orb}| \ll \epsilon_* \ll \Delta\epsilon$. Here $\epsilon_* = GM_*/R_*$ is the approximate specific binding energy of the star prior to disruption. Since $|\epsilon_{\rm orb}| \ll \Delta\epsilon$, the value of $\Delta\epsilon$ sets the fallback timescale for the most tightly bound debris,

$$t_{\rm fall} = 3.5 \times 10^6 \text{ s } M_6^{1/2} m_*^{-1} r_*^{3/2}. \tag{1.6}$$

Here $M_6 = M_{\rm BH}/(10^6 M_\odot)$. It is generally expected (Ulmer 1999; Strubbe and Quataert 2009), although far from established, that after a few fallback times, energy dissipation in shocks will circularize the returned tidal debris into an accretion disk, which can begin transporting gas to the SMBH through viscous processes. The exact nature of the circularization mechanism is quite uncertain, because of the inherent difficulty in numerically simulating thin debris streams travelling between a pericenter $\sim 10R_{\rm g}$ and an apocenter $\sim 10^4 R_{\rm g}$. If the material circularizes without significant loss of angular momentum in outflows, it will have a specific energy

$$|\epsilon_{\rm circ}| = \frac{GM_{\rm BH}}{2R_{\rm p}}, \tag{1.7}$$

in the limit of initially parabolic orbits. We plot the hierarchy of specific energies in Fig. 1.2.

Although we discuss the complex details of disk formation in greater detail in § 1.4 and Chap. 6, we will skip ahead here to discuss basic properties of the disk, assuming it has been established. The viscous timescale at a radius R in the disk will be

$$t_{\rm visc} = \alpha^{-1}\Omega^{-1}(R)\left(\frac{H}{R}\right)^{-2}, \tag{1.8}$$

which is generally much shorter than both the mass fallback timescale and the time t since tidal disruption. Here $\alpha < 1$ is the dimensionless Shakura-Sunyaev viscosity parameter (Shakura and Sunyaev 1973), $H(R)$ is the disk scale height, and $\Omega(R)$ is the orbital frequency. Material that returns to the disk is quickly accreted onto the SMBH, leading to a roughly steady-state accretion flow. The rate at which this accretion flow is fed with mass will be $\dot{M} = (\mathrm{d}M/\mathrm{d}\epsilon)(\mathrm{d}\epsilon/\mathrm{d}t)$. For Keplerian orbits, the derivative of orbital energy with respect to orbital period is $\mathrm{d}\epsilon/\mathrm{d}t \propto t^{-5/3}$ (Phinney 1989). If we now make the assumption, valid at late times, that the distribution of stellar debris mass $\mathrm{d}M/\mathrm{d}\epsilon$ is roughly flat with orbital specific energy, then

$$\dot{M} = \frac{M_*}{3t_{\rm fall}}\left(\frac{t}{t_{\rm fall}}\right)^{-5/3}. \tag{1.9}$$

This equation is often taken as evidence that the luminosity of a TDE flare should decline as $t^{-5/3}$; however, this is only true for the bolometric luminosity (Lodato and Rossi 2011), and is only valid at late times. At early times, our assumption of constant $\mathrm{d}M/\mathrm{d}\epsilon$ is not valid and the original structure of the disrupted star is imprinted onto the light curve evolution (Lodato et al. 2009; Guillochon and Ramirez-Ruiz 2013). For most SMBHs below the Hills mass, this rate of mass accretion is initially highly super-Eddington. If we assume a radiative efficiency $0 < \eta < 1$, the Eddington-limited mass fallback rate

$$\dot{M}_{\rm Edd} = 1.37 \times 10^{21}\ {\rm kg\ s^{-1}}\ \eta_{-1}^{-1} M_6 \tag{1.10}$$

and the peak rate of mass fallback (i.e. mass fallback at $t = t_{\rm fall}$) is

$$\frac{\dot{M}_{\rm peak}}{\dot{M}_{\rm Edd}} = 133\eta_{-1} M_6^{-3/2} m_*^2 r_*^{-3/2}. \tag{1.11}$$

Here we have defined $\eta_{-1} = \eta/0.1$. While super-Eddington, the thick, radiation pressure-dominated accretion flow may drive a powerful outflow capable of powering an exceptionally bright electromagnetic transient (Strubbe and Quataert 2009; Strubbe and Quataert 2011); we elaborate on this possibility in § 1.5. The fallback rate will decline below the Eddington limit at a time

$$t_{\rm Edd} = 2.1\ {\rm yr}\ \eta_{-1}^{3/5} M_6^{-2/5} m_*^{1/5} r_*^{3/5}, \tag{1.12}$$

after which the accretion disk will settle into a cooler and geometrically thinner configuration (Ulmer 1999). The timescales we have presented here are compared in Fig. 1.3.

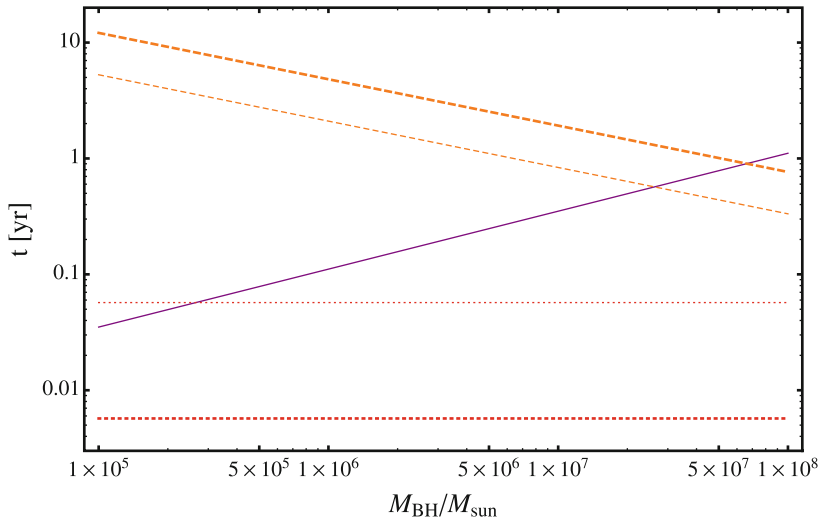

Fig. 1.3 Timescales relevant for the disruption of a solar type star by a SMBH. The *solid purple line* is $t_{\rm fall}$ as given by Eq. (1.6). The *red dotted lines* are the viscous timescale, Eq. (1.8) at an initial disk outer edge of $2R_{\rm t}$ and assuming $H/R = 0.5$; the *thick line* assumes $\alpha = 0.1$ and the *thin line* assumes $\alpha = 0.01$. The *dashed orange lines* represent the Eddington timescale, Eq. (1.12), for radiatively efficient accretion onto Schwarzschild ($\eta = 0.1$, thin curve) and extremal Kerr ($\eta = 0.4$, thick curve) SMBHs. Early time accretion fails to be super-Eddington for $M_{\rm BH} \gtrsim$ few $\times\, 10^7 M_\odot$. Matter circularized into the disk will generally accrete rapidly ($t_{\rm fall} \gg t_{\rm visc}$), although this assumption can break down for very small $M_{\rm BH}$ and α

1.2.2 The Role of General Relativity

Because real black holes are highly relativistic objects, the simple Newtonian picture presented above will be complicated by GR effects. Indeed, the first mentions of stellar tidal disruption in the literature were made by relativists interested in exotic ways to activate the classical Penrose process (Wheeler 1971). Although this original motivation no longer seems realistic, GR effects still lead to qualitatively new behavior that can be studied by TDE observations.

One simple effect concerns whether stars can be tidally disrupted or not. The Hills mass is an approximate limit in two ways, both involving the neglect of general relativity (GR) in Eq. (1.4). First, most astrophysical TDEs are expected to arise from zero energy, parabolic orbits. In GR, the minimum pericenter distance for such an orbit overlaps with the innermost bound circular orbit, or IBCO (Bardeen et al. 1972). For a non-spinning SMBH, the IBCO is located at $4R_{\rm g}$, where $R_{\rm g} = GM_{\rm BH}/c^2 = R_{\rm s}/2$. So, for non-spinning black holes, a more accurate Hills mass would have a prefactor of $4.0 \times 10^7\ M_\odot$. However, SMBH spin (in dimensionless units, a) can reposition the IBCO between $1R_{\rm g}$ (prograde equatorial orbits, $a = 1$) and $5.83R_{\rm g}$ (retrograde equatorial orbits, $a = -1$). The IBCO is also angle-dependent, and for prograde (retrograde) orbits will increase (decrease) as the orbit becomes increasingly inclined.

Favorable combinations of SMBH spin and stellar angle-of-incidence can lead to observable TDE flares for SMBH masses an order of magnitude larger than Eq. (1.4), as was shown in Beloborodov et al. (1992) and Kesden (2012b).

General relativistic gravity can also have more subtle implications. In Newtonian gravity, the vertical collapse of the star is governed by self-similar equations (Carter and Luminet 1983); this is not the case in GR (Luminet and Marck 1985, also § 1.3, § 6.2.2), which can lead to multiple compressions and bounces for high-β orbits. Circularization of TDE debris streams may be aided by apsidal GR precession, or hindered by nodal GR precession (Kochanek 1994); these possibilities are explored in greater detail in § 1.4 and § 6.4. Finally, Lense-Thirring torques felt by the circularized accretion disk can induce nearly rigid body precession, as is described in Chap. 7.

1.3 Tidal Disruption Event Rates

1.3.1 Two Body Relaxation

Most stars in a galaxy travel on effectively collisionless orbits, with trajectories determined by the smooth, large-scale potential of the galaxy rather than by discrete interactions with other stars. If we view a population of stars as a fluid out of thermodynamic equilibrium, the collisionless Boltzmann equation is generally an accurate approximation, with which the dynamics of isolated or interacting galaxies can be studied. Quantitative justification can be found for these claims by calculating, to order of magnitude, the two-body relaxation timescale for orbits in a uniform density stellar environment (Binney and Tremaine 2008, Eq. 1.38):

$$t_{\rm r} \sim 0.1 \frac{N}{\ln N} t_{\rm orb}. \tag{1.13}$$

Here N is the number of stars in the system, and $t_{\rm orb}$ is the orbital timescale. For a typical galaxy, $N \sim 10^{11}$ and $t_{\rm orb} \gtrsim 10^6$ yr, so $t_{\rm r} \gg t_{\rm Hubble}$: the galaxy is effectively collisionless.

However, the assumptions of a smooth background potential and collisionless orbits can break down in regions of extreme stellar density, such as globular clusters and galactic nuclei. For many of these dense stellar systems, $t_{\rm r} \lesssim t_{\rm Hubble}$, so two-body interactions relax stellar distribution functions toward equilibria within a Hubble time. We refer to such dense stellar systems as "collisional," even though physical collisions between stars are generally rare; our terminology refers primarily to close gravitational two-body encounters that alter stellar orbits. This type of relaxation is a crucial component of TDE rate calculations.

In the vicinity of a SMBH, the population of stars can be treated as a distribution function $f(\vec{x}, \vec{v})$ over a six dimensional phase space. For now, we only consider spherically symmetric stellar systems, meaning that these phase space coordinates

map to a conserved specific energy and angular momentum, i.e. $f(\epsilon, J)$. This distribution function will be depleted in a zone of phase space known as the "loss cone[5]," defined in terms of specific angular momentum as

$$J_{\rm LC}^2(\epsilon) \approx 2GM_{\rm BH}R_{\rm t}. \tag{1.14}$$

As in prior sections, $M_{\rm BH}$ is the black hole mass and $R_{\rm t}$ the tidal radius (we will specialize for now to the idealized case of single-mass stellar populations). Any star with specific orbital angular momentum $J = |\vec{x} \times \vec{v}| < J_{\rm LC}$ will be tidally disrupted on an orbital timescale, as its pericenter $R_{\rm p} < R_{\rm t}$. In a purely collisionless stellar system, the loss cone will drain on dynamical timescales and leave a permanent scar on $f(\vec{x}, \vec{v})$. However, in a collisional stellar environment, the relaxation of stars through ϵ and J space will slowly refill the loss cone (Bahcall and Wolf 1976; Frank and Rees 1976; Lightman and Shapiro 1977; Cohn and Kulsrud 1978). For the highly eccentric orbits which produce most TDEs, the angular momentum relaxation timescale $t_{\rm J}$ is much less than the energy relaxation timescale, $t_{\rm r}$. Specifically, the time it takes for J to change by its initial value is

$$t_{\rm J}(\epsilon, e) = t_{\rm r}(\epsilon)\frac{J^2}{J_{\rm c}^2(\epsilon)} \approx t_{\rm r}(\epsilon)(1 - e^2). \tag{1.15}$$

Here $J_{\rm c}(\epsilon)$ is the angular momentum of a circular orbit at fixed energy. Likewise, e is the orbital eccentricity at fixed semimajor axis $a(\epsilon)$, in the limit of the almost Keplerian orbits where $a(\epsilon) < r_{\rm infl}$. We have defined the SMBH's radius of influence, $r_{\rm infl}$, to be the radius which contains twice the black hole's mass in stars.

The relaxational repopulation of loss cone orbits occurs in two different regimes (Frank and Rees 1976; Lightman and Shapiro 1977). Close to the SMBH, where the loss cone is much larger than typical collisional perturbations ($\Delta J \ll J_{\rm LC}$), stars slowly diffuse into the loss cone across many orbital periods. In this "diffusive" regime, almost all TDEs have $\beta \approx 1$. Far from the SMBH, $\Delta J \gg J_{\rm LC}$, and a star can safely wander into and out of the loss cone many times during a single orbit. In this "pinhole" regime, stars are tidally disrupted with a large range of β values. The two regimes can be differentiated with a parameter,

$$q(\epsilon) = \frac{\Delta J^2(\epsilon)}{J_{\rm LC}^2(\epsilon)} = \frac{P(\epsilon)}{t_{\rm LC}(\epsilon)}, \tag{1.16}$$

where $P(\epsilon)$ is the orbital period, and $t_{\rm LC}(\epsilon) = t_{\rm r}(\epsilon)(R_{\rm t}/a(\epsilon))^2$ is the characteristic time it takes for J to change by $J_{\rm LC}$. The diffusive regime occurs for $q(\epsilon) \ll 1$; the pinhole regime for $q(\epsilon) \gg 1$.

[5] This terminology was taken by analogy from plasma kinetic theory in the 1970s (Cohn and Kulsrud 1978). At the time, American fusion research focused on magnetic confinement devices known as magnetic mirrors, which eventually proved nonviable due to plasma leaks from a geometrically conical region of phase space.

Although the idealized theory of collisional stellar dynamics near loss cones was developed long ago, it was only more recently that observations of nearby galactic nuclei enabled realistic TDE rates to be calculated (Magorrian and Tremaine 1999; Wang and Merritt 2004). For most observed galaxies, the net flux of stars into the loss cone peaks near a radius $r_{\rm crit}$, which is defined as the radius where a circular orbit has $q(\epsilon_{\rm crit}) = 1$. This critical radius, from where most TDEs originate, is by coincidence $\sim r_{\rm infl}$ (Wang and Merritt 2004). Therefore most TDEs arise from orbits at $\sim 10^0 - 10^1$ pc scales, validating § 1.2's approximation of parabolic trajectories.

Using empirically constructed galaxy models based on *Hubble Space Telescope* (*HST*) observations by the Nuker team (Lauer et al. 1995), both Magorrian and Tremaine (1999) and Wang and Merritt (2004) have estimated TDE rates over a sample of nearby galaxies. Both of these papers find TDE rates 10^{-4} yr$^{-1} \lesssim \dot{N}_{\rm TDE} \lesssim 10^{-6}$ yr^{-1}, with the integrated rate dominated by low mass galaxies that contain a steep, power law stellar density profile. TDE rates in large galaxies are suppressed by the shallower ("cored") stellar density profiles, and also by the Hills mass limit. Both of these works may slightly underestimate the true TDE rate; Magorrian and Tremaine (1999) systematically overestimates SMBH masses, while Wang and Merritt (2004) ignores the enhancement to $\dot{N}_{\rm TDE}$ from axisymmetric stellar potentials (which we elaborate on in the next sections).

1.3.2 Resonant Relaxation

Well inside a SMBH's radius of influence, the central potential of the black hole is so dominant that subrelativistic stellar orbits trace nearly closed Keplerian ellipses. If we time-average these orbits over many orbital periods, we can think of a stellar population as a system of mass-weighted wires exerting torques on each other (Rauch and Tremaine 1996). The Poisson noise produced by the discreteness of the stellar distribution function $f(\vec{x}, \vec{v})$ leads to each wire feeling net torques from the larger population of wires. Over a "coherence timescale," $t_{\rm coh}$, these torques are coherent rather than stochastic, and can therefore lead to rapid changes in orbital parameters (unlike the uncorrelated random walk through phase space produced by two-body relaxation). The relevant $t_{\rm coh}$ is the time it takes for the system of wires to change appreciably. Because the wires are fixed in space over a coherence timescale, the system's potential is stationary and orbital energy (therefore semimajor axis) is constant for each star. However, other orbital parameters are not.

Coherent changes in an orbit's eccentricity, e, are referred to as "scalar resonant relaxation" (SRR); coherent changes in the orbit's orientation, $\hat{J}$, are referred to as "vector resonant relaxation" (VRR). The VRR timescale is generally orders of magnitude shorter than the SRR timescale (Hopman and Alexander 2006). Both SRR and VRR lead to rapid evolution of $\vec{J}$ for timescales $t < t_{\rm coh}$, but random walks (in e and $\hat{J}$, respectively) for $t > t_{\rm coh}$. Orbits at fixed semimajor axis a experience

retrograde "mass precession" from the background stellar potential on a timescale

$$t_{\rm m} \sim \frac{M_{\rm BH}}{N(<a)M_*} P(a), \tag{1.17}$$

where $N(<a)$ is the number of stars at smaller semimajor axis, and P(a) is orbital period. For large values of J, this is the dominant source of precession, and $t_{\rm coh} \approx t_{\rm m}$. Closer to the black hole, GR apsidal precession dominates and $t_{\rm coh} \approx t_{\rm GR}$, where

$$t_{\rm GR} = \frac{8}{3}\frac{J^2}{J^2_{\rm IBCO}} P(a), \tag{1.18}$$

and $J_{\rm IBCO} = 4GM_{\rm BH}/c$ is the Newtonian angular momentum of an IBCO-grazing parabolic orbit.

The dynamics of SRR change dramatically for pericenters very close to the SMBH, where GR torques have more subtle effects than simple reductions of the coherence time. Recent work has identified a "Schwarzschild barrier" in $\{a, e\}$ space, along the locus of orbital parameters where the SRR timescale $t_{\rm SRR} = t_{\rm GR}$. Contrary to some previous expectations, orbits do not simply accumulate at this barrier but instead bounce backwards to lower eccentricity states. This greatly reduces SRR's ability to produce high-eccentricity encounters between stellar mass objects and an SMBH (Merritt et al. 2011; Brem et al. 2012).

Even prior to the discovery of the Schwarzschild barrier, detailed calculations had found that resonant relaxation would be a subdominant source of TDEs relative to standard two-body relaxation (Rauch and Tremaine 1996; Rauch and Ingalls 1998; Hopman and Alexander 2006; Madigan et al. 2011). This is because the bulk of stellar flux into the loss cone comes from scales $r_{\rm crit} \sim r_{\rm infl}$ at which resonant relaxation is ineffective due to mass precession from the stellar potential. However, SRR was once thought to dominate the rate of "extreme mass ratio inspirals" (EMRIs). In an EMRI, a compact stellar mass object spirals into an SMBH under gravitational radiation reaction. If observed by a *LISA*-like instrument, EMRIs would serve as superb tracers of the Kerr spacetime, enabling precision tests of GR by measuring SMBH multipole moments (Sopuerta 2010). An important side motivation for studying TDEs is to better understand the nuclear stellar populations and relaxation processes that generate EMRIs. However, the existence of the Schwarzschild barrier severely reduces realistic EMRI rates (Merritt et al. 2011)[6], and also reduces the contribution of SRR to the TDE rate even further. It is therefore reasonable to disregard SRR in TDE rate calculations, except in unusual situations where two-body relaxation is suppressed or a large population of stars exists at very small semimajor axis.

[6] It has recently been argued (Brem et al. 2012) that a subpopulation of very high eccentricity EMRIs may successfully penetrate the barrier; these were previously disregarded because it was thought they would plunge directly into the horizon. Properly accounting for SMBH spin shows that many of these "plunge" EMRIs can in fact accumulate high SNR in the *LISA* band (Amaro-Seoane et al. 2013).

1.3.3 Alternative Relaxational Mechanisms

Beyond two-body and resonant relaxation in spherical potentials, other mechanisms can also feed stars to SMBHs. In particular, axisymmetric or triaxial stellar potentials, infalling massive perturbers, SMBHBs, and the tidal separation of stellar binaries have all been suggested as ways to enhance a galaxy's TDE rate. We will briefly review each of these mechanisms here.

A significant enhancement to the TDE rate can arise if the central distribution of stars is axisymmetric or triaxial. Orbits in nonspherical potentials generally fail to conserve all components of angular momentum, and orbits in fully triaxial potentials generally conserve no components of angular momentum. Over many orbital times, this lets an individual orbit sample pericenters of arbitrarily low value, eventually falling inside the tidal radius and causing a TDE. Axisymmetric potentials can lead to modest, factor of a few enhancements to the TDE rate (Magorrian and Tremaine 1999; Vasiliev and Merritt 2013). Orbits in these potentials still conserve the component of angular momentum parallel to the symmetry axis, but in a fully triaxial potential no component of $\vec{J}$ is conserved (Poon and Merritt 2004), and a large subpopulation of stars live on centrophilic, chaotic orbits. In such a potential, $\dot{N}_{\rm TDE}$ can be enhanced by a factor $\sim$10 relative to the two-body relaxation baseline (Merritt and Poon 2004). Interestingly, the enhancement is greatest for large SMBHs near the Hills limit, which can achieve rates up to $\dot{N}_{\rm TDE} \sim 10^{-3}$ yr^{-1}. However, the long-term stability of these potentials remains unclear; in many cases, triaxial potentials evolve toward axisymmetry, reducing the TDE rate enhancement (Poon and Merritt 2004). Due to a lack of observational data, it is unclear whether the stable triaxial configurations form naturally in galaxy evolution.

Periodically, the orbits of stars in a galactic nucleus can be perturbed by an infalling massive object—a giant molecular cloud, or a star cluster, for example. These perturbations will scatter stars through phase space, helping to fill the inner regions of the loss cone and enhancing the TDE rate. This enhancement has been estimated to be substantial, and can contribute at leading order to the total TDE rate. However, because these massive perturbers are unlikely to penetrate inward of $r_{\rm crit}$ without themselves being tidally disrupted, their enhancement to the two-body $\dot{N}_{\rm TDE}$ is at most a factor of a few (Perets et al. 2007).

A massive perturber can have a greater effect on the TDE rate if it penetrates well into the empty or diffusive loss cone regime. The hardening of a SMBHB, or SMBH-IMBH binary, can accomplish this. At orbital separations comparable to the larger black hole's influence radius, the combination of Kozai effects (Ivanov et al. 2005) and chaotic three-body interactions (Chen et al. 2009, 2011) can lead to a huge enhancement in the TDE rate, perhaps up to $\sim 10^{-1}$ disruptions per year. This phase is short-lived, however, typically lasting $\sim 10^5$ yr and ending once ejection and disruption of the available stars has led the SMBH binary system to stall its hardening (Chen et al. 2011). Nonetheless, the total number of stars disrupted is substantial, and TDEs generated by SMBHBs may account for up to $\sim$3 % of the total TDE rate (Chen et al. 2011; Wegg and Bode 2011). Following the merger of an SMBHB, GW

recoil will tilt the loss cone in phase space, instantaneously refilling a portion of it; this can also elevate the TDE rate to $\sim 10^{-1}$ yr (Stone and Loeb 2011) and will be discussed in greater detail in Chap. 3.

A final source of stars to be disrupted arises when a SMBH tidally separates a binary star system (Hills 1988). One star is ejected at high speeds, often to become a hypervelocity star. The other becomes bound to the SMBH, and its subsequent orbital evolution (driven by a combination of two-body relaxation, SRR, and GW emission) determines whether it will be tidally disrupted (Amaro-Seoane et al. 2012a). If GW emission dominates, the bound star will circularize efficiently and begin stably transferring mass to the SMBH at a low luminosity (Dai and Blandford 2011). Although such mass transfer is interesting and potentially detectable, it differs qualitatively from a violent TDE. If two-body angular momentum relaxation or SRR is able to drive $R_{\rm p} < R_{\rm t}$, a TDE will be produced; however, the discovery of the Schwarzschild barrier has made this scenario somewhat uncertain. Nonetheless, the production rate of bound stars from binary separation is so large that if a substantial fraction can evolve to low angular momentum orbits, they could dominate the TDE rate and perhaps contribute substantially to SMBH growth (Bromley et al. 2012). TDEs originating from this channel might visibly differ from standard TDEs due to their lower eccentricity, which would manifest in a nonstandard light curve (Hayasaki et al. 2013, see also Chap. 6).

1.4 Dynamics of Disruption

The pioneering work of Carter and Luminet (1983) introduced a shorthand for the dynamical phases of strong star-SMBH tidal encounters which we adapt for our purposes in this paper. In phase I, the star is still a distance $R > R_{\rm t}$ from the SMBH, and exists in a slightly perturbed hydrostatic equilibrium. During this phase, the weak tidal forces from the SMBH begin to excite oscillatory modes in the star, which can be described with a straightforward linear multipole formalism (Press and Teukolsky 1977). For nondisruptive tidal encounters ($\beta \lesssim 1$), the star survives its first pericenter passage, although some mass may be lost from its envelope. Repeated pericenter passages likely occur if the star is in the "diffusive" loss cone regime, and can lead to continued mode excitation. On longer timescales the dissipation of mode energy can lead to thermal expansion of the star's envelope (Novikov et al. 1992), modulations of stellar luminosity (Alexander and Morris 2003), and runaway tidal stripping of the star (Li and Loeb 2013).

1.4.1 Vertical Collapse and Crunch: (Semi-)Analytic

Alternatively, if $\beta \gtrsim 1$, a violent and fully disruptive TDE will ensue. In phase II of a TDE, $R < R_{\rm t}$ and the star's internal forces are subdominant to the tidal acceleration

it experiences. During this stage of stellar disruption, especially if β is large, the star undergoes approximate tidal free fall, with its fluid elements moving on roughly ballistic or geodesic trajectories (altered slightly by the subdominant internal forces). It is in this regime where the dynamics of the tidal tensor,

$$\ddot{r}_i = -C_{ij} R_j, \tag{1.19}$$

are most relevant. In this notation, the vector components R_i represent positions of stellar fluid elements in the star's center of mass frame. The Newtonian tidal tensor (Brassart and Luminet 2008) is given by

$$C^{\rm N}_{ij} = \frac{G M_{\rm BH}}{R^3}\left(\delta_{ij} - 3\frac{R_i R_j}{R^2}\right). \tag{1.20}$$

Denoting $X = R\cos f$, $Y = R\sin f$, and the Z direction (normal to the orbital plane) as the 1st, 2nd, and 3rd principal axes, respectively, the nonzero components of $C^{\rm N}_{ij}$ are

$$C^{\rm N}_{11} = \frac{M_{\rm BH}}{R^3}\left(1 - 3\cos^2 f\right) \tag{1.21}$$

$$C^{\rm N}_{22} = \frac{M_{\rm BH}}{R^3}\left(1 - 3\sin^2 f\right) \tag{1.22}$$

$$C^{\rm N}_{33} = \frac{M_{\rm BH}}{R^3} \tag{1.23}$$

$$C^{\rm N}_{12} = \frac{M_{\rm BH}}{R^3}\left(-3\cos f \sin f\right). \tag{1.24}$$

An analogous, general relativistic tidal tensor can be defined for Schwarzschild or Kerr spacetimes; we write the Schwarzschild case out in Eqs. (6.21–6.24). In both cases, C_{ij} is a symmetric tensor, so $C_{21} = C_{12}$. The most important qualitative difference between the Newtonian and GR tidal tensors concerns the vertical, C_{33} component: in the Newtonian case, $\ddot{z} \propto z$, leading to a roughly homologous collapse (perfectly homologous if internal forces are neglected). Vertical tidal compression in general relativistic gravity is stronger and not self-similar.

Phase II of a TDE comes to an end when the vertical compression of the star has adiabatically increased internal pressure to the point where it competes with and then dominates both tidal acceleration and the inertia of the star's vertical collapse. The resulting vertical "bounce" of the star defines the short-lived phase III of a TDE, where the vertical pressure gradient leads to a rapid reversal of the ongoing compression. For $\beta \approx 1$, phases II and III will be overlapping and ill-defined, because in a marginal disruption (i) the tides do not strongly compress the star, (ii) the star does not remain in the tidal sphere for long, and (iii) internal forces never become truly subdominant. Further complications to this simple picture arise from the fact that different portions of the star enter the tidal sphere at different times, so that the "leading edge" of the star collapses and bounces before the center; also, the existence of a strong density contrast between the mean stellar density and the stellar core will

alter the picture of tidal free fall, as the core can only disrupt at a radius $R_t' < R_t$ (Guillochon et al. 2009).

The complex dynamics of phases I-III of stellar tidal disruption intermingle orbital mechanics, hydrodynamics, GR, and in some cases even nuclear fusion reactions. These dynamics have been studied analytically, semi-analytically using the so-called "affine model," and with the use of direct numerical simulation, in either one or three dimensions. We now will quickly review the existing literature on these stages of a TDE.

The earliest analytic estimates of hydrodynamic effects in phases II and III date back to Carter and Luminet (1982) and Carter and Luminet (1983), who were initially interested in detonating tidally compressed stars through runaway thermonuclear reactions. By analyzing the vertical equation of motion for a tidally free falling column of star, i.e. Eqs. (1.19) and (1.23), these authors estimated that the external "piston" of tidal acceleration will compress the column until the star's internal energy reaches

$$U_c \sim \beta^2 U_*, \tag{1.25}$$

the star's central density reaches

$$\rho_c \sim \beta^{-2/(\gamma-1)} \rho_*, \tag{1.26}$$

and the star's central temperature reaches

$$T_c \sim \beta^2 T_*. \tag{1.27}$$

In these approximate equations, $U_* = GM_*/R_*$, ρ_* is the pre-disruption central density of the star, T_* is the pre-disruption central temperature of the star, and γ is the star's adiabatic index. The duration of peak compression, i.e. phase III, will only last for a timescale

$$\tau_c \sim \beta^{-(\gamma+1)/(\gamma-1)} \tau_*, \tag{1.28}$$

where $\tau_* = \sqrt{R_*^3/(GM_*)}$. In Stone et al. (2013b), we coupled these hydrodynamic scaling relations to a more precise analytic model for tidal free fall to investigate the β dependence of $\Delta\epsilon$; this is described in Chap. 5.

Much early progress on the problem of stellar tidal disruption was made using the framework of the affine model (Carter and Luminet 1983), which combines the tensor virial theorem with the assumption that a tidally disrupting star can be thought of as nested ellipsoidal shells. The affine model accounts for the SMBH tidal field, stellar self-gravity, and hydrodynamic forces, and can loosely be thought of as an extension of stellar perturbation theory (Press and Teukolsky 1977) to nonlinear regimes, but restricted to the $\ell = 2$ mode. The earliest work in the affine framework validated the approximate hydrodynamic scaling relations in Eqs. (1.25), (1.26), (1.27), and (1.28). Later papers calibrated these relations and surveyed more widely the joint parameter space of β and M_* (Luminet and Carter 1986). Comparisons to full hydrodynamical

simulations indicate that the affine approximation becomes much less applicable after phase III of a disruption, when the stellar matter deviates strongly from the ellipsoidal approximation. The affine model was later placed on a more formal footing (Carter and Luminet 1985), and extended to include the effects of GR (Luminet and Marck 1985) and thermonuclear reactions (Luminet and Pichon 1989). The increased vertical tidal acceleration due to general relativistic gravity, i.e. Eq. (6.19), can lead to the star recollapsing and undergoing a second vertical bounce, provided its orbit is relativistic ($R_{\rm p} \sim R_{\rm IBCO}$) and deeply penetrating ($\beta \gg 1$). During single or multiple collapses of a main sequence star, the conditions for explosive helium burning are generally not satisfied, but alpha-capture and proton-capture reactions may lead to significant nucleosynthesis. Within the affine framework, these reactions change the composition of the star at the $\sim 1-5\,\%$ level and for $\beta \gtrsim 10$ release many times the star's original binding energy, but are still energetically subdominant to the tidally imprinted spread of debris energy, $\Delta\epsilon$ (Luminet and Pichon 1989).

More recent extensions of the affine model allow individual ellipsoidal shells to have different properties and orientations (Ivanov and Novikov 2001), enabling a treatment of partial mass loss in encounters that are not fully disruptive ($\beta \lesssim 1$). Later work using the extended affine model found reasonably good agreement between its results and those of three dimensional grid-based simulations (Ivanov et al. 2003). The extended affine model has also been used to produce realistic, angle-dependent cross-sections for disruption and swallowing of main sequence stars by spinning SMBHs (Ivanov and Chernyakova 2006).

1.4.2 Vertical Collapse and Crunch: Hydrodynamic Simulations

Although the affine model and its descendants are computationally efficient and provide analytic insight, they are ultimately limited by their assumptions, so for a fully self-consistent treatment of stellar tidal disruption it is necessary to use hydrodynamical simulations. Such simulations discretize either mass or volume and then integrate the equations of hydrodynamics in a Lagrangian or Eulerian way, respectively. For the problem of stellar TDEs, the Lagrangian approach is generally implemented with Smoothed Particle Hydrodynamics (Lucy 1977, hereafter SPH) algorithms, dating back to the pioneering work of Nolthenius and Katz (1982), which was limited by the small number of SPH particles used per simulation (40). Subsequent simulations by Bicknell and Gingold (1983) increased the number of SPH particles to 2000, and found significantly less tidal compression than in the affine model. This was later attributed to numerical viscosity and insufficient vertical resolution (Luminet and Carter 1986), but as we shall see, disagreements along these lines have persisted with more modern simulations. Later generations of three dimensional SPH simulations verified analytic expectations for $\Delta\epsilon$ (Evans and Kochanek 1989, but only for the $\beta = 1$ case), examined the role of GR by adapting SPH to curved spacetimes (Laguna et al. 1993), followed the evolution of returning debris streams (Ayal et al. 2000), measured the imprint of stellar structure on the early-time, rising

portion of a TDE lightcurve (Lodato et al. 2009), and simulated debris circularization in eccentric center of mass trajectories (Hayasaki et al. 2013, see also Chap. 6).

Complementary efforts by grid-based hydrodynamics codes began later, with early work focusing on partial mass loss and mode excitation in weak tidal encounters (Khokhlov et al. 1993b), as well as the transition to complete disruption for higher β values (Khokhlov et al. 1993a). Similar techniques were combined with the GR tidal tensor and center of mass trajectories to examine the impact of relativity on disruptions of white dwarfs by IMBHs (Frolov et al. 1994). A subsequent paper conducted the first systematic exploration of parameter space for nondisruptive tidal encounters (Diener et al. 1997). More recently, grid-based one dimensional simulations have followed vertically collapsing columns of star at high resolution with the aim of precisely capturing shocks launched during phase III, both in Newtonian (Brassart and Luminet 2008) and general relativistic (Brassart and Luminet 2010) gravity. These one dimensional works found degrees of compression in close agreement with earlier affine model studies (Luminet and Marck 1985; Luminet and Carter 1986), but in disagreement with state of the art three dimensional Eulerian simulations (Guillochon et al. 2009), which found a significantly smaller degree of vertical compression. This difference is likely due to a combination of lower resolution in the three dimensional simulations, physical three dimensional effects (e.g., pressure waves communicating between the fully collapsed, phase III leading edge of the star, and the more central portions of the star still undergoing phase II compression), and possible inaccuracies introduced via one dimensional initial conditions[7]. A parameter study of three dimensional simulations has also investigated the β dependence of the $\mathrm{d}M/\mathrm{d}\epsilon$ mass distribution, finding both the critical β values leading to full disruption, and a lack of β dependence in fully disruptive encounters (Guillochon and Ramirez-Ruiz, 2013). This last finding parallels analytic work (Stone et al. 2013b) presented in Chap. 5 of this thesis.

1.4.3 Debris Expansion and Circularization

Following the vertical bounce of the star, internal forces again become negligible, beginning phase IV of a TDE: free expansion. At this point, half the star's mass is unbound from the SMBH and enters onto its escape trajectory, while the other half remains bound. In this phase of expansion, the star is governed by the same tidal equations that dominated phase II. As mentioned before, this can lead to another vertical collapse for deeply plunging, relativistic orbits. Eq. (1.19) ceases to describe the dynamics of the stellar debris as it leaves the tidal sphere, due to its increasing physical size and (for low β) the reemerging importance of internal forces. Phase V of a TDE - the dynamics of thin, gaseous debris streams - is the least studied, due to the difficulty of direct numerical simulation. The most tightly bound debris stream

[7] James Guillochon, Morgan MacLeod, and Enrico Ramirez-Ruiz, private communication.

has an eccentricity

$$e_{\rm min} = 1 - \beta^{-1} \left(\frac{M_{\rm BH}}{M_*} \right)^{-1/3}, \tag{1.29}$$

implying that the orbital apocenter will be at least two orders of magnitude larger than orbital pericenter for star-SMBH TDEs. The evolution of the stellar debris as it leaves the tidal sphere depends sensitively on both β and the initial structure of the star. For marginal, $\beta \approx 1$ disruptions, a surviving stellar core can accrete a large portion of the debris through gravitational collapse. Even for fully disruptive $\beta \approx 1$ encounters, self-gravity can have important effects on stream evolution (Kochanek 1994).

Two mechanisms for debris circularization have been proposed so far in the literature. In the first of these models, apsidal GR precession causes tightly bound debris that has completed its second pericenter passage to intersect with less bound debris still returning from its first apocenter. Shocks will form in the large-angle collision between these streams, dissipating energy and leading to circularization (Rees 1988), a process which has been seen in our hydrodynamical simulations of eccentric ($e = 0.8$) TDEs around SMBHs (Hayasaki et al. 2013, also see § 6.4). This circularization mechanism could be delayed, perhaps strongly, by nodal GR precession from Lense-Thirring torques around rapidly spinning SMBHs (Kochanek 1994). An alternate type of circularization can arise from vertical compression of stellar debris during second (and later) pericenter passages, when the thin streams are funneled by tidal acceleration into a vertically compressed "nozzle." The convergent flow at pericenter leads to shocks. Direct energy dissipation in the nozzle is unlikely to be an efficient circularizer; if we assume roughly ballistic motion for the stellar debris between the first and second pericenter passages, the specific kinetic energy of vertical collapse at pericenter return will be $\epsilon_z \sim \beta^2 (G M_*/R_*)$, so that even if 100% of this energy is dissipated in shocks, the gas will need to return to pericenter

$$N_{\rm peri} \sim \frac{1}{2\beta} \left(\frac{M_{\rm BH}}{M_*} \right)^{2/3} \tag{1.30}$$

times in order to circularize[8]. However, shocks in the nozzle do change the orbital parameters of the gas exiting pericenter, which can lead to an effective apsidal precession, circularizing the gas through collisions and shocks with material returning from its first apocenter passage (as in the GR precession case). This type of circularization has been seen in simulations of stars on parabolic orbits disrupted by $10^3 M_\odot$ IMBHs (Ramirez-Ruiz & Rosswog 2009), but it is unclear whether this mechanism

[8] This argument could break down if a large fraction of the debris re-collapses due to gravitational instability, but it is not clear whether that would aid or hinder nozzle-driven circularization (it would certainly hinder GR-driven circularization, by reducing the stream cross-section and magnifying the impact of nodal GR precession). This is because the collapsed streams will see a higher effective β, but will likely have a lower specific internal energy than the original star.

scales up to $e = 1$, star-SMBH disruptions[9]. Analogously, the GR-mediated circularization seen in the $e = 0.8$, star-SMBH TDEs of Hayasaki et al. (2013) has not been demonstrated to scale up to the canonical $e = 1$, star-SMBH TDE scenario. The question of debris circularization is a subtle one that needs to be resolved before theorists can hope to understand the earliest emission from stellar tidal disruption flares. This is an important question to address because the early-time, rising portion of a TDE light curve may encode the parameters of the disrupted star (Lodato et al. 2009; Guillochon and Ramirez-Ruiz 2013). A second motivation for understanding debris circularization is that if GR precession is the dominant mechanism, the spin of the SMBH may be encoded into the circularization timescale.

1.5 Accretion of Circularized Debris

Although the process of debris circularization is complex and, as of now, poorly understood, it is reasonable to assume that at some point after tidal disruption, a circularized accretion flow will exist around the SMBH. The evolution and emission of this transient accretion disk has been the subject of much theoretical study, as it relates much more directly to observations than do many of the subtle dynamical processes in § 1.3 and § 1.4.

The short viscous timescales of these disks suggest that mass accretion onto the SMBH is limited by the supply of fallback material into the disk, rather than internal viscous processes. For example, in the simple analytic slim disk model of Strubbe and Quataert (2009), the time since disruption is greater than Eq. (1.8) for $\sim 1 - 3$ yr. On timescales longer than this, a reservoir of fallback material will accumulate, and the supply of fuel to the SMBH will be governed by the (now slow) viscous transport of material within the accretion disk (Cannizzo et al. 1990). For SMBHs with $M_{\rm BH} \lesssim 2 \times 10^7\ M_\odot$, the disk will initially pass through a stage of super-Eddington accretion, before the mass fallback rate declines and the disk becomes cool and geometrically thin. At very late times, the disk may once again become thick as it transitions into a radiatively inefficient mode of accretion.

While the late-time evolution of the disk has been described analytically by Cannizzo et al. (1990), the early-time disk evolution can be studied with the time-dependent slim disk model of Strubbe and Quataert (2009). In this model, the disk can be treated as a multicolor blackbody, where each disk mass annulus of radius R

[9] The SPH simulations of Ayal et al. (2000) appear to capture nozzle-driven circularization in $e = 1$, $M_{\rm BH} = 10^6 M_\odot$ TDEs. However, the reliability of these results may be limited by (i) the difficulty of accurately capturing shocks in SPH codes, (ii) the low particle resolution ($N = 5000$) of these simulations, and (iii) the particle-splitting algorithm employed to address resolution issues, since the vertical compression of the star will be sensitive to spurious changes in stream geometry. If vertical compression at pericenter is under-resolved, the net effect will be unphysical velocity perturbations in the orbital plane (Guillochon et al. 2009; Stone et al. 2013b) and correspondingly unphysical apsidal precession.

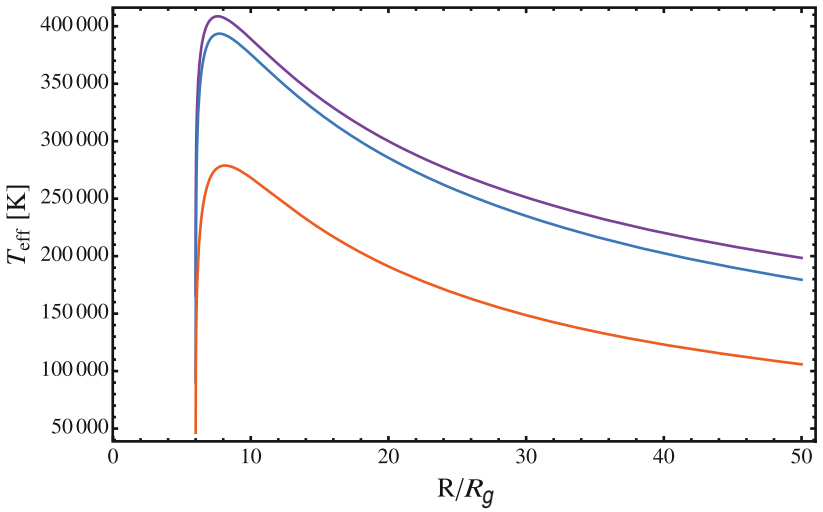

Fig. 1.4 Temperature profiles for the "slim disks" of Strubbe and Quataert (2009). All curves represent disks formed from the disruption of a solar-type star by a $10^6 M_\odot$ SMBH. The purple curve is at a time $t = t_{\rm fall}$, the blue curve is at a time $t = 10t_{\rm fall}$, and the orange curve is at a time $t = 20t_{\rm fall}$. The accretion rate reaches the Eddington limit at $\approx 19t_{\rm fall}$

possesses an effective temperature

$$T_{\rm eff}^4 = \frac{3GM_{\rm BH}\dot{M}f}{8\pi\sigma R^3}\left\{\frac{1}{2}+\left[\frac{1}{4}+\frac{3}{2}f\left(\frac{10\dot{M}}{\dot{M}_{\rm Edd}}\right)^2\left(\frac{R}{R_{\rm S}}\right)^{-2}\right]^{1/2}\right\}^{-1}, \tag{1.31}$$

and scale height

$$\frac{H}{R} = \frac{3f}{4}\frac{10\dot{M}}{\dot{M}_{\rm Edd}}\frac{R_{\rm S}}{R}\left\{\frac{1}{2}+\left[\frac{1}{4}+\frac{3}{2}f\left(\frac{10\dot{M}}{\dot{M}_{\rm Edd}}\right)^2\left(\frac{R}{R_{\rm S}}\right)^{-2}\right]^{1/2}\right\}^{-1}. \tag{1.32}$$

Here σ is the Stefan-Boltzmann constant, and $f = 1-(R_{\rm ISCO}/R)^{1/2}$. We can also compute the disk surface density profile, $\Sigma(R)$, using the relation

$$\Sigma = \frac{\dot{M}}{3\pi\alpha H\Omega_{\rm K}}, \tag{1.33}$$

where $\Omega_{\rm K}$ is the Keplerian orbital frequency. We plot the temperature, height, and surface density profiles in Figs. 1.4, 1.5, and 1.6, respectively. Because of the simplicity of this model, we will make use of it several times in this paper (Chaps. 3, 7).

Although the bolometric luminosity of TDE accretion disks (at early times, when $t < t_{\rm visc}$) may scale as $L \propto \dot{M} \propto t^{-5/3}$, disk emission is likely peaked in the UV

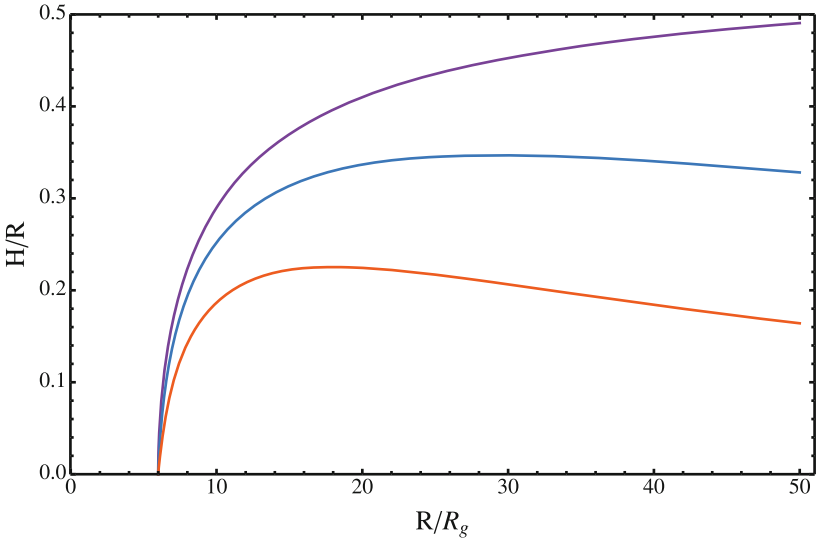

Fig. 1.5 Normalized disk height (H/R) profiles for the "slim disks" of Strubbe and Quataert (2009). The line styles are the same as in Fig. 1.4

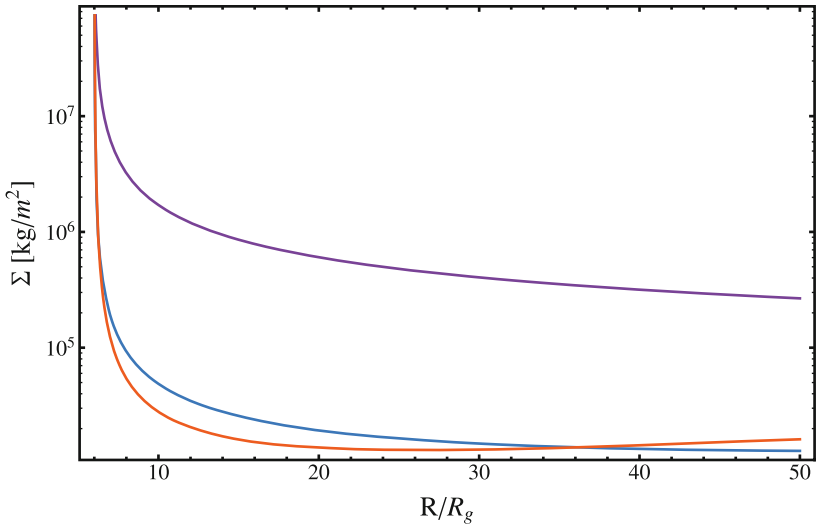

Fig. 1.6 Surface density profiles for the "slim disks" of Strubbe and Quataert (2009). The line styles are the same as in Fig. 1.4

or soft X-ray, and wavelengths far from this peak will see distinct time evolution. In particular, if we are observing the Rayleigh-Jeans tail of disk emission (as will usually be the case for optical instruments), $L \propto t^{-5/12}$ (Lodato and Rossi 2011). At very late times, observations may move to wavelengths shorter than the blackbody temperature of the inner disk edge; at this point the observed luminosity will exponentially decline in time. It remains unclear why so many UV and optical observations of TDEs see luminosity declining with approximately $t^{-5/3}$ power laws (Gezari et al. 2012, for example); these observations may suggest significant reprocessing of disk luminosity.

At the low end of the SMBH mass function, a significant source of non-continuum emission may be emission lines formed when the unbound debris reprocesses hard radiation from the central accretion disk. The half of the star that is dynamically ejected expands as it travels away from the SMBH, forming a wall of gas subtending a solid angle

$$\Delta\Omega \sim 48^{1/2}(R_*/R_\mathrm{t})^{3/2} \sim 7 \times 10^{-3} M_6^{-1/2} m_*^{1/2} \tag{1.34}$$

on the sky (Strubbe and Quataert 2009). The gas remains mostly neutral, but with a very thin ionization front that emits broad emission lines (the velocity dispersion of the gas is $\Delta v \approx \sqrt{\Delta\epsilon} \approx 4.4 \times 10^6$ m s$^{-1} M_6^{1/2} m_*^{1/3} r_*^{-1/2}$). These lines are generally weak, but are stronger for small SMBHs and at late times (Strubbe and Quataert 2009). Recombination in the ejected gas may also power a short-lived optical transient (Kasen and Ramirez-Ruiz 2010). However, recent simulations (Guillochon et al. 2014) suggest that gravitational recollapse of unbound streams with $\beta \lesssim 3$ would reduce their covering fraction by orders of magnitude, effectively eliminating all emission lines from these events.

During the earliest stages of disk accretion, when $t < t_\mathrm{Edd}$, the accretion disk will be geometrically thick and radiation pressure dominated. There are many uncertainties about such super-Eddington accretion flows, but most existing radiation hydrodynamics simulations indicate that they can drive powerful outflowing winds (Ohsuga et al. 2005; Ohsuga and Mineshige 2011). As these outflows expand and adiabatically cool, their photosphere emits like a blackbody peaked in the optical. The presence of a strong super-Eddington outflow can increase the optical luminosity of a TDE by orders of magnitude, strongly enhancing detectability by optical time domain surveys (Strubbe and Quataert 2009; Lodato and Rossi 2011). Such an outflow would be characterized by strong UV absorption lines (Strubbe and Quataert 2011). A qualitatively different model for the super-Eddington stage of a TDE flare would be the formation of a roughly spherical envelope, near hydrostatic equilibrium and supported by radiation pressure (Loeb and Ulmer 1997). A more spherical geometry could be achieved if circularization is delayed by Lense-Thirring precession, and the orbital planes of the debris streams are strongly isotropized. However, achieving hydrostatic equilibrium requires a fine-tuning of $\dot{M} \approx \dot{M}_\mathrm{Edd}$, and significantly super-Eddington accretion rates will lead to an expansion of the envelope that may develop into a wind rather than reaching a new equilibrium (Ulmer et al. 1998).

A final source of electromagnetic emission in TDEs is the launching of collimated relativistic jets. Such jets are seen in a wide range of accreting black hole systems, from puny galactic microquasars to the largest extragalactic blazars. Only, recently,

however, has interest in TDE jets arisen, with a handful of theoretical papers (Farrar and Gruzinov 2009; Giannios and Metzger 2011) preceding the observational discovery of one (Bloom et al. 2011; Zauderer et al. 2011; Levan et al. 2011) or possibly two (Cenko et al. 2012b) relativistic TDE flares by the *Swift* satellite. These unexpected observational discoveries have sparked much theoretical interest in TDE jets. These jets have been studied as sources of ultra high energy cosmic rays (Farrar and Gruzinov 2009), tools for measuring SMBH spin (Stone and Loeb 2012a), and probes of the gaseous circumnuclear medium (De Colle et al. 2012; Metzger et al. 2012). Furthermore, the relatively clean initial conditions of a TDE makes such jets ideal laboratories to examine open questions about the roles played by net magnetic flux (Giannios and Metzger 2011) and disk-jet misalignment (Stone and Loeb 2012a, Chap. 7) in jet launching mechanisms.

1.6 Observed Flares

The first strong candidate tidal disruption flares were found by X-ray instruments in the mid-1990s (Brandt et al. 1995; Grupe et al. 1995; Bade et al. 1996). In the nearly 20 years since then, roughly twenty more events have been found. The rate of TDE detection is increasing rapidly, as is the quality of observations. Upcoming time-domain optical surveys, in particular the *LSST*, could discover hundreds to thousands of TDEs *every year* (Gezari et al. 2009; Strubbe and Quataert 2009), finally realizing the promise of TDEs as probes of SMBH demography. In this section, we review the history of TDE observations.

1.6.1 X-ray and UV Observations

The satellite Röntgensatellit (*ROSAT*) conducted a low-cadence X-ray and EUV survey which detected several candidate tidal disruption flares (Brandt et al. 1995; Grupe et al. 1995; Bade et al. 1996; Komossa and Bade 1999; Komossa and Greiner 1999). The long time lag between observations ($\gtrsim$6 months) makes it challenging to compare these early flares to detailed TDE models, but in general the strongest candidates (e.g. RX J1242.6-1119A) possessed several convincing characteristics:

- Large amplitude nuclear X-ray variability. Standard AGN vary their X-ray luminosity by factors of a few, rather than the multiple orders of magnitude expected for TDEs.
- A relatively soft X-ray spectrum, consistent with models of TDE accretion disks.
- No signs of prior host galaxy AGN activity in optical spectroscopy (e.g. no narrow line region).

From these earliest TDE candidates it was already clear that multiwavelength observations are key for distinguishing TDEs from other sources of high-energy emission.

Followup *HST* spectroscopy helped to clarify the *ROSAT* candidate hosts, classifying one as a likely AGN and two others as inactive galaxies (Gezari et al. 2003). Likewise, *Chandra* followup observations found evidence for huge (factors of $10^2 - 10^4$) declines in the X-ray luminosity of all three strong *ROSAT* TDE candidates, supporting the TDE hypothesis (Halpern et al. 2004). Attempts to extrapolate a TDE rate from the *ROSAT* sample (Donley et al. 2002), although limited by selection effects and small number statistics, found a low rate, $\sim 10^{-5}$ galaxy^{-1} yr^{-1}, broadly consistent with (albeit somewhat below) theoretical expectations (Magorrian and Tremaine 1999).

A similar X-ray survey performed with *XMM-Newton* identified two more likely TDE flares (Esquej et al. 2008) with the aid of X-ray and optical followup. Other *XMM* TDE candidates were later detected (Saxton et al. 2012b), while *XMM* followup was also used to strengthen the case for *ROSAT* flares (Komossa et al. 2004). In the UV, the *GALEX* satellite identified three candidate TDE flares (Gezari et al. 2006; Gezari et al. 2008; Gezari et al. 2009), all of which seemed to originate from inactive galactic nuclei. All of the *GALEX* flares were fit surprisingly well by $t^{-5/3}$ decay laws and simple blackbody spectra, and the masses inferred from simple TDE models, while somewhat imprecise, were in agreement with galaxy scaling relations. The large fitted size of the emitting blackbodies, $\sim 10 R_{\rm t}$, may imply a large shell of matter reprocessing emission from the inner disk, as in Loeb and Ulmer (1997); Ulmer et al. (1998).

1.6.2 Optical Detection of TDEs

At longer wavelengths, two TDE candidates have been found (van Velzen et al. 2011b) in *Sloan Digital Sky Survey* (*SDSS*) archival searches (in combination with *GALEX* archival data). *SDSS* data combined with followup spectroscopy has also found a sample of seven extreme coronal line emitters (ECLEs), which can be interpreted as light echoes of recent SMBH flares, possibly originating in stellar tidal disruption (Komossa et al. 2009; Wang et al. 2011; Wang et al. 2012). Although this novel spectroscopic diagnostic shows great promise as a way to detect TDEs, and to probe the central gas distributions of distant galaxies, it remains relatively unexplored from a theoretical perspective. Due to selection effects, it is also difficult to correlate against other samples of TDE candidates; most prior searches explicitly discarded TDE candidates with strong line emission as a cut against pre-existing AGN (Wang et al. 2012). An improved theoretical understanding of the light echoes generated by TDEs would help validate the ECLE sample of TDE candidates.

The advent of time domain optical astronomy raises the prospect of a large, high cadence TDE sample. However, optically-selected TDE flares are more susceptible to confusion with (intrinsically more common) nuclear Type II supernovae, and also depend sensitively on the uncertain details of super-Eddington accretion. One such TDE candidate found by the *Palomar Transient Factory* was observed to decay very quickly, over $\approx$10 days (Cenko et al. 2012a). If this was in fact a tidal disruption

flare, it emphasizes the need for high cadence optical surveys. Very recently, the discovery of a UV/optical flare with *GALEX* and *Pan-STARRS* data has provided our most detailed look at a presumptive TDE (Gezari et al. 2012). The excellent time resolution of this event's observations allows detailed comparisons to TDE models. The authors even compare the "rising" portion of the light curve to predictions about the effects of stellar structure variation across the main sequence (Lodato et al. 2009). The most mysterious aspect of this TDE candidate, however, is the presence of helium lines and the absence of hydrogen lines. Tidally disrupting helium stars at a significant fraction of the total TDE rate is a nontrivial dynamical challenge, but so too is hiding the hydrogen from the disruption of a main sequence star.

1.6.3 Relativistic TDEs

Finally, there appears to be a subset of TDE flares capable of emitting powerful relativistic jets; if seen on-axis, these blazar-like objects can be observed at cosmological distance in hard X-rays and soft γ-rays. The 2012 discovery of two such relativistic TDEs by the *Swift* satellite has generated much interest in these events, as they offer a new TDE detection method, probe the central regions of distant galactic nuclei, and serve as laboratories for studying jet launching mechanisms. The first event, Swift J1644+57, was observed in the nucleus of a galaxy at a redshift of $z = 0.354$, and has been widely interpreted as the onset of a tidal disruption flare (Bloom et al. 2011; Burrows et al. 2011; Levan et al. 2011) due to rapid variability and lack of prior activity, although alternative explanations exist (Quataert and Kasen 2012). Despite optical nondetection of this flare (Bloom et al. 2011), possibly due to dust extinction, Swift J1644+57 has been observed in radio wavelengths (Zauderer et al. 2011), where the late time radio light curve indicates jet interaction with circumnuclear gas (Zauderer et al. 2013). The second event, Swift J2058+05, was seen at a redshift of $z = 1.1853$ (Cenko et al. 2012b). Unlike Swift J1644+57, this event was bright in the optical and so far lacks a detected host galaxy.

Even off-axis, the late-time radio afterglows of these jets may be detectable (although Doppler boosting will reduce the observed flux). *Very Large Array* (*VLA*) followup observations of seven previously detected TDE candidates all failed to detect 5 GHz radio emission (van Velzen et al. 2013). Different *VLA* observations of seven X-ray selected TDE candidates found two possible radio counterparts (Bower et al. 2013), possibly indicating a dichotomy in TDE jet production, with unknown variables (such as SMBH spin, orbital pericenter, or spin-orbit alignment) dictating whether or not jets occur.

Taken together, observations at all wavelengths provide convincing evidence for tidal disruption flares in rough agreement with our first-order theoretical picture. The onus is now on theorists to improve existing models for the rates and properties of these flares, both to better understand our existing sample of events and to maximize the scientific yield of future surveys. Only by combining future observations with improved theoretical modeling can we use these dramatic events to probe GR phenomena, and to study SMBH demographics across cosmic time.

Chapter 2
Tidal Disruption Rates from Two-Body Relaxation

2.1 Introduction

In this chapter, we review the standard TDE rate calculation in greater detail than was covered in the introduction. This is meant to provide context for the following two chapters of this thesis, which cover original work on ways in which tidal disruption rates are affected by SMBH recoil. These standard TDE rate estimates are also highly valuable calculations in their own right! Throughout this chapter, we will follow the relatively recent work of Wang and Merritt (2004), which represents a simplification of many other works on TDE rate calculations (Lightman and Shapiro 1977; Cohn and Kulsrud 1978; Magorrian and Tremaine 1999). This approach is therefore pedagogically appealing, but the interested reader is advised to thoroughly review the classical two-body relaxation literature for a fuller picture.

2.2 Two Body Relaxation

The loss cone of a SMBH can be defined as the region in angular momentum space for which

$$J^2 < J_{\rm LC}^2(\epsilon) = 2r_{\rm t}^2(\psi(r_{\rm t}) - \epsilon) \approx 2GM_{\rm BH}r_{\rm t}, \tag{2.1}$$

where $M_{\rm BH}$ is the black hole mass, $r_{\rm t}$ is the stellar tidal radius, J is specific orbital angular momentum, ϵ is specific orbital energy, and $\psi(r)$ is the gravitational potential at a radius r from the SMBH, which is assumed to lie in the bottom of the stellar potential well[1]. Throughout this chapter we employ the common stellar dynamical convention of negating the standard definitions of orbital energy and gravitational

[1] In this chapter we denote three dimensional radii with r rather than R to avoid confusion with an angular momentum-like variable.

N. C. Stone, *The Tidal Disruption of Stars by Supermassive Black Holes,*
Springer Theses, DOI 10.1007/978-3-319-12676-0_2

potential; that is to say, $\psi > 0$ and, for bound stars, so is ϵ. The gravitational potential is defined as

$$\psi(r) = \psi_*(r) + \frac{GM_{\rm BH}}{r}. \tag{2.2}$$

We will now make the assumption of a spherical star cluster surrounding the SMBH, with a stellar mass density profile $\rho(r)$. We will also employ the equivalent stellar number density profile, $n(r)$, throughout this section. This enables us to write the stellar potential as

$$\psi_*(r) = \frac{GM(r)}{r} + 4\pi G \int_{r'}^{\infty} \rho(r')r'\mathrm{d}r', \tag{2.3}$$

where $M(r)$ is the total stellar mass enclosed at a radius r. With this potential in hand, we can calculate the stellar distribution function using the Eddington formula:

$$\begin{aligned} f(\epsilon) &= \frac{1}{\pi^2\sqrt{8}} \frac{\mathrm{d}}{\mathrm{d}\epsilon} \int_0^{\epsilon} \frac{\mathrm{d}n}{\mathrm{d}\psi} \frac{\mathrm{d}\psi}{\sqrt{\epsilon - \psi}} \\ &= \frac{1}{\pi^2\sqrt{8}} \left(\int_0^{\epsilon} \frac{\mathrm{d}^2 n}{\mathrm{d}\psi^2} \frac{\mathrm{d}\psi}{\sqrt{\epsilon - \psi}} + \frac{1}{\sqrt{\epsilon}} \left(\frac{\mathrm{d}n}{\mathrm{d}\psi} \right)_{\psi=0} \right). \end{aligned} \tag{2.4}$$

Using the distribution function $f(\epsilon)$, we can now calculate the flux of stars into the loss cone, $\mathcal{F}(\epsilon)$. Integrating this over all energies will give the total stellar disruption rate for a given galaxy,

$$\dot{N}_{\rm TDE} = \int \mathcal{F}(\epsilon)\mathrm{d}\epsilon. \tag{2.5}$$

To calculate $\mathcal{F}(\epsilon)$, we define the angular momentum proxy

$$R = \frac{J^2}{J_{\rm LC}^2}, \tag{2.6}$$

which we shall use to define an orbit-averaged angular momentum diffusion coefficient,

$$\bar{\mu}(\epsilon) = \frac{2}{P(\epsilon)} \int_{r_{\rm p}}^{r_{\rm a}} \frac{\mathrm{d}r}{v_{\rm r}(r)} \lim_{R->0} \frac{\langle (\Delta R)^2 \rangle}{2R}. \tag{2.7}$$

Here $P(\epsilon)$ is the orbital period, $v_{\rm r}(r)$ is the radial component of orbital velocity, and the locally-defined angular momentum diffusion coefficient is

$$\lim_{R->0} \frac{\langle (\Delta R)^2 \rangle}{2R} = \frac{32\pi^2 r^2 G^2 M_*^2 \ln\Lambda}{3J_{\rm c}^2(\epsilon)} \left(3I_{1/2}(\epsilon) - I_{3/2}(\epsilon) + 2I_0 \right). \tag{2.8}$$

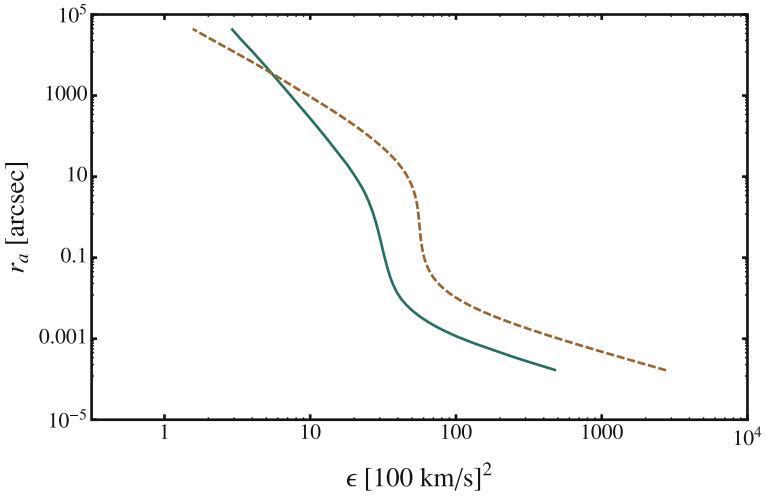

Fig. 2.1 The apocenter of a radial orbit, $r_{\rm a}$, plotted against orbital energy ϵ, for the cusp galaxy NGC 4551 (*solid green line*) and the core galaxy NGC 4168 (*dashed brown line*). NGC 4551 has $M_{\rm BH} = 10^{7.11} M_\odot$, while NGC 4168 has $M_{\rm BH} = 10^{7.89} M_\odot$

For simplicity we assume that all stars in the cusp have the same mass[2], M_*. The angular momentum of a circular orbit with energy ϵ is $J_{\rm c}(\epsilon)$, and the Coulomb logarithm is $\ln \Lambda$. We have also defined the auxiliary integrals

$$I_0(\epsilon) = \int_0^\epsilon f(\epsilon') {\rm d}\epsilon' \tag{2.9}$$

and

$$I_{n/2} = (2\psi(r) - 2\epsilon)^{-n/2} \int_\epsilon^{\psi(r)} \left(2\psi(r) - 2\epsilon'\right)^{n/2} f(\epsilon') {\rm d}\epsilon'. \tag{2.10}$$

We can now specify the flux of stars per unit time per unit energy into the loss cone as

$$\mathcal{F}(\epsilon){\rm d}\epsilon = 4\pi^2 J_{\rm c}^2(\epsilon) P(\epsilon) \bar{\mu}(\epsilon) \frac{f(\epsilon)}{\ln^{-1} R_0(\epsilon)} {\rm d}\epsilon. \tag{2.11}$$

The quantity $R_0(\epsilon)$ accounts for the fact that our distribution function, which we have so far treated as isotropic, is not exactly so; very radial orbits have been depleted due to interactions with the loss cone. $R_0(\epsilon)$ is the value of R beneath which no more stars exist, and is given by

$$R_0(\epsilon) = R_{\rm LC}(\epsilon) \times \begin{cases} \exp\left(-q(\epsilon)\right), & q(\epsilon) > 1 \\ \exp\left(-0.186 q(\epsilon) - 0.824\sqrt{q(\epsilon)}\right), & q(\epsilon) < 1. \end{cases} \tag{2.12}$$

[2] Generalizing this calculation to a realistic present day mass spectrum increases TDE rates by a factor $\lesssim 2$ (Magorrian and Tremaine 1999).

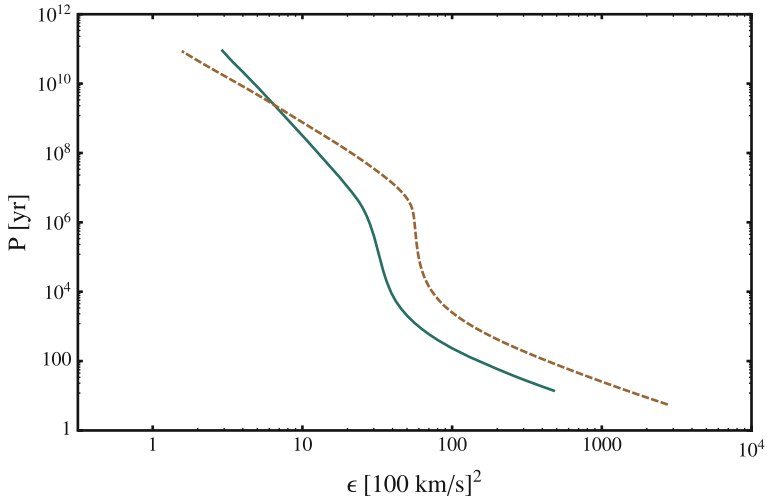

Fig. 2.2 The period of a radial orbit, $P(\epsilon)$, plotted against orbital energy ϵ. The line types are the same as in Fig. 2.1

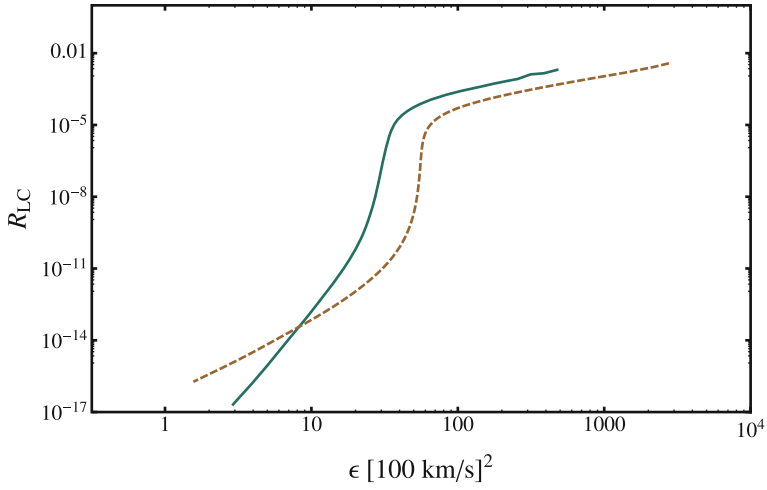

Fig. 2.3 The geometric size of the loss cone, $R_{\rm LC}(\epsilon) = J^2/J_{\rm c}(\epsilon)$, plotted against orbital energy ϵ. The line types are the same as in Fig. 2.1

The dimensionless quantity $q(\epsilon)$ can be thought of as the ratio of per-orbit changes in R to the R value of a loss cone orbit (all at fixed energy). It is defined as

$$q(\epsilon) = \frac{P(\epsilon)\bar{\mu}(\epsilon)}{R_{\rm LC}(\epsilon)}, \tag{2.13}$$

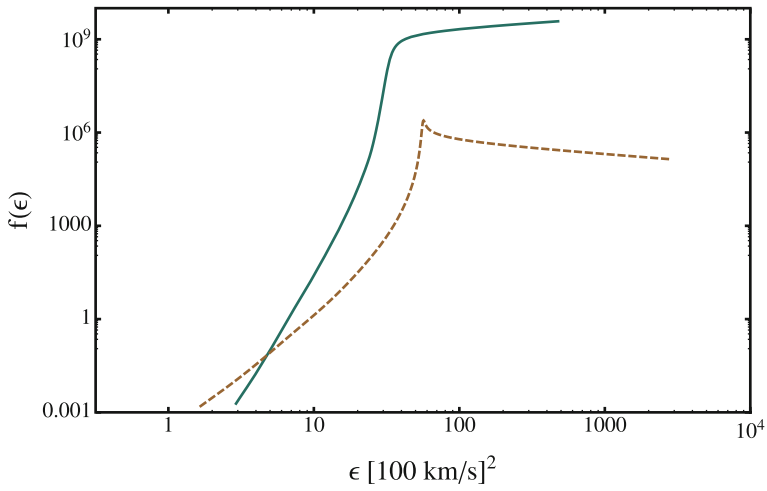

Fig. 2.4 The distribution function of stars, $f(\epsilon)$, plotted against orbital energy ϵ. Qualitatively different behavior is seen for the core galaxy (whose distribution function peaks at a finite ϵ) and the cusp galaxy (whose distribution function monotonically increases toward small radii). The line types are the same as in Fig. 2.1

and it demarcates the boundary between two different regimes of loss cone dynamics. When $q \ll 1$, stars diffuse slowly through angular momentum space, taking small steps that eventually result in grazing disruptions ($r_p \approx r_t$; $\beta \approx 1$). This "diffusive" regime is the one that dominates for stars near the SMBH. Beyond a critical radius r_{crit}, $q(\epsilon)$ grows quickly in value until $q \gg 1$. In this "pinhole" regime, the loss cone is close to full because stars can jump in and out of it multiple times per orbit. Notably, this produces TDEs that sample a full distribution of β, with $\dot{N}_{TDE}(\beta) \propto 1/\beta$.

2.3 Tidal Disruption Rates in Realistic Galaxies

We now have defined the theoretical formalism to calculate TDE rates in a galactic nucleus with known SMBH mass M_{BH} and stellar mass density profile $\rho(r)$ (assuming a mean stellar mass M_* to calculate $n(r) = \rho(r)/M_*$). However, $\rho(r)$ can only be inferred indirectly from observations of distant galactic nuclei. What is actually measured is the surface brightness profile $I(s)$, where s is a projected radial coordinate. In order to retrieve $\rho(r)$ from $I(s)$, we must assume (or measure) the mass to light ratio Υ, and also make the assumption of spherical symmetry.

Although many parametrizations for $I(s)$ exist in the literature, we will employ the "Nuker" surface brightness density profile

$$I(s) = I_b 2^{\frac{B-\Gamma}{\alpha}} \left(\frac{s}{s_b}\right)^{-\Gamma} \left(1 + \left(\frac{s}{s_b}\right)^{\alpha}\right)^{\frac{\Gamma-B}{\alpha}}. \tag{2.14}$$

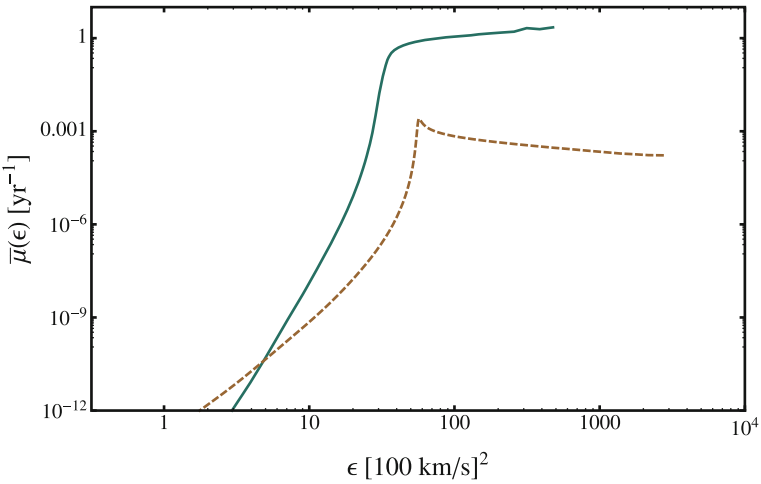

Fig. 2.5 The orbit-averaged angular momentum diffusion coefficient, $\bar{\mu}(\epsilon)$, plotted against orbital energy ϵ. The line types are the same as in Fig. 2.1

This five-parameter model is essentially a broken power law for the surface density profile; B is the inner power law slope, Γ is the outer power law slope, and α is a parameter governing the behavior at the break radius s_b. The normalization I_b is the magnitude of the surface brightness at $s = s_\mathrm{b}$. Using an assumed or measured Υ, we can deproject a measured $I(s)$ into $\rho(r)$ using the Abel inversion

$$\rho(r) = -\frac{\Upsilon}{\pi}\int_r^\infty \frac{\mathrm{d}I}{\mathrm{d}s}\frac{\mathrm{d}s}{\sqrt{s^2 - r^2}}. \tag{2.15}$$

Once we know $\rho(r)$, it is straightforward to calculate $M(r)$ and $\psi(r)$, and from there, to calculate TDE rates using the formalism of the previous section.

As a demonstration of this method, we now follow the example of Wang and Merritt (2004), and plot several quantities of interest for the galaxies NGC 4551 and NGC 4168. The SMBH masses for these galaxies, as inferred from the $M_\mathrm{BH} - \sigma$ relation, are $M_\mathrm{BH} = 10^{7.11} M_\odot$ and $M_\mathrm{BH} = 10^{7.89} M_\odot$, respectively. In Figs. 2.1 and 2.2 we plot the apocenters and periods of radial orbits against orbital energy. Figure 2.3 shows the small geometric size of the loss cone, $R_\mathrm{LC}(\epsilon)$, against orbital energy, while Fig. 2.4 shows the stellar distribution functions for both galaxies. Interestingly, $f(\epsilon)$ shows qualitatively different behavior for core and cusp galaxies: in core galaxies, the distribution function peaks near the SMBH influence radius, but in cusp galaxies it increases monotonically toward small radii. Figure 2.5 plots the orbit-averaged angular momentum diffusion coefficient, $\bar{\mu}(\epsilon)$, which like $f(\epsilon)$ shows different behavior for core and cusp galaxies. The related quantity $q(\epsilon)$ is plotted in Fig. 2.6, and, finally, we show flux into the loss cone, $\mathcal{F}(\epsilon)$, in Fig. 2.7. The colored text in this figure shows the integrated loss cone flux, i. e. the TDE rate for each galaxy.

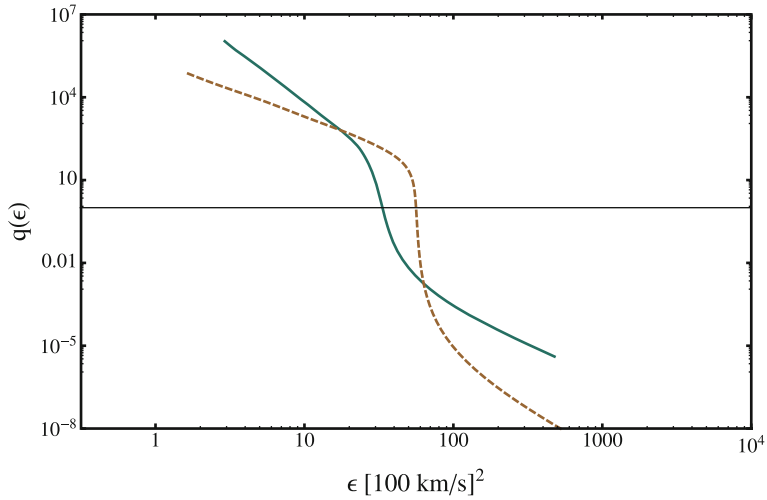

Fig. 2.6 The normalized per-orbit diffusion in R, $q(\epsilon) \approx (\Delta J(\epsilon)/J_{\rm LC}(\epsilon))^2$, plotted against orbital energy ϵ. The thin black line indicates where $q(\epsilon) = 1$; this defines a critical energy (and therefore a critical radius) where flux into the loss cone transitions from diffusive to pinhole. The line types are the same as in Fig. 2.1

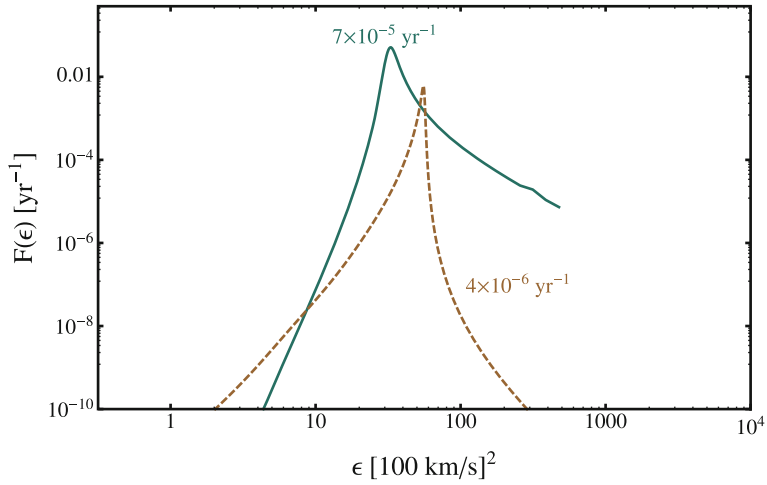

Fig. 2.7 The flux of stars into the loss cone, per unit energy per unit time, $\mathcal{F}(\epsilon)$, plotted against orbital energy ϵ, for the galaxies NGC 4551 and 4168. Integrals of these curves dϵ are shown as colored text (i. e. the total number of TDEs per galaxy per year). The line types are the same as in Fig. 2.1. Note that this function is very sharply peaked in energy space, with the vast majority of tidally disrupted stars coming from a relatively narrow range in orbital energies

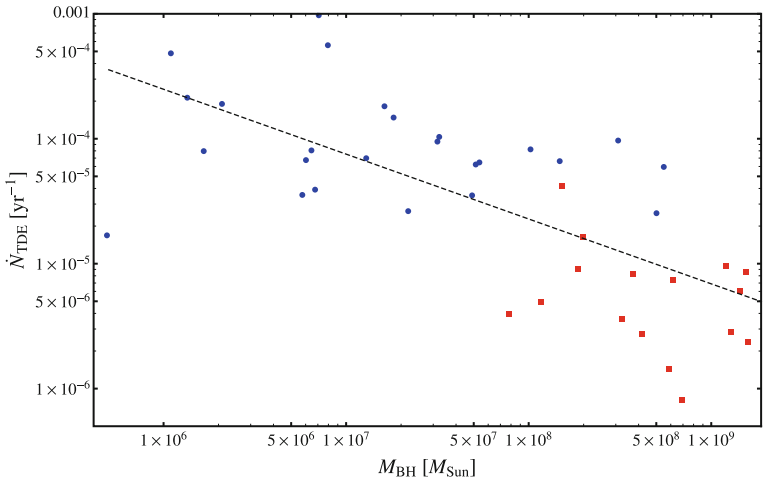

Fig. 2.8 The per galaxy rate of tidal disruption events, $\dot{N}_{\rm TDE}$, in units of $\rm yr^{-1}$, plotted against $M_{\rm BH}$. The blue circles show cusp galaxies, and the red squares show core galaxies; both are taken from the sample in Wang and Merritt (2004). The dashed *black line* shows a simple best fit power law to the entire sample ($\dot{N}_{\rm TDE} \propto M_{\rm BH}^{-0.52}$). The large scatter above and below the best fit power law is due to intrinsic scatter in Nuker parameters, particularly Υ and Γ

Generally speaking, the highest TDE rates occur in smaller galaxies, for two reasons. The first reason is that high-resolution *HST* imaging indicates a bimodality in nuclear surface brightness profiles: smaller ("cusp") galaxies tend to have higher values of the Nuker parameter $\gamma \approx 1$, indicating steeper central density profiles and denser star clusters with shorter relaxation times. Larger galaxies preferentially have low-density "cores," with $\gamma \approx 0$ and correspondingly longer relaxation times. These cores are thought to be scoured by the inspiral of a binary SMBH system following a galaxy merger; smaller galaxies generally lack them because the larger gas fractions in smaller galaxies allow the rebuilding of stellar cusps after the SMBH merger. The second reason is that in dense cusp galaxies, $\dot{N}_{\rm TDE}$ actually increases with decreasing SMBH mass, while the opposite is true for core galaxies. Specifically, Wang and Merritt (2004) find that for constant σ,

$$\dot{N}_{\rm TDE} \propto M_{\rm BH}^{\delta}, \qquad (2.16)$$
$$\delta = \frac{27 - 19\gamma}{6(4-\gamma)},$$

where $\gamma \approx 1 + \Gamma$ is defined as the 3D power law slope of stellar density, i. e. $\rho(r) \propto r^{-\gamma}$. When $\gamma < 27/19$, $\delta > 0$ and the TDE rate increases with increasing SMBH mass.

Because the specific TDE rate is highest for low-mass galaxies (as can be seen in Fig. 2.8), and because low-mass galaxies are more numerous, it has long been thought that large samples of TDEs could serve as excellent probes for the uncertain bottom end of the SMBH mass function. In particular, while almost all galaxies

with stellar bulge masses $M > 10^9 M_\odot$ are believed to host a central SMBH, the occupation fraction below this mass is unclear. Estimating this occupation fraction represents an important scientific goal for future TDE observations.

Ultimately, tidal disruption events are quite rare. Past work has estimated typical values of $\dot{N}_{\rm TDE} \sim 10^{-4} - 10^{-5}$ yr^{-1} (Magorrian and Tremaine 1999; Wang and Merritt 2004), although this may be increased by a factor of a few due to the effects of nonspherical, axisymmetric stellar cusps. Interestingly, this theoretical estimation is somewhat above the rates inferred from observational samples of TDEs (Donley et al. 2002), which is puzzling, as the TDE rate due to two-body relaxation is a lower limit that can be increased by, e. g., massive perturbers or strongly triaxial cusps. However, inferred rates are convolved with complicated selection effects, currently suffer from small number statistics, and in any event are being compared to theoretical estimates which themselves carry large uncertainties, so this discrepancy is not yet severe.

The following two chapters of this thesis describe original work by the author on TDE rates in a specific and unusual type of galaxy: one where the central SMBH is recoiling out of the center due to the anisotropic emission of gravitational radiation following the merger of two SMBHs.

Chapter 3
Prompt Tidal Disruption of Stars as an Electromagnetic Signature of Supermassive Black Hole Coalescence

N. Stone & A. Loeb The Monthly Notices of the Royal Astronomical Society, *Vol. 412, pp. 75–80, 20011*

3.1 Introduction

In the last decade, a series of breakthroughs in numerical relativity made it possible to simulate black hole binary coalescence on the computer, in fully dynamical spacetime (Pretorius 2005; Baker et al. 2006; Campanelli et al. 2006). The most important astrophysical result of these new techniques has been a self-consistent calculation of gravitational wave (GW) kicks: the recoil imparted via momentum conservation to a newly merged black hole. The final stages of black hole inspiral and merger are accompanied by anisotropic GW emission, which has been numerically demonstrated to produce typical recoil kicks $\sim 10^{2-3}$ km s^{-1}. The magnitude of the kick depends most sensitively on the initial binary mass ratio and on the spin vectors of the black holes. Kicks are maximized for mass ratios somewhat below unity ($q \approx 1/3$) and for large values of black hole spin. Non-spinning black holes have a maximum recoil velocity ~200 km s^{-1}, but the right angular configurations of large-magnitude spin vectors will produce "superkicks" with $v_{\rm k} \approx 4000$ km s^{-1}, or even larger "hangup kicks" with $v_{\rm k} \approx 5000$ km s^{-1}. In principle, a perfectly symmetric configuration (e. g. non-spinning, equal mass black holes) would result in a recoilless merger.

Supermassive black holes (SMBHs) in the universe are expected to form binaries as a consequence of hierarchical structure formation and galaxy mergers (Escala et al. 2005; Mayer et al. 2007; Callegari et al. 2009; Colpi and Dotti 2009). If their mass ratio is not too extreme ($q \gtrsim 0.1$), dynamical friction will efficiently sink a pair of SMBHs to the center of a newly merged galaxy in less than a Hubble time (Wetzel and White 2010). Three body interactions with central stars will harden the binary down to ~pc scales, but eventually depletion of these stars will render this angular momentum sink ineffective. At this point, the SMBH binary (SMBHB) has entered the "final parsec problem," as the GW merger timescale does not become less than a Hubble time for binaries with $\gtrsim 10^{-3}$ pc separation (Begelman et al. 1980).

N. C. Stone, *The Tidal Disruption of Stars by Supermassive Black Holes,*
Springer Theses, DOI 10.1007/978-3-319-12676-0_3

There are many possible solutions to the final parsec problem, which can be broadly classified as "wet" and "dry" in nature. Assuming that one of these mechanisms is able to harden SMBH binaries down to a scale where GW emission takes over, the binary will eventually merge.

Merging SMBH binaries provide copious sources of gravitational radiation for future space-based laser interferometers, or for existing Pulsar Timing Arrays (PTAs). Space-based laser interferometers, such as the European Space Agency's planned eLISA instrument[1], are most sensitive to SMBH binaries with masses $M_{\rm BH} \sim 10^6 M_\odot$. PTAs such as NANOGrav[2], the Parkes Pulsar Timing Array[3], or the European Pulsar Timing Array[4], are most sensitive to lower frequency GWs emitted by SMBHBs with total mass $\gtrsim 10^8 M_\odot$ (Sesana et al. 2009). A major challenge for both of these SMBHB detection methods is poor sky localization: error boxes of $\sim 10 - 100$ square degrees are typical for each method (Sesana and Vecchio 2010).

If prompt electromagnetic (EM) counterpart signals to the GW-driven coalescence of SMBHBs exist, then sky positions could be accurately determined and SMBHB mergers could be used as "standard sirens" in cosmology (Holz and Hughes 2005; Arun et al. 2009; Schutz 2009; Bode et al. 2010). The GW signal gives a highly accurate luminosity distance measurement, which, when combined with the redshift of the host galaxy, would allow precision cosmology independent of the standard cosmic distance ladder. Identification of host galaxies in SMBHB mergers is also of interest for the study of SMBH demographics, and the final parsec problem.

These considerations have motivated much theoretical work aimed at identifying viable EM counterparts. With the exception of the mechanism outlined here, all of these possible counterparts rely on the existence of a circumbinary disk, whose properties are uncertain in wet mergers and which may be absent entirely from dry merger SMBHBs. Most disk-related counterparts are made difficult to detect by pre-merger decoupling of the SMBHB from its circumbinary disk. Decoupling occurs once the rate of energy loss due to GWs exceeds the the rate of energy extraction due to gas inflow; the consequence is that a large cavity exists in the disk at the time of merger and for $\sim 7(1+z)(M_{\rm BH}/10^6 M_\odot)^{1.32}$ year afterward (Milosavljević and Phinney 2005). Disk luminosity is significantly reduced as a result (Schnittman and Krolik 2008). Some examples of counterparts, arranged in order of time after the SMBHB merger, include:

- Viscous dissipation of GWs in the circumbinary disk will heat its gas and produce a weak EM transient in the hours after the GWs pass through the disk. Unfortunately, this signal is likely too weak to outshine the luminosity produced by standard viscous heating of accretion disks (Kocsis and Loeb 2008).

[1] https://www.elisascience.org/.

[2] http://nanograv.org/.

[3] http://www.atnf.csiro.au/research/pulsar/ppta/.

[4] http://www.epta.eu.org/.

- The viscous refill of the inner regions of the disk will rebrighten its spectrum at UV and X-ray wavelengths, but on unfavorable timescales of 10–10^3 year (Milosavljević and Phinney 2005).
- Shocks produced in the disk by the rapid change in the central potential (from a combination of GW mass loss and recoil) will dissipate as heat, enhancing the infrared luminosity of the disk over timescales of $\sim 10^4$ year (Lippai et al. 2008; Schnittman and Krolik 2008).
- The portion of the disk within a radius $\sim GM_{\rm BH}/v_{\rm k}^2$ of the merged SMBH will remain bound to it after the recoil kick. This bound disk will appear anomalous both kinematically (due to a velocity offset between it's broad lines and the narrow lines of the host galaxy) and spatially (Loeb 2007; Bonning et al. 2007; Shields and Bonning 2008; Komossa et al. 2008; Comerford et al. 2009; Shields et al. 2009). The lifetime of this signature is limited by the draining of disk gas into the kicked SMBH, which will lead to order of magnitude declines in disk luminosity by 10^6–10^7 year after the recoil (Blecha and Loeb 2008).

In this chapter we outline an entirely different type of prompt EM counterpart, one which does not rely on the uncertain properties of pre-existing gas disks. In particular, we find that the post-merger recoil of a SMBH results in a series of stellar tidal disruption events (TDEs), with an effective rate that is up to four orders of magnitude higher than that for stationary SMBHs. This enormous enhancement occurs because TDE rates in normal galaxies are set by slow relaxational processes that repopulate a depleted loss cone; here we study the instantaneous tilting of the loss cone in phase space due to a GW kick.

Such a TDE burst could serve as an effective EM counterpart if observed in the years following detection of a GW signal from a coalescing SMBHB. In the most optimistic scenarios considered, multiple TDEs could occur within the same galaxy on timescales of human interest. A sequence of multiple TDEs within the same galaxy is vanishingly unlikely when considering TDEs produced by two-body relaxation (which occur at rates $\lesssim 10^{-4}$ year^{-1}). Repeating TDEs could potentially serve as an indicator of SMBHB merger and recoil even independent of a GW signal, although careful future study must be undertaken to separate this explanation from one other recently considered alternative: TDE rate enhancements due to chaotic orbits and the Kozai effect around wide SMBHBs (Ivanov et al. 2005; Chen et al. 2009).

3.2 Tilting the Loss Cone

As discussed earlier, stars are tidally disrupted when their orbital pericenters $R_{\rm p}$ fall below $R_{\rm t}$. In the usual scenario (a spherically symmetric potential around a stationary SMBH), this condition can be written in terms of specific angular momentum J:

$$J^2 = |\vec{x} \times \vec{v}|^2 < J_{\rm LC}^2 \approx 2GM_{\rm BH}R_{\rm t}. \tag{3.1}$$

Orbits that satisfy $J < J_{\rm LC}$ fall into the loss cone. Near the SMBH, the loss cone is empty, and stars are fed to the black hole by relaxational processes that impart typical per-orbit angular momentum perturbations $\Delta J \ll J_{\rm LC}$. Stars in this regime slowly diffuse into the loss cone. Far from the SMBH (the "pinhole" regime), the tiny angular size of the loss cone means that $\Delta J \gg J_{\rm LC}$, and stars will pass in and out of the loss cone many times per orbit. Both regimes contribute to the total TDE rate in normal galaxies, with the stellar density profile determining which one dominates. Regardless, TDE rates set by two-body relaxation are generally quite low, between 10^{-4} year^{-1} and 10^{-6} year^{-1} (Wang and Merritt 2004; Magorrian and Tremaine 1999).

The mechanism for TDE production considered here is quite different, and relies on the fact that the timescale for SMBH kicks due to GW recoil ($\sim R_{\rm g}/c$) is effectively instantaneous when compared to the long orbital periods of nearby stars. If we adopt the reference frame of the SMBH, surrounding stars instantaneously translate through velocity space so that a new loss cone can be written as

$$J^2 = |\vec{x} \times (\vec{v} - \vec{v}_{\rm k})|^2 < J_{\rm LC}^2 \approx 2GM_{\rm BH}R_{\rm t}, \tag{3.2}$$

This new loss cone overlaps with non-empty portions of phase space very near to the SMBH; any stars in these regions are firmly in the diffusive regime of two-body scattering and will therefore be destroyed on an orbital time. To quantify the properties of this sequence of TDEs (in particular, the number of stars in the tilted loss cone, and their orbital periods), we adopt a simple parametrization for the stellar density profile around a coalescing SMBHB:

$$\rho(r) = \rho_0(r/r_0)^{-\gamma}, \tag{3.3}$$

making the assumptions of spherical symmetry and (almost) isotropic velocities. A small but crucial anisotropy in the stellar velocity distribution must be added to reflect regions of phase space emptied by the orbital dynamics of the SMBHB. This will likewise truncate $\rho(r)$ below some r; both complications are discussed after a few more preliminaries.

A spherically symmetric, isotropic power law stellar density profile requires the pre-kick stellar distribution function

$$f(r, v) = C(2GM_{\rm BH}/r - v^2)^{\gamma - 3/2}, \tag{3.4}$$

where $f(r, v)$ is defined within the velocity space sphere

$$\vec{v}^2 < 2GM_{\rm BH}/r. \tag{3.5}$$

The normalization constant

$$C = \frac{(3-\gamma)(\gamma - 1/2)\Gamma(\gamma+1)}{2\pi^{5/2}\Gamma(\gamma+1/2)} \frac{M_{\rm BH}}{r_{\rm infl}^3} \left(\frac{r_{\rm infl}}{2GM_{\rm BH}}\right)^{\gamma}. \tag{3.6}$$

Here $r_{\rm infl}$ is the SMBH influence radius, defined as the radius containing twice the SMBH's mass in stars. High resolution observations of galactic nuclei have produced empirical fits for $r_{\rm infl}(M_{\rm BH})$ (Merritt et al. 2009). In particular,

$$r_{\rm infl} = 24(M_{\rm BH}/10^8 M_\odot)^{0.51}\ {\rm pc}, \tag{3.7}$$

although if we limit ourselves to "core" galaxies ($\gamma \approx 1$) then

$$r_{\rm infl} = 35(M_{\rm BH}/10^8 M_\odot)^{0.56}\ {\rm pc}. \tag{3.8}$$

The set of stars that will be tidally disrupted due to the post-merger tilt of the loss cone is the intersection of Eqs. (3.2) and (3.5). We count the number of disrupted stars, N, by integrating the relevant distribution function within the bounds of these three inequalities. Because of its relatively high dimensionality (and sensitivity to very small portions of the domain that contain the highest stellar densities), this integral is time-consuming and easiest to perform with Monte Carlo methods. Although both bound and unbound stars can contribute to the total number of stars disrupted post-merger, in practice only a small fraction ($\lesssim$10 %) of disrupted stars are on hyperbolic orbits. Hyperbolic TDEs are in principle interesting because an orbit with center of mass energy $|\epsilon_{\rm orb}| \sim \Delta\epsilon$ would not asymptote to the standard $\dot{M} \propto t^{-5/3}$ power law, and an orbit with $|\epsilon_{\rm orb}| \gg \Delta\epsilon$ would not produce any bound debris with which to make an accretion disk! However, in order to achieve $\epsilon_{\rm orb} \approx v_{\rm k}^2/2 \sim \Delta\epsilon$, kick velocities $v_{\rm k} \gtrsim 2000$ km s^{-1} are required; such kicks, while physically possible, are quite rare.

Although the total number of stars N is of interest, the quantity of greater observational relevance is $N_<(t)$, defined as the number of stars with orbital periods less than $t/2$ years that inhabit the post-recoil loss cone (the factor of 2 comes from the fact that almost all stars in the post-merger loss cone begin their final orbit very near apocenter). A small correction to this calculation comes from the fact that the final burst of gravitational radiation removes $\lesssim$5 % (Campanelli et al. 2006) of the pre-merger combined SMBH mass (so that in addition to receiving a kick, stars become marginally less bound). This reduces N by $\approx$10 %, a correction we include in our calculations.

Both N and, especially, $N_<(100)$, are quite sensitive to the innermost stars around the SMBHB at the moment of coalescence, implying that the simplistic treatment of $\rho(r)$ and $f(r, v)$ given above is inadequate. In the following sections, we consider more realistic stellar densities and distribution functions that account for the portions of stellar phase space excavated during an SMBHB inspiral. The depletion of stars by interactions with an SMBHB will proceed differently for gas-poor ("dry") and gas-rich ("wet") mergers, so we consider these cases separately.

3.3 The Final Parsec Problem

When two galaxies merge, dynamical friction will efficiently bring their SMBHs (of masses M_1 and M_2, with $M_1 > M_2$) down to small radii provided the mass ratio $q = M_1/M_2$ is not too unequal; typically $q < 10$ is required for dynamical friction

to operate in less than a Hubble time. Once a SMBHB has formed, it will harden via three-body encounters with surrounding stars; as stars enter the gravitational "blender" of the binary, they are ejected and extract its energy and angular momentum. The binary can be thought of as possessing a loss cone analogous to the phase space region discussed earlier around single black holes. The binary loss cone is the set of stellar orbits with pericenters less than twice the binary semimajor axis. This process scours a low-density "core" into the pre-existing stellar density profile (Merritt, 2006). However, once the SMBHB has reached a small enough separation that there are no longer enough stars to further harden its orbit, orbital evolution will stall. This typically occurs at ∼pc scales, but the gravitational radiation timescale for a circular SMBHB with semimajor axis a is

$$T_{\rm GW} = 2.53 \times 10^5 \text{ year } \left(\frac{a}{10^{14}\text{ m}}\right)^4 \left(\frac{\zeta}{1}\right)^{-1} \left(\frac{M_1+M_2}{10^8 M_\odot}\right)^{-3}, \qquad (3.9)$$

where $\zeta = 4M_1M_2/(M_1+M_2)^2$. This timescale only falls below a Hubble time at $a \sim$ mpc scales. This apparent barrier to merger of black hole binaries is the so-called "final parsec problem" (Milosavljević and Merritt 2001), although so many solutions to it have been proposed that it is no longer clear whether it even qualifies as a problem! Among the possible solutions are

1. Collisional binary loss cone repopulation: two-body relaxation around SMBHBs can repopulate the binary loss cone and harden a binary to the point where gravitational radiation takes over. However, this process is inefficient for all but the smallest SMBHB systems, requiring $M_1 + M_2 \lesssim 10^7\ M_\odot$ (Merritt et al. 2009).
2. Collisionless binary loss cone repopulation: the presence of significant non-sphericity - either axisymmetry or triaxiality (Merritt and Poon 2004) - in the stellar potential around the SMBHB will result in non-conservation of stellar angular momentum. Depending on the orientation of a star's orbital plane with respect to the potential's principal axes, stellar orbits will (collisionlessly) vary their pericenters over time, greatly expanding the population of stars vulnerable to extractive three-body encounters with the SMBHB. This scenario has been the subject of much recent excitement, and may provide a general solution to the final parsec problem (Khan et al. 2013, for example).
3. Further galaxy mergers: a galaxy containing a stalled SMBHB will occasionally merge with a third galaxy. The introduction of a third SMBH can lead to rapid orbital hardening from either the Kozai effect or strong encounters (Hoffman and Loeb 2007).
4. Circumbinary gas disks: in a wet merger, a massive circumbinary disk may form. Tidal torques from this disk will harden the SMBHB (Dotti et al. 2010), although the efficiency of this may be hampered by star formation in Toomre-unstable regions of the disk, which can choke off gas supply to the innermost disk annuli (Thompson et al. 2005).

In dry mergers, only the first three of these solutions can drive a SMBHB to coalescence, but in wet mergers the fourth solution is also possible.

3.3.1 Dry Mergers

Any GW signal produced in the aftermath of a dry galactic merger will require one of scenarios 1-3 to operate. In this section we ignore scenario 3 due to the large number of associated uncertainties, and instead focus on the first two solutions to the final parsec problem: collisional and collisionless repopulation of the SMBHB loss cone. In both of these scenarios, we define the SMBH influence radius using Eq. (3.8).

If collisional processes dominate, then the shallow stellar core excavated by the SMBHB's earlier inspiral will be repopulated as surrounding stars diffuse in orbital energy. This process builds up a Bahcall-Wolf equilibrium cusp (Bahcall and Wolf 1976) around the SMBHB out to a radius of $\approx 0.2 r_{\rm infl}$ (Merritt et al. 2009); beyond this point, relaxation times are too long to modify the original core profile. In our collisional scenario, we therefore consider a $\gamma = 1$ profile extending from $r_{\rm infl}$ down to $0.2 r_{\rm infl}$ (which determines the overall mass normalization), but smoothly join a $\gamma = 1.75$ profile at $r = 0.2 r_{\rm infl}$ and extend that density profile inward. Alternatively, if collisionless processes dominate, there is insufficient time for inner regions of the stellar profile to relax into a cuspier equilibrium, and the core profile ($\gamma = 1$) extends down to small radii.

Regardless of the slope of the stellar density profile, we must also determine an innermost cutoff to place on the stellar population. The numerical simulations of Merritt et al. (2007) indicate that, in the regime of collisional loss cone repopulation, GW energy losses will decouple the SMBHB from the stellar cusp at a semimajor axis of $a_{\rm eq} \sim 10^{-3} r_{\rm infl}$. In both scenarios, we remove all stars with semimajor axes interior to this radius (a conservative choice for collisionless loss cone repopulation). Because angular momentum relaxation proceeds faster than energy relaxation for non-circular orbits, the gap in angular momentum space (pericenter) will be significantly smaller than this gap in semimajor axes. Following Merritt and Wang (2005), the timescale to refill a gap in angular momentum space is

$$T_{\rm gap} = \frac{r_{\rm J}}{r_{\rm infl}} T_{\rm r}, \tag{3.10}$$

where the relaxation time at the radius of influence is given by (Merritt et al. 2009)

$$T_{\rm r} \approx 8.0 \times 10^9 {\rm year} \left(\frac{M_{\rm BH}}{10^6 M_\odot} \right)^{1.54}. \tag{3.11}$$

Here $r_{\rm J}$ is the gap in angular momentum space; we remove all stars with pre-kick pericenters smaller than the value of $r_{\rm J}$ at which $T_{\rm gap} = T_{\rm GW}$.

Beyond the issue of inner boundaries, we must also consider the actual functional form of the two-dimensional distribution function $f(E, J)$. Cohn and Kulsrud (1978) demonstrated that in steady state, solutions to the orbit-averaged Fokker-Planck equation depend logarithmically on J at fixed values of E. We adopt a simpler functional form, where $f(E, J)$ is constant with respect to J within the region permitted by decoupling; this increases $N_<(t)$ by a factor $\approx 2-4$. We make this simplification for two reasons; the first is that the loss cone of a SMBHB does not behave in a purely

sink-like fashion as in Cohn and Kulsrud (1978) (i.e. stars scattered by the SMBHB may remain on bound orbits). The second reason is that the near-radial orbits most affected by a logarithmic distribution in J are the ones least well-described by the Cohn and Kulsrud (1978) steady-state solution; they interact more strongly with the non-Keplerian potential of the SMBHB, and may also be subject to strong star-star scatterings not described by a Fokker-Planck approach.

A final correction to our Monte Carlo integral is incorporation of a Salpeter initial mass function (IMF) where $dN_\star/dM_\star \propto M_\star^{-2.35}$ for $0.1M_\odot < M_\star < 100M_\odot$. The large number of low mass stars in this IMF causes them to dominate the disruption rate; $N_<(100)$ would be reduced by a factor of a few if we switch to a more extreme, top-heavy IMF, as is sometimes discussed for galactic nuclei (Bartko et al. 2010).

3.3.2 *Wet Mergers*

If the final parsec problem is instead solved dissipatively, through the presence of a massive circumbinary disk, then the resulting stellar profile will be different. Stellar densities will be reduced by the lack of time needed for relaxation to refill the core scoured by SMBHB inspiral (Merritt et al. 2009). Conversely, *in situ* star formation may increase stellar densities at small radii relative to a gas-free scenario. The capture and subsequent migration of pre-existing stars into disk-aligned orbits (Syer et al. 1991) would have a similar effect. Because of the complex and uncertain physics of both star formation (Shlosman and Begelman 1987; Alexander et al. 2008) and migration (Goodman and Tan 2004), we consider a simple set of parameters to describe the final outcome: $\gamma = \{1.5, 1.75, 2.0\}$. In all wet merger cases, we estimate the radius of influence as Eq. (3.7), as wet mergers are believed to be responsible for the (re)building of dense stellar cusps.

As in the dry mergers discussed above, we use decoupling arguments to determine the innermost permitted pericenters of stellar orbits that will exist when the SMBHs coalesce. In a thin disk, the viscous timescale at the marginally self-gravitating radius is (Goodman and Tan 2004)

$$T_{\rm visc} = 4.2 \times 10^5 \text{ yr } \alpha_{0.3}^{-1/3} \kappa^{-1/2} \mu^{1/3} \left(\frac{\epsilon_{0.1}}{\ell_E}\right)^{1/6} M_8^{1/2}, \tag{3.12}$$

where κ is the opacity in units of the Thomson opacity, μ is the mean atomic weight of disk gas, $\alpha_{0.3}$ is the Shakura-Sunyaev viscosity parameter scaled to 0.3, $\epsilon_{0.1}$ is the radiative efficiency scaled to 0.1, $\ell_{\rm E}$ is the total luminosity in units of the Eddington limit, and $M_{\rm BH} = M_8 \times 10^8 M_\odot$. We can determine the decoupling radius (and innermost stellar pericenter) by equating $T_{\rm visc} = T_{\rm GW}$. Because $T_{\rm visc}$ has only a weak power law dependence on most parameters (aside from $M_{\rm BH}$), we take their fiducial values as representative. For simplicity, we assume that the remaining stars are able to isotropize into a spherical distribution after decoupling. Although this may at first glance seem unlikely (as in this scenario, $T_{\rm visc} \ll T_{\rm r}$ by assumption),

we note that relaxation rates are orders of magnitude faster in thin disks of stars than in spherical distributions of stars with the same radial extent (Stewart and Ida 2000); significant, albeit not full, isotropization is therefore likely. Since the IMF of stars formed in circumbinary disks is highly uncertain, as is the mass accretion history of stars migrating through disks, we assume $M_\star \sim 1 M_\odot$ for wet mergers. Finally, we note that in wet mergers, accretion of gas onto the SMBHs during their inspiral is likely to align their spins and seriously suppress kicks above $\sim$200 km s^{-1} (Bogdanović et al. 2007; Dotti et al. 2010).

3.4 Other Considerations

We neglect in our calculation two potentially important physical effects. The first concerns orbital resonances around the SMBHB; in analogy to resonant migration in planetary systems (Yu and Tremaine 2001), stars can be captured into mean-motion resonance with an inspiraling SMBHB. This effect has the potential to make our calculations very conservative, as resonant migration would deliver stars far inside the decoupling radius. Several papers have examined the special 1:1 Lagrange point resonance and found that stars trapped around the L4 or L5 Lagrange points can migrate inward to tens of Schwarzschild radii from the system barycenter (Seto and Muto 2010), only breaking out of resonance when post-Newtonian precession terms become too strong (Schnittman 2010). There are many more higher-order mean motion resonances; these clearly affect stellar orbits during SMBHB inspiral (Chen et al. 2009, Figs. 5, 6, 7). Subsequent work has shown that higher order MMRs can also deliver stars to tens of Schwarzschild radii (Seto and Muto 2011).

The second effect we neglect is that of redshift. A TDE burst at redshift z will be delayed in onset by a factor of $1 + z$ due to relativistic time dilation; this will also lengthen the duration of each observed flare (while reducing their luminosity). Although these effects have a mild negative impact on detectability (except for severely cadence-limited surveys), high redshift galaxies are observed to have higher mean densities, with $\bar{\rho} \propto (1 + z)^3$ (Oesch et al. 2010). If this observation holds down to the much smaller scales of high-z galactic nuclei, then the net enhancement in the TDE rate would go $\propto (1 + z)^2$ per galaxy. In this paper, however, we set $z = 0$ as the net effect of z on our results is ambiguous and likely modest, and in any event most optically detected TDEs occur at low redshift (although the minority of relativistic TDEs can be found at moderate, $z \approx 1$, redshifts).

As a final note, for simplicity we only consider equal mass SMBH mergers. This choice of parameters is likely conservative for major mergers; an uneven mass ratio would increase $T_{\rm GW}$ and, therefore, $N_<(t)$. On the other hand, very extreme mass ratios ($q \lesssim 0.1$) will reduce expected kick velocities, which, as we show in the next section, will suppress $N_<(t)$ once $v_{\rm k} \lesssim 200$ km s^{-1}.

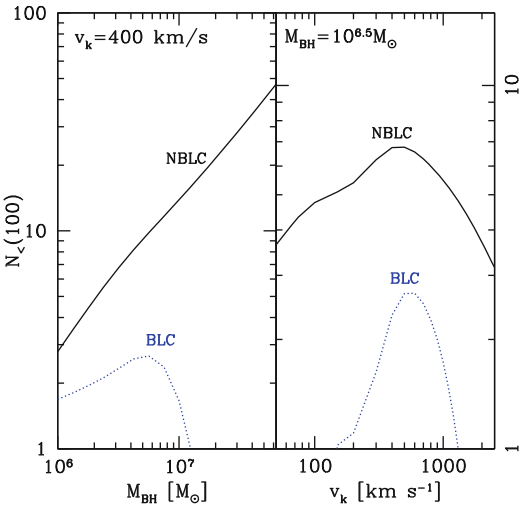

Fig. 3.1 The expectation value for $N_<(100)$, the number of stars disrupted within 100 years of SMBHB coalescence. This plot shows results for dry mergers that solve the final parsec problem through collisional refill of the binary loss cone, producing a joint core-cusp stellar density profile. The dotted blue line ("BLC") represents our fiducial scenario, where the joint core-cusp profile is truncated for stars whose pericenters or semimajor axes fall within the binary loss cone at the time of decoupling. The solid black line ("NBLC") does not truncate the stellar density profile at small radii; although this curve is not physically motivated, it illustrates the importance of the innermost ($\sim$100) stars for $N_<(100)$. The *left panel* shows $N_<(100)$ as a function of SMBH mass $M_{\rm BH}$ (at fixed $v_{\rm k} = 400$ km s^{-1}), while the right panel shows $N_<(100)$ as a function of kick velocity $v_{\rm k}$ (at fixed $M_{\rm BH} = 10^{6.5} M_\odot$)

3.5 Event Rates

In Fig. 3.1, we present the results of our MC integrals in our most physically-motivated model: the joint core-cusp profile that describes the stellar profile left over after an SMBHB is brought down to GW-dominated scales by collisional loss cone repopulation. This model (labeled BLC in the figure) removes all stars with the semi-major axes or pericenters that would fall into the binary loss cone after decoupling. Figure 3.1 illustrates that there is a "sweet spot," in both kick velocity and black hole mass, for maximizing $N_<(100)$. Specifically, we find interesting numbers of post-merger TDEs when $M_{\rm BH} \lesssim 10^7 M_\odot$ and 200 km s^{-1} $\lesssim v_{\rm k} \lesssim$ 1000 km s^{-1}. $N_<(100)$ is suppressed at low $v_{\rm k}$ by overlap between the pre- and post-merger loss cones; at the highest velocities, it is instead suppressed by the unbinding of the vast majority of cusp stars. The total number of stars in the post-kick loss cone grows with increasing $M_{\rm BH}$, but $N_<(100)$ turns over near $M_{\rm BH} \approx 5 \times 10^6 M_\odot$ due to the fact that orbital periods also increase with $M_{\rm BH}$. Once the SMBH mass grows significantly higher than this, essentially all short-period stars are removed by the pre-merger binary loss cone. The $\gamma = 1$ curve representative of collisionless loss cone repopulation does

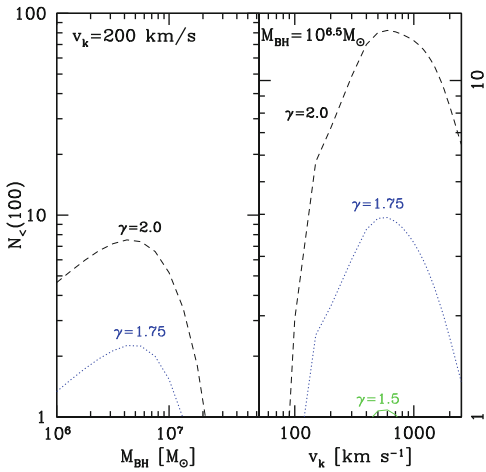

Fig. 3.2 The expectation value for $N_<(100)$ in the wet merger scenario. The panels are the same as in Fig. 3.1 (although in this plot the left panel has $v_k = 200$ km s^{-1} to reflect the lower kick velocities expected in wet mergers), but the line types indicate different power law slopes for a simple cusp parametrization of the stellar density profile. Specifically, the solid green line, dotted blue line, and dashed black line represent $\gamma = 1.5$, $\gamma = 1.75$, and $\gamma = 2.0$ power-law cusps

not produce a significant number of post-merger TDEs, and is therefore not shown here.

Figure 3.1 also shows a second curve (labeled NBLC) that disregards the effects of the pre-merger binary loss cone. This curve is not physically motivated, but is shown for illustrative purposes: the large enhancement in $N_<(100)$ seen in the NBLC results indicates the sensitivity of the TDE burst to a relatively small number of stars. The total number of stars removed from the pre-merger binary loss cone is only $\sim$100 for $M_{\rm BH} = 10^6 M_\odot$; this highlights the potential importance of resonant migration.

As stated in the previous section, our models for wet mergers are considerably more uncertain, but the simple parametrizations we use are shown in Fig. 3.2. Our results indicate that if star formation and/or disk migration is able to produce stellar density cusps with slopes of $\gamma \gtrsim 1.75$, interestingly large values of $N_<(100)$ will result, and sequential TDEs may be observable from an individual galaxy.

Finally, in Fig. 3.3, we plot against time the cumulative number of stars disrupted from the tilted, post-merger loss cone. In this figure we use only the joint-core cusp model representative of collisional binary loss cone refill (and remove the stars remaining in the binary loss cone at the time of decoupling). The "sweet spot" for detectability occurs for SMBHs with $10^6 M_\odot \lesssim M_{\rm BH} \lesssim 10^7 M_\odot$, and 400 km s^{-1} $\lesssim$ v_k $\lesssim$ 800 km s^{-1}; the expectation value of the first post-kick disruption in this parameter range is $\approx$30 year, although we note that the cumulative probability distributions extend with nontrivial values down to smaller delay times (for example, a recoiling SMBH with $M_{\rm BH} = 10^6 M_\odot$ and $v_k = 400$ km s has a $\approx$15 % chance of disrupting a star less than a decade after recoil). Interestingly, this range of parameter space largely overlaps with both the peak sensitivity of *LISA*-like instruments, and typical recoil velocities for SMBHBs coalescing in dry mergers. Although not shown in Fig. 3.3, optimistic parameter values ($\gamma = 2$) for wet mergers can produce TDEs with delay times as low as $\sim$1 year.

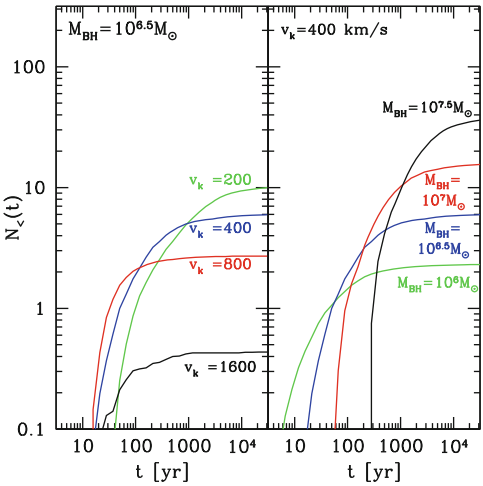

Fig. 3.3 Expectation values for $N_<(t)$, the number of stars disrupted within t years of SMBHB coalescence. In the left panel, we fix the SMBH mass at $10^{6.5} M_\odot$ and show $v_k = \{200, 400, 800, 1600\}$ km s^{-1} kicks as green, blue, red, and black lines, respectively. In the right panel, we fix the kick velocity at 400 km s^{-1} and show $M_{BH} = \{10^6, 10^{6.5}, 10^7, 10^{7.5}\}$ black holes as green, blue, red, and black lines, respectively. Within the "sweet spot" of parameter space ($10^6 M_\odot \lesssim M_{BH} \lesssim 10^7 M_\odot$, and $400 \lesssim v_k \lesssim 800$ km s^{-1}), the number of stars in the tilted post-kick loss cone is typically between 1 and 10. The typical delay time between SMBH recoil and the first disruption is $\approx$30 year, but with a nontrivial ($\gtrsim$10 %) chance of a first disruption occurring within 10 years of recoil for the smallest SMBHs ($M_{BH} \lesssim 10^6 M_\odot$)

Figure 3.3 shows how the delay until the first post-kick disruptions changes with black hole mass and kick velocity. Here we consider the joint core-cusp model (with removal of pre-merger loss cone by the binary), and find that the first disruption is expected to occur between three and five decades after SMBH coalescence for black holes with masses between $10^6 M_\odot$ and $10^7 M_\odot$, and kick velocities between 400 and 800 km s^{-1}. Fortunately, this region of parameter space falls within both the black hole mass range *LISA* is likely to observe, and the range of physically plausible recoil velocities for dry mergers. In the most event-rich wet merger scenarios, the first TDEs could occur as soon as $\sim$1 year after coalescence.

3.6 Discussion

The merger of two SMBHs is likely to result in a sequence of tidal disruption flares, with an averaged rate orders of magnitude above that for normal galaxies. In gas-poor mergers with combined mass $M_{BH} \lesssim 10^7 M_\odot$ (the rough upper limit for collisional solutions to the final parsec problem), the first flare can occur a few decades after coalescence, and the enhancement to the TDE rate is a factor $\sim 10^4$. Gas-poor mergers that solve the final parsec problem in a collisionless way will see much longer

delays and much lower total numbers of recoil-induced TDEs. More speculatively, the first flare could occur on a timescale of years if resonant migration is able to transport stars inward past the decoupling radius. Kick velocities of 200 km $s^{-1} \lesssim v_k \lesssim 1000$ km s^{-1} maximize the total number of recoil-induced TDEs, and minimize the time to the first TDE.

Our predictions for gas-rich mergers are more uncertain, as they depend on the uncertain physics of star formation and stellar migration in circumbinary disks. If either of these mechanisms are able to seed significant numbers of stars down to the radius where SMBHB evolution decouples from viscous disk evolution, then total rates could be enhanced and delay times decreased.

Kick velocities typical for mergers of comparable-mass, spinning SMBHs will produce an EM counterpart to *LISA*-band GW signals, albeit one that may be delayed by several decades. Further study is needed to determine if resonant migration or the interplay between stars and circumbinary disks can reduce delay times to the order of years or less. Regardless, identification of an EM counterpart to a GW signal will identify the host galaxy, and allow measurement of important cosmological parameters independent of the standard cosmic distance ladder (Holz and Hughes 2005). Optimistically, optical transient surveys such as PTF[5], Pan-STARRS[6], and (most promisingly) LSST[7] may be able to observe sequential tidal disruption events in a single galaxy, offering a signature of SMBH recoil even without a corresponding GW signal. Such a detection would calibrate the expected *LISA* event rate.

[5] http://www.astro.caltech.edu/ptf/.

[6] http://pan-starrs.ifa.hawaii.edu/public/.

[7] http://www.lsst.org/lsst.

Chapter 4
Tidal Disruption Flares of Stars From Moderately Recoiled Black Holes

N. Stone & A. Loeb The Monthly Notices of the Royal Astronomical Society, *Vol. 422, pp. 1933–1947, 2012*

4.1 Introduction

In this chapter, we calculate the rates at which stellar tidal disruption events (TDEs) will be produced by supermassive black holes recoiling due to anisotropic gravitational wave emission. These black holes are kicked out of their galactic nuclei following the merger of their progenitors, with velocities $v_{\rm k} \sim 10^{2-3}$ km s^{-1}. Although most kicked SMBHs will eventually return to the center of their host galaxy, during their peregrinations they will tidally disrupt both bound and unbound stars. We broadly survey the parameter space of kick velocities and galaxy properties, and find that the rates of detectably offset tidal disruption flares are of interest for *LSST*. In particular, emission produced thermally from a compact accretion disk can result in $\sim$1 TDE per year for which *LSST* would observe a spatial offset; if super-Eddington outflows exist, that number would increase to $\sim$10 TDEs per year. Stars bound to the recoiling SMBH dominate its disruption rate, and under optimistic choices of kick velocities could contribute up to 1 % of the all-sky tidal disruption event rate.

Since 2005, advances in numerical relativity have demonstrated that mergers of black hole binaries are generically accompanied by anisotropic gravitational wave (GW) emission. Because GWs carry linear momentum, the merged black hole recoils in the direction opposite to that of the net GW momentum flux (Pretorius 2005; Baker et al. 2006; Campanelli et al. 2006). Supermassive black holes (SMBHs) in the universe are believed to generally form binaries following the mergers of their host galaxies; the eventual coalescence of these binaries will impart a kick to the merger product. Kick velocities are strong functions of both the binary mass ratio and the spin vectors of the merging black holes; mass ratios $\sim 1/3$ and maximal spins tend to maximize the kick velocity $v_{\rm k}$. The absolute masses of the merging black holes are irrelevant to $v_{\rm k}$, as general relativity is scale free.

Non-spinning black hole kicks are typically kicked at $v_{\rm k} \sim 100$ km s^{-1}, while rapidly spinning black holes can produce $v_{\rm k} \gtrsim 1000$ km s^{-1}. The high end of this distribution easily exceeds the escape velocities of even the largest galaxies, and will produce rogue SMBHs escaping into intergalactic space. However, these "superkicks" are relatively rare, and a much more common outcome will be

N. C. Stone, *The Tidal Disruption of Stars by Supermassive Black Holes,*
Springer Theses, DOI 10.1007/978-3-319-12676-0_4

$v_k \sim 300$ km s^{-1} (Schnittman and Buonanno 2007; Lousto et al. 2010a, b). In this case, the SMBH will remain bound to the galaxy, and will oscillate on nearly radial orbits for 10^{6-9} year before dynamical friction pulls it back into its galactic nucleus (Blecha and Loeb 2008; Sijacki et al. 2011; Blecha et al. 2011).

Recoiling SMBHs are of great scientific interest, both as signposts of hierarchical galaxy evolution and as a unique prediction of strong field GR. Two broad categories of recoil signatures have been predicted. Indirect stellar dynamical signatures include the excavation of a low-density stellar core in a galactic nucleus (Gualandris and Merritt 2008) and the survival of a small "hypercompact" stellar system bound to the recoiling SMBH, which would appear similar to a globular cluster but with significantly higher velocity dispersion (O'Leary and Loeb 2009; Merritt et al. 2009; O'Leary and Loeb 2012). More direct signatures from accreting, recoiling SMBHs also could exist: if the merging SMBH binary has a circumbinary disk around it, part of the disk can follow the recoiling SMBH and accrete at later times, producing a spatially or kinematically offset quasar (Madau and Quataert 2004; Loeb 2007). Because of the finite supply of gas, this source of accretion power will turn off after at most $\sim 10^7$ years (Blecha and Loeb 2008; Blecha et al. 2011). Many observational candidates exist for these offset AGN (Komossa et al. 2008; Shields et al. 2009; Civano et al. 2010), but it is hard to definitively claim that they are due to recoiling SMBHs (Bogdanović et al. 2009).

An alternate source of accretion luminosity around wandering SMBHs is the tidal disruption of stars; light curves or SEDs from these events could possess analogous spatial or kinematic offsets. Komossa and Merritt (2008, KM08) investigated this possibility and concluded that offset TDEs could serve as promising indicators of recoiling SMBHs, particularly for the subset of SMBH kicks that unbind the black hole from its host galaxy. In this chapter we generalize the work of KM08 to realistic (and generally bottom-heavy) kick velocity distributions so as to compute observable rates of spatially or kinematically offset tidal disruption flares.

We note that even though offset tidal disruption flares should appear very distinct from TDE flares produced through standard channels, there are several possible sources of confusion. SMBHs can also be ejected from galactic nuclei in triple-SMBH interactions (Hoffman and Loeb 2007); the rates of these are highly uncertain but generally require a lack of efficient solutions to the final parsec problem. Recent theoretical suggestions that the final parsec problem can be quickly solved by nuclear triaxiality (Khan et al. 2013) may therefore eliminate this channel for producing kicked SMBHs, but resolving this question is beyond the scope of this paper. A more serious source of confusion could be tidal disruptions produced in a galaxy with two SMBHs. A hard SMBH binary should produce an enormous enhancement in the TDE rate for a period of $\sim 10^5$ years, as stellar orbits are depleted by a combination of the Kozai effect and chaotic three-body interactions (Ivanov et al. 2005; Chen et al. 2009; Wegg and Bode 2011; Chen et al. 2011). However, these TDEs will have no observable spatial offset. At earlier times in the history of a galaxy merger, an SMBH pair will exist at wider separation. Tidal disruption flares from such a configuration would have a large spatial offset, but could potentially be distinguished from flares from a recoiling SMBH by the existence of two centers of light in the host galaxy.

Finally, many galaxies may possess a population of loosely bound IMBHs (relics of hierarchical galaxy assembly placed in the halo by past episodes of GW recoil). These black holes can tidally disrupt stars from their small bound clouds (O'Leary and Loeb 2012), but could likely be distinguished from recoiling SMBHs by their lower masses. In any case, detection of tidal disruption flares from halo IMBHs would also be an exciting example of GW recoil!

This chapter is organized as follows. § 4.2 outlines the theoretical model we use to estimate TDE rates as a function of kick velocity and host galaxy parameters. In § 4.3, we outline the actual rate calculation and the parameter distributions we integrate over. § 4.4 is a discussion of the results of our model, and § 4.5 concludes the chapter by summarizing the utility of TDE flares as signatures of SMBH recoil.

4.2 Model

In order to estimate the offset TDE rate in a given galaxy, we must calculate three important quantities:

1. The trajectory of a recoiling SMBH through the bulge (and perhaps halo) of its host galaxy.
2. The rate of tidal disruptions of unbound bulge stars.
3. The rate of tidal disruptions of stars from the bound cloud, which over time can relax into loss cone orbits.

In this section, we estimate distributions of SMBH kick velocities (§ 4.2.1), outline the basics of TDE light curves (§ 4.2.2), select a parametrization for the galaxy density and potential profiles (§ 4.2.3), and compute the rates of TDEs from unbound (§ 4.2.4) and bound (§ 4.2.5) stars. In general, we employ the light curve models and rate calculation formalism of Strubbe and Quataert (2009, hereafter SQ09), but applied to the synthetic population of recoiling SMBHs produced by our model. In § 4.2.6 we discuss the flux and resolution constraints of realistic surveys, with a focus on *LSST*.

4.2.1 Gravitational Wave Recoil

The kick velocity v_k imparted to a SMBH by anisotropic GW emission depends on only a handful of parameters: the mass ratio and spin vectors (both amplitude and orientation) of the original binary. If both progenitor black holes are non-spinning, then the maximum attainable v_k is modest, $\approx$175 km s^{-1}. Increasing magnitudes of progenitor spins a_1 and a_2 increase the maximum possible v_k, but in a way that depends sensitively on the relative orientations of the spin vectors and the orbital angular momentum vector. Full numerical relativity simulations are required to determine v_k, but these simulations can also be used to calibrate analytic fitting formulas to high

accuracy (Lousto et al. 2010a). In principle, maximal spin amplitudes and carefully selected spin orientations can produce "superkicks" with $v_k \approx 4000$ km s^{-1}, but these are unlikely to be common: from a theoretical perspective, superkicks require some fine tuning of spin vector orientations, and from an observational perspective, virtually all galaxy bulges seem to possess SMBHs (Ferrarese and Ford 2005; Blecha et al. 2011). The strength of this observational constraint, is, however, limited by the hierarchical history of galaxy assembly (Schnittman 2007).

Clearly, a realistic distribution of kick velocities will depend sensitively on the assumed distribution of pre-merger spin magnitudes; for example, the isotropic spin angles simulated by Lousto et al. (2010b) found over 23 % of kicks exceeding 1000 km s^{-1} for $a_1 = a_2 = 0.97$. SMBH spin magnitudes are measured through the Fe Kα line, and sometimes are observed to be near-extremal (Brenneman and Reynolds 2006), but such observations can only be performed for actively accreting SMBHs and are therefore troubled by complex selection effects. The orientations of SMBH spin vectors will depend on the environment in which the SMBH binary hardens; gas-rich galaxy mergers likely produce a circumbinary accretion disk that can align pre-merger SMBH spins (Bogdanović et al. 2007). Aligned spins produce a much more bottom-heavy v_k distribution than do isotropic spin angles, although circumbinary disks can also produce counter-alignment (King et al. 2005; Lodato and Pringle 2006), which results in intermediate v_k values. An analysis of wet mergers indicates that hot accretion flows (adiabatic $\gamma = 5/3$) are less efficient at aligning SMBH spin vectors than are cold accretion flows ($\gamma = 7/5$), but in both cases the median kick velocity for equal mass mergers is quite small, $\lesssim$70 km s^{-1} (Dotti et al. 2010, although considering a range of mass ratios would likely increase typical v_k). Furthermore, relativistic spin precession may be capable of producing alignment or counter-alignment even in the absence of circumbinary gas (Kesden et al. 2010). For all of these reasons, it is necessary to generalize the analysis of KM08 to realistic kick velocity distributions, which will only rarely feature kick velocities above galactic escape speeds.

In the remainder of this chapter, we employ the three kick velocity distributions presented in Lousto et al. (2010a), Fig. 2, which represent the results of Monte Carlo simulations for isotropic spins (dry mergers), spins aligned to within 30° (hot wet mergers), and spins aligned to within 10° (cold wet mergers). These simulations further assume a uniform distribution of q between 0 and 1, and spin magnitudes uniformly sampled between 0 and 0.9 (for the dry merger case) or between 0.3 and 0.9 (for the wet merger case). We calculate SMBH trajectories assuming v_k values of 100, 200, 300, 400, 500, 600, 700, 800, and 900 km s^{-1}, and perform a weighted average of the resulting TDE rates based on the Lousto et al. (2010a) v_k distributions. Although this approach neglects certain physical complications, such as relativistic spin precession (Kesden et al. 2010) and realistic spin magnitude distributions (Volonteri et al. 2005; Berti and Volonteri 2008), it brackets the parameter space of SMBH spin orientations, which is likely the dominant uncertainty in calculating astrophysical v_k distributions.

4.2.2 Tidal Disruption Emission

In this paper we employ the disk and super-Eddington outflow models presented in SQ09 and Strubbe and Quataert (2011); the disk models are summarized in § 1.5, and we present the super-Eddington outflows here. It is important to note that the super-Eddington outflows described in this section were derived using an incorrect expression for $\Delta\epsilon$, so that they only give the correct result for $\beta = 1$, $R_\mathrm{p} = R_\mathrm{t}$ events. Fortunately, these are the only TDEs relevant for recoiling SMBHs, as will be discussed later in the paper.

Numerical simulations of super-Eddington accretion indicate that radiation pressure can drive a powerful wind from such accretion disks. If we approximate the outflow as spherical, its photospheric radius will be given by

$$R_\mathrm{ph} \sim 10 f_\mathrm{out} f_\mathrm{v}^{-1} \left(\frac{\dot{M}_\mathrm{r}}{\dot{M}_\mathrm{Edd}}\right) R_{p,3R_\mathrm{S}}^{1/2} R_\mathrm{S}, \tag{4.1}$$

and its photospheric temperature will be

$$T_\mathrm{ph} \sim 2 \times 10^5 \left(\frac{f_\mathrm{v}}{f_\mathrm{out}}\right)^{1/3} \left(\frac{\dot{M}_\mathrm{r}}{\dot{M}_\mathrm{Edd}}\right)^{-5/12} \times M_6^{-1/4} R_{p,3R_\mathrm{S}}^{-7/24} \text{ K}. \tag{4.2}$$

Peak emission will occur at $\max(t_\mathrm{fall}, t_\mathrm{edge})$, where the time for the photosphere's outer edge to become optically thin is

$$t_\mathrm{edge} \sim 1 \ f_\mathrm{out}^{3/8} f_\mathrm{v}^{-3/4} M_6^{5/8} R_{p,3R_\mathrm{S}}^{9/8} m_*^{3/8} r_*^{-3/8} \text{ days}. \tag{4.3}$$

In the above equations, we have parametrized the outflow wind velocity as

$$v_\mathrm{w} = f_\mathrm{v} \left(\frac{GM_\mathrm{BH}}{r_\mathrm{p}}\right)^{1/2}, \tag{4.4}$$

where $f_\mathrm{v} \sim 1$. The mass ejected in the outflow is likewise parametrized as

$$\dot{M}_\mathrm{out} = f_\mathrm{out} \dot{M}_\mathrm{r}, \tag{4.5}$$

where $f_\mathrm{out} = 0.1$ for the remainder of this paper. We assume a radiative efficiency $\eta = 0.1$ to compute the Eddington-limited mass accretion rate $\dot{M}_\mathrm{Edd}$, and also employ the normalizations $M_6 = M_\mathrm{BH}/(10^6 M_\odot)$, $R_{\mathrm{p},3R_\mathrm{S}} = R_\mathrm{p}/(3R_\mathrm{S})$, and $R_\mathrm{S} = 2GM_\mathrm{BH}/c^2$.

A major uncertainty in our work is whether kinematic offsets can be detected by Doppler shifts in TDE emission or absorption lines. Past agreement on line emission from unbound tidal debris (Bogdanović et al. 2004; Strubbe and Quataert 2009; Kasen and Ramirez-Ruiz 2010; Strubbe and Quataert 2011) has recently been called into question by numerical simulations demonstrating recollapse of unbound debris into thin, self-bound structures with negligible covering fraction (Guillochon et al.

2014, although this may not apply to $\beta \gtrsim 3$ TDEs). However, even if we neglect this recent development, the large velocity spread in the unbound debris ($\Delta v \approx (2\Delta\epsilon)^{1/2} \gtrsim 0.1c$) is both a significant fraction of the speed of light, and dependent on unknown parameters such as the inclination of the star's pre-disruption orbit.

Absorption lines formed during reprocessing of disk radiation by a super-Eddington outflow may be a more promising tool for the detection of kinematic offsets. Most of these lines are in the UV, although weaker lines could exist in the optical and soft X-ray (Strubbe and Quataert 2011). The bulk outflow velocity $v_{\rm w}$ is very large, which will produce an effective broadening, so that determination of the SMBH velocity may require detailed modeling if (as seems likely) $f_{\rm v} \sim 1$. Alternative models of the super-Eddington phase of TDEs could be more conducive to production of narrow absorption lines (Loeb and Ulmer 1997), but in the remainder of this paper we consider detection of kinematic offsets to be significantly more speculative than that of spatial offsets, which can be straightforwardly accomplished with photometric subtraction.

A recoiling black hole will tidally disrupt stars from the small stellar cloud that remains bound to it; it will also disrupt unbound stars randomly passing nearby. In the next subsections, we outline our formalism for calculating both these rates. We conservatively choose $M_* = M_\odot$ and $R_* = R_\odot$; neglect of a stellar present day mass function likely decreases TDE rates by a factor $\approx$2 (Magorrian and Tremaine 1999).

4.2.3 Host Galaxy Structure

Calculations of TDE rates in galaxies with stationary SMBHs (Syer and Ulmer 1999; Magorrian and Tremaine 1999; Wang and Merritt 2004) often model the background stellar density using the Nuker parametrization for surface brightness:

$$I(s) = I_{\rm b} 2^{\frac{B-\Gamma}{\alpha}} \left(\frac{s}{s_{\rm b}}\right)^{-\Gamma} \left(1 + \left(\frac{s}{s_{\rm b}}\right)^{\alpha}\right)^{-\frac{B-\Gamma}{\alpha}}. \tag{4.6}$$

This surface brightness profile was developed to model high-resolution *HST* observations of nearby ellipticals and bulges (Lauer et al. 1995), and asymptotes to power law behavior at small ($I(s) \propto s^{-\Gamma}$) and large ($I(s) \propto s^{-B}$) radii. In Eq. (4.6), s is projected distance, $s_{\rm b}$ is the break radius, and the dimensionless index α determines the smoothness of the break between the inner and outer power laws. An Abel inversion will yield the three dimensional stellar density profile, which likewise asymptotes to power law behavior of $\rho(r) \propto r^{\gamma}$ ($\rho(r) \propto r^{\beta}$) when $r \ll s_{\rm b}$ ($r \gg s_{\rm b}$). The power law indices $\gamma \approx \Gamma + 1$ and $\beta \approx B + 1$.

Observed Nuker galaxies are bimodally distributed with respect to the inner power law index Γ: "core" galaxies have relatively flat ($\Gamma \approx 0$) central density profiles, while "cusp" galaxies have steeper central density profiles ($\Gamma \approx 1$). This dichotomy may emerge during the process of binary SMBH coalescence: as a binary SMBH hardens, it will eject a large number of stars from the host galaxy's nucleus, scouring a core

in a previously steeper central density profile (Merritt and Milosavljević 2005). In a dry merger, the scoured core will persist, but a cusp can be rebuilt via *in situ* star formation in a gas-rich merger (Kormendy et al. 2009; Blecha et al. 2011). We therefore associate observed core (cusp) galaxies as good approximations for the post-recoil stellar bulge in dry (wet) mergers. Because observed core galaxies are generally quite large, we create a mock galaxy catalog using scaling relations in order to cover the relevant range of parameter space. Three important scaling relations for our purposes are the relation between bulge mass M_* and $M_{\rm BH}$ (Marconi and Hunt 2003)

$$M_* = 4.06 \times 10^{10} M_\odot \left(\frac{M_{\rm BH}}{10^8 M_\odot} \right)^{1.04}, \tag{4.7}$$

and the empirically calibrated scaling laws for SMBH influence radii $r_{\rm infl}$ in core

$$r_{\rm infl} = 35 \text{ pc} \left(\frac{M_{\rm BH}}{10^8 M_\odot} \right)^{0.56} \tag{4.8}$$

and cusp

$$r_{\rm infl} = 22 \text{ pc} \left(\frac{M_{\rm BH}}{10^8 M_\odot} \right)^{0.55} \tag{4.9}$$

galaxies. The SMBH influence radius is the radius that contains a stellar mass equal to $2M_{\rm BH}$.

An important limitation of the Nuker parametrization for our purposes is its assumption of spherical symmetry; this is important because kicked SMBHs are initially on radial orbits. In a spherical potential, these orbits remain radial, and their repeated passages through the exact center of the galaxy will quickly damp out their motion via stellar dynamical friction (Gualandris and Merritt 2008). However, in an axisymmetric or triaxial potential, small torques from the stellar bulge will stochastically change the recoiling SMBH's pericenter, suppressing energy losses due to dynamical friction. Because the assumption of spherical symmetry will artificially reduce the wandering lifetime of kicked black holes, we use an ad hoc density-potential pair that captures the most physically important feature of the Nuker profile (broken power law behavior) but that is by construction axisymmetric. We use the spheroidal isodensity surfaces

$$\rho_*(m) = \begin{cases} K_1 m^{-\gamma} & m < m_{\rm b} \\ K_2 m^{-\beta} & m_{\rm b} \le m < m_{\rm max} \\ 0 & m \ge m_{\rm max} \end{cases} \tag{4.10}$$

where we have defined an axisymmetric pseudoradius

$$m^2 = \frac{r^2}{a^2} + \frac{z^2}{c^2}. \tag{4.11}$$

Here r and z are cylindrical coordinates, and our isodensity spheroids have axis ratios of a and c, with $a > c$. We define the parameters using the most recent Nuker sample (Lauer et al. 2005): $\gamma = \Gamma + 1$, $\beta = B + 1$, and $m_{\rm b} = s_{\rm b}$. Because these parameters are not strong functions of M_* (within the subpopulations of core and cusp galaxies), we approximate them as having Gaussian distributions, with means and variances calculated from Lauer et al. (2005). The parameters K_1, K_2, and $m_{\rm max}$ are chosen so as to normalize the total bulge mass to M_*, to produce the correct value of $r_{\rm infl}$, and to ensure continuity at the break pseudoradius $m_{\rm b}$. Our final free parameter, $\epsilon = 1 - c/a$, is calibrated from the observed isophote ellipticities in Lauer et al. (2005), once again assuming a Gaussian distribution.

Because so few core galaxies exist with $M_{\rm BH} < 10^8 M_\odot$, it is not obvious that scaling relations for their parameters (Faber et al. 1997) can be reliably extended down to low masses. This is particularly problematic because it is only SMBHs with $M_{\rm BH} \lesssim 10^8 M_\odot$ that are capable of tidally disrupting stars outside their event horizons. Most recoiling SMBHs capable of tidally disrupting stars will therefore originate in the merger of two cuspy galaxies, but the merger product can nonetheless look like a core galaxy if the pre-merger gas fraction is low or if all star formation occurs prior to the final stages of the SMBH binary inspiral. Our mock catalog is built around the two following scenarios:

1. Large amounts of free gas allow star formation to rebuild a nuclear cusp. In this scenario, we calibrate all our free parameters $\{\gamma, \beta, s_{\rm b}, \epsilon\}$ directly off the observed sample of cusp galaxies in Lauer et al. (2005). The merged galaxy will also have a fraction $f_{\rm g}$ of its baryonic mass in a gas disk; we present our model for this in § 4.2.4.
2. The SMBH binary excavates a core, and a stellar cusp fails to rebuild because either there is not enough free gas, or because star formation happens prior to core scouring. In this scenario, β is calibrated from the Lauer et al. (2005) sample of cusp galaxies, as are initial parameter values $\gamma_0, s_{\rm b,0}$. However, we set $f_{\rm g} = 0$ take ϵ and a final power law slope $\gamma_{\rm f}$ from the subsample of core galaxies; we also calculate a final break radius $s_{\rm b,f}$. To do this we manually excavate a mass deficit $\Delta M = 2M_{\rm BH}$, which increases the initial break radius by a factor of a few:

$$s_{\rm b,f} = \left(\frac{\dfrac{\Delta M}{4\pi K_1 (1-e^2)^{1/2}} - s_{\rm b,0}^{3-\gamma_0} \dfrac{\beta - \gamma_0}{(3-\beta)(3-\gamma_0)}}{s_{\rm b,0}^{\beta-\gamma_0} \dfrac{\gamma_{\rm f} - \beta}{(3-\gamma_{\rm f})(3-\beta)}} \right)^{1/(3-\beta)} . \tag{4.12}$$

In the above equation, we have defined $e = \sqrt{1 - (c/a)^2}$.

Now that we have fully defined our isodensity profiles, it is simple to use the method of homoeoids (Binney and Tremaine 2008, Sect. 2.5) to calculate isopotential curves through numerical integration. Even numerical calculation of two-integral distribution functions is quite challenging (Hunter and Qian 1993), so for simplicity we

calculate a velocity dispersion in the spherical limit and substitute in m for r:

$$\sigma^2(r) = 2\pi G K_2 \left(\frac{2s_{\rm b}^{3-\beta}}{r(3-\gamma)(1+\beta)} + \frac{r^{2-\beta}}{(3-\beta)(\beta-1)} - \frac{2s_{\rm b}^{3-\beta}}{r(3-\beta)(1+\beta)} \right) \tag{4.13}$$

when $r > s_{\rm b}$, and

$$\sigma^2(r) = 2\pi G K_1 s_{\rm b}^{2-2\gamma} r^{\gamma} \left(\frac{2}{(3-\gamma)(1+\beta)} + \frac{1}{(3-\beta)(\beta-1)} - \frac{2}{(3-\beta)(1+\beta)} + \frac{1}{(3-\gamma)(1-\gamma)} \right) - \frac{2\pi G K_1 r^{2-\gamma}}{(3-\gamma)(1-\gamma)} \tag{4.14}$$

when $r < s_{\rm b}$. The above estimates for σ are inaccurate for $r \lesssim r_{\rm infl}$ because the velocity dispersion will be modified by the central black hole, and they can also break down at large radii because of the presence of a dark matter halo (which we will parametrize below). Therefore, instead of using the above analytic expressions, we numerically compute a one-dimensional velocity dispersion (again in the spherical limit, substituting in the pseudoradius):

$$\sigma^2 = \frac{1}{\rho(r)} \int_r^{\infty} \rho(r') \frac{GM(r')}{r'^2} {\rm d}r'. \tag{4.15}$$

Here $M(r)$ is the total enclosed mass and $\rho(r)$ the total density at a radius r. Because we have derived this integral assuming spherical symmetry, the dynamical friction and gravitational focusing equations introduced in § 4.2.4 will be modestly inaccurate.

For the largest kicks velocities, wandering SMBHs can be ejected into the dark matter halo surrounding their host galaxy. We parametrize the gravitational influence of this using the the standard NFW profile (Navarro et al. 1997),

$$\rho_{\rm NFW} = \frac{\rho_0}{(r/a_{\rm s})(1+r/a_{\rm s})^2}. \tag{4.16}$$

In the NFW profile, the density normalization ρ_0 and scale factor $a_{\rm s}$ are calculated assuming a concentration parameter of 10 and by truncating the dark matter halo at the virial radius r_{200} where $\rho_{\rm NFW}(r_{200}) = 200\rho_{\rm c}$ ($\rho_{\rm c}$ is the cosmological critical density). The total mass in dark matter, $M_{\rm tot}$, is calculated using the $M_{\rm BH}$-$M_{\rm tot}$ relation (Bandara et al. 2009),

$$M_{\rm BH} = 1.51 \times 10^8 \left(\frac{M_{\rm tot}}{10^{13} M_{\odot}} \right)^{1.55}. \tag{4.17}$$

We conservatively assume a spherically symmetric dark matter halo (a nonspherical halo would extend the lifetimes of recoiling SMBHs).

Because the dynamical friction time for an inspiraling satellite galaxy will exceed the Hubble time when the mass ratio $q \lesssim 0.1$ (Wetzel and White 2010), we restrict ourselves to major mergers ($q > 0.1$). Major merger rates have been estimated by Hopkins et al. (2010) using the analytic fitting formula

$$\frac{dN_{\rm major}}{dt} = 0.04\left(1+\left(\frac{M_{\rm min}}{M_0}\right)^{0.8}\right) \times (1+z)^{\beta(M_{\rm min})}\ {\rm Gyr}^{-1}, \tag{4.18}$$

where total bulge mass $M_{\rm bulge} > M_{\rm min}$, z is redshift, and $M_0 = 2\times 10^{10} M_\odot$. Furthermore,

$$\beta(M_{\rm min}) = 1.5 - 0.25\log\left(\frac{M_{\rm min}}{M_0}\right). \tag{4.19}$$

Throughout this calculation we use a ΛCDM cosmology with parameters taken from Spergel et al. (2007): $\Omega_\Lambda = 0.73$, $\Omega_{\rm M} = 0.27$, and $H_0 = 71$ km s^{-1} Mpc^{-1}.

To summarize: we assemble a mock galaxy catalog by first choosing a value for $M_{\rm BH}$, and then using Lauer et al. (2005) to draw a parameter set $\{\gamma, \beta, s_{\rm b}, \epsilon\}$ for the desired merger scenario (either a wet merger that rebuilds a stellar cusp, or an "effectively dry" merger that does not). Our fiducial choices of $M_{\rm BH}$ are $10^6, 10^{6.5}, 10^7, 10^{7.5}$, and $10^8 M_\odot$, which we interpolate across the SMBH mass function from Hopkins et al. (2007).

4.2.4 *Interactions with the Galaxy*

To model the disruption rate of unbound stars, we evolve the SMBH's trajectory under the influence of gravity and dynamical friction through galaxies with the axisymmetric Nuker density profiles described above. We use the fifth-order Dormand-Prince method (with an embedded fourth-order Runge-Kutta integrator for adaptive timestepping) described in Press et al. (2002, Chap. 17). The effects of dynamical friction are approximated with the Chandrasekhar formula (Chandrasekhar 1943),

$$\vec{F}_{\rm df} = -I(M)\frac{4\pi\rho(GM_{\rm BH})^2}{\sigma^2}\frac{\vec{v}_{\rm BH}}{v_{\rm BH}}, \tag{4.20}$$

with σ the local velocity dispersion and ρ the local density of the medium causing the drag. For a collisionless medium, such as a stellar population,

$$I_{\rm dry}(M) = \frac{\ln(\Lambda)}{M^2}\left({\rm erf}\left(\frac{M}{\sqrt{2}}\right) - \sqrt{\frac{2}{\pi}} M e^{-M^2/2}\right) \tag{4.21}$$

where $M = v_{\rm BH}/\sigma$ is the Mach number. The Coulomb logarithm can be fit numerically (Escala et al. 2004), and for the case of SMBHs on radial orbits, is well matched by a value of $\ln\Lambda = 2.5$ (Gualandris and Merritt 2008). Dynamical friction is the force which ultimately causes the kicked black hole to settle back into a near-stationary position in the center of its host galaxy, on timescales ranging from 10^6 to 10^9 years (Madau and Quataert 2004; Blecha and Loeb 2008). The Chandrasekhar formula is derived assuming a uniform and infinite background of stars, and it is not immediately clear how appropriate that is for a steep density profile in galactic nuclei, or for a black hole massive enough to excite a response in the stellar population. The applicability of the Chandrasekhar formula to bound, recoiling black holes has been considered before (Gualandris and Merritt 2008), and for appropriately chosen $\ln\Lambda$ it was found to be fairly accurate until the point when the mass interior to the black hole's apogalacticon is of order $M_{\rm BH}$. After this, coherent oscillations develop in the stars interior to the black hole's trajectory, and dynamical friction is found to become dramatically less effective at removing the black hole's orbital energy. We terminate our calculations at the onset of this orbital phase, both because our trajectory approximation would become quite inaccurate and also because TDEs caused by a slow-moving SMBH near the center of a galaxy would not be distinguishable from those caused by a stationary black hole. During these calculations, we neglect the extra "core scouring" caused by black hole recoil (Gualandris and Merritt 2008). The stellar population in the galactic center responds to a moving SMBH by expanding, with a mass of stars equal to a few $M_{\rm BH}$ being displaced from the galactic center for kicks close to escape velocity (and the effect is reduced for slower ones). Neglect of this effect likely reduces the SMBH wandering time and causes us to underestimate the total number of TDEs per galaxy merger, but probably not by much, as axisymmetry of the stellar potentials prevents the SMBHs from returning exactly to the center of their host galaxies where core scouring is most relevant. We emphasize that dynamical friction removes the most orbital energy during passages through the densest regions of the SMBH's trajectory. Therefore trajectories with nonzero angular momentum (due to an axisymmetric potential) last longer before settling back into the galactic center than would center-crossing ones in spherical geometries.

In a dry merger it is sufficient to consider dynamical friction off stars and not gas. This regime could also apply to wet mergers where the gas is used up in star formation (while the SMBH binary is stalled) or dispersed in binary quasar feedback. We identify both of these scenarios with our "excavated core" galaxies. If significant quantities of gas survive until the recoil phase of the merger, however, it is necessary to consider the effects of gas dynamical friction, which would apply more to our "pure cusps." Previous work (Blecha et al. 2011) has indicated the effect of leftover gas is to decrease black hole wandering times, reducing the observable number of offset TDEs. To quantify this effect, Eq. (4.21) still applies; we simply need to use gas density rather than stellar density for ρ, substitute a local sound speed $c_{\rm s}$ for σ, and modify the dimensionless parameter $I(M)$ (for gas, $M = v_{\rm BH}/c_{\rm s}$). The new

dimensionless functions are

$$I_{\rm subsonic}(M) = \frac{1}{2}\ln\left(\frac{1+M}{1-M}\right) - M \tag{4.22}$$

in the subsonic regime, and

$$I_{\rm supersonic}(M) = \frac{1}{2}\ln\left(1-\frac{1}{M^2}\right) + \ln\left(\frac{v_{\rm BH}t}{r_{\rm min}}\right) \tag{4.23}$$

in the supersonic regime (Ostriker, 1999). However, these formulae have been shown to overestimate gas dynamical friction in the slightly supersonic regime, so we adopt the prescription of Escala et al. (2004) and use the Chandrasekhar formula for $I(M)$, with $\ln\Lambda = 4.7$ for $M \geq 0.8$ and $\ln\Lambda = 1.5$ for $M < 0.8$. We follow the prescriptions of Blecha and Loeb (2008) and assume that most of the gas in the galaxy has settled into a disk, which we align with the oblate plane of the galaxy. We employ a slightly less complicated version of their model, as only two of their four disk zones are relevant for our dynamical modeling: zones III and IV (zones I and II only exist in the presence of a central SMBH). Zone III, the portion of the disk influenced by the SMBH potential before the recoil kick, is truncated on its inner edge at the kick radius,

$$r_{\rm k} = \frac{GM_{\rm BH}}{v_{\rm k}^2}, \tag{4.24}$$

and transitions to zone IV at $r = r_{\rm infl}$. Zone IV is an exponential disk with scale $r_{\rm disk}$. The disk surface density in zone III will be

$$\Sigma_{\rm III} = \left(\frac{4}{\pi Q^2}\right)\left(\frac{\dot{M}_\alpha^2}{\alpha^2 G}\right)^{1/3} r^{-1}, \tag{4.25}$$

while in zone IV, the surface density is

$$\Sigma_{\rm IV} = \frac{M_{\rm disk}(>r_{\rm infl})}{2\pi r_{\rm disk}(r_{\rm infl}+r_{\rm disk})e^{-r_{\rm infl}/r_{\rm disk}}} e^{-r/r_{\rm disk}}. \tag{4.26}$$

Here we take the viscosity parameter $\alpha = 0.1$, and set the Toomre parameter $Q = 1$ (Toomre, 1964) under the assumption that star formation feedback roughly balances cooling, leaving the disk marginally stable. The accretion rate $\dot{M}_\alpha$ can be found by mass normalization of equation (4.25) so that $M_{\rm III} = 2 f_{\rm gas} M_{\rm BH}$:

$$\dot{M}_\alpha = \left(\frac{f_{\rm gas} M_{\rm BH} Q^2}{4(r_{\rm infl}-r_{\rm k})}\right)^{3/2} \alpha G^{1/2}. \tag{4.27}$$

The scale distance $r_{\rm disk}$ is then found by requiring continuity between zones III and IV: $\Sigma_{\rm III}(r_{\rm infl}) = \Sigma_{\rm IV}(r_{\rm infl})$. Densities in both disk zones decay exponentially with height z, with scale height

$$h_{\rm III} = \frac{Q^2}{8} r \tag{4.28}$$

taken from Blecha and Loeb (2008). In zone IV, the scale height

$$h_{\rm IV} = \frac{\dot{M}_\alpha \kappa_\Omega}{3\pi^2 \alpha Q G \Sigma_{\rm IV}^2} \tag{4.29}$$

is solved for using the identities $\dot{M}_\alpha = 3\pi\alpha c_{\rm s} h \Sigma$ and $c_{\rm s} = (G\dot{M}_\alpha/\alpha)^{1/3}$. Here κ_Ω is the epicyclic frequency, and is calculated from the numerically integrated potentials of the isodensity shells in Eq. (4.10).

In our models we consider values of $f_{\rm g}$ (gas as a fraction of total baryonic mass) of 0 and 0.3. The latter value is taken as a conservative upper limit for remnant gas fraction at the time of black hole merger, as self-consistent hydrodynamical simulations (Mihos and Hernquist 1996) have shown that $\geq$50 % of the initial gas fraction, $f_{\rm g,i}$ in a merger is expelled or converted into stars by the time of black hole coalescence. Observation indicates that $f_{\rm g,i} \lesssim 0.6$ for $M_{\rm BH} > 10^6 M_\odot$ at low redshift (Hopkins et al. 2010, Fig. 7), so $f_{\rm g} = 0.3$ is a conservative case, likely to result in SMBH orbits which decay somewhat faster and produce fewer offset tidal disruptions than in more general wet mergers with smaller $f_{\rm g}$.

At each point along the SMBH's trajectory we consider an instantaneous "tidal disruption cylinder" of length $v_{\rm BH}\Delta t$ and radius equal to the gravitationally focused tidal disruption radius. This lets us simply calculate instantaneous tidal disruption rates along the trajectory,

$$\dot{N}_{\rm u} = \rho_* v \pi R_{\rm t}^2 \left(1 + \frac{2GM_{\rm BH}}{R_{\rm t} v^2}\right) \tag{4.30}$$

which can be integrated to get a time-averaged TDE rate, or $N_{\rm TDE}$, the total number of stars disrupted per recoil event. Here $v = \sqrt{v_{\rm BH}^2 + \sigma^2}$, with σ given by Eqs. (4.13) and (4.14).

4.2.5 Interactions with the Bound Cloud

The initial size of the bound cloud is determined by the magnitude of the received kick, and can be approximated as encompassing all stars within $r_{\rm k}$. The mass of the bound cloud is found by KM08 to be a fraction f_b of the black hole mass, where

$$f_b = F(\gamma)\left(\frac{2GM_{\rm BH}}{r_{\rm infl} v_{\rm k}^2}\right)^{3-\gamma}. \tag{4.31}$$

Here γ is the same as in Eq. (4.10), $r_{\rm infl}$ is the influence radius, the interior of which contains a mass in stars twice $M_{\rm BH}$, and $F(\gamma) = 11.6\gamma^{-1.75}$. For most cloud sizes the disruption rate of bound stars will be determined by resonant relaxation into the SMBH's empty loss cone, exponentially depleting the population of stars inside on a timescale $\tau \approx 3.6 G M_{\rm BH}^2/(v_{\rm k}^3 m_*)$ (KM08). In practice, the e-folding time is at

least an order of magnitude below 10^{10} years for most of the $10^6 M_\odot$ and $10^{6.5} M_\odot$ black holes which escape from their host galaxies, strongly suppressing the averaged intergalactic TDE rate.

One exception to this picture is if $r_k \sim r_{infl}$; in this case nonresonant relaxation could become important, and resonant relaxation alone will significantly underestimate the TDE rate. This regime is of minimal significance for this paper, however, since small kicks are likely to produce few spectrally and no spatially offset flares. A more significant exception is for relatively low-mass SMBHs, which can reach an energy relaxation timescale in less than their wandering time. Relaxation will eventually allow the cloud to expand in radius (O'Leary and Loeb 2009), changing the time evolution of the tidal disruption rate from exponential depletion to $\propto t^{-3/2}$ (O'Leary and Loeb 2012). Therefore, we adopt KM08's prescription for resonant relaxation,

$$\dot{N}_b \approx C_{RR}(\gamma) \frac{\ln \Lambda}{\ln (r_k/r_t)} \frac{v_k}{r_k} f_b e^{-t/\tau} \tag{4.32}$$

when $t < t_r$, but transition to $\dot{N}_b \propto t^{-3/2}$ at later times. The energy relaxation timescale t_r is taken to be (O'Leary and Loeb 2012)

$$t_r = 10^9 \text{ years} \left(\frac{M_{BH}}{10^5 M_\odot} \right)^{5/4} \left(\frac{r_k}{r_{infl}} \right)^{1/4}. \tag{4.33}$$

This power law disruption rate is only relevant for $M_{BH} < 10^{6.5} M_\odot$, but for lower mass SMBHs we transition to power law depletion after an energy relaxation time. For both scenarios, the initial disruption rate is

$$\dot{N}_b \approx 1.5 \times 10^{-6} \left(\frac{M_{BH}}{10^7 M_\odot} \right) \left(\frac{r_{infl}}{10 \text{ pc}} \right)^{-2} \times \left(\frac{v_k}{10^3 \text{ km s}^{-1}} \right)^{-1} \text{ year}^{-1}. \tag{4.34}$$

One uncertainty is the resonant relaxation coefficient C_{RR}, found by KM08 to have a value of 0.14 for $\gamma = 1$. Since the spatial power law exponents for core galaxies are close to 1, we adopt this value, though it is less well motivated for cuspier galaxies.

We also consider growth of the bound cloud by capture of members of binary star systems. This three-body interaction is treated in the same way as tidal disruption of unbound stars, except instead of a stellar tidal disruption radius we use an "orbital tidal disruption radius", given by

$$r_{t,o} = a_{bin} \left(\frac{M_{BH}}{2 m_*} \right)^{1/3}, \tag{4.35}$$

where a_{bin} is the binary semimajor axis. While one member of the binary is ejected at high velocities (Hills, 1988), the other is bound to the black hole, with apoapsis r_{max} given by

$$r_{max} \approx \frac{G M_{BH}}{v_{eject}^2} \left(\frac{m_*}{M_{BH}} \right)^{1/6} \left(\frac{a}{0.1 \text{ AU}} \right)^{1/2} \tag{4.36}$$

(Yu and Tremaine 2003), with $v_{\rm eject} \approx 145\,{\rm km\ s^{-1}}$ (Hills, 1988). To calculate the rate of these captures, we assume Öpik's Law (Öpik, 1924), a flat distribution of binary semimajor axes a in units of $\log(a)$, between a_{min} and a_{max}. Following Vereshchagin et al. (1988) and Kouwenhoven et al. (2007) we adopt $a_{min} = 5R_\odot$ and $a_{max} = 5 \times 10^6 R_\odot$. We only consider captures with $r_{\rm max} < r_{\rm t,c}$, with the cloud's tidal radius conservatively given by $r_{\rm t,c} = r_{\rm infl}$. This refill mechanism is in principle capable of counterbalancing losses due to tidal disruption and evaporation from the cloud. Without a refill source, resonant relaxation into the loss cone will normally cause the population of the bound cloud to evolve due to $\dot{N}_{\rm TDE} \propto N$, leading to a population (and TDE rate) depleted exponentially in time, at least until $t = t_{\rm r}$. We can roughly see the effect of stellar capture into the bound cloud if we assume

$$\dot{N} = -kN + m, \tag{4.37}$$

with k the average frequency with which bound stars evaporate or are scattered into the loss cone and m a time-averaged capture rate. This differential equation has the solution

$$N(t) = N(0)e^{-kt} + \frac{m}{k}(1 - e^{-kt}). \tag{4.38}$$

By itself, relaxation will deplete the bound cloud, but 3-body capture allows the number of stars in the cloud to asymptotically approach a nonzero value. If the time-averaged binary capture rate is high enough (i.e. if $m/k > N(0)$), then the size of the cloud would even grow over time. The importance of this effect is determined for each galaxy/kick velocity pair.

A final consideration is stability of the bound cloud to perturbations. Analytically, it seems unlikely that interactions with unbound stars will eject significant numbers of bound stars from the cloud: if the cloud stars are bound to the black hole with typical energy $E_{\rm bind} \sim -v_{\rm k}^2 m_*$, and during encounters with unbound stars a change in energy $\Delta E \sim Gm_*^2/r_{\rm p}$ is available (where $r_{\rm p}$ is the closest approach of the two stars), encounters must be within $r < r_{\rm p} \sim r_{\rm k}(m_*/M_{\rm BH})$. For a $10^7 M_\odot$ black hole on typical trajectories, this works out to at most ~1 unbound stars making close enough approaches to eject a bound star during the SMBH's passages through the bulge.

4.2.6 Observability of Recoil-Induced TDEs

To translate the total recoil-induced TDE rate into a rate of *identifiably* recoil-induced TDEs, it is necessary to consider observational constraints. LSST's rapid cadence, high sensitivity and thorough sky coverage make it an ideal survey to detect disruption flares - as mentioned in § 4.2.2, LSST could detect up to thousands of TDEs per year. LSST's limiting g-band magnitude is 25 (LSST Science Collaboration et al. 2009); because of LSST's short cadence we assume any flares brighter than that will be detected. The detectability of a spatial offset will depend on how well the

TDE centroid can be distinguished from the host galaxy centroid after photometric frame subtraction. For LSST the expected differential astrometric precision will be $\sim 0.7''/\mathrm{SNR}$ (LSST Science Collaboration et al. 2009). Using the LSST Science Manual's prescription for $\mathrm{SNR}^{-1} = \sigma_{\mathrm{tot}} = \sqrt{\sigma_{\mathrm{sys}}^2 + \sigma_{\mathrm{rand}}^2}$, we infer astrometric precision by calculating the signal to noise ratio for each event in our sample. We also calculate the rate of spectroscopically identifiable flares associated with a recoiling SMBH. Although UV spectroscopy would be ideal, soft X-ray spectrometers - SXS, for example, on the planned ASTRO-H mission (Takahashi et al. 2010), expected to be operating contemporarily with LSST - should be able to identify the absorption lines discussed in § 2.2, if they exist with sufficient equivalent width. To investigate this possibility, we consider a fiducial case of absorption lines at 10 keV, observed by SXS followup with an energy resolution of 7 eV. If the outflowing wind can be accurately modeled, these lines would allow black hole velocities down to ~ 200 km s^{-1} to be spectrally resolvable. As mentioned before, it is not clear that the super-Eddington phase of accretion will produce winds in which a ~ 200 km s^{-1} offset is detectable, so predictions of kinematic offsets should be regarded as somewhat hypothetical. Because spatial and kinematic offsets are angle-dependent, we average the observable quantities over all inclination angles for the host galaxy.

4.3 TDE Rate

Using the potentials and frictional forces described above, we integrate the trajectories of five different black hole masses at nine different kick velocities and seven inclination angles in galaxies with eighteen different possible permutations of mass-independent structural parameters, for a total of 11340 runs (the final factor of two comes from wet vs dry mergers). During preliminary test runs, a very weak dependence of the wandering time on β and γ was apparent (once variation in β and γ due to the core/cusp dichotomy is allowed for), so we set those quantities equal to their average values. Among the remaining structural parameters, we only varied ϵ and $s_{\mathrm{b},0}$.

We terminate our trajectory calculations after a Hubble time, if the black hole has left the stellar bulge (and its attendant sources of friction) with escape velocity, or upon the onset of the "Phase II" orbital oscillations of Gualandris and Merritt (2008), discussed in § 4.2.4.

To calculate the total observable rate of TDEs due to recoiling black holes, Υ, we use a modified version of Eq. (31) in SQ09. Specifically,

$$\frac{\mathrm{d}\Upsilon}{\mathrm{d}\ln M_{\mathrm{BH}}} = \int_{R_{\mathrm{ISCO}}}^{R_{\mathrm{t}}} \int_0^{\mathrm{d}_{\mathrm{max}}(R_{\mathrm{p}})} 4\pi r^2 f_{\mathrm{sky}} \frac{\mathrm{d}n}{\mathrm{d}\ln M_{\mathrm{BH}}} \times \frac{\mathrm{d}\upsilon(r, R_{\mathrm{p}})}{\mathrm{d}\ln R_{\mathrm{p}}} \mathrm{d}r \mathrm{d}\ln R_{\mathrm{p}} \tag{4.39}$$

Here $d_{\rm max}(R_{\rm p})$ represents the maximum comoving distance a TDE flare with given pericenter $R_{\rm p}$ can be seen at, using a 25 AB g-band magnitude limit. LSST will detect flares at cosmological distances, so it is necessary to employ a K-correction, which has a modest impact on $d_{\rm max}$. The rate $\upsilon(r, R_{\rm p})$ is integrated over inclination/azimuth angles and galaxy properties, and is the rate at which either TDE flares are produced at a distance r by TDEs with $R_{\rm p}$. Further cuts are added to the integrand to calculate the rate at which observably spatially offset TDE flares, or observably kinematically offset TDE flares are produced, using the criteria described in § 4.2.6 (with an average over azimuthal angles to account for projection effects). In our average over galaxy properties, we give $M_{\rm BH}$-dependent weights to the "pure cusp" and "excavated core" scenarios from § 4.2.3. These weights are determined in two ways. The first is to bin the the Lauer et al. (2005) galaxy sample and compute the fraction of cusps and cores in each σ bin (with the small minority of intermediate cases taken as 50 % core, 50 % cusp). The σ bins are translated into masses from the measured σ using a recent calibration (Graham et al. 2011) of the $M_{\rm BH} - \sigma$ relation (Tremaine et al. 2002). The second approach is to bin the larger Lauer et al. (2007) sample in magnitude $M_{\rm V}$, and to then translate to $M_{\rm BH}$ using the relation between $M_{\rm BH}$ and V-band magnitude in Bentz et al. (2009) (specifically, the "FITEXY FF05 ellipticals - outliers" fit). We average the results of these two methods, and find that for $M_{\rm BH}/M_{\odot}$ of $10^6, 10^{6.5}, 10^7, 10^{7.5}$, and 10^8, the fractions of core galaxies are $0.03, 0.125, 0.125, 0.114$, and 0.302, respectively.

To calculate $d_{\rm max}$ for super-Eddington flares we use Eqs. (4.1), (4.2), and (4.3), while to do the same for disk emission we use Eq. (1.4). For simplicity, we neglect the less important emission from photoionized, unbound disruption debris, noting that this is a conservative approximation. For disruptions from the bound cloud, resonant relaxation slowly diffuses stars across the loss cone in phase space, meaning that nearly all bound TDEs will have $R_{\rm p} \approx R_{\rm t}$. Unbound stars will have a wider variety of $R_{\rm p}$, but the geometry of gravitational focusing will bias them towards $R_{\rm p} \approx R_{\rm t}$ as well. For these reasons we simplify Eq. (4.39) by taking $R_{\rm p} = R_{\rm t}$. This approximation produces slightly more disk emission (due to physically larger disks), and significantly less luminous super-Eddington flares, than does the flat distribution of TDEs across $\ln R_{\rm p}$ assumed in SQ09. Consequently, our results show a much less pronounced difference in the observable TDE rate between the disk emission and super-Eddington outflows cases.

We then interpolate the results of these trajectory calculations over three different black hole physics scenarios, as discussed in § 2.1. In the first scenario, a lack of free gas during the SMBH inspiral leaves the spin vectors of the SMBH binary randomly aligned with each other, producing a top-heavy kick distribution and a high average value of dimensionless spin ($a_{\rm BH} = 0.73$). The other two scenarios involve wet mergers with warmer and cooler gas, producing spin vectors aligned to within 30 and 10°, respectively, and remnant mean spins of $a_{\rm BH} = 0.88$ and $a_{\rm BH} = 0.90$. Because the disruption of stars by $10^8 M_{\odot}$ black holes is so sensitive to $a_{\rm BH}$ ($a_{\rm BH} > 0.92$ required), we bracket these fiducial assumptions (the $a_{\rm BH}$ values above are the peaks of the remnant spin probability distributions in Lousto et al. (2010a)) about remnant spin with $a_{\rm BH} = 0$ and $a_{\rm BH} = 0.99$ cases. We also consider

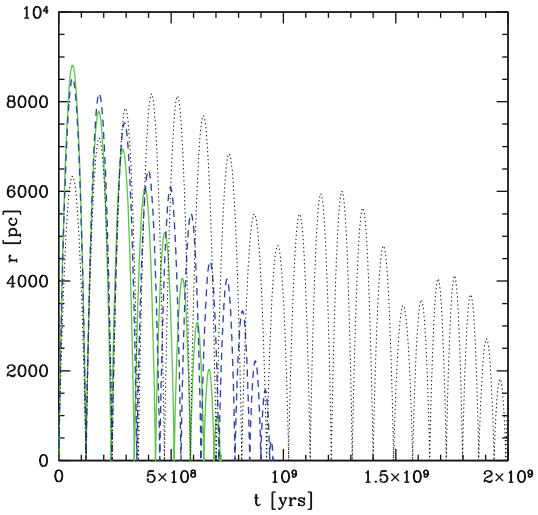

Fig. 4.1 The importance of asphericity on SMBH trajectories. All the lines represent trajectories of $10^7\ M_\odot$ SMBHs kicked at 400 km s^{-1} in a gas-free core galaxy. The green solid line is the course of a SMBH kicked in the plane of the galaxy's two semimajor axes, while the blue dot-dashed line represents a SMBH kicked 15 ° above the plane, and the black dotted line a SMBH kicked 45 ° above the plane

two different cases of tidal disruption physics; one in which the super-Eddington mass outflows proposed by SQ09 exist (for simplicity we take their canonical case of $f_v = 1$ and $f_{out} = 0.1$), and the other in which they do not. In the latter, optical emission is limited to the Rayleigh-Jeans tail of the newly-formed accretion disk.

4.4 Results and Discussion

Figures 4.1 and 4.2 illustrate the importance of nonspherical potentials for the lifetimes of wandering black holes. In the axisymmetric stellar potential that we employ, stars initially on radial orbits will quickly acquire angular momentum unless they lie on a principal axis of the stellar ellipsoid or in the equatorial plane. The latter is true of the 0°, green orbit, which is seen in Fig. 4.1 to decay somewhat faster than the blue, 15° orbit and dramatically faster than the 45°, black orbit. For the dry mergers illustrated here, the variation in decay time is due entirely to differences in stellar dynamical friction, which is the strongest at orbital pericenter. In the wet merger scenarios we considered, recoils in the plane of the gas disk are very quickly damped out, but axisymmetry in the stellar potential still affects orbital lifetimes for other inclination angles. Figure 4.2 illustrates the torques that act on orbits out of the equatorial plane, and in the inset we can see that those torqued orbits are able to avoid close pericenter passages, explaining their longevity.

The total number of disruptions per merger, N_{TDE}, was found to be fairly insensitive to the power-law slopes γ and β, but 1σ changes in s_b or ϵ can change N_{TDE} by a factor of a few. The sensitivity to s_b really reflects a sensitivity to the ratio v_k/v_{esc}, as the wandering time can jump by $\sim 1-2$ orders of magnitude when v_k/v_{esc} rises above a value $\sim 0.5-0.6$ (where v_{esc} here is the escape velocity of the stellar bulge). This

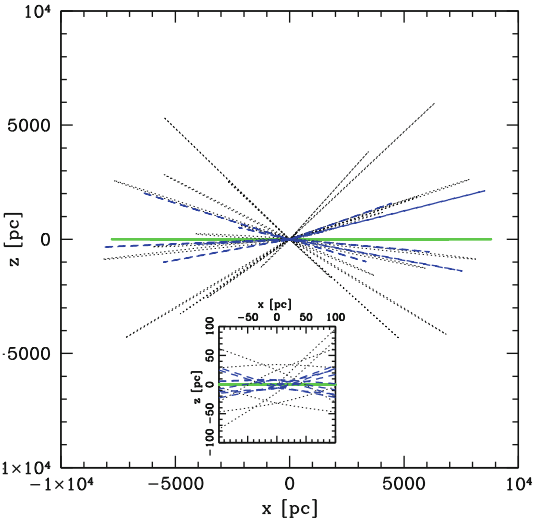

Fig. 4.2 The same black holes as in Fig. 4.1, now viewed in two dimensions. The inset plot zooms in on the central 100 parsecs to highlight the lack of center crossings for SMBHs ejected at nonzero inclination angles

sensitivity to kick velocity is due to the decreased effectiveness of dynamical friction once the SMBH begins passing through the galactic center at high velocities, giving the black hole more time to disrupt bound cloud stars. Because the SMBHs spend most of their near-radial orbit at apocenter, most bound cloud disruptions occur at an observably offset distance. As a side note, the binary capture mechanism introduced in § 4.2.5 was found to operate at negligible levels.

Figures 4.3 and 4.4 illustrate how our results vary with assumptions about the kick velocity distribution, final spin amplitudes of the SMBHs, and existence of super-Eddington outflows. In both figures, bound cloud disruptions are represented as thick lines and unbound stellar disruptions as thin lines. The total number of disruptions is shown as a solid line, while those with an observable spatial offset are shown with a dotted line, and those with an observable kinematic offset are shown with a dashed line. Unless otherwise noted, discussion of TDE rates in this section refers only to SMBHs which remain bound to their host galaxy.

Figure 4.3 displays $\mathrm{d}\Upsilon/\mathrm{dln}M_{\mathrm{BH}}$, the number of TDEs observed by LSST per year per logarithmic black hole mass, for our models without super-Eddington emission. Both the unaligned ($<180°$) and moderately aligned ($<30°$) progenitor spin models produce interesting values of Υ. Both bound and unbound disruption rates are dominated by the highest black hole mass permitted by its spin amplitude to disrupt stars; for the first row (fiducial a_{BH} values), this corresponds to $10^{7.5}M_{\odot}$, while for the second row ($a_{\mathrm{BH}} = 0.99$) it is $10^{8}M_{\odot}$ and for the third row ($a_{\mathrm{BH}} = 0.0$) it is $10^{7}M_{\odot}$. We note here that $10^{7}M_{\odot}$ black holes can always disrupt solar-type stars, but require a modest amount of spin in order for the ISCO to lie inside the tidal radius, which we take as a precondition for either disk or super-Eddington outflow emission (thereby neglecting the short-lived X-ray shock breakout signature of the TDE, explored in Guillochon et al. (2009), which LSST would not detect). Almost

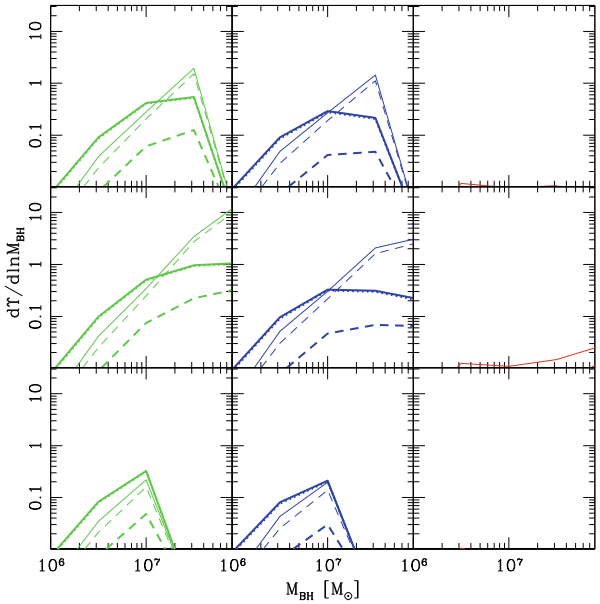

Fig. 4.3 Mass dependence of total TDE rates, Υ. In the left (*green*) column, we show the unaligned spin case; in the middle (*blue*), spins aligned to within 30°; and the right (*red*), spins aligned to within 10°. The top row has fiducial final spin amplitudes, while the middle has $a_{\rm BH} = 0.99$ and the bottom row has $a_{\rm BH} = 0.0$. The thick lines represent disruptions of bound stars; the thin lines, disruptions of unbound stars. The solid lines represent total number of disruptions, while dotted lines represent disruptions with observable spatial offsets and dashed lines represent disruptions with observable kinematic offsets. In this plot only disk emission is considered

all bound cloud disruptions have an observable spatial offset, while unbound disruptions never have an observable offset. On the other hand, a higher fraction of unbound disruptions possess an observable kinematic offset relative to the bound cloud disruptions. Both these correlations are easily explainable: due to high orbital eccentricity, the SMBHs in our sample spend the majority of their time far from the galactic nucleus, so most bound cloud disruptions occur with a large physical offset and low velocity. At the same time, virtually all unbound disruptions occur during perigalacticon, where the SMBHs move at their highest velocities. The highly aligned (<10°) progenitor spin model produces a negligible number of disruptions; high kick velocities are suppressed, and SMBHs escape the galactic nucleus too infrequently to disrupt significant numbers of stars.

In Fig. 4.4, we display $d\Upsilon/d\ln M_{\rm BH}$ for models with super-Eddington flares. The results are similar to those in Fig. 4.3, although $d\Upsilon/d\ln M_{\rm BH}$ is everywhere greater than or equal to its values in the previous figure. Two special points of contrast are the large increase in observable disruptions at the low end of the SMBH mass function, and the (corresponding) increase in disruptions for the highly aligned progenitor spin model. The addition of super-Eddington flares has, as expected, little effect

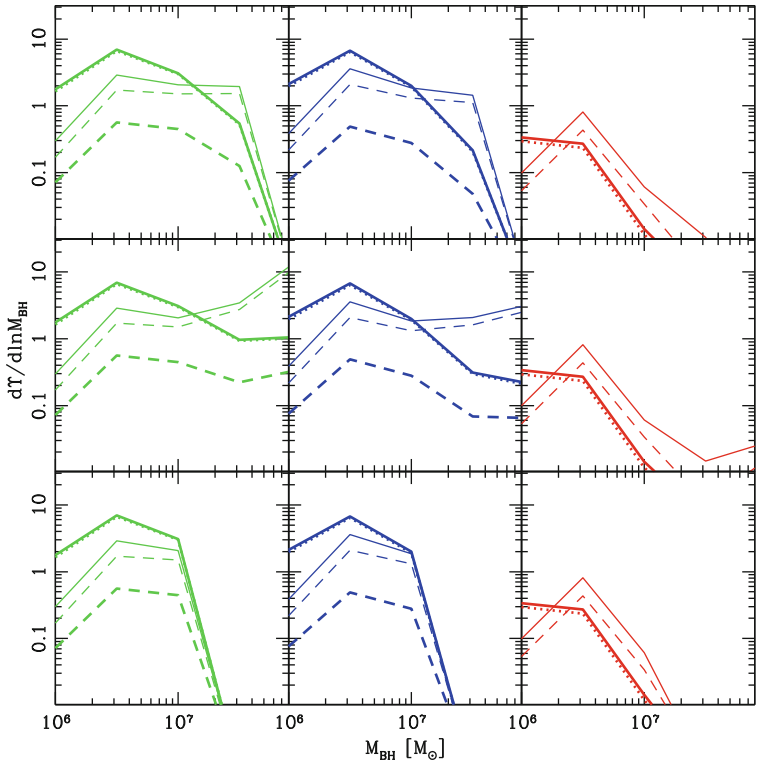

Fig. 4.4 The same as the previous figure, but assuming the existence of super-Eddington outflows

on values of $d\Upsilon/d\ln M_{BH}$ above $10^7 M_\odot$, but disruption flares become dramatically more visible for $10^6 M_\odot$ and $10^{6.5} M_\odot$ SMBHs.

Figure 4.5 displays $d\Upsilon_s/d\ln M_{BH}$, the mass dependence of the total observable (spatially offset) rate Υ_s, integrated over all kick velocities and all galaxies in our mock catalog, and given fiducial spin values. Υ_s is, as discussed in § 4.2.6, the rate of spatially offset flares that will be identified as offset by LSST's automatic photometric subtraction, without any followup observations. When we integrate over black hole mass, we find that two of our kick velocity distributions produce a robustly observable (∼10) number of disruptions per year assuming super-Eddington flares, while the third produces a more marginal number of TDEs, of order unity per year. Likewise, progenitor spin distributions aligned to within 180° or within 30° produce ∼1 flare per year with an observable spatial offset if we are only able to observe disk emission. Higher-mass SMBHs contribute the most to observable disk flares, due to the lower temperatures and higher optical luminosities of their disks, while super-Eddington accretion flares are dominated by the lower-mass end of the SMBH distribution. Although the rate enhancement from inclusion of super-Eddington outflows is almost a factor of 10, this is considerably lower than the comparable factor in SQ09. The

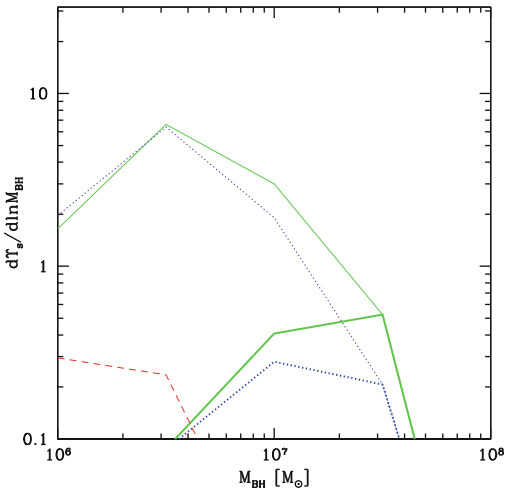

Fig. 4.5 Mass dependence of the total, galaxy- and velocity-averaged rate of spatially offset TDEs, Υ_s, in the case of fiducial spin. 180, 30, and 10° progenitor spin alignment correspond to solid green lines, dotted blue lines, and dashed red lines, respectively. Thick lines represent disk emission only, while the thin lines correspond to disk plus super-Eddington outflows

reason for this disparity is that the brightest super-Eddington outflows correspond to the deepest plunges (lowest R_p) into the tidal disruption region. SQ09 considered a logarithmically flat distribution of R_p, while we took a constant $R_p = R_t$, for the reasons explained in § 3.

A variety of observable TDE rates are displayed in Table 4.1. These numbers have been integrated over galaxy type, kick velocity distribution, inclination angle, and black hole mass function, and indicate that the ultimate observability of recoil-induced TDEs will depend strongly on both the existence of super-Eddington flares, and the average distribution of pre-merger spin alignments. In this table, Υ values for fiducial SMBH spins are shown, with the $a_{BH} = 0$ and $a_{BH} = 0.99$ cases appearing as lower and upper limits in parentheses. It is only in the case where super-Eddington flares do not exist *and* substantial progenitor spin alignment occurs where we expect LSST to observe negligible numbers of spatially offset TDEs per year. We note that if the progenitor spins are unaligned, or even aligned with scatter $\geq$30°, the tidal disruption rate from recoiling black holes is almost 1 % of the total inferred TDE rate ($\sim 10^{-5}$year^{-1} per galaxy) for all galaxies. For most of our models, the number of kinematically offset TDEs, Υ_k, is comparable to Υ_s, although we note again that the theoretical basis for expecting appropriate absorption lines in a super-Eddington outflow is less secure than that for a simple spatial offset. We have also included in Table 4.1 the rates of spatially and kinematically offset TDEs for SMBHs which escape their host galaxy altogether, labeling these as $\Upsilon_{s,esc}$ and $\Upsilon_{k,esc}$. Only in the case of unaligned spins and super-Eddington outflows are $\Upsilon_{s,esc} \sim \Upsilon_s$ and $\Upsilon_{k,esc} \sim \Upsilon_k$; in all other scenarios the number of observable TDEs due to ejected SMBHs is at least a factor of 7 smaller than the number due to bound SMBHs.

For most of the models we have considered, a large majority of the TDEs associated with recoiling SMBHs occur for black holes bound to their host galaxy. This is due to two factors: both the relatively low fraction of SMBHs recoiled at escape

Table 4.1 Total number of offset TDEs observable by LSST per year (Υ_s, Υ_k) in different models. The fiducial spin case is given first, and is bracketed in parentheses by the $a_{BH} = 0$ and $a_{BH} = 0.99$ cases.

Spin Alignment [°]	super-Eddington?	Υ_s[TDEs year^{-1}]	Υ_k[TDEs year^{-1}]	$\Upsilon_{s,esc}$[TDEs year^{-1}]	$\Upsilon_{k,esc}$[TDEs year^{-1}]
10	no	0 (0, 0)	0 (0, 0)	0 (0, 0)	0 (0, 0)
10	yes	0.5 (0.5, 0.5)	0.5 (0.5, 0.5)	0 (0, 0)	0 (0, 0)
30	no	0.6 (0.3, 0.9)	1.4 (0.2, 4.8)	0.07 (0.04, 0.08)	0.05 (0.03, 0.05)
30	yes	10 (10, 11)	5.6 (4.5, 9.0)	1.5 (1.5, 1.5)	1.2 (1.3, 1.2)
180	no	1.0 (0.4, 2.6)	2.0 (0.2, 17.2)	0.6 (0.4, 0.8)	0.5 (0.3, 0.6)
180	yes	12 (11, 13)	6.1 (4.4, 21.3)	8.1 (8.0, 8.2)	6.4 (6.4, 6.5)

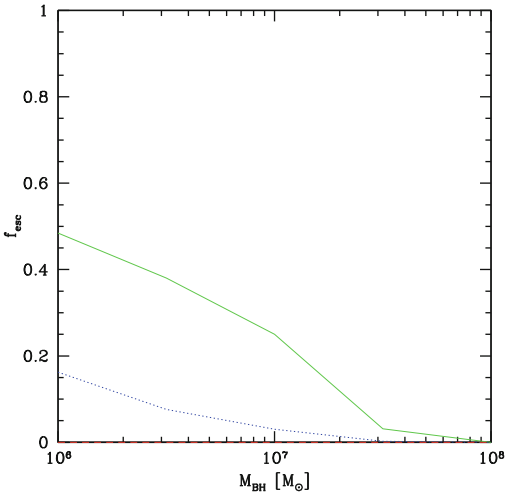

Fig. 4.6 Fraction of recoiled SMBHs which escape into intergalactic space, as a function of black hole mass, for the three different kick velocity distributions. As in the previous figure, the green solid line represents the 180° alignment distribution, the dotted blue the 30°, and the dashed red (not visible; a negligible fraction of SMBHs from this distribution escaped their host galaxies) the 10°

velocity (see Fig. 4.6 for a plot of the SMBH escape fraction, $f_{\rm esc}$), and the smaller, more rapidly decaying bound clouds of those low-mass SMBHs which do escape. This highlights the importance of searching for SMBHs bound to the bulge or halo of their host galaxy; although the intergalactic TDEs of the KM08 scenario offer a cleaner signal, they are intrinsically much fewer in number. Our work has differed from KM08 primarily in considering much wider ranges of $v_{\rm k}$, using kick velocity distributions motivated by merger gas content. Our treatment of disruption rates for a given $v_{\rm k}$ is mostly similar, with the exception of incorporating the results of O'Leary and Loeb (2012) for late-time relaxation in the bound cloud.

Finally, it is worth summarizing the primary assumptions we made in this work, where we have tried to err on the side of conservatism. To simplify our calculations, we neglected emission from the unbound TDE debris, although that can substantially increase optical (non-super-Eddington) emission for low-mass SMBHs (SQ09). Our SMBH wandering lifetimes were likely reduced by the fact that we limited ourselves to axisymmetric stellar bulge geometries, and even more importantly only considered spherical dark matter haloes. Our simple choice of stellar mass function is slightly conservative for calculations of TDE rate.

4.5 Conclusions

In this paper, we have generalized the work of KM08 to include a mock galaxy catalogue and physically motivated distributions of kick velocities, so as to estimate the observability of offset tidal disruption flares. We have demonstrated that super-Eddington flares from recoiling black holes, if they exist along the lines envisioned in SQ09, will be observably offset to LSST in numbers ranging from ∼1 to ∼10

TDEs per year. This is true for a broad range of assumptions about kick velocity distributions and galactic structure. This subset of transients would contain important scientific value as evidence of black hole recoil, and could potentially constrain the v_k distribution. If super-Eddington flares do not exist or if they differ significantly from the SQ09 picture (for example, if $f_{out} \ll 0.1$), optical emission from the accretion disks of TDEs around recoiling black holes will still be accessible to LSST, although here the case is more marginal. If a large fraction of local universe SMBH mergers proceed without significant spin alignment, the prospects for optical detection of disk emission from recoiling TDEs are relatively good, but moderate amounts of alignment would likely suppress this. Importantly, the majority of recoiled SMBHs will remain bound to their host galaxies, making photometric subtraction critical for identification of recoil-associated disruption flares. Depending on the nature of the super-Eddington phase of accretion, a comparably large population of kinematically offset flares is potentially detectable, but would require spectroscopic followup to be realized.

We have also shown that confusion with TDEs from stationary SMBHs will not be a major challenge in the detection of off-nuclear TDEs, leaving supernova contamination as the main concern. If the scientific potential of spatially offset TDEs is to be utilized, it will be necessary to construct transient survey pipelines which do not employ the typical "galactic center" cut when searching for TDEs. Although the challenges inherent to TDE identification have been discussed elsewhere (van Velzen et al. 2011b), the distinctive lightcurve and color evolution of tidal disruption flares are helpful in separating them. The large number of TDEs expected to be observed by time domain surveys in the coming decade will calibrate our understanding of these events, so that once LSST is online, it may be able to confirm the SMBH recoil predictions of numerical relativity.

Chapter 5
Consequences of Strong Compression in Tidal Disruption Events

N. Stone, R. Sari, & A. Loeb The Monthly Notices of the Royal Astronomical Society, *Vol. 435, pp. 1809–1824, 2013*

The dynamics of stellar tidal disruption depend strongly on how deeply the victim star's orbit plunges into the tidal sphere. In this Chapter, we show that most previous estimates of the spread in debris energy, $\Delta\epsilon$, are inaccurate when $\beta = R_t/R_p > 1$; the traditional formula for $\Delta\epsilon$ can be incorrect by orders of magnitude for high β events. After presenting a revised formula that is independent of β and correct to leading order, we develop a new analytic model for tidal disruption events (TDEs) and employ this to test our conclusion that $\Delta\epsilon$ does not depend on β. We find that $\Delta\epsilon$ is not modified at leading order by general relativistic effects, stellar spin, or the hydrodynamic bounce of a tidally compressed star, although it is possible that a combination of these factors could restore some β dependence to $\Delta\epsilon$. We present a first estimate of high frequency gravitational wave emission that accompanies the compression of a star during high β events, and find that the Advanced LIGO horizon for tidal disruptions of white dwarfs by intermediate mass black holes can be tens of megaparsecs.

5.1 Introduction

Many different theoretical methods exist for studying stellar tidal disruption. These range from the purely analytic (Rees 1988; Phinney 1989), to the semi-analytic methods of the "affine model" pioneered by Carter and Luminet (1983, hereafter CL83) and further developed in subsequent papers (Carter and Luminet 1985; Luminet and Marck 1985; Luminet and Carter 1986), to numerical hydrodynamic simulations, of both the Eulerian (Khokhlov et al. 1993a; Frolov et al. 1994; Guillochon et al. 2009; Guillochon and Ramirez-Ruiz 2013) and Lagrangian (Nolthenius and Katz 1982; Evans and Kochanek 1989; Laguna et al. 1993; Lodato et al. 2009; Hayasaki et al. 2013) varieties. These approaches have built on each other to improve our theoretical understanding of TDEs; however, in this paper we argue that they have overlooked a critical feature of deeply plunging tidal disruption events. In particular, the "frozen-in" spread in debris orbital energy ($\Delta\epsilon$) has been overestimated by past analytic work in the $\beta \gg 1$ limit, and this overestimate has gone unnoticed

N. C. Stone, *The Tidal Disruption of Stars by Supermassive Black Holes,*
Springer Theses, DOI 10.1007/978-3-319-12676-0_5

by numerical simulations because of the focus of past simulations on the $\beta = 1$ events that dominate the TDE rate. Calculating a correct leading-order $\Delta\epsilon$ is the first focus of this paper; the second is to analytically study the vertical compression (or "pancaking") phase of a TDE, which has been explored by the affine model but is quite difficult for full numerical simulations to resolve.

In § 5.2 we argue that the conventional expression for $\Delta\epsilon$ is incorrect, sometimes by orders of magnitude, and propose a more accurate leading-order expression for this important dynamical quantity. In § 5.3 we introduce a new analytic model that describes the tidal free fall experienced by a star between R_t and R_p. This formalism is in some ways a simplification of the affine model, but possesses somewhat more flexible initial conditions and, appealingly, can be written in closed form. Using this new model for tidal free fall, in § 5.4 we analyze redistribution of orbital energy during the hydrodynamic bounce of a tidally compressed star. More complicated scenarios involving desynchronized collapse and general relativistic corrections are considered in § 5.5 and § 5.6, respectively. In § 5.7 we perform novel calculations estimating the frequencies and wave strain of gravitational waves (GWs) emitted during the bounce phase: interestingly, we find that these GWs may be detectable by Advanced LIGO for white dwarfs disrupted by intermediate mass black holes. In § 5.8, we apply our revised estimates of $\Delta\epsilon$ to more directly observable quantities, and find that the most strongly super-Eddington accretion rates predicted in past literature are unlikely to be physical. A general discussion of the results in § 5.9 concludes this work.

5.2 Dynamical Energy Spread

To leading order, a tidally disrupted star's internal forces become subdominant shortly after it passes inward of R_t. After this point, the star's fluid elements travel on roughly ballistic trajectories, and to a reasonable approximation, their orbital energies have "frozen in." In the standard literature (Evans and Kochanek 1989; Kochanek 1994; Ulmer 1999; Kasen and Ramirez-Ruiz 2010; Strubbe and Quataert 2009; Lodato and Rossi 2011), the spread in frozen-in energy is given by

$$\Delta\epsilon = k\frac{GM_{BH}R_*}{R_p^2}. \tag{5.1}$$

This equation can be obtained in two ways: either by Taylor expanding the SMBH potential around the star at the point of pericenter passage (the point where internal forces are most subdominant), or by the simple calculation $\Delta\epsilon = V_p\Delta V_p \sim GM_{BH}R_*/R_p^2$. Here we have defined the pericenter velocity $V_p = (2GM_{BH}/R_p)^{1/2}$, and the impulsive delta-v at pericenter $\Delta V_p = A_pT_p$. Using $V_p = (2GM_{BH}/R_p)^{1/2}$, where tidal acceleration at pericenter $A_p \sim (GM_{BH}/R_p^2)(R_*/R_p)$ and the dynamical time $T_p \sim (GM_{BH}/R_p^3)^{-1/2}$.

This reasoning is, however, incorrect. A simple Taylor expansion of the SMBH potential would accurately evaluate the frozen-in energy spread for a static sphere

of matter, but by the time the star reaches pericenter, it is highly nonspherical due to tidal stretching. More importantly, its fluid elements are moving on geodesic trajectories with a large velocity shear; the differential energy between two fluid elements depends not just on their relative positions (captured by a Taylor expansion) but also on their velocities. Equivalently, it is not accurate to estimate $\Delta V_{\rm p}$ as $A_{\rm p} T_{\rm p}$. This is because the eigenvectors of the Newtonian tidal tensor rotate as the tidally free falling star progresses along its parabolic center of mass trajectory (Brassart and Luminet 2008). Let us define $\hat{X}$ as the direction connecting the star and the SMBH; $\hat{Y}$ as the direction in the orbital plane orthogonal to $\hat{X}$; and $\hat{Z}$ as the direction perpendicular to the orbital plane. These three basis vectors are the eigenvalues of the tidal tensor; the star is stretched in the $\hat{X}$ direction but compressed in the $\hat{Y}$ and $\hat{Z}$ directions. The rotation of $\{\hat{X}, \hat{Y}\}$ across a parabolic orbit limits the total stretching and compression suffered by the star within the orbital plane, and invalidates the above estimate of $\Delta V_{\rm p}$ (however, the fixed direction of $\hat{Z}$ produces extreme compression orthogonal to the orbital plane, which will be discussed in much greater detail in § 5.3 and § 5.4).

Given the above problems with the traditional formula for $\Delta\epsilon$, we propose this alternative:

$$\Delta\epsilon = k \frac{G M_{\rm BH} R_*}{R_{\rm t}^2}. \tag{5.2}$$

When the star is located at $R = R_{\rm t}$, it is to first order still a static, spherical ball of gas; a simple Taylor expansion of the SMBH potential is therefore an accurate estimate of the spread in orbital energy across the star. However, it is not immediately obvious that Eq. (5.2) measures a *frozen-in* energy spread: the star's internal forces are not nearly as subdominant at $R = R_{\rm t}$ as they are at $R_{\rm p}$ for $\beta > 1$ events. We perform the following post-hoc check on our revised formula: the internal forces of the star produce accelerations $A_{\rm in} \sim G M_*/R_*^2$; this produces a perturbation to the frozen-in energy spread of order $\Delta\epsilon_{\rm in} \lesssim G M_{\rm BH} R_*/R_{\rm t}^2$. We note that this is an upper limit on the amount that internal forces can modify the frozen-in $\Delta\epsilon$; internal forces do the most work on the star's fluid elements at $R = R_{\rm t}$, but at this point pressure and self-gravity are still self-canceling to first order (Carter and Luminet 1983, Fig. 4), as the star was originally in hydrostatic equilibrium. Our estimate for $A_{\rm in}$ is therefore too large, as is $\Delta\epsilon_{\rm in}$; however, even these upper limits imply that Eq. 5.2 is correct to leading order, and there is no β dependence in the energy spread that freezes in at the tidal radius. It is worth noting that similar conclusions were reached by Sari et al. (2010, hereafter SKR10) on the tidal separation of binary stars by SMBHs.

Could additional pieces of physics that we have not yet accounted for modify this conclusion? To approach this question with an open mind, we adopt the more general equation

$$\Delta\epsilon = k \beta^n \frac{G M_{\rm BH} R_*}{R_{\rm t}^2}, \tag{5.3}$$

where $n = 2$ in the standard literature, and $n = 0$ in our revised picture. We will now determine if additional physics can restore a β dependence (i.e. $n \neq 0$) to $\Delta\epsilon$; after addressing this question, we consider the observational implications of a revised n in § 5.8.

5.3 Free Solutions, and Free Collapse

Other factors could influence or invalidate the simple analytic argument presented in § 5.2, such as redistribution of energy during the period of maximum compression, GR corrections, stellar spin, or simply work done on the star's fluid elements by subdominant internal forces inside the tidal sphere. In this section, we introduce a new analytic model for the tidal free fall of a disrupted star that will help us approach these issues.

Because the dominant source of TDEs is expected to be stars scattered onto radial orbits from $\sim$ pc scales (Magorrian and Tremaine 1999; Wang and Merritt 2004), we assume a parabolic orbit for the center of mass of the star, with distance from the SMBH given by:

$$R = \frac{2R_{\rm p}}{1+\cos f}. \tag{5.4}$$

For such an orbit, time t is related to true anomaly f via

$$t = \frac{1}{3}\left(\frac{2R_{\rm p}^3}{GM_{\rm BH}}\right)^{1/2} \tan(f/2)\left(3+\tan^2(f/2)\right), \tag{5.5}$$

although the differential form

$$\frac{df}{dt} = \frac{1}{8^{1/2}}(1+\cos f)^2\sqrt{\frac{GM_{\rm BH}}{R_{\rm p}^3}} \tag{5.6}$$

is more generally useful. We set $t = f = 0$ at $R = R_{\rm p}$, and use $\dot{f} > 0$ throughout this paper.

The sequence of events in a TDE, first noted by CL83, will be useful shorthand for us, so we introduce it here. Phase I (near-equilibrium) of a TDE lasts while $R > R_{\rm t}$, and the star remains in approximate if slightly perturbed equilibrium. Phase II (free fall) begins when the star crosses the tidal sphere and becomes gravitationally unbound; in this paper we will treat the transition between Phases I and II as instantaneous, an assumption we justify below in § 5.5. The assumption of tidal free fall is very useful because of the existence of analytic, "free" solutions to the Hill equations in the parabolic restricted 3-body problem, but it is not immediately obvious that internal forces in the star can be neglected for $R < R_{\rm t}$. To first order the approximation seems reasonable because the ratio of tidal acceleration to self-gravitational acceleration grows quickly, as $a_{\rm t}/a_{\rm g} \approx (R_{\rm t}/R)^3$ for the bulk of the star.

Furthermore, the star's internal pressure and self-gravity partially cancel each other, further reducing their combined contribution. For now, we assume the validity of the free fall assumption, but after developing further machinery we will justify it further in § 5.5.

During this free fall, the star is compressed perpendicular to the orbital plane (along $\hat{Z}$) and in one direction within the orbital plane, while being stretched along the other in-plane direction. Although for the limiting case of radial infall the problem is self-similar in all three dimensions (SKR10), the rotation of the line connecting the star's center of mass to the SMBH breaks the in-plane similarity. By the time the star has reached pericenter, the $\hat{X}$ direction (which is parallel to the line between the SMBH and the orbital pericenter), is compressed, and $\hat{Y}$ is stretched, but the distortions are both much smaller than the compression orthogonal to the orbital plane. Shortly after passing pericenter, synchronous tidal free fall in the $\hat{Z}$ direction leads to very strong compression of the star, which is eventually reversed by hydrodynamic forces. Phase III (bounce) begins when hydrodynamical forces become strong enough to begin slowing the collapse of the star along its vertical axis. Once the star's collapse has reversed, hydrodynamical forces quickly become negligible again, and Phase IV (the rebound) begins, with stellar gas once again moving on ballistic trajectories.

We take as initial conditions for Phase II a spherically symmetric star at the tidal sphere, with fluid elements possessing initial positions $\vec{r}$ (the coordinate origin tracks the star's center of mass) and initial velocities in the center of mass frame $\vec{u}(\vec{r})$. Making the approximation that upon entering the tidal sphere, internal forces become negligible unless and until compression triggers shock formation or isentropic pressure buildup, we take the pre-shock trajectories of these fluid elements to be completely ballistic. This means that their trajectories are given by the parabolic Hill equations, $\vec{r}_{\rm H} = \{x_{\rm H}, y_{\rm H}, z_{\rm H}\}$. Unlike the $\{\hat{X}, \hat{Y}, \hat{Z}\}$ coordinates, which rotate as f progresses, the $\{\hat{x}, \hat{y}, \hat{z}\}$ which are used in the Hill equations define a fixed lab frame. The free solutions to these equations, neglecting self-gravity, can be written in closed form (SKR10) using coordinates where distance has been normalized by R_* and time by $\sqrt{R_*^3/(GM_*)}$; we denote such coordinates in this paper by writing tildes over them. All other coordinates are in physical units, unless otherwise noted. The equations of motion themselves are derived in Appendix A. Although there are 6 independent solutions to these equations, motion out of the orbital plane is decoupled from motion within it, so only two are relevant for perturbed motion in the $\hat{z}$ direction:

$$\begin{aligned} \tilde{z}_{\rm H} &= E\tilde{z}_{\rm E} + F\tilde{z}_{\rm F} \\ \tilde{z}_{\rm E} &= \frac{1}{\beta}\frac{2\sin f}{1+\cos f} \\ \tilde{z}_{\rm F} &= \frac{1}{\beta}\frac{2\cos f}{1+\cos f}. \end{aligned} \tag{5.7}$$

Here E and F are undetermined coefficients that are set by the initial conditions described above. In particular, if we require that a fluid element of initial position

$z = z_0$ has initial velocity $w = \dot{z} = 0$ at $f = f_t$, where the true anomaly upon entry into the tidal sphere is given by

$$f_t = -\arccos(2/\beta - 1), \tag{5.8}$$

then

$$E = -\tilde{z}_0\sqrt{\beta - 1} \tag{5.9}$$

$$F = \tilde{z}_0. \tag{5.10}$$

If we introduce a tidal potential Ψ felt in the rest frame of the star, the tidal acceleration is given by SKR10 as

$$\ddot{\tilde{z}} = -\frac{\partial\Psi}{\partial\tilde{z}} = -\beta^3\frac{(1+\cos f)^3}{8}\tilde{z}. \tag{5.11}$$

We note that the self-similarity of Eq. 5.11 implies that the free solutions all collapse to $z = 0$ simultaneously at a true anomaly f_c, although physically this collapse will be reversed shortly before by the buildup of pressure gradients strong enough to counteract the tidal forces compressing the star. However, it is useful to solve for f_c using Eq. 5.7:

$$\tan f_c = \frac{1}{(\beta - 1)^{1/2}}. \tag{5.12}$$

From this formula we see that in the limit of $\beta \to \infty$, collapse along the z-axis occurs at $f_c = 0$, i.e. at pericenter, while in the marginal disruption limit of $\beta \to 1$, collapse occurs at $f_c = \pi/2$, i.e. at a fixed point past pericenter. We have already mentioned that the free solutions become less valid for small β due to the increasing importance of internal forces, but we can see from Eq. 5.12 a second, stronger, inconsistency at low β, which is that the free solutions dictate vertical collapse after the disrupted star leaves the tidal sphere, i.e. $f_c > |f_t|$. This occurs for $\beta \lesssim 1.3$.

Although the onset of Phase III is dictated by compression in the $\hat{z}$ direction, the outcome of the bounce will be affected by motion within the orbital plane during Phase II, when $f < f_c$. We therefore describe here the free solutions within the orbital plane (SKR10):

$$\tilde{x}_H = A\tilde{x}_A + B\tilde{x}_B + C\tilde{x}_C + D\tilde{x}_D$$

$$\tilde{y}_H = A\tilde{y}_A + B\tilde{y}_B + C\tilde{y}_C + D\tilde{y}_D$$

$$\tilde{x}_A = -\frac{1}{\beta}\frac{\sin f}{1+\cos f}$$

$$\tilde{y}_A = \frac{1}{\beta}\frac{\cos f}{1+\cos f}$$

$$\tilde{x}_B = -\frac{1}{\beta}\sin f$$

$$\tilde{y}_{\rm B} = \frac{1}{\beta}(1+\cos f) \tag{5.13}$$

$$\tilde{x}_{\rm C} = \frac{1}{\beta}(2-\cos f)$$

$$\tilde{y}_{\rm C} = -\frac{1}{\beta}\cos f \tan(f/2)$$

$$\tilde{x}_{\rm D} = \frac{1}{\beta}(8+12\cos f)\tan^4(f/2)$$

$$\tilde{y}_{\rm D} = \frac{1}{\beta}\frac{35\sin f - 2\sin(2f) + 3\sin(3f)}{(1+\cos f)^2}$$

If we consider a point on the star with an initial position, relative to the star's center of mass, of (x_0, y_0, z_0) and zero initial velocity (here, as before, "initial" refers to $f = f_{\rm t}$, i.e. crossing into the tidal sphere), then we have 4 initial conditions for 4 unknowns: $\{A, B, C, D\}$. Using Eq. 5.8, we find

$$A = \frac{1}{\beta^2}\left(-8\tilde{x}_0\sqrt{\beta-1} + 2\tilde{y}_0(\beta^2+2\beta-4)\right) \tag{5.14}$$

$$B = \frac{1}{5\beta^2}\Big(2\tilde{x}_0\sqrt{\beta-1}(\beta^3-4\beta^2+8) + \tilde{y}_0(9\beta^3-12\beta^2-8\beta+16)\Big) \tag{5.15}$$

$$C = \frac{1}{\beta^2}\left(\tilde{x}_0(2\beta^2+\beta-2) - 2\tilde{y}_0\sqrt{\beta-1}(\beta^2-1)\right) \tag{5.16}$$

$$D = -\frac{1}{20\beta^2}\left(\tilde{x}_0(\beta-2) + 2\tilde{y}_0\sqrt{\beta-1}\right) \tag{5.17}$$

All six of the free solutions we have listed can be thought of as slight perturbations to a different orbital element of the parabolic center of mass trajectory, boosted into the center of mass frame. The free solutions represent freely falling particles in a Newtonian potential, but with a coordinate origin following a parabolic center of mass trajectory.

We have now exactly specified the motion of the idealized star's fluid elements in the orbital plane during Phase II. We plot the vertical free solutions for a variety of β in Fig. 5.1, and snapshots from motion within the orbital plane in Fig. 5.2. Here we list several important features of the free solutions, when they are initialized with static spheres of matter at $f = f_{\rm t}$:

- For $f > f_{\rm t}$, an initially spherical shell of matter will deform into a sequence of roughly ellipsoidal shapes. It is simple to demonstrate that they do not generally take the form of true ellipsoids, however.
- Initially concentric spherical shells of matter remain concentric, with in-plane principal axes that remain aligned with those of other concentric shells.
- Slices of the star through the orbital plane (z=0) maintain reflection symmetry across their rotating in-plane principal axes.

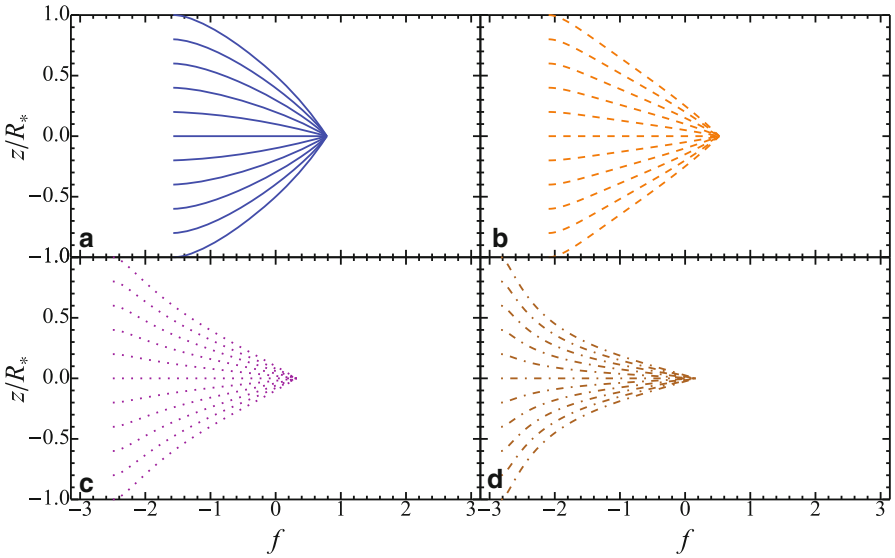

Fig. 5.1 Normalized height $\tilde{z} = z/R_*$ versus true anomaly f for the vertical collapse of one-dimensional stars at varying β. The solid blue curves in panel (**a**) are $\beta = 2$; the dashed orange curves in panel (**b**) are $\beta = 4$; the dotted purple curves in panel (**c**) are $\beta = 10$; the dot-dashed brown curves in panel (**d**) are $\beta = 40$. Each scenario is initialized at $f = f_t(\beta)$. Note that $f = 0$ corresponds to pericenter

- The derivation of the free solutions assumes that $R_*/R \ll 1$ (SKR10). If we neglect stretching of the star, this is equivalent to requiring $\beta \ll (M_{BH}/M_*)^{1/3}$, a condition that is in general easily satisfied: a $10^6 M_\odot$ SMBH, if non-spinning, cannot disrupt solar-type stars with $\beta \gtrsim 11$ (higher β values will place the pericenter interior to the marginally bound circular orbit, and the star will plunge directly into the horizon). Even a maximally spinning SMBH of this mass cannot disrupt solar-type stars with $\beta \gtrsim 47$. The effects of tidal stretching will make it somewhat harder to satisfy this assumption, but only for the minority of the star's mass that is strongly stretched.

The free solutions allow us to directly solve for the stellar axis ratio as a function of f or t, and it is trivial to do so numerically, but there is an exact analytic solution as well. If we denote the lengths of the long and short principal axes of our tidally distorted star (within the orbital plane) as r_{long} and r_{short}, respectively, we can solve for them by rewriting $\tilde{x}_0 = \cos\theta_0$, $\tilde{y}_0 = \sin\theta_0$, and finding the appropriate θ_0. More specifically, we set $\frac{d}{d\theta} R_H^2(f) = 0$ (with $R_H^2 = x_H^2 + y_H^2$), and solve for θ_{ex}, the values of θ_0 which extremize R_H. More physically, we are searching for the initial angles θ_{ex} around the star which at a later orbital phase f will correspond to its principal axes in the orbital plane. Once we have the initial angular positions of the principal axes, θ_{ex}, we can plug in to Eqs. (5.13) and solve for the size of the principal axes at a later true anomaly $f > f_t$. We also find the misalignment angle ν between the long

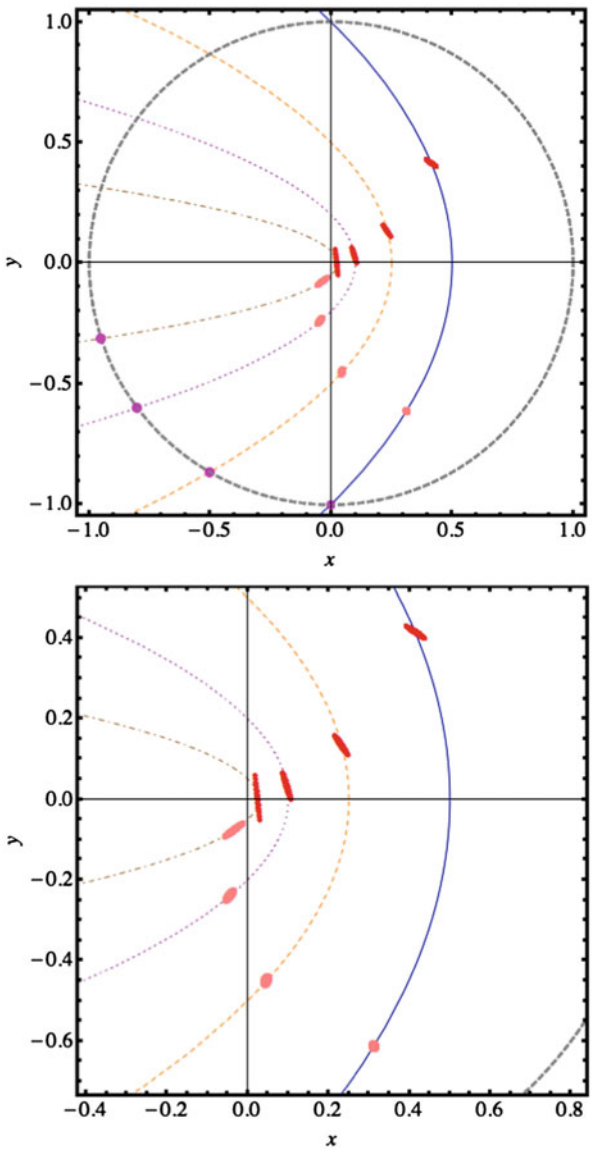

Fig. 5.2 The x and y coordinates (in units of R_t, which for the $10^6 M_\odot$ SMBH in this example is 100 $R_\odot$) of the free solutions for varying β, translated so that the origin lies on the SMBH. As before, we mark the $\beta = 2$ trajectory as solid blue, $\beta = 4$ as dashed orange, $\beta = 10$ as dotted purple, and $\beta = 40$ as dot-dashed brown. The free solutions for an initially circular midplane slice of a star are magenta at $f = f_t$, pink at $f = 0.7 f_t$, and red at $f = f_c$. The tidal radius is marked as a gray dashed circle. The right plot is a zoomed-in version of the left. The free solutions are breaking down for the $\beta = 40$ curve near pericenter, as the long axis of the star exceeds the orbital radius in size

in-plane principal axis and the orbital velocity vector. The in-plane stellar geometry is presented in Fig. 5.3.

The algebra involved in this solution is unenlightening, so we leave the general solution $\theta_{ex}(f)$ for numerical work and only derive analytic expressions for $\theta_{ex}(f_c)$, which is the situation of greatest interest. The details are contained in Appendix B, but we plot the results below in Fig. 5.4. Specifically, these are the sizes of the

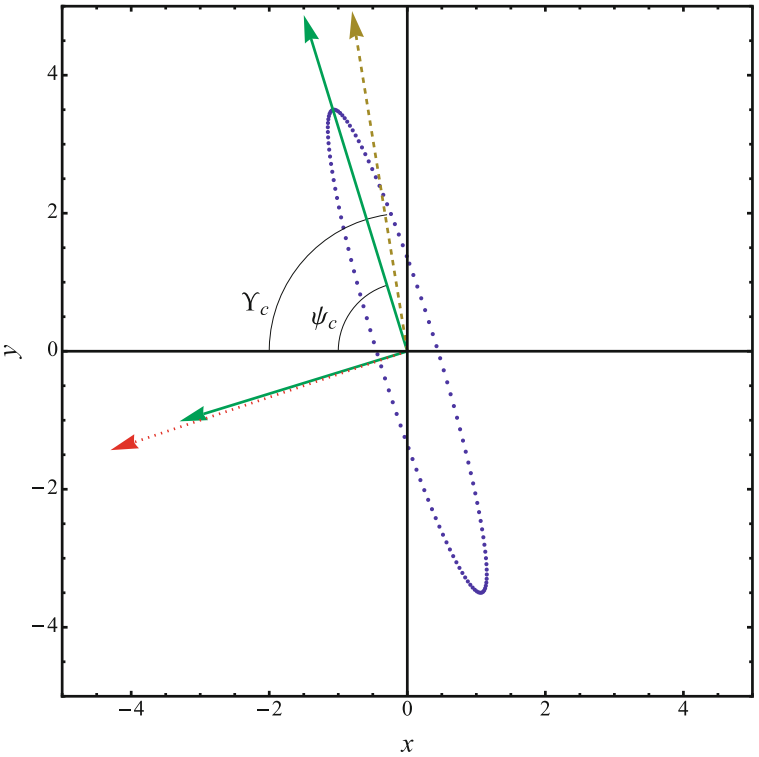

Fig. 5.3 An initially ($f = f_t$) circular ring of stellar fluid elements has been tidally distorted by the time it reaches $f = f_c$. The principal axes of the distorted, free-falling body are the solid green vectors, the center of mass velocity is the dashed yellow vector, and the direction to the SMBH is the dotted red vector. The angle ψ_c (Υ_c) is measured between the negative $\hat{x}$ direction and the long principal axis (stellar velocity vector). We define the misalignment angle $\nu_c = \Upsilon_c - \psi_c$

principal axes at $f = f_c$. For comparison we plot curves of the high β limiting behavior, for which $\tilde{r}_{\rm long} \approx \frac{4}{5}\beta^{1/2} + \frac{22}{5}\beta^{-1/2}$ and $\tilde{r}_{\rm short} \approx 2\beta^{-1/2} - \frac{23}{2}\beta^{-3/2}$.

The primary interesting feature of the axis ratio calculations is that for disruptions of stars by supermassive black holes, the physically relevant range of $r_{\rm long}$ and $r_{\rm short}$ is quite narrow, being confined between 3 and 5 for the former, and 0.3 to 0.5 for the latter. For the tidal disruption of a star by an intermediate mass black hole (IMBH), or perhaps more exotic disruption scenarios, a larger range of β (and therefore $r_{\rm long}$, $r_{\rm short}$) can be attained, but for star-SMBH TDEs only a surprisingly narrow range of principal axis lengths are accessible. This implies that the naive Taylor expansion of the SMBH potential as the star passes through $R = R_p$, i.e. Eq. 5.1, will fail primarily because of internal velocities within the free-falling stellar debris, and only secondarily because of distortions in the star's shape.

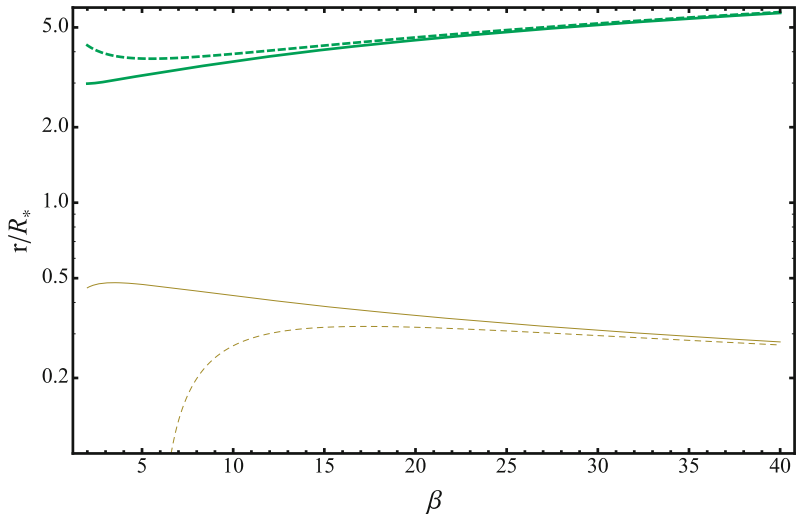

Fig. 5.4 The principal axis lengths, $r_{\rm long}$ and $r_{\rm short}$, of the distorted star (at $f = f_{\rm c}$) vs β. Here $r_{\rm long}$ is plotted as thick green curves; $r_{\rm short}$ as thin yellow curves. The exact solutions are solid lines, while the dashed curves are the high-β Taylor expansions given by Eqs. (B.6), (B.7)

As we shall see in § 5.4, when estimating energy redistribution during maximum vertical compression, the misalignment angle ν plays a larger role than the slowly-varying axis ratio. This will prove relevant when calculating corrections to $\Delta\epsilon$, and is shown in Fig. 5.5. The angle $\nu_{\rm c}$ (as elsewhere, the subscript c denotes evaluation at $f = f_{\rm c}$) is found to be a rapidly decreasing function of β; to leading order, $\tan\nu_{\rm c} \propto \beta^{-3/2}$.

We can now use the free solutions $\{A, B, C, D, E, F\}$ to quantify precisely the spread in debris energy at the tidal radius. Because these solutions can be thought of physically as perturbations to the orbital elements of a parabolic trajectory, all possess exactly zero energy except for the in-plane "D" solution, which has specific energy given by

$$\epsilon = -\frac{20GM_*D}{R_*}\left(\frac{M_{\rm BH}}{M_*}\right)^{1/3}\beta, \tag{5.18}$$

where D is the coefficient of the fourth in-plane free solution, corresponding to slight variations in the eccentricity of a near-parabolic orbit (SKR10). If we initialize our free solutions with an unperturbed sphere, i.e. Eqs. 5.14, then we find a specific energy for each fluid element of

$$\epsilon_u = \frac{GM_{\rm BH}R_*}{R_{\rm t}^2}\left(\tilde{x}_0(1-2/\beta) + 2\tilde{y}_0\sqrt{\beta^{-1}-\beta^{-2}}\right), \tag{5.19}$$

where $\tilde{x}_0$ and $\tilde{y}_0$ are the initial positions of a debris stream relative to the star's center of mass at $R = R_{\rm t}$ normalized by the stellar radius. Notably, the specific energy is to

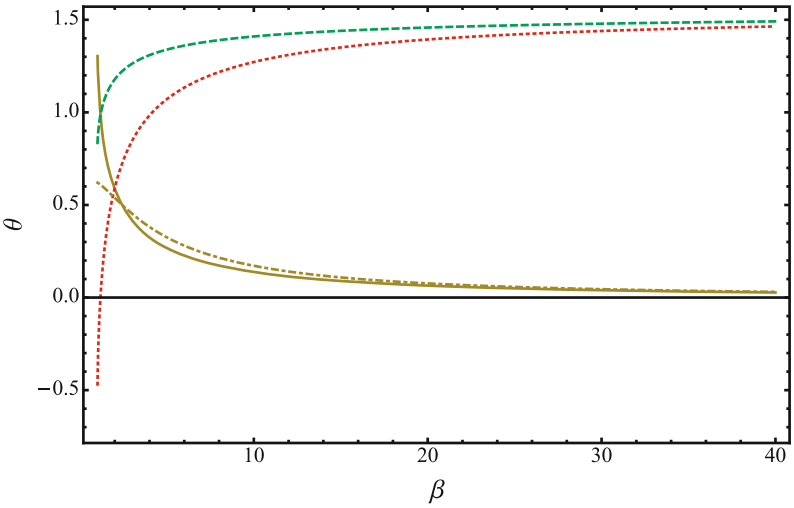

Fig. 5.5 Curves illustrating misalignment of the tidally raised bulge and the orbital velocity vector at the point of z-collapse ($f = f_c$). The red dotted curve is the angle between the negative x-axis and the tidal bulge (ψ_c), the green dashed curve is the angle between the negative x-axis and the orbital velocity vector, and the solid yellow curve is the difference between them, i.e. the misalignment angle (ν_c). These angles are plotted against the penetration factor β. The high β limit for ν_c is the dot-dashed yellow curve

leading order independent of β, with the weak β-dependence becoming negligible at high penetration factors. Defining $\tilde{x}_0 = \tilde{r}_0 \cos\theta_0$ and $\tilde{y}_0 = \tilde{r}_0 \sin\theta_0$ ($0 \leq \tilde{r}_0 \leq 1$ is the initial internal radius, and $0 \leq \theta_0 < 2\pi$ is the initial azimuthal angle), we can analytically extremize Eq. 5.19 with respect to θ_0, to find that the spread in energy of these unperturbed free solutions is actually fully independent of β:

$$\Delta\epsilon_u = \frac{2GM_{BH}R_*}{R_t^2}. \tag{5.20}$$

In our idealized model of a spherical, stationary star undergoing tidal free fall, the assumption of energy freeze-in at the moment of disruption implies $n = 0$, and no β dependence in $\Delta\epsilon_u$. This result reflects an assumption of our model: by imposing energy freeze-in at the tidal radius, the energy spread of the debris will simply be the potential spread across the star at that point. This picture is complicated slightly if our initial conditions become more general, and in particular a weak β dependence, below leading order, can be reintroduced for spinning stars (see § 5.5.3).

Energy freeze-in can be understood geometrically: curves of constant specific energy across the test particles of a spherical (static) star are lines with slope $\tilde{y}_0/\tilde{x}_0 = (2-\beta)/(2\sqrt{\beta-1})$. Since this slope $\tilde{y}_0/\tilde{x}_0 = \cot f_t$, these lines are orthogonal to $\hat{X}(f = f_t)$, and the zero-energy D=0 line is the one passing through the center of the star. On one side of that line, stellar matter is closer to the SMBH and remains gravitationally bound; the half of the star on the other side of the line is unbound.

In the following three sections, we examine the robustness of this model, and consider possible corrections to our expressions for $\Delta\epsilon$. With limited exceptions, we find that the arguments made in this section remain generally valid.

5.4 Total Vertical Collapse and Bounce

For $f \approx f_c$, motion in the vertical direction has decoupled from in-plane motion and the star undergoes a homologous vertical collapse. In this regime, the vertical velocity of the free solutions near the point of maximum collapse is very close to a constant value, with $w_c \propto \beta$, a result known since CL83, although the exact value, for arbitrary f_c, is

$$w_c = \beta \tilde{z}_0 \left(\frac{GM_*}{2R_*}\right)^{1/2} \left((1-\beta^{-1})^{1/2}+1\right). \tag{5.21}$$

With this formula we can begin thinking about Phase III of a tidal disruption event, and in particular whether it can alter Eq. 5.20.

As we have seen in the previous section, once $f \approx f_c$, the majority of the star simultaneously "pancakes" into a sheet of matter strongly compressed in the vertical direction. If non-gravitational forces were truly negligible, an idealized, one-dimensional ($\hat{z}$ extent only) star would momentarily possess zero height at $f = f_c$, but in reality sufficient compression will create a pressure gradient strong enough to oppose free fall in the z-direction. The resulting bounce will reverse the vertical free fall and lead to vertical expansion at speeds comparable to w_c. The vertical rebound will have a limited impact on $\Delta\epsilon$ because it is effectively decelerated by the tidal potential (for example, if we generously approximate the rebound as elastic due by reflecting w at $f = f_c$, the asymptotic free solution velocity $w \to 0$ as $f \to \pi$), but the smaller rebound velocities $\Delta v_x, \Delta v_y$ in the orbital plane can in principle have more significant effects, as $\Delta\epsilon \sim V_p \Delta v$. In this section we assume the bounce is adiabatic; in particular, we neglect both dissipation in shocks and the thermonuclear energy release from the compression of the stellar core. For a more thorough discussion of these possibilities see Luminet and Pichon (1989); Brassart and Luminet (2008).

During Phase III of a TDE, the requirement that central pressure rises to halt the kinetic energy of collapse ($\sim M_* w_c^2$) implies that the star's peak internal specific energy will be

$$U_c \sim \beta^2 U_* \left(\sqrt{1-\beta^{-1}}+1\right)^2 \tag{5.22}$$

where $U_* = GM_*/R_*$. Assuming a polytropic equation of state $P = K\rho^\gamma$, and furthermore that strong compression in the $\hat{z}$ direction means that the density enhancement will be due to collapse in $\hat{z}$ alone (since the cross-sectional area within the orbital plane, $\approx \pi r_{long} r_{short}$ remains roughly constant), gives a minimum stellar

height and maximum stellar density of

$$\frac{z_{\min}}{R_*} \sim \frac{\rho_*}{\rho_c} \sim \beta^{-2/(\gamma-1)}, \tag{5.23}$$

where ρ_* is the mean pre-disruption stellar density. The duration of maximum compression will be roughly $\tau_c \sim w_c/(R_*^2 P_c)$. This yields a steep power of the impact parameter, specifically

$$\tau_c \sim \beta^{-(\gamma+1)/(\gamma-1)}\tau_*, \tag{5.24}$$

with $\tau_* = 1/\sqrt{G\rho_*}$. Although we have only derived these formulas at the order of magnitude level, they have been calibrated over a wide range of β by both the affine model (Luminet and Carter 1986) and one-dimensional hydrodynamical simulations (Brassart and Luminet 2008) (hereafter BL08). Specifically, for $\gamma = 5/3$ polytropes, the affine model found $U_c \approx 1.2U_*\beta^2$, $\rho_c = 1.3\rho_*\beta^3$ and $\tau_c = 8.5\tau_*\beta^{-4}$, calibrations which were essentially duplicated in BL08. Likewise, $z_{\min} \approx 4.5\beta^{-3}R_*$ if we assume that the rise in density comes entirely from homologous, vertical stellar collapse (i.e. that the in-plane area of the compressed star is $\sim r_{\rm long}r_{\rm short}$).

If we assume that the pressure-driven bounce acts isotropically (i.e. that shear stresses from viscosity or shocks remain unimportant), then the relevant changes in velocity can be estimated as $\rho_c \Delta v_i/\tau_c \sim \Delta P_c/r_i$, with r_i the physical dimension of the star parallel to the pressure gradients that impart Δv_i. Specifically,

$$\begin{aligned} \Delta v_z &\sim \sqrt{U_c}\frac{z_{\min}}{z_{\min}} \\ \Delta\vec{v}_{\rm short}\cdot\hat{V}_c &\sim \sqrt{U_c}\frac{z_{\min}}{r_{\rm short}}\sin(\nu_c) \\ \Delta\vec{v}_{\rm long}\cdot\hat{V}_c &\sim \sqrt{U_c}\frac{z_{\min}}{r_{\rm long}}\cos(\nu_c), \end{aligned} \tag{5.25}$$

where we have denoted the direction of the orbital velocity at $f = f_c$ as the dimensionless unit vector $\hat{V}_c$. As β increases, the increasing central pressure would enhance the in-plane velocity perturbations, but is counterbalanced by the increasingly extreme compression of the star, i.e. the increasing ratio of the vertical pressure gradient to in-plane pressure gradients. The latter factor win out, and the velocity perturbations decrease with increasing β.

This leads to energy perturbations within the orbital plane at bounce of $\Delta\epsilon_{\rm III} \sim V_c\Delta v$. Using our exact formulae for axis lengths and alignment, we plot the results in Fig. 5.6, along with the limiting behavior at high β, which is well-approximated by the Taylor expansions in Appendix A as:

$$\Delta\epsilon_{\rm III,short} \sim 31\beta^{-5/2}\Delta\epsilon_u \tag{5.26}$$

$$\Delta\epsilon_{\rm III,long} \sim 9\beta^{-2}\left(1+\frac{11}{2\beta}\right)^{-1}\Delta\epsilon_u. \tag{5.27}$$

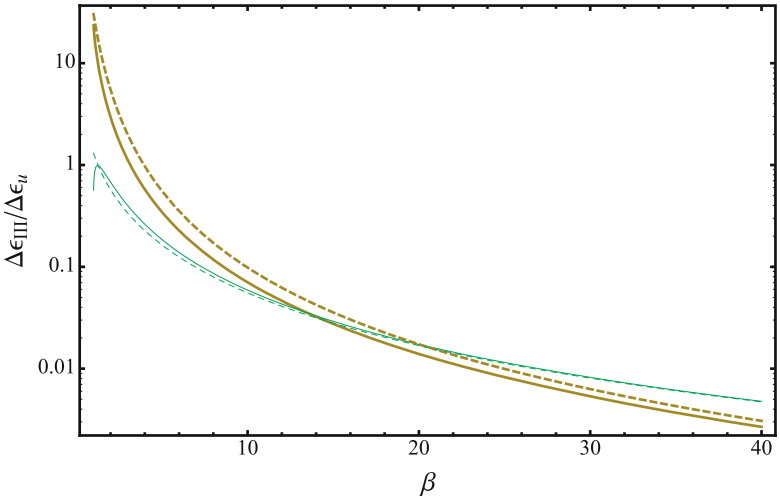

Fig. 5.6 Fractional specific energy perturbations during the bounce phase. We plot perturbations along the short axis of the star as thick yellow curves, and along the short axis as thin green curves. Exact solutions are solid lines, and the leading order behavior from Eqs. (5.26) and (5.27) are dashed lines. The bounce represents at most a factor ≈ 2 correction to specific energy of the stellar debris for $4 \gtrsim \beta \gtrsim 3$; above these values, the bounce is negligible. Below $\beta \approx 3$, a larger correction is possible, but the free solutions become somewhat unreliable. The high degree of alignment between the stellar bulge and the orbital velocity vector causes perturbations along the long axis to actually dominate those along the short axis above $\beta \approx 15$

Here we have assumed $\gamma = 5/3$, and that $z_{\rm min} \approx 5R_*\beta^{-3}$ based on the BL08 calibration. We have also approximated $V_{\rm c} \approx V_{\rm p}$, which is accurate for high β though a mild overestimate at low β. Even with this overestimate, we can see from Fig. 5.6 that only for $\beta \lesssim 3$ (where our model's assumption of tidal free fall begins to break down) can the pressure-driven bounce along the short principal axis of the star provide an order unity enhancement to the total spread in (in-plane) debris energy. The contribution of the bounce along the longer principal axis remains negligible at all β.

Because the z-component of $\vec{V}_{\rm c} = 0$, the spread in kinetic energy of vertical motion at the time of bounce is given by

$$\Delta\epsilon_{\rm III,z} \sim \Delta v_{\rm z}^2 \sim \beta^2 \frac{GM_*}{R_*}. \tag{5.28}$$

Interestingly, for $\beta \gtrsim 10$ the total spread in kinetic energy at the time of bounce is dominated by $\Delta\epsilon_{\rm III,z}$, not $\Delta\epsilon_{\rm u}$. However, the instantaneous vertical kinetic energy at $f = f_{\rm c}$ will disappear as $f \to \pi$. Even neglecting dissipation of the kinetic energy of vertical free fall into shocks, and assuming a perfectly elastic bounce, the tidal potential (Eq. 5.11) will efficiently decelerate the vertical motion of the debris during the phase IV rebound and later expansion. This can be seen by continuing the free solutions past $f = f_{\rm c}$, which corresponds to a reflection of vertical velocity.

Here we have ignored energy release from thermonuclear burning at the time of maximum compression, which in principle could increase $\Delta\epsilon$. However, past estimates made in the framework of the affine model (Luminet and Pichon 1989, Table 8) found that for the range of β values considered ($5 \leq \beta \leq 20$), the total thermonuclear energy release was less than U_c, making it unlikely to change the analysis of this section.

Of course, our analysis of energy redistribution in Phase III depends critically on how synchronously the vertical collapse of the star proceeds. If individual "columns" of the star do not collapse in the homologous manner implied by Eq. 5.11, it is unlikely z_{min} will reach the extreme values predicted by the simple arguments in this section. Alternatively, if separate columns collapse in a desynchronized way, it is possible that pressure waves from collapsed regions of the star will propagate upstream to uncollapsed regions and cause them to rebound prematurely. In either scenario, the effective z_{min} will be enhanced, enabling greater coupling of the bounce energy to motions within the orbital plane, and increasing the values of $\Delta\epsilon_{III,short}$ and $\Delta\epsilon_{III,long}$. Therefore, Eq. 5.20 should be regarded as a lower bound on $\Delta\epsilon$ - a higher value of n would be favored if the desynchronization of vertical collapse transfers kinetic energy to in-plane motions more efficiently than in our estimates here. A similar effect should arise in hydrodynamical simulations of TDEs that lack sufficient vertical resolution to capture the maximum compression of the star (we discuss this further in § 5.9; see also Guillochon et al. 2009). In the following section, we consider physical sources of desynchronization.

5.5 Desynchronization

The synchronous vertical collapse of a one-dimensional star into a thin, pancake-like sheet only occurs if the initial distribution of vertical velocities is self-similar, i.e. the initial vertical velocity $w_0(z_0) \propto z_0$. In previous sections we have assumed the trivial self-similarity of $w_0 = 0$. Deviations from self-similarity will be seeded at early times by the nonlinear hydrodynamics of actual disruption at the tidal radius R_t, and also later, as the self-gravity and pressure of the stellar debris perturbs the free solutions for $f < f_c$. In this section we quantify in an approximate way the effect of desynchronization on our idealized earlier conclusions, finding that both the stellar properties during Phase III (important for any shock breakout signal) as well as $\Delta\epsilon$ could be significantly altered. However, we then argue that past hydrodynamical simulations indicate that desynchronization is likely to be suppressed in physical TDEs, justifying our use of the parabolic free solutions. Finally, we consider the desynchronization of stellar collapse in three dimensions.

5.5.1 Desynchronized Free Solutions

At $f = f_t$, during the transition from Phase I to Phase II, velocity perturbations of order $\sim \sqrt{GM_*/R_*}$ could be imprinted on the free-falling stellar debris. Normalizing our initial conditions $\{z_0, w_0\}$ in units of R_* and $\sqrt{GM_*/R_*}$, we derive coefficients for the "perturbed" (i.e. $w_0 \neq 0$) vertical free solutions to be

$$E_p = -\tilde{z}_0\sqrt{\beta - 1} - \tilde{w}_0\sqrt{\frac{1}{2\beta}}(\beta - 2) \tag{5.29}$$

$$F_p = \tilde{z}_0 + \tilde{w}_0\sqrt{\frac{2}{\beta}}\sqrt{\beta - 1}. \tag{5.30}$$

Therefore the true anomaly of a perturbed vertical collapse to $z = 0$ is

$$\tan(f_c') = \frac{\tilde{z}_0 + \tilde{w}_0\sqrt{2}\sqrt{\beta - 1}/\sqrt{\beta}}{\tilde{z}_0\sqrt{\beta - 1} + \tilde{w}_0\sqrt{2}(\beta/2 - 1)/\sqrt{\beta}}. \tag{5.31}$$

We note that both f_c and f_c' go $\propto \beta^{-1/2}$ in the large β limit. Unless $w_0 \propto z_0$, the collapse will be non-homologous, with f_c' depending on z_0. Modest deviations from homologous initial conditions will desynchronize the collapse, which we illustrate by plotting the desynchronized free solutions for $\beta = 2$ and $\beta = 10$. We can see that in both cases, the time at which the free solutions cross the orbital plane becomes strongly desynchronized, which complicates our previously simple treatment of the transition from "tidal free fall" to "pressure-driven bounce" and also raises the possibility that the vertical kinetic energy of free fall could be effectively isotropized and transferred to motions within the orbital plane, restoring a β dependence to $\Delta\epsilon$.

We can estimate the amount of desynchronization by using trigonometric identities and Eqs. 5.12 and 5.31 to find $\Delta f = f_c' - f_c$. Specifically,

$$\tan(\Delta f) = \frac{\tilde{\lambda}_0}{\sqrt{2\beta} + \tilde{\lambda}_0\sqrt{\beta - 1}}, \tag{5.32}$$

where $\tilde{\lambda}_0 = \tilde{w}_0/\tilde{z}_0$.

Interestingly, both Figs. 5.7 and 5.8 show that most of the star's desynchronized free solutions have two crossings of the orbital plane, raising the possibility of a double bounce in desynchronized collapse scenarios (something previously seen only due to GR effects, e. g. Luminet and Marck (1985) - see § VI). But is it realistic to expect desynchronized collapse?

5.5.2 Validity of Free Solutions in One Dimension

From the above discussion, it is clear that only modest deviations from self-similarity in the initial velocity perturbations w_0 will produce a strongly non-homologous vertical collapse at most realistic β. We can quantify the magnitude of the initial velocity

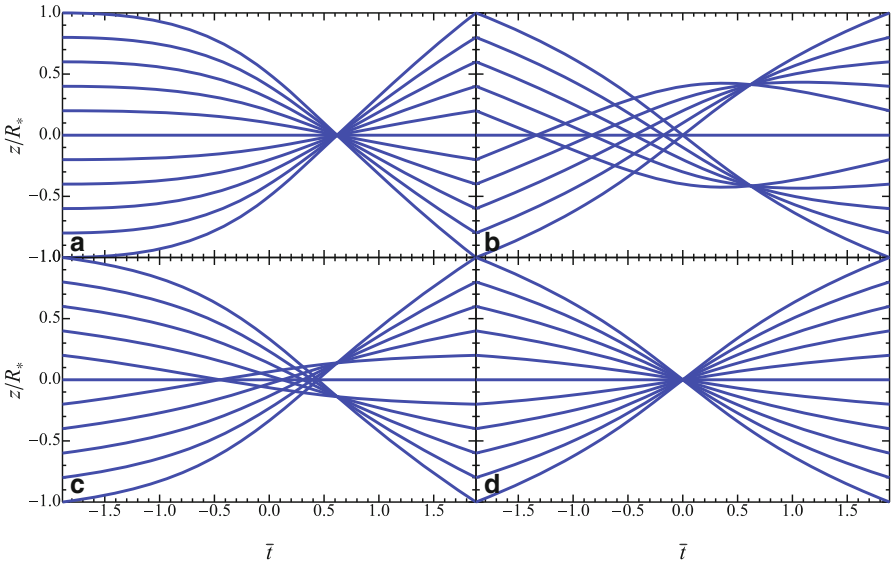

Fig. 5.7 Here we plot several sets of free solutions ($\tilde{z}$ versus $\bar{t}$) for $\beta = 2$. In panel **a**, the initial vertical velocity $w_0 = 0$. In panel **b**, all fluid elements in the star receive initial velocity perturbations $|w_0| = \sqrt{GM_*/R_*}$; in panel **c**, $|w_0| = \sqrt{GM_*/R_*}/3$. In panel **d**, the star receives homologous velocity perturbations $w_0 = -\tilde{z}_0\sqrt{GM_*/R_*}$, causing synchronous collapse *before* pericenter passage

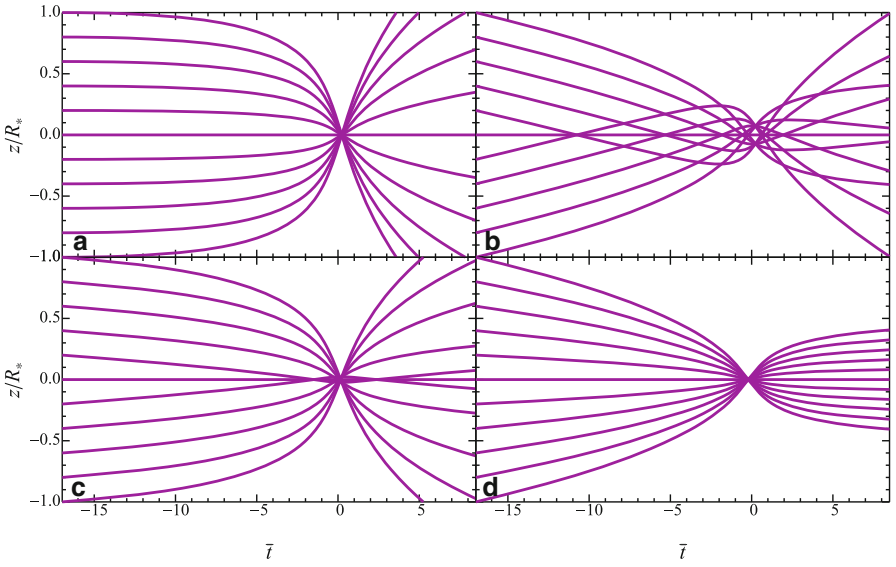

Fig. 5.8 The same as Fig. 5.7, but for $\beta = 10$. Desynchronization is less severe at higher β

perturbations $\tilde{\lambda}_0$ required to significantly desynchronize one-dimensional collapse by making the approximation (valid for small Δf) that the desynchronization timescale $\Delta t_{1D} \approx \Delta f \sqrt{R_p^3/(GM_{BH})}$. If we then require $\Delta t_{1D} < \tau_c = \chi_c \tau_*$, then for a $\gamma = 5/3$ polytrope (with $\chi_c \approx 8.5$) and inwardly directed velocity perturbations we find the condition that

$$|\tilde{\lambda}_0| \lesssim \frac{\sqrt{2\beta}\tan(2\chi_c \beta^{-5/2})}{1+\sqrt{\beta-1}\tan(2\chi_c\beta^{-5/2})}. \tag{5.33}$$

The factor of ≈ 2 inside the argument of the tangent comes from the difference between $\tau_* = \sqrt{1/G\rho_*}$ and $\sqrt{R^3/(GM_*)}$. This condition grows more restrictive as β increases, with the right hand side of Eq. 5.33 roughly proportional to β^{-2}.

For one-dimensional stellar collapse, high-resolution hydrodynamical simulations indicate that a highly homologous collapse is physically realized (BL08). As noted before, this is likely due to a combination of two factors: the partial cancellation of stellar pressure with self-gravity, and also that $a_t/a_g \approx (R_t/R)^3$. This explanation is supported by past investigations of stellar tidal disruption in the affine ellipsoids approximation: for example, Fig. 4 in CL83 shows the first order cancellation of pressure and self-gravity for early parts of Phase II. Three results of BL08 further support the validity of the unperturbed free solutions in Phase II of a TDE:

- The actual collapse of the star is visually homologous during Phase II, as seen by the near-linearity of a vertical velocity versus height plot at different times (BL08, Fig. 2). Although the figure deviates slightly from homologous collapse at large radii, possibly due to the fact that the low-density outermost regions of the star are disrupted slightly before the higher density inner regions (like the peeling of onion shells), these outer deviations do not appear to affect the key dynamics of the bounce.
- The maximum central compression $\rho_c \sim \beta^{2/(\gamma-1)}\rho_*$ in accordance with the assumption of fully synchronized tidal free fall (BL08, Eq. 43). We note that this is a geometric proxy for z_{min}.
- The bounce of the collapsing star occurs after pericenter passage (BL08, Table 5). As shown above, this places a strong constraint on the initial velocity perturbations. In particular, let us consider a perfectly homologous collapse for the sake of argument, with $\tilde{w}_0 = -\tilde{\lambda}_0 \tilde{z}_0$. Eq. 5.31 will only be positive (i.e. bounce after pericenter passage) if $\tilde{\lambda}_0 < (\sqrt{2}\beta\sqrt{\beta-1})^{-1}$, a rather small perturbation ($\tilde{\lambda} < 0.04$ for $\beta = 7$, as is relevant here).

These numerical results indicate that realistic one-dimensional stars behave during Phase II much like the unperturbed free solutions we presented in § 5.3, supporting our earlier assumption that debris energy "freezes in" from $f = f_t$ down to the bounce, at $f = f_c$.

A final source of one-dimensional desynchronization can arise from the star's internal, pre-disruption density gradient, which will cause the core of the star (with density ρ_{core}) to see an effective β_{core} less than the mean β. If a star on a parabolic orbit has a mean density ρ_*, and its core in isolation on that orbit would possess

$\beta_{\rm core} = \beta(\rho_*/\rho_{\rm core})^{1/3}$, we can alter our desynchronization formula to read $\tau_{\rm c} \gtrsim \sqrt{R_{\rm p}^3/(GM_{\rm BH})(f_{\rm c,core} - f_{\rm c})}$, or for a $\gamma = 5/3$ polytrope

$$\beta_{\rm core} \gtrsim 1 + \left(\tan\left(f_{\rm c} + 8.5\beta^{-5/2}\right)\right)^{-1/2}. \tag{5.34}$$

This condition is restrictive: if $\beta = 3$ (10), it implies a maximum density contrast $\rho_{\rm core}/\rho_* = 6$ (53). The fact that this effect does not lead to significantly non-homologous collapse in the BL08 simulations implies that this lower bound on $\beta_{\rm core}$ must be generous.

5.5.3 *Validity of Free Solutions in Three Dimensions*

The full problem of tidal disruption is three dimensional, and some three dimensional simulations (Laguna et al. 1993; Guillochon et al. 2009) have indicated that one-dimensional descriptions of the bounce phase (Luminet and Carter, 1986) may strongly overestimate the degree of compression. However, lack of vertical resolution in the three dimensional simulations makes it difficult to interpret the discrepency, and some high resolution simulations (Rosswog et al. 2009) do find degrees of compression closer to our analytic expectations in § 5.4. Although the impact of higher dimensional effects on Phase III of a TDE will only be resolved through higher resolution hydrodynamical simulations, we present here a simple analytic argument suggesting that a star made of many columns, each undergoing homologous collapse, should attain $z_{\rm min}$ comparable to one-dimensional predictions.

Three dimensional desynchronization is an important effect that cannot be ignored at high β: the bounce timescale $\tau_{\rm c} \approx 8.5\tau_*\beta^{-4}$ for $\gamma = 5/3$, while the time it takes the bulk of the star to pass across the tidal radius is $\Delta t_{\rm 3D} \approx 1.4\tau_*(M_*/M_{\rm BH})^{1/3}$. This implies that for β larger than a critical value,

$$\beta_{\rm d} = 1.6\left(\frac{M_{\rm BH}}{M_*}\right)^{1/12}, \tag{5.35}$$

$\tau_{\rm c} \ll \Delta t_{\rm 3D}$, and the leading edge of the star will collapse and rebound well before the trailing edge. If we assume that the star is truly in tidal free fall during Phase II, and seed velocity perturbations remain as small in three dimensions as has been indicated in one dimensional simulations, then each column of the star will reach its maximum compression at different t but the same $f_{\rm c}$.

This $f_{\rm c}$ remains fixed in space, much like a nozzle, as the star passes through it. An example of this "tidal nozzle" has been seen in hydrodynamical simulations of tidal disruptions of white dwarfs; for example, Fig. 6 of Rosswog et al. (2009). Even if we assume the maximum compression predicted by one-dimensional models of stellar collapse ($z_{\rm min} \approx 4.5R_*\beta^{-3}$, for $\gamma = 5/3$), the sound speed in the stellar midplane, $c_{\rm s,c}$, will remain a small fraction of the stellar orbital velocity. Specifically $c_{\rm s,c}/V_{\rm p} \approx \beta^{1/2}(M_*/M_{\rm BH})^{1/3}$, indicating that unphysically large β values are

required for pressure waves from the region of maximum compression to communicate upstream to the Phase II material. Unless three dimensional effects influence earlier stages of a TDE (by seeding large perturbations during the transition from Phase I to Phase II), it seems unlikely that the star will be prevented from reaching the strong compressions suggested by models of one-dimensional collapse. Among other things, this highlights the importance of thermonuclear network calculations for high-β TDEs (Luminet and Pichon 1989).

A further complication is the desynchronization due to the "effective β" seen by different regions of the star with different pre-disruption densities. This will have the effect of spreading f_c out over a range of angles for different parts of the star. As the star passes through phase III compression, the nozzle point will move from a starting point slightly ahead of pericenter outward along the orbit (as higher density regions of the star get disrupted), and then inward, back to its starting point. We leave a detailed analysis of this for future work.

With these caveats in mind, we generalize the work of § 5.3 to perturbed in-plane free solutions, i.e. where every fluid element at $f = f_t$ has initial positions $\{x_0, y_0\}$ but also initial velocities $\{u_0, \upsilon_0\}$. The in-plane coefficients for the corresponding "perturbed" free solutions are

$$A_p = \frac{1}{\beta^2}\Big(- 8\tilde{x}_0\sqrt{\beta-1} + 2\tilde{y}_0(\beta^2+2\beta-4)\Big) + \frac{2\sqrt{2}}{\beta^{3/2}}\Big(\tilde{u}_0(2-3\beta) + \tilde{v}_0\sqrt{\beta-1}(\beta-2)\Big) \tag{5.36}$$

$$B_p = \frac{1}{5\beta^2}\Big(2\tilde{x}_0\sqrt{\beta-1}(\beta^3-4\beta^2+8) + \tilde{y}_0(9\beta^3 - 12\beta^2 - 8\beta + 16)\Big) + \frac{1}{5\sqrt{2}\beta^{3/2}}\Big(\tilde{u}_0(\beta^3-8\beta^2 + 28\beta - 16) + 2\tilde{v}_0\sqrt{\beta-1}(3\beta^2-6\beta+8)\Big) \tag{5.37}$$

$$C_p = \frac{1}{\beta^2}\Big(\tilde{x}_0(2\beta^2+\beta-2) - 2\tilde{y}_0\sqrt{\beta-1}(\beta^2-1) - \sqrt{2\beta}\Big(\tilde{u}_0(1-2\beta)\sqrt{\beta-1} + \tilde{v}_0(\beta-1)^2\Big)\Big) \tag{5.38}$$

$$D_p = -\frac{1}{20\beta^2}\Big(\tilde{x}_0(\beta-2) + 2\tilde{y}_0\sqrt{\beta-1} - \sqrt{2\beta}(\tilde{u}_0\sqrt{\beta-1} + \tilde{v}_0)\Big). \tag{5.39}$$

If we now calculate the perturbed specific energy of the free solutions, we find

$$\epsilon_p = \frac{GM_{BH}R_*}{R_t^2}\Big(\tilde{x}_0(1-2/\beta) + 2\tilde{y}_0\sqrt{\beta^{-1}-\beta^{-2}} \tag{5.40}$$

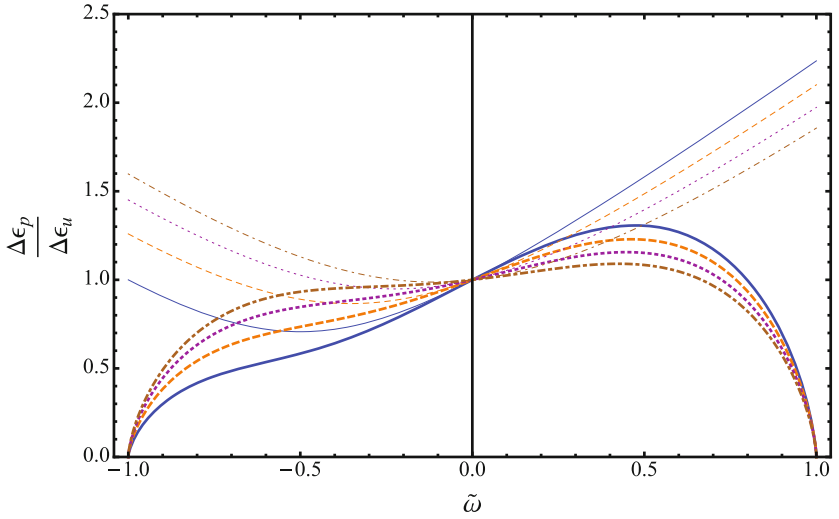

Fig. 5.9 The enhancement $\Delta\epsilon_{\rm p}/\Delta\epsilon_{\rm u}$ to the energy spread for initially unperturbed free solutions, when pre-disruption stellar spin (along an axis parallel to orbital angular momentum) is considered. The energy spread is plotted against pre-disruption spin $\tilde{\omega}$, where $\tilde{\omega}$ is stellar spin normalized by the breakup spin $\sqrt{GM_*/R_*^3}$. As in previous plots, the solid blue, dashed orange, dotted purple, and dot-dashed cyan curves represent $\beta = 2, \beta = 4, \beta = 10$, and $\beta = 40$, respectively. The thin lines represent the dynamical effects of stellar spin when the tidal radius is held constant; in the more realistic thick lines, the tidal radius is also allowed to vary with stellar spin

$$-\sqrt{2/\beta}(\tilde{u}_0\sqrt{\beta-1}+\tilde{v}_0)\Big),$$

where the initial velocities have been normalized by $\sqrt{GM_*/R_*}$. Again, there is no leading order β dependence in the specific energy, although a calculation of $\Delta\epsilon_{\rm p}$ does not find it completely β-independent as in Eq. 5.20. Nonetheless, the assumption of tidal free fall during Phase II implies clearly that the frozen-in $\Delta\epsilon$ should be, to leading order, independent of β. As a simple test case, we now apply these perturbed free solutions to a uniformly spinning star, with normalized angular velocity $\tilde{\omega} = \omega/\sqrt{GM_*/R_*^3}$ such that $\tilde{\omega} = 1$ is approximately the breakup frequency (and the spin is taken as parallel to the orbital angular momentum). In Eq. 5.40, we relabel $\tilde{x}_0 = \tilde{r}_0\cos\theta_0$, $\tilde{y}_0 = \tilde{r}_0\sin\theta_0$, $\tilde{u}_0 = -\tilde{\omega}\tilde{r}_0\sin\theta_0$, $\tilde{v}_0 = \tilde{\omega}\tilde{r}_0\cos\theta_0$, and then extremize $\Delta\epsilon$ with respect to θ_0.

Results for constant $R_{\rm t}$ are plotted as thin lines in Fig. 5.9; in general, prograde pre-disruption stellar spin will enhance the energy spread $\Delta\epsilon$ by a small factor, $\lesssim 2$. Low β and high $\tilde{\omega}$ will maximize this energy spread. Generally, retrograde spins will decrease the energy spread by smaller factors. The difference between prograde and retrograde behavior is geometrical: for prograde spins, the unbound (bound) half of the star tends to receive positive (negative) specific energy perturbations $\Delta\epsilon \sim V_{\rm t}\omega_0 r_0$, where $V_{\rm t}$ is the center of mass velocity at the tidal radius. For retrograde spins, this behavior is reversed, although for retrograde spins close to breakup the

non-orthogonality of $\hat{X}$ and $\vec{V}$ allows an enhancement to $\Delta\epsilon_{\rm p}$. The alignment of $\hat{X}$ and $\vec{V}$ at $f = f_{\rm t}$ increases as β increases, so that the highest values of β see similar energy spreads for both prograde and retrograde spins.

However, an important complication[1] is that for spins near breakup (prograde or retrograde), the tidal radius will increase, decreasing the spread in specific debris energy. Using Eq. 13 of Kesden (2012b), we derive that

$$R_{\rm t}(\tilde{\omega}_0) = R_*(M_{\rm BH}/M_*)^{1/3}(1-\tilde{\omega}_0^2)^{-1/3}. \tag{5.41}$$

This differs by a factor of $2^{1/3}$ from the equivalent formula in Kesden (2012b) due to a slight difference in the definition of $R_{\rm t}$. The effect of the growing tidal radius leads to sharp decreases in $\Delta\epsilon_{\rm p}$ for spins very close to breakup, and, for $\tilde{\omega}_0 \gtrsim 0.5$, dominates the dynamical spin effects described in the previous paragraph. The combined effects of a variable tidal radius and the dynamical contribution of stellar spin to frozen-in energy are plotted as thick lines in Fig. 5.9. In general, $\Delta\epsilon_{\rm p}$ is within a factor of 2 of $\Delta\epsilon_{\rm u}$ except for $\tilde{\omega}_0 \gtrsim 0.9$ or $\tilde{\omega}_0 \lesssim -0.6$.

We note here that large stellar spins misaligned with the orbital angular momentum vector could have a much greater impact on $\Delta\epsilon$ by inducing vertical desynchronization. A thorough investigation of misaligned spin effects is beyond the scope of this work, but as an idealized limiting case we apply Eq. 5.33 to approximate, as a function of β, the maximum stellar spin allowed before the Phase III bounce would be vertically desynchronized. Specifically, we set $w_0 = \omega_0 r_0$. More specifically, Eq. 5.33 lets us calculate the regions of parameter space in which the dynamical desynchronization of stellar compression (due to the spread of velocities in a spinning star) stretches out for longer than the hydrodynamical bounce time. We plot these results in Fig. 5.10, and find that combinations of high β and relatively rapid values of stellar spin are needed to strongly desynchronize the vertical collapse.

Figure 5.9 can be taken as representative of the effects of both primordial stellar spin, and the angular momentum imparted during tidal spin-up of the star prior to its full disruption, during the transition between phases I and II of a TDE. Tidal spin-up is unlikely to produce misaligned spin, however, so the more dramatic type of desynchronization suggested by Fig. 5.10 can only come from the star's original, pre-disruption spin. Furthermore, tidal spin-up may produce effects similar to the thin curves of Fig. 5.9, provided the spin-up occurs close to the tidal radius of an equivalent, nonspinning star.

For one dimensional stellar collapse, the frozen-in $\Delta\epsilon$ will dominate the post-bounce $\Delta\epsilon$ for all β. For three dimensional collapse, the numerical literature is less clear, but we have argued here that three-dimensional effects are unlikely to strongly redistribute energy to in-plane motion, with the possible exception of when sufficiently rapid stellar spin is misaligned with the orbital plane, or perhaps when a similar misalignment between SMBH spin and orbital angular momentum exists.

[1] This was pointed out to us by Michael Kesden.

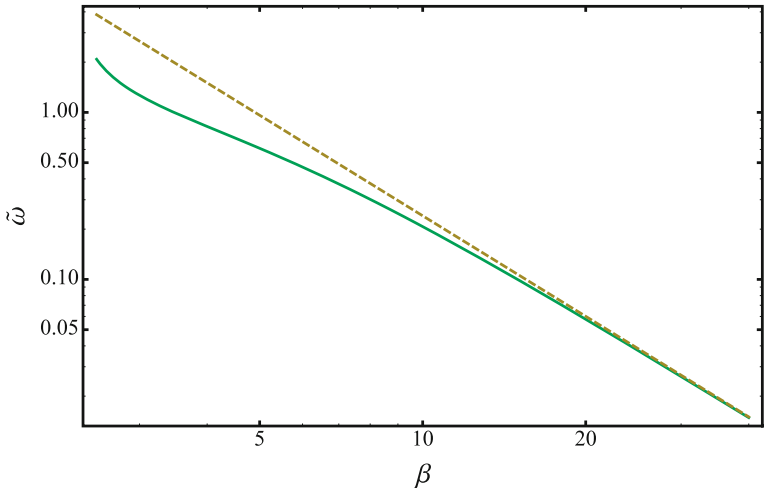

Fig. 5.10 The maximum value of normalized stellar spin $\tilde{\omega}$ that will not produce significant 1D desynchronization leading into the phase III bounce. We plot the exact value calculated from Eq. 5.33 as a solid green line, and the asymptotic behavior $\tilde{\omega} \lesssim 2\sqrt{2}\chi_c\beta^{-2}$ as a dashed yellow line. Regions above the curves will experience desynchronization of vertical collapse

5.6 General Relativistic Corrections

The results of all prior sections have assumed purely Newtonian gravity; however, for SMBHs with masses $M_{\rm BH} > 10^6 M_\odot$, tidal disruption of solar-type stars occurs at an orbital distance $R_{\rm t} \lesssim 50 R_{\rm g}$. Here the gravitational radius $R_{\rm g} = GM_{\rm BH}/c^2$. At these small separations, ballistic motion follows the geodesics of the Schwarzschild or Kerr metric rather than free-fall trajectories in Newtonian gravity: general relativity (GR) is important. A fully relativistic analysis of the problem of tidal disruption is beyond the scope of this paper, although it has been treated in the past in the case of the affine model (Luminet and Marck 1985), and in one-dimensional hydrodynamical simulations (Brassart and Luminet 2010). If we treat the internal dynamics of the star in a Newtonian way (i.e. assume tangentially flat space-time in the small region occupied by the star), then Eq. 5.11's description of vertical collapse will be modified, to become

$$\ddot{z}_{\rm GR} = \frac{\partial \Psi}{\partial z}\left(1 + 3\frac{L^2}{r^2}\right), \tag{5.42}$$

where L is the orbital angular momentum of the star, r is the orbital radius of the star (both in geometrized units) and we have limited ourselves to non-spinning black holes. The qualitative results of both Luminet and Marck (1985) and Brassart and Luminet (2010) were that the increased strength of the GR tidal field (relative to Newtonian gravity) can actually result in multiple vertical collapses, each followed by separate bounces which are reversed by the relativistically enhanced tidal field. For all

but the most deeply-plunging TDEs ($\beta \gtrsim 30$), the maximum compression is obtained on the first vertical collapse and is similar to the Newtonian $z_{\rm min}$ (Luminet and Marck 1985, Fig. 5.10). Therefore, even though the formation of multiple outgoing shockwaves could be an important outcome of relativistic compression, the first-order spread in debris energy is unlikely to be affected by multiple compressions for $\beta \lesssim 30$.

A separate relativistic effect concerns modifications to the pre-bounce spread in debris energy, $\Delta\epsilon$. Eq. 5.2 was derived by Taylor expanding the Newtonian gravitational potential about the star's position when it crossed into the tidal sphere, then subtracting the zeroth-order component. We will now repeat that procedure for a post-Newtonian (PN) effective potential which incorporates leading-order GR effects for non-spinning, Schwarzschild black holes. Specifically, we use the 1PN harmonic coordinate Lagrangian presented in Blanchet (2006, Eq. 174):

$$\mathcal{L}^{\rm harm} = \frac{Gm_1m_2}{2r_{12}} + \frac{m_1v_1^2}{2} + \frac{1}{c^2}\Big(-\frac{G^2m_1^2M_2}{2r_{12}^2} + \frac{m_1v_1^4}{8} + \frac{Gm_1m_2}{r_{12}}\Big(-\frac{1}{4}(\vec{n}_{12}\cdot\vec{v}_1)(\vec{n}_{12}\cdot\vec{v}_2) + \frac{3}{2}\vec{v}_1^2 - \frac{7}{4}(\vec{v}_1\cdot\vec{v}_2)\Big)\Big) \tag{5.43}$$

We define the effective potential as $\Phi_{eff} = K - \mathcal{L}^{\rm harm}$, where K represents the kinetic energy component of the Lagrangian, i.e. those terms which depend only on velocities. This equation was derived for arbitrary mass-ratio systems, but here we identify the star as particle 1, the SMBH as particle 2, and have dropped all terms proportional to v_2 or m_1/m_2. The Taylor expansion of Φ_{eff} up to first PN order, around $R = R_{\rm t}$, is given by

$$\Delta\epsilon_{\rm GR} = \frac{GM_{\rm BH}R_*}{R_{\rm t}^2}\left(1 + \frac{3V_{\rm t}^2}{2c^2} - \frac{R_{\rm g}}{R_{\rm t}}\right). \tag{5.44}$$

From this equation, it is clear that GR corrections to the Newtonian potential will only matter for large, $M_{\rm BH} > 10^7 M_\odot$ SMBHs, with tidal radii close to or within the ISCO. However, all TDEs due to such black holes, or even more massive ones (Kesden, 2012b), will have debris energy spreads modified by GR around the $\sim$2 level (although we caution that our PN approximation breaks down for tidal radii approaching the ISCO). In this discussion we have neglected spin effects, but they may also play an important role for the subset of TDEs with $R_{\rm p} \lesssim R_{\rm ISCO}$. During completion of this paper, a more precise formalism was presented for estimating the GR corrections described in this section (Kesden, 2012a). The results indicate generally small (factors $\lesssim$3) GR corrections which are maximized when the spread in energy of a spherical star is calculated near the ISCO, in qualitative agreement with our findings. We note however that Kesden (2012a) uses the older, less accurate approach to treating "frozen-in" debris energy, i.e. evaluating the spread in energy at $R_{\rm p}$ rather than $R_{\rm t}$. The primary difference between our approaches is that if debris energy freezes in at the tidal radius, GR corrections to $\Delta\epsilon$ can only reach large, $\sim$2 levels for $M_{\rm BH} \gtrsim 10^{7.5} M_\odot$. TDEs around low-mass SMBHs will see negligible GR corrections to $\Delta\epsilon$, even if β is large.

5.7 Gravitational Waves

The parabolic motion of a star past orbital pericenter will produce low-frequency gravitational waves due to time variation in the quadrupole moment of the star-SMBH system. For pericenters $R_{\rm p} < R_{\rm t}$, past work has indicated that such a signal could be marginally detectable with a LISA-like instrument (Kobayashi et al. 2004). Analogous work has focused on the inspiral of a white dwarf (WD) into an intermediate-mass black hole, where a similar signal could be generated by a violent disruption (Rosswog et al. 2009; Haas et al. 2012), or a longer-lived GW signal could be accompanied by electromagnetic transients due to inspiral and stable mass transfer (Zalamea et al. 2010). An alternate, internal source of GWs in TDEs comes from time variation of the star's own quadrupole moment during the Phase III vertical rebound, which was estimated in the past to generate gravitational waves with strain $h \propto \beta^3$ (Guillochon et al. 2009).

In this section, we present more detailed estimates of the "internal" GWs due to stellar pancaking and rebound, a process analogous to GW generation during core-collapse supernovae (CCSNe). As we shall demonstrate, TDE GWs are weakened relative to those in CCSNe due to lower collapse velocities and bounce accelerations, but are increased due to the large degree of stellar asymmetry, and perhaps also by the correspondingly long lever arm of collapse in the quadrupole moment tensor.

Specifically, we consider GW emission at the moment of maximum stellar compression, which we for now take to be synchronized throughout the star (but which will actually occur at different times for each point in the star, as seen in § 5.5). The two polarization components of a GW signal, h_+ and $h_\times$, can be read off of the transverse traceless GW strain

$$h_{\rm ij}^{\rm TT} = \frac{2G}{dc^4}\ddot{J}_{\rm ij}^{\rm TT}, \tag{5.45}$$

where d is the distance from the observer to the source, $J_{ij} = I_{ij} - \frac{1}{3}\delta_{ij}\delta^{kl}I_{kl}$ is the reduced quadrupole moment tensor, $J_{ij}^{\rm TT}$ is a projection of J_{ij}, and I_{kl} is the standard quadrupole moment tensor:

$$\ddot{I}_{kl} = \int {\rm d}^3\vec{r}\rho \times \tag{5.46}$$

$$\begin{pmatrix} 2\dot{x}^2 + 2x\ddot{x} & 2\dot{x}\dot{y} + \ddot{x}y + x\ddot{y} & 2\dot{x}\dot{z} + \ddot{x}z + x\ddot{z} \\ 2\dot{x}\dot{y} + \ddot{x}y + x\ddot{y} & 2\dot{y}^2 + 2y\ddot{y} & 2\dot{y}\dot{z} + \ddot{y}z + y\ddot{z} \\ 2\dot{x}\dot{z} + \ddot{x}z + x\ddot{z} & 2\dot{y}\dot{z} + \ddot{y}z + y\ddot{z} & 2\dot{z}^2 + 2z\ddot{z} \end{pmatrix}.$$

To order of magnitude in the limit of fully synchronous vertical collapse, and neglecting the (weak) β dependence of all x and y terms, we then have

$$\frac{\ddot{I}_{kl}}{M_* R_*^2 \tau_*^{-2}} \sim \int {\rm d}^3\vec{r} \begin{pmatrix} \beta^0 & \beta^0 & \beta^5 \\ \beta^0 & \beta^0 & \beta^5 \\ \beta^5 & \beta^5 & \beta^2 \end{pmatrix},$$

where we have taken $\gamma = 5/3$ (as we will for the remainder of this section) and approximated $z \sim \beta^{-3} R_*$, $\dot{z} \sim \beta\sqrt{GM_*/R_*}$, and $\ddot{z} \sim \dot{z}/\tau_c \sim \beta^5 GM_*/R_*^2$.

If only diagonal terms are considered, the second derivative of the quadrupole tensor will be $\propto \beta^2$. However, the extremely steep β^5 dependence of the off-diagonal $\ddot{I}_{xz}$ and $\ddot{I}_{yz}$ terms indicates that viewing angles not closely aligned with $\hat{z}$ could in principle observe copious GW production. This steeper β dependence arises from the $y\ddot{z}$ and $x\ddot{z}$ terms, which couple the long (and only weakly β dependent) lever arms within the orbital plane to the rapid vertical acceleration of the bounce. We note that physically, $\ddot{I}_{xz} \sim 10\ddot{I}_{yz}$ because for the large β where GW emission is relevant, $\hat{y}$ will be aligned with the star's longest principal axis.

However, two degrees of symmetry present in this problem will substantially reduce the magnitudes of $\ddot{I}_{xz}$ and $\ddot{I}_{yz}$. The free solutions indicate that to lowest order, tidally free-falling bodies should possess reflection symmetry about their in-plane principal axes. There is also an additional symmetry of reflection about the orbital plane. If these symmetries are exact, the off-diagonal terms in Eq. 5.46 will integrate to 0. The in-plane symmetries are broken when $R_*/R \sim 1$, i.e. for deeply plunging disruptions around low-mass SMBHs. The orbital plane reflection symmetry is more robust, and likely can only be broken by misalignment between the orbital plane and SMBH or stellar spin, which is beyond the scope of this paper. For the remainder of this section, we treat GW emission from off-diagonal terms as speculative, but the large magnitude of these terms in the integrand should motivate future work on disruptions of spinning stars, or TDES around spinning SMBHs.

For $\beta < \beta_d$, three-dimensional desynchronization is unimportant and the star collapses almost simultaneously, emitting GWs with a peak frequency of $\approx 1/\tau_c$, which, using the calibration of $\tau_c \approx 8.5\beta^{-4}\tau_*$ from the affine model and one-dimensional hydro simulations (§ 5.4), gives

$$f_{GW} \approx 15 \text{ Hz} \left(\frac{\beta}{25}\right)^4 m_*^{1/2} r_*^{-3/2}, \tag{5.47}$$

where we have normalized $m_* = M_*/M_\odot$ and $r_* = R_*/R_\odot$. Low mass stars have an easier time achieving high frequencies; if we use the relation $R_* \propto M_*^{0.8}$ for main sequence stars with $M_* \leq M_\odot$, we find $f_{GW} \approx 10$ Hz at $\beta = 15$, for $M_* = 0.1 M_\odot$.

These frequencies are located on the far edge of the Advanced LIGO band, although with steep β dependence. Because the three-dimensional desynchronization discussed in § 5.5 results in the leading edge of the star collapsing before the trailing edge (which lags by a time Δt_{3D}), the GW signal will be smeared out over a range of frequencies between $1/\Delta t_{3D}$ and $1/\tau_c$ when $\beta > \beta_d$. This smears out the gravitational wave emission by a factor $\Delta t_{3D}/\tau_c$, giving us the strain estimates

$$h_+ \approx 1 \times 10^{-25} m_*^2 r_*^{-1} d_{10}^{-1} \begin{cases} \left(\frac{\beta}{\beta_d}\right)^2, & \beta \lesssim \beta_d \\ \left(\frac{\beta}{\beta_d}\right)^{-2} M_6^{1/6}, & \beta \gtrsim \beta_d \end{cases} \tag{5.48}$$

$$h_\times \approx 1 \times 10^{-23}\ \Xi m_*^2 r_*^{-1} d_{10}^{-1} \begin{cases} \left(\frac{\beta}{\beta_{\rm d}}\right)^5, & \beta \lesssim \beta_{\rm d} \\ \left(\frac{\beta}{\beta_{\rm d}}\right) M_6^{5/12}, & \beta \gtrsim \beta_{\rm d} \end{cases} \tag{5.49}$$

Here d_{10} is distance to the source normalized to 10 megaparsecs, and for clarity (i.e. to separate diagonal and off-diagonal components of $\ddot{J}_{ij}$ into different polarization states) we have assumed a line of sight along the y axis so that $dh_+ = G(\ddot{J}_{xx} - \ddot{J}_{zz})/c^4$, and $dh_\times = 2G\ddot{J}_{xz}/c^4$. As in § 5.5, $\beta_{\rm d} \approx 6$ is the critical β value above which TDEs experience significant three dimensional desynchronization. We have defined a parameter, Ξ (which is most likely $\ll 1$), to parametrize the unknown degree of reflection asymmetry in Phase III of a TDE.

The prospects for high frequency GW observation of TDEs involving main sequence stars appear dim, unless $\Xi \gtrsim 0.1$. If we limit ourselves to GWs from $\ddot{I}_{zz}$, then disruptions of abundant low mass stars have an easier time falling within the Advanced LIGO band, but produce too little strain to be detected; disruptions of solar-type stars produce a barely detectable strain at $d \sim 1$ Mpc, but will lie outside the Advanced LIGO band for $\beta \lesssim 25$.

Tidal disruptions of white dwarfs by intermediate mass black holes appear more promising: a WD of mass 1 $M_\odot$ and radius 6×10^6 m disrupted at $\beta = 5$ by a $10^4 M_\odot$ IMBH will produce $h_+ \approx 6 \times 10^{-24}$ from a distance of 20 Mpc (neglecting all strain from off-diagonal terms in $\ddot{J}_{ij}$). The peak emission frequency $f_{\rm GW} \approx$ 60 Hz, but the existence of IMBHs is sufficiently uncertain that we do not attempt a rate estimate. We note that the level of emission seen at $\sim$ 50 Hz frequencies in full numerical relativity simulations of WD-IMBH disruptions (Haas et al. 2012) was approximately $\times 10^3$ smaller than our prediction. This may not surprising, as the maximum density enhancement seen in these simulations is $\lesssim$10, not $\sim$200 as predicted by one-dimensional models ($\gamma = 5/3, \beta \approx 10$). It is likely that this discrepency is at least partially due to insufficient vertical resolution: after disruption, the smallest grid cell in these simulations is $\approx R_{\rm WD}/40$. Furthermore, Newtonian and pseudo-Newtonian simulations of $\beta \approx 10$ WD TDEs (Rosswog et al. 2009) find maximum degrees of vertical compression $\sim$100, in approximate agreement with the arguments presented in § 5.4 and 5.5.

5.8 Observational Implications

In this section, we discuss the observational implications of a revised $\Delta\epsilon$ for optical transient searches. In general, we predict longer decay times but lower initial mass fallback rates than prior works (Strubbe and Quataert 2009).

Using the introduced index n, we rederive here a number of important consequences of Eq. 5.3 in a parametrized way. The fallback time for the most tightly bound debris is

$$t_{\rm fall} = 3.5 \times 10^6 \text{ sec } k^{-3/2} \beta^{-3n/2} M_6^{1/2} m_*^{-1} r_*^{3/2}, \tag{5.50}$$

where we have used the normalizations $M_6 = M_{\rm BH}/(10^6 M_\odot)$, $m_* = M_*/M_\odot$, and $r_* = R_*/R_\odot$. The rate of mass fallback evolves with time t as

$$\dot{M}_{\rm fall} \approx \frac{M_*}{3t_{\rm fall}} \left(\frac{t}{t_{\rm fall}}\right)^{-5/3}, \tag{5.51}$$

and is initially super-Eddington for disruptions of solar-type stars by SMBHs with $M_{\rm BH} \lesssim 10^{7.5} M_\odot$. Assuming a radiative efficiency $0 < \eta < 1$, the peak (i.e. time of first pericenter return) mass fallback rate is given by

$$\frac{\dot{M}_{\rm peak}}{\dot{M}_{\rm Edd}} \approx 133\, \eta_{-1} k^{3/2} \beta^{3n/2} M_6^{-3/2} m_*^2 r_*^{-3/2}, \tag{5.52}$$

implying that the maximum black hole mass that can undergo a phase of super-Eddington accretion is given by

$$M_{\rm BH,max} = 2.6 \times 10^7 M_\odot \eta_{-1}^{2/3} k \beta^n m_*^{4/3} r_*^{-1}. \tag{5.53}$$

The mass fallback rate becomes sub-Eddington at a time

$$t_{\rm Edd} = 6.6 \times 10^7 \text{ sec } \eta_{-1}^{3/5} k^{-3/5} \beta^{-3n/5} M_6^{-2/5} m_*^{1/5} r_*^{3/5}, \tag{5.54}$$

although if $t_{\rm Edd} < t_{\rm fall}$ there is no super-Eddington accretion phase. Here we have set $\eta_{-1} = \eta/.1$. Considering the dependences of Eqs. 5.50, 5.52, 5.53, and 5.54 on n we see that adopting Eq. 5.2 can have dramatic effects on TDEs from stars on deeply plunging ($\beta > 3$) orbits. In particular, using the correct values of $\Delta\epsilon$ reduces the peak mass fallback rate, decreasing the maximum SMBH mass that can produce a super-Eddington accretion phase. On the other hand, for TDEs with super-Eddington accretion, the duration of the super-Eddington phase is extended for (realistic) low-n values.

We plot the effect of n on the mass fallback rate in Fig. 5.11. In previous literature ($n = 2$) a wide variety of mass fallback curves were possible, with high peaks and fast decay times accompanying large β values. If $n = 0$, however, the mass fallback rate is generally independent of β. Under simplifying assumptions about the relationship of disk luminosity to $\dot{M}$ (often but inaccurately taken as $L \propto \dot{M}$; for complications see Lodato et al. (2009); Lodato and Rossi (2011)), the fallback timescale can be inferred by sufficiently long lightcurve observations. Alternatively, in the future it may be possible to measure $t_{\rm fall}$ directly, by measuring the delay between the onset of accretion and a prompt signal accompanying stellar disruption (either X-ray shock breakout or GWs). In either case, the β independence of $t_{\rm fall}$ will simplify parameter extraction, in particular measurement of $M_{\rm BH}$.

Adopting $n = 0$ will also alter the distribution of β in the TDEs detected by individual wide-field surveys, $\dot{N}_{\rm det}(\beta)$. This is a quantity distinct from the distribution of the intrinsic TDE rate, $\dot{N}_{\rm TDE}(\beta)$, which scales as $\dot{N}_{\rm TDE} \propto \beta^{-1}$ for two-body relaxation in the "pinhole" regime (Brassart and Luminet 2008). Alternatively, if the dominant source of loss cone fueling is two-body relaxation in the "diffusion"

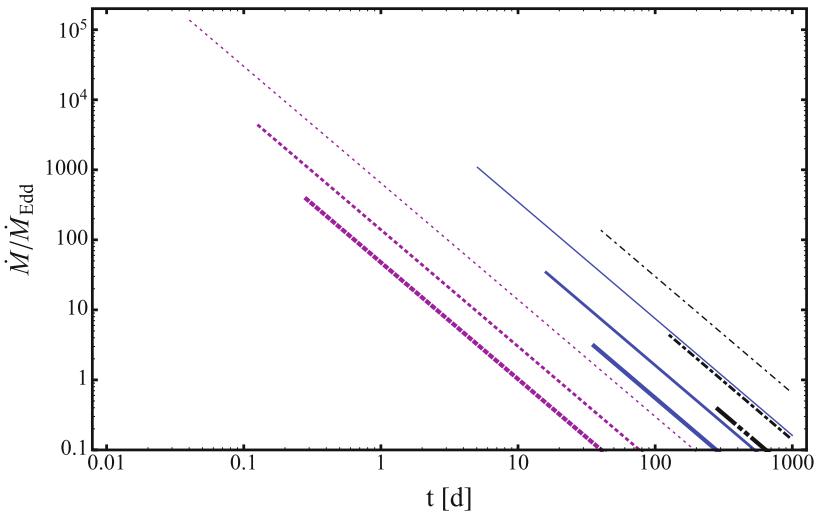

Fig. 5.11 Mass fallback curves (normalized by the Eddington fallback rate) versus time since disruption in days, for a variety of TDEs. SMBH masses of $10^6 M_\odot$, $10^7 M_\odot$, and $5 \times 10^7 M_\odot$ are plotted as thin, normal, and thick curves, respectively. Likewise, β values of 1, 2, and 10 are plotted as *black dot-dot-dashed, blue solid, and purple dotted* curves assuming $n = 2$, the power law index defined by $\Delta\epsilon \propto \beta^n$ - see Eq. 5.3. If $n = 0$, the *black dot-dot-dashed curves* represent all β values. Here we consider solar-type stars, and for simplicity set $k = 1$ and $\eta = 0.1$

regime, almost all TDEs will have $\beta = 1$; however, since most SMBHs are supplied with stars coming from the boundary between these regimes we will consider the pinhole regime for the remainder of this section (as it is the relaxational regime with nontrivial β dependence). If the TDE rate is dominated by the effects of an axisymmetric (Vasiliev and Merritt 2013) or triaxial (Merritt and Poon 2004) stellar potential, the distribution of β will also follow the pinhole regime's scaling.

If we first consider UV or soft X-ray surveys sensitive to the peak frequencies of TDE disk emission, then the peak luminosity $L \propto \dot{M}_{\rm peak} \propto \beta^{3n/2}$, implying a survey horizon $r_{\rm hor} \propto \beta^{3n/4}$ and a detection rate $\dot{N}_{det} \propto \beta^{(9n-4)/4}$. Optical detections of TDE disks will not be sensitive to the event's bolometric luminosity but rather to emission on the Rayleigh-Jeans tail, for which $L \propto \dot{M}^{1/4}$ and $\dot{N}_{\rm det} \propto \beta^{(9n-16)/16}$ (Lodato and Rossi 2011). However, both of these scaling relations for $\dot{N}_{\rm det}$ assume a purely flux-limited survey; in the old picture of TDE energy spread ($n = 2$), high-β events would be favored by their high flux but disfavored by their shorter timescales of peak emission. If the timescale of peak emission, $t_{\rm fall}$, is less than the survey cadence, $t_{\rm cad}$, then the probability of detection will be approximately reduced by the factor $t_{\rm fall}/t_{\rm cad}$. This gives $\dot{N}_{\rm det} \propto \beta^{(3n-4)/4}$ and $\dot{N}_{\rm det} \propto \beta^{(-15n-16)/16}$ for X-ray and optical disk emission, respectively.

Although the details remain uncertain, several recent papers (Strubbe and Quataert 2009; Lodato and Rossi 2011) have predicted that super-Eddington, radiation-driven outflows may dominate early emission from TDE accretion disks, particularly at long

Table 5.1 Here we display the scaling exponents s for the β dependence of the TDE detection rate, $\dot{N}_{\rm det}(\beta) \propto \beta^s$. In the first column we describe the frequency and source of emission (SE indicates a super-Eddington outflow); in the second we give s for the standard scenario $n = 2$ and a high-cadence survey; in the third we again consider s in the standard scenario, but for a slow-cadence survey; in the final column we give s for our revised $\Delta\epsilon$, with $n = 0$, at any cadence. In this table $\nu_{\rm bb}$ refers to the "blackbody" frequency of peak emission (the super-Eddington outflow is assumed to have a thermal spectrum; the disk emission is better modeled as a multicolor blackbody)

Scenario	$n = 2$ ($\frac{t_{\rm fall}}{t_{\rm cad}} > 1$)	$n = 2$ ($\frac{t_{\rm fall}}{t_{\rm cad}} < 1$)	$n = 0$
Disk, $\nu \approx \nu_{\rm bb}$	7/2	1/2	-1
Disk, $\nu < \nu_{\rm bb}$	1/8	-23/8	-1
SE, $\nu \approx \nu_{\rm bb}$	-2/5	-17/5	-7/10
SE, $\nu < \nu_{\rm bb}$	81/16	33/16	-33/16

wavelengths. Using a simple blackbody model with peak frequency $\nu_{\rm bb}$ (Lodato and Rossi 2011), which predicts a peak luminosity $L \propto \beta^{97/24}$ at frequencies $\nu < \nu_{\rm bb}$, or $L \propto \beta^{2/5}$ for $\nu > \nu_{\rm bb}$, we can repeat the above calculations. The β dependence of all different scenarios are presented in Table 5.1. With $n = 0$, all observational strategies are biased in favor of low β detections, including many strategies that once favored high β TDEs.

5.9 Discussion

In this Chapter we have analyzed the tidal disruption and free fall of a star in the context of "free solutions" to the Hill equations of the parabolic restricted three-body problem. The important conclusions of this work are the following:

1. During the tidal disruption of a star, debris energy freezes in at $R = R_{\rm t}$, not $R = R_{\rm p}$.
2. Consequently, the spread in debris energy is smaller than in past analytic predictions. This will result in flares with longer fallback times, i.e. ones that decay more slowly but have smaller initial fallback rates. Fewer TDEs will drive powerful super-Eddington outflows than has been predicted in the past.
3. The spread in debris energy is generally dominated by the freeze-in energy, although redistribution of the kinetic energy of vertical collapse to in-plane motions may result in slight variation in $\Delta\epsilon$ for low $\beta(\lesssim 5)$. Rapidly spinning stars may see a stronger version of this effect at high β if their spins are misaligned with the orbital angular momentum vector.
4. The leading order GR corrections to the frozen-in value of $\Delta\epsilon$ are small, and generally negligible unless $R_{\rm p} \lesssim 6R_{\rm g}$. For such TDEs (i.e. all TDEs for SMBH masses above $10^{7.5} M_\odot$) we have derived for the first time the 1PN modifications to $\Delta\epsilon$.

5. The free solution model we have introduced is, in the limit of spherical and static initial conditions, an approximate simplification of the affine model . However, the ability to include a range of nonspherical or dynamic initial conditions gives it a degree of flexibility not present in the affine model. Furthermore, the deformations to an initially spherical body in tidal free fall are not ellipsoids, as is assumed by the affine model.
6. Gravitational waves are generated from variation in the internal quadrupole moment of a tidally disrupting star, reaching peak amplitude at the moment of maximum compression and bounce. GW emission is likely dominated by a single term in the quadrupole moment tensor, $\ddot{I}_{zz} \propto \beta^2$. For main sequence stars, these are unlikely to be detectable by ground-based GW interferometers. GWs from the tidal disruption of WDs by IMBHs are more promising targets, and for modest β values ($\sim$5) could be detectable to tens of megaparsecs.
7. Gravitational wave emission from nondiagonal terms in the star's quadrupole moment could alter the previous conclusion, since $\ddot{I}_{xz}, \ddot{I}_{yz} \propto \beta^5$. However, in order for these terms to possess a nonzero prefactor, the reflection symmetry of the TDE about the orbital plane must be broken by either SMBH or stellar spin. Whether this can be done without desynchronizing the vertical collapse and weakening the β dependence of $\ddot{I}_{xz}, \ddot{I}_{yz}$ is unclear.

The existing hydrodynamical literature did not until very recently support the first three of these conclusions. With a few exceptions, prior work has focused mainly on the common $\beta = 1$ events, for which Eqs. 5.1 and 5.2 are identical. In Laguna et al. (1993), the authors conducted SPH simulations in a static Schwarzschild background geometry for $\beta = \{1, 5, 10\}$. They found that the fallback time scaled approximately as $t_{\rm fall} \propto \beta^{-1.5}$ and the velocity of unbound ejecta $\upsilon_{\rm ej} \propto \beta^{0.5}$, both of which imply the intermediate value of $n = 1$, for the power-law index defined in Eq. 5.3 as $\Delta\epsilon \propto \beta^n$. However, the limited resolution of their simulations (7000 SPH particles) makes it unclear whether they would have possessed the midplane resolution to resolve the phase of maximum compression; indeed, they find that $\rho_{\rm c} \propto \beta^{1.5-2}$, a scaling well below analytic predictions as well as the higher-resolution one-dimensional simulations of BL08.

It is also possible that our approximations have underestimated the efficiency with which the bounce phase can redistribute the energy of vertical collapse to motions within the orbital plane, perhaps due to neglect of GR effects during phase III. Alternatively, the simulations of Laguna et al. (1993) may be altered by entropy production due to artificial viscosity, as suggested by the authors.

More recent hydrodynamical simulations of high-β disruptions did not publish details on the spread of debris energy (Kobayashi et al. 2004; Guillochon et al. 2009), although we note that Kobayashi et al. (2004), using a one-dimensional mesh code, found results in qualitative agreement with BL08. On the other hand, Guillochon et al. (2009) found a vastly lower degree ($\rho_{\rm c} \approx 4\rho_*$) of central compression for a $\beta = 7$ event than what is predicted analytically, by the affine model, or by one-dimensional hydrodynamic simulations, with the difference attributed to a combination of insufficient midplane resolution, the internal density gradient of the star, and the physical,

three-dimensional effects discussed in § 5.5. We have shown that some multidimensional effects are unlikely to be large due to the proximity of the sonic point to the region of maximum compression. Desynchronization due to density differences in the star, which will result in the core seeing a different "effective β" than the rest of the star, may be an exception to this.

During the completion of this paper, an independent numerical study (Guillochon and Ramirez-Ruiz 2013) was posted which found an approximate constancy in $\Delta\epsilon$ for $1 \lesssim \beta \lesssim 4$, in the course of a thorough investigation of low-β TDEs. This result is broadly compatible with our paper, although further hydrodynamical simulations will be required to explore high β values, and to test our prediction of desynchronized collapse for rapidly rotating, misaligned stars (which could restore a β dependence to $\Delta\epsilon$, for deeply plunging disruptions). Like Guillochon and Ramirez-Ruiz (2013), we argue that the assumption of frozen-in debris energy is made much more valid by assuming the energy freezes in when internal forces become negligible at $R = R_{\rm t}$, not at later times.

We note that the free solutions are of course an approximation to the physical reality of tidal disruption, and neglect a number of important physical effects. Some areas in particular need of further clarification by hydrodynamical simulation are the velocity and shape perturbations induced on the star by the nonlinear hydrodynamics of tidal disruption at $R \approx R_{\rm t}$. Although BL08 found these effects to generally be negligble for Phase II and III of a TDE, their simulations were one-dimensional and it is conceivable that in three dimensions the picture may change. The free solutions also fail to capture GR effects relevant for large β values, although we have argued based on our own analysis and past literature that these effects do not qualitatively change our conclusions. Furthermore, we have not considered the effects of SMBH spin, which if misaligned with the orbital plane may be able to desynchronize stellar collapse.

Despite these limitations, the free solutions are a simple yet powerful method for considering the tidal free fall of disrupted bodies. Although we have focused on the disruption of main sequence stars by supermassive black holes, we stress that much of our analysis is general and applies equally well to other scenarios, such as tidal disruption of white dwarfs by intermediate mass black holes, or of planets or asteroids by more compact bodies. In all of these scenarios, the decoupling of vertical from in-plane motion will strongly compress the disrupted object, often by many orders of magnitude. In future work, we aim to apply the free solutions to these alternative physical regimes, as well as to internal motions such as pre-disruption rotation or post-disruption shock formation.

Chapter 6
General Relativistic Effects in Tidal Disruption Flares

K. Hayasaki, N. Stone, & A. Loeb The Monthly Notices of the Royal Astronomical Society, *Vol. 434, pp. 909–924, 2013*

6.1 Introduction

In this chapter, we review the literature on ways in which general relativity (GR) can strongly modify aspects of stellar tidal disruption. It is natural to expect that GR should play an important role in TDEs, as these events occur deep in the potential wells of supermassive black holes (SMBHs): for a $10^6 M_\odot$ SMBH, the gravitational radius $R_g = GM_{BH}/c^2$ is roughly 1/47 the value of the tidal radius R_t. For a $M_{BH} = 10^8 M_\odot$ SMBH, $R_g \approx R_t/2$: the tidal radius has almost moved inside the horizon! We focus on three particular manifestations of GR:

- Modifications to the "Hills mass," the maximum mass SMBH capable of disrupting a given star. This mass is quite sensitive to SMBH spin, and can be increased by up to an order of magnitude for favorable (prograde equatorial) orbits around rapidly spinning SMBHs.
- Repeated tidal compressions and bounces during disruption. A TDE with both high β and a relativistic pericenter will undergo more than one vertical collapse and bounce, unlike in the Newtonian regime.
- Circularization of the debris from stellar tidal disruption. General relativistic effects likely play a crucial role in this process.

GR has other important effects on TDEs as well. In Chap. 5, we discussed more speculative manifestations of GR (desynchronization of the vertical collapse for misaligned SMBH spin; high frequency GWs from the bounce). Because of the important role of asymmetries in these scenarios, further study will likely require numerical simulations. In Chap. 8, we will discuss a more direct way in which TDEs can be used to measure SMBH spin. But first, we will examine the existing literature.

N. C. Stone, *The Tidal Disruption of Stars by Supermassive Black Holes,*
Springer Theses, DOI 10.1007/978-3-319-12676-0_6

6.2 SMBH Spin and the Hills Mass

As was described in § 1, the Hills mass (Eq. 1.4) exists because the tidal radius $R_t \propto M_{BH}^{1/3}$ while the horizon scale $R_S \propto M_{BH}$. For $M_{BH} > M_{Hills}$, stars are not disrupted until they have fallen inside the horizon; from an outside observer's perspective, they are swallowed whole. Eq. 1.4 defined M_{Hills} in the simplest possible, Newtonian way: by equating $R_t = R_S$ and solving for M_{BH}. However, this neglects two important relativistic effects:

1. In GR, orbits near black hole horizons cannot penetrate arbitrarily close to the event horizon. For non-spinning black holes, an innermost stable circular orbit (ISCO) exists at $6R_g$, while an unstable circular orbit exists at $4R_g$. This unstable circular orbit (which we will refer to as the IBCO, or innermost bound circular orbit) is also the minimum pericenter to which a parabolic orbit can plunge while still escaping to infinity. Parabolic orbits cannot have pericenters interior to the IBCO without plunging directly into the horizon. Both the IBCO and the ISCO are modified by SMBH spin.
2. Our calculation of R_t in Eq. (1.1) was likewise approximate; a more accurate calculation must compare the self-gravitational acceleration felt at the surface of the star to eigenvalues of the general relativistic tidal tensor[1]. For highly relativistic orbits, with $R_p \approx R_{IBCO}$, these eigenvalues depend strongly on SMBH spin.

Interestingly, for non-spinning black holes, the errors introduced into Eq. (1.4) by neglect of these points will largely self-cancel. However, rapidly spinning SMBHs will have a much larger (somewhat smaller) Hills mass for prograde (retrograde) orbits, as we discuss below. First, however, we must introduce the basics of geodesic motion in Kerr spacetime.

6.2.1 The Kerr Metric

The Kerr metric describes the geometry of spacetime around spinning black holes. The metric can be written with several different choices of coordinates, but in this subsection, we follow the presentation of Bardeen et al. (1972). Specifically, line elements in the Kerr metric are given in Boyer-Lindquist (approximately, spherical polar) coordinates $\{t, r, \theta, \phi\}$ as

$$\begin{aligned} ds^2 = &-(1 - 2Mr/\Sigma)dt^2 - (4Ma\sin^2\theta/\Sigma)dtd\phi \\ &+ (\Sigma/\Delta)dr^2 + \Sigma d\theta^2 + (r^2 + a^2 + 2Ma^2 r\sin^2\theta/\Sigma)\sin^2\theta d\phi^2. \end{aligned} \tag{6.1}$$

[1] Of course, the most accurate calculation would require a general relativistic hydrodynamical simulation. In this section, as in the rest of this thesis, we focus mainly on an analytic treatment of stellar tidal disruption.

In this equation, as in the rest of this subsection, we will use relativistic units where $G = c = 1$. For brevity (and unlike in other sections of this thesis), we denote black hole mass and spin as M and a, respectively. This definition of the Kerr metric uses the support functions

$$\Delta = r^2 - 2Mr + a^2 \tag{6.2}$$

$$\Sigma = r^2 + a^2 \cos^2\theta. \tag{6.3}$$

If we set $a = 0$, we recover the limit of the Schwarzschild metric. Ballistic motion of test particles (such as stars) around SMBHs admits four conserved quantities: energy E, z-component of angular momentum L, Carter constant Q, and (trivially) particle mass μ. Orbits are determined by the four geodesic equations, which can be written as first order ODEs using the affine parameter $\lambda = \tau/\mu$:

$$\Sigma \frac{\mathrm{d}r}{\mathrm{d}\lambda} = \pm\sqrt{V_\mathrm{r}} \tag{6.4}$$

$$\Sigma \frac{\mathrm{d}\theta}{\mathrm{d}\lambda} = \pm\sqrt{V_\theta} \tag{6.5}$$

$$\Sigma \frac{\mathrm{d}\phi}{\mathrm{d}\lambda} = -(aE - L/\sin^2\theta) + aT/\Delta \tag{6.6}$$

$$\Sigma \frac{\mathrm{d}t}{\mathrm{d}\lambda} = -a(aE\sin^2\theta - L) + (r^2 + a^2)T/\Delta. \tag{6.7}$$

Here we have defined effective potentials

$$T = E(r^2 + a^2) - La \tag{6.8}$$

$$V_\mathrm{r} = T^2 - \Delta(\mu^2 r^2 + (L - aE)^2 + Q) \tag{6.9}$$

$$V_\theta = Q - \cos^2\theta(a^2(\mu^2 - E^2) + L^2/\sin^2\theta). \tag{6.10}$$

Although analytic solutions for these geodesics have recently been found (Fujita and Hikida 2009), they are in general complicated functions of incomplete elliptic integrals, and yield limited insight. It is often more straightforward to solve the geodesic equations numerically. Direct integration of Eqs. (6.4–6.7) requires a careful treatment of turning points in r and θ; however, these turning points can be removed using the coordinate transformations of Drasco and Hughes (2004).

Several radii of interest exist. The event horizon for Kerr black holes is located at

$$r_\mathrm{h} = M + \sqrt{M^2 - a^2}, \tag{6.11}$$

while in the equatorial plane the ISCO is given by

$$r_\mathrm{ISCO} = M\left(3 + Z_2 \mp ((3 - Z_1)(3 + Z_1 + 2Z_2))^{1/2}\right), \tag{6.12}$$

$$Z_1 = 1 + (1 - a^2/M^2)^{1/3}\left((1 + a/M)^{1/3} + (1 - a/M)^{1/3}\right), \tag{6.13}$$

$$Z_2 = (3a^2/M^2 + Z_1^2)^{1/2}. \tag{6.14}$$

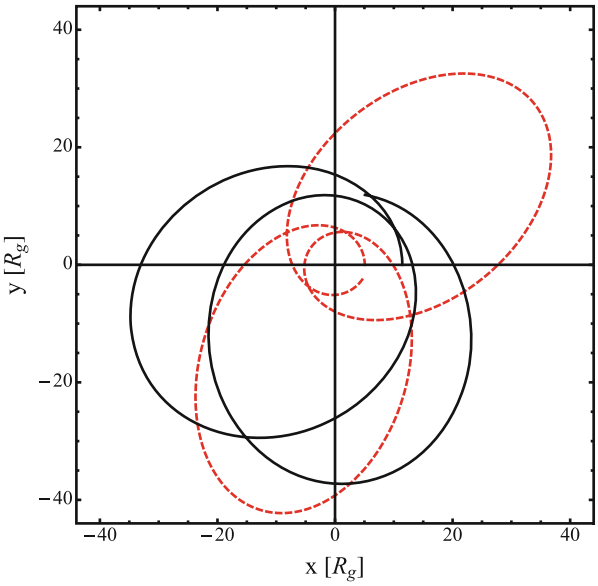

Fig. 6.1 A pair of geodesics describing test particle motion around a Kerr black hole with $a = 0.68$ (both geodesics have $Q = 0$ and are confined to the equatorial plane). The solid black curve shows the first two radial orbits of an $E = 0.98$, $L = 4.5$ trajectory; the dashed red curve shows the first two radial orbits of an $E = 0.98$, $L = 3.5$ trajectory. Notably, the lower angular momentum geodesic undergoes much greater per-orbit pericenter precession

Likewise, the IBCO radius that defines the minimum pericenter of a parabolic orbit is

$$r_{\rm IBCO} = 2M \mp a + 2M^{1/2}(M \mp a)^{1/2}. \tag{6.15}$$

Later in this section, we will need to calculate the angular momentum of IBCO orbits; in general, any circular, equatorial orbit has a vertical angular momentum component given by

$$L = \frac{\pm M^{1/2}(r^2 \mp 2aM^{1/2}r^{1/2} + a^2)}{r^{3/4}(r^{3/2} - 3Mr^{1/2} \pm 2aM^{1/2})^{1/2}}. \tag{6.16}$$

In the above formulas, the upper sign always refers to prograde equatorial orbits, while the lower sign refers to retrograde ones. In Fig. 6.1 we plot sample geodesics for a pair of orbits in the equatorial plane of a Kerr black hole with $a = 0.68$. The orbits have the same energy but different angular momentum; the one with lower angular momentum has a smaller pericenter and a correspondingly faster rate of pericenter precession.

6.2.2 Relativistic Tidal Tensors

Previously , we wrote the Newtonian tidal tensor C_{ij} (defined as $\ddot{r}_i = -C_{ij}r_j$) in Eq. (1.20) as $C_{ij}^{\rm N} = (GM_{\rm BH}/R^3)(\delta_{ij} - 3R_iR_j/R^2)$. Likewise, the general relativistic tidal tensor in Schwarzschild spacetime ($G = c = 1$) is given by (Brassart & Luminet, 2010)

$$C_{11}^{\rm S} = \frac{GM_{\rm BH}}{R^3}\left(1 - 3\frac{R^2+L^2}{R^2}\cos^2 F\right) \tag{6.17}$$

$$C_{22}^{\rm S} = \frac{GM_{\rm BH}}{R^3}\left(1 - 3\frac{R^2+L^2}{R^2}\sin^2 F\right) \tag{6.18}$$

$$C_{33}^{\rm S} = \frac{GM_{\rm BH}}{R^3}\left(1 + 3\frac{L^2}{R^2}\right) \tag{6.19}$$

$$C_{12}^{\rm S} = \frac{GM_{\rm BH}}{R^3}\left(-3\frac{R^2+L^2}{R^2}\cos F \sin F\right) \tag{6.20}$$

The Schwarzschild case differs from the Newtonian one in two notable ways: tidal accelerations are increased by the addition of terms $\sim L^2/R^5$, and we have used a slightly different orbital anomaly, replacing the Newtonian f with a variable F that equals 0 at pericenter and evolves as $\dot{F} = EL/(R^2+L^2)$. Here E and L are the GR specific orbital energy and angular momentum, respectively. The Kerr metric tidal tensor, relevant for spinning SMBHs, is provided in Marck (1983a); Marck (1983b); Kesden (2012b). The full Kerr tidal tensor is beyond the scope of this thesis, but in order to calculate the relativistic Hills mass we will need to use its eigenvalues for orbits restricted to the equatorial plane. In this limit, the Kerr tidal tensor becomes

$$C_{11}^{\rm S} = \frac{GM_{\rm BH}}{R^3}\left(1 - 3\frac{R^2+K}{R^2}\cos^2 \Psi\right) \tag{6.21}$$

$$C_{22}^{\rm S} = \frac{GM_{\rm BH}}{R^3}\left(1 - 3\frac{R^2+K}{R^2}\sin^2 \Psi\right) \tag{6.22}$$

$$C_{33}^{\rm S} = \frac{GM_{\rm BH}}{R^3}\left(1 + 3\frac{K}{R^2}\right) \tag{6.23}$$

$$C_{12}^{\rm S} = \frac{GM_{\rm BH}}{R^3}\left(-3\frac{R^2+K}{R^2}\cos \Psi \sin \Psi\right), \tag{6.24}$$

where $K = Q + (L - aE)^2$ and the phase angle Ψ is a generalization of F (but for our purposes, it suffices to know that $\Psi = 0$ at pericenter). All point-mass tidal tensors (Newtonian, Schwarzschild, or Kerr) have two positive eigenvalues corresponding to squeezing, and one negative eigenvalue that represents stretching. The Kerr tensor has eigenvalues

$$\beta_{-} = -2\left(1+\frac{3K}{2R^2}\right)\frac{M}{R^3} \tag{6.25}$$

$$\beta_{+,1} = \left(1+\frac{3K}{R^2}\right)\frac{M}{R^3} \tag{6.26}$$

$$\beta_{+,2} = \frac{M}{R^3}. \tag{6.27}$$

6.2.3 The Relativistic Hills Mass

Following Kesden (2012b), we define the following criterion for stellar tidal disruption:

$$r_{\rm IBCO} < R_* \left(\frac{|\beta_-|}{M_{\rm BH}/r_{\rm IBCO}^3}\right)^{1/3}\left(\frac{M_{\rm BH}}{M_*}\right)^{1/3}. \tag{6.28}$$

When this inequality is satisfied, stars can be disrupted on non-plunging orbits. If we equate the two sides of this inequality, we have an implicit equation for $M_{\rm BH}$; solving it numerically (using the equatorial prograde IBCO radius) gives the Hills mass for a given star. The eigenvalue β_- depends on orbital angular momentum, which can be calculated for any circular, prograde Kerr orbit using Eq. (6.16). We show Hills masses for a variety of main sequence stars in Fig. 6.2, using the lower main sequence mass-radius relation $R_* \approx R_\odot (M_*/M_\odot)^{0.8}$ (Magorrian and Tremaine 1999). Inclusion of relativistic effects increases the Hills mass by almost an order of magnitude when one compares Schwarzschild SMBHs to extremal Kerr SMBHs.

The mass-radius relation for white dwarfs of mass $M_{\rm WD}$ is approximately (Zalamea et al. 2010)

$$R_{\rm WD} = 0.013 R_\odot \left(\frac{M_{\rm Ch}}{M_{\rm WD}}\right)^{1/3}\left(1-\frac{M_{\rm WD}}{M_{\rm Ch}}\right)^{0.447}, \tag{6.29}$$

where $M_{\rm Ch} = 1.43 M_\odot$ is the Chandrasekhar mass. We plot Hills masses for white dwarf tidal disruptions in Fig. 6.3. Schwarzschild SMBHs (defined as $M_{\rm BH} > 10^6 M_\odot$) are unable to tidally disrupt white dwarfs; however, when considering extremal Kerr black holes, the Hills mass moves up to a few $\times\, 10^6 M_\odot$.

6.3 Multiple Compressions

In Chap. 5, we explored the vertical compression of a star during its passage through the tidal sphere. A Newtonian treatment of the tidal tensor yielded a vertical acceleration $\ddot{z} \propto -z$, which translates physically into a homologous vertical collapse

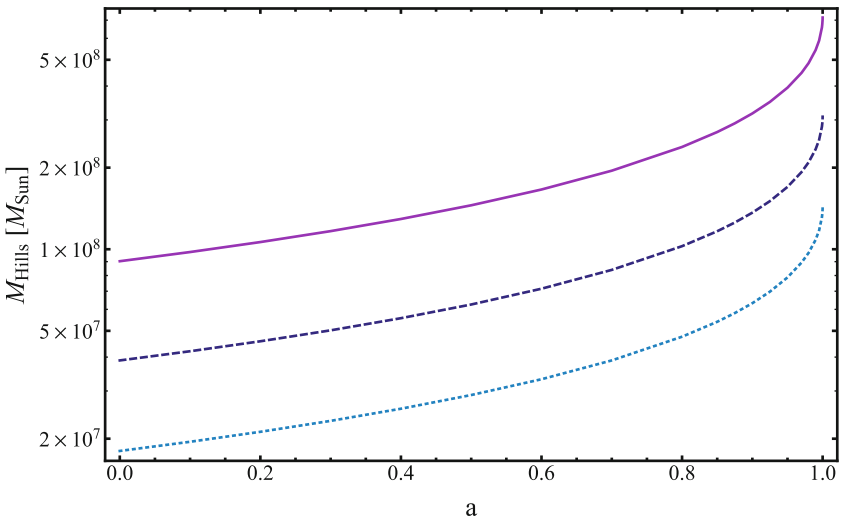

Fig. 6.2 The general relativistic Hills mass for main sequence stars tidally disrupted by black holes with dimensionless spins a. The solid purple line is for stars with $M_* = M_\odot$; the dashed blue line is for $M_* = 0.3M_\odot$; the dotted light blue line is for $M_* = 0.1M_\odot$. Note that this is the *maximum* Hills mass, i.e. the Hills mass for stars on prograde equatorial orbits. Stars on tilted orbits will see a significantly lower Hills mass (which in fact will decrease below the $a = 0$ value if the orbit is retrograde)

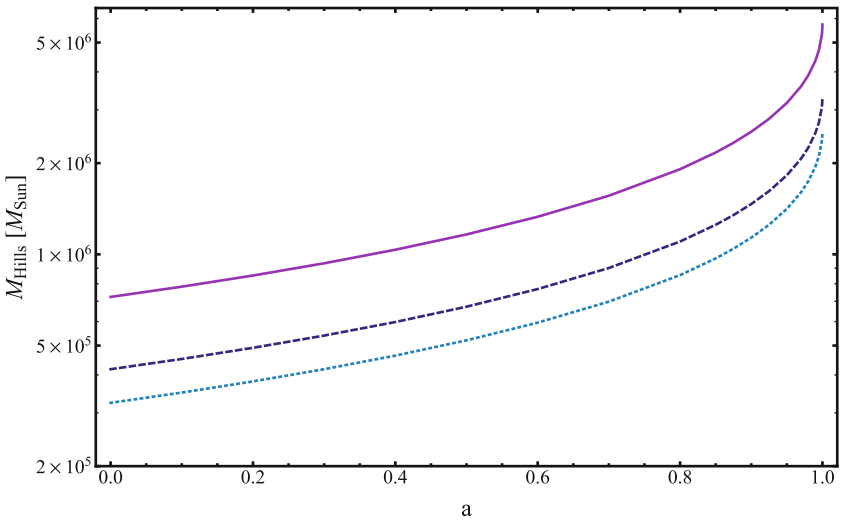

Fig. 6.3 The same as Fig. 6.2, but now for tidal disruptions of white dwarf stars. The solid purple line is for $M_* = 0.2M_\odot$; the dashed blue line is for $M_* = 0.6M_\odot$; the dotted light blue line is for $M_* = M_\odot$

occurring shortly after pericenter passage. However, in the previous section, we have seen that the relativistic tidal tensor has a very different functional form. The stronger tidal accelerations present in GR give $\ddot{z} \propto -z(1 + 3K/R^2)$ (for equatorial orbits), using the relativistic definitions of K and R. For a combination of high β and relativistic $R_{\rm p}$, this can lead to qualitatively new behavior in TDEs: the point of peak compression can occur *before* pericenter passage, leading to a hydrodynamic bounce that is followed by a *second* stage of collapse and compression, all within the tidal sphere. Extreme events can even suffer three or more cycles of tidal compression and bounce.

Few three dimensional numerical simulations of tidal disruption exist that incorporate general relativistic effects (even using an approximate post-Newtonian or pseudo-Newtonian potential); of those in the literature, none have resolved multiple compression and bounce cycles[2]. To date, the only works published on the phenomena of relativistic multiple compressions are either in the framework of the affine model (Luminet and Marck 1985), or one dimensional hydrodynamics simulations. The more recent simulations of Brassart and Luminet (2010) indicate that subsequent compression/bounce phases are not as extreme as the first, which produces the highest central pressures and temperatures. Whether multiple compressions have an observable signature is unclear: repeated X-ray shock breakout signals are one possibility, as are repeated high-frequency GW bursts (§ 5.7), but both of these possibilities are speculative at this point.

6.4 Circularization of Debris

The mechanism by which loosely bound debris streams from a tidal disruption event are able to dissipate their orbital energy and circularize into a luminous accretion disk remains mysterious, and is one of the most important unsolved problems in TDE physics. Our lack of knowledge of this process complicates our ability to translate theoretical predictions for mass fallback rates $\dot{M}(t)$ into light curves: the usual assumption that bolometric luminosity $L \propto \dot{M}$ assumes that returning material

[2] Most three dimensional hydrodynamical simulations of TDEs that incorporate relativity are not in the correct regime of parameter space to produce multiple compressions; others are resolution limited. The highest resolution numerical simulation that plausibly *should* have seen multiple compression cycles is Rosswog et al. (2009). However, this simulation focused on tidal disruption of white dwarfs, which were seen to experience significant thermonuclear energy injection during the first bounce phase; the lack of subsequent bounces may therefore have been physical.

circularizes rapidly into an accretion disk[3]. Interestingly, the circularization of tidal debris may be mediated by general relativistic effects.

The first suggestion that GR could play a role in TDE circularization was made by Rees (1988), who argued that relativistic apsidal precession (precession of the longitude of pericenter, within the orbital plane) would cause debris streams to self-intersect at large angles, creating strong shocks that could efficiently dissipate orbital energy into heat. Shortly afterwards, Cannizzo et al. (1990) pointed out that this circularization process could be delayed for stars disrupted on non-equatorial orbits around spinning SMBHs. In this regime, nodal precession (precession of the orbital plane due primarily to the Lense-Thirring effect) would cause sufficiently narrow debris streams to miss each other at the self-intersection points predicted for the coplanar case. In general, nodal precession is much weaker than apsidal precession: the lowest-order orbit averaged values of both are given by (Merritt et al. 2009)

$$\delta\omega = A_{\rm S} - 2A_{\rm J}\cos\iota - \frac{1}{2}A_{\rm Q}(1 - e\cos^2\iota) \tag{6.30}$$

$$\delta\Omega = A_{\rm J} - A_{\rm Q}\cos\iota \tag{6.31}$$

$$A_{\rm S} = \frac{6\pi}{c^2}\frac{GM_{\rm BH}}{a(1-e^2)} \tag{6.32}$$

$$A_{\rm J} = \frac{4\pi a_{\rm BH}}{c^3}\left(\frac{GM_{\rm BH}}{a(1-e^2)}\right)^{3/2} \tag{6.33}$$

$$A_{\rm Q} = \frac{3\pi a_{\rm BH}^2}{c^4}\left(\frac{GM_{\rm BH}}{a(1-e^2)}\right)^{2}. \tag{6.34}$$

where $\delta\omega$ is the total per-orbit shift in the longitude of pericenter, and $\delta\Omega$ is the total per-orbit shift in the line of ascending nodes. Here $a_{\rm BH}$ is the dimensionless SMBH spin, while a and e are orbital semimajor axis and eccentricity, respectively. $A_{\rm S}$, $A_{\rm J}$, and $A_{\rm Q}$ represent lowest-order precession contributions from the greater strength of GR relative to Newtonian gravity, frame-dragging, and the SMBH quadrupole moment. Whether or not the streams are able to self-intersect depends both on the total amount of nodal precession and on the width of the streams, which is set internally by hydrodynamic equilibrium; properties of thin debris streams have been modeled in a semi-analytic way by Kochanek (1994).

The process of debris circularization has never been self-consistently produced in hydrodynamical simulations of realistic TDEs, so it remains unclear whether the required dissipation comes from shocks at stream self-intersections, or from some other process. Debris streams in a typical TDE have pericenters $R_{\rm p} \sim 10R_{\rm g}$ and

[3] It also assumes that radiative efficiency is roughly independent of the Eddington ratio $L/L_{\rm Edd}$. Several different analytic models for the luminosity of super-Eddington accretion flows exist, and make different predictions on this point. Interestingly, the most recent radiation hydrodynamic simulations seem to suggest roughly constant radiative efficiencies across the Eddington limit, with most super-Eddington emission being released in outflowing material (Sadowski et al. 2014).

apocenters $R_a \sim 10^4 R_g$, creating a huge and, so far, intractable, dynamic range for any simulation to follow. Computer simulations of TDE circularization have, therefore, had to cheat in various ways. One approach is to scale down the black hole mass: circularization has been successfully simulated in encounters between stars and IMBHs with $M_{BH} = 10^3 M_\odot$ (Ramirez-Ruiz and Rosswog 2009; Guillochon et al. 2014). Interestingly, these simulations are Newtonian, and circularization appears to be driven by dissipation of energy during tidal compression of debris streams returning to pericenter. This purely hydrodynamic mechanism does not appear to scale up well to larger black hole masses, however (Guillochon et al. 2014).

An alternate approach, adopted in this thesis research (Hayasaki et al. 2013), has been to simulate star-SMBH encounters, but with an eccentric rather than parabolic center of mass trajectory. Because this book's focus is on analytic rather than numerical work, we will not go into the full details of Hayasaki et al. (2013) here, but instead outline the important results. Specifically, we have performed Smoothed Particle Hydrodynamics (SPH) simulations of stellar tidal disruption; the Lagrangian and mass-discretized nature of SPH is useful in following narrow streams of gas over a large dynamic range. These simulations account for the self-gravity of the stellar gas, and use a fixed background potential for the gravitational field of the SMBH. To simulate the effects of relativistic precession, we have modified an SPH code (Okazaki et al. 2002) to employ the pseudo-Newtonian potential of Wegg (2012):

$$\Phi(r) = -\frac{\alpha G M_{BH}}{r} - \frac{(1-\alpha) G M_{BH}}{r - R_x} - \frac{G M_{BH} R_y}{r^2}. \tag{6.35}$$

This potential is a generalization of the well-known Paczynski-Wiita potential (Paczyński and Wiita 1980) that much more accurately captures apsidal precession of highly eccentric orbits. The free parameters are calibrated to be $\alpha = -4(2+\sqrt{6})/3$, $R_x = (4\sqrt{6} - 9) R_g$, and $R_y = -4(2\sqrt{6} - 3) R_g/3$.

In our simulations, we first initialize a polytropic gas sphere using the Lane-Emden equation, and allow it to relax in vacuum; as can be seen in Fig. 6.4, this does not change the star's configuration greatly. After the star reaches its equilibrium, it is placed into the gravitational field of the SMBH, with an initial velocity (uniform across the star) corresponding to center of mass trajectories with the desired β and e. In our simulations, we have considered $\beta = \{1, 5\}$ and $e = \{1.0, 0.98, 0.8\}$. The most extreme of these simulations ($e = 0.8$, $\beta = 5$) quickly produce a circularized accretion disk through shocks at relativistic stream self-intersection points; our simulations did not run long enough to capture the circularization process for other parameter choices.

As was hypothesized by Rees (1988), we see debris streams crash into each other at supersonic velocities due to the influence of apsidal precession: a sequence of snapshots is shown in Fig. 6.5. The shocks that form begin a process of runaway circularization: the orbital energy dissipated into heat reduces the orbital period of the gas, decreasing the time to the next self-intersection. The circularization we observe is entirely due to relativistic precession: Fig. 6.6 shows snapshots from our control simulation done in Newtonian gravity, where almost no dissipation occurs during the run time of the simulation. Of course, these results do not account for the influence of

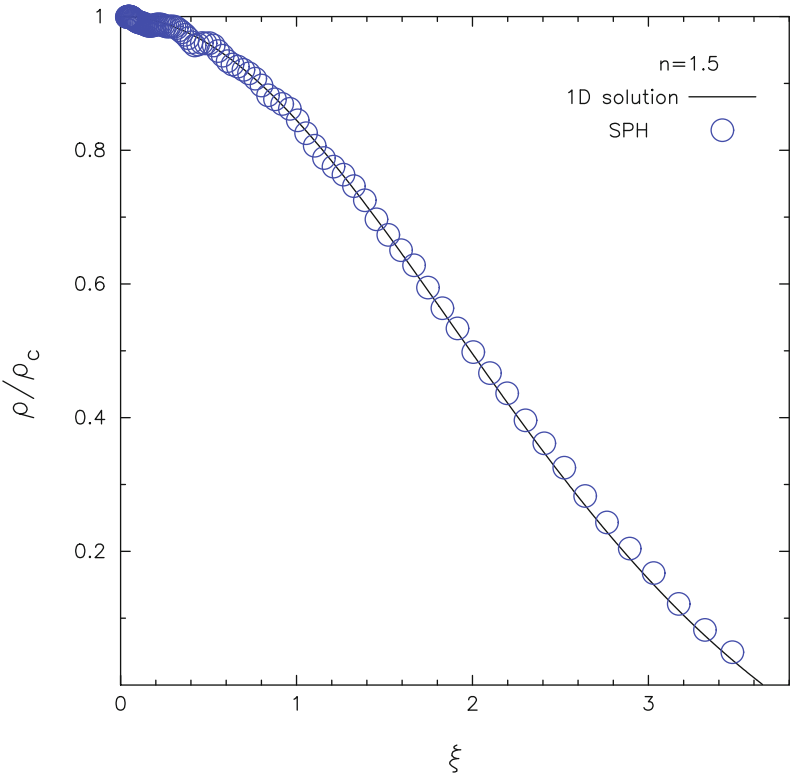

Fig. 6.4 The initial density profile (normalized to central density ρ_c) of the stars we simulate in Hayasaki et al. (2013). Here we plot ρ against a dimensionless radius χ. The numerical solution to the Lane-Emden equation is shown as a black line; the blue circles are the equilibrium configuration reached by our SPH simulation after a few dynamical times

SMBH spin, and even more importantly we have assumed a (perhaps unphysically) low value of orbital eccentricity. On the other hand, at fixed pericenter R_p, the total per-orbit apsidal precession (Eq. 6.30) is a *very* weak function of orbital eccentricity, so it is not unreasonable to assume that parabolic TDEs should see self-intersecting debris streams similar to those produced in our simulations. The ultimate resolution of this question remains a topic for future research.

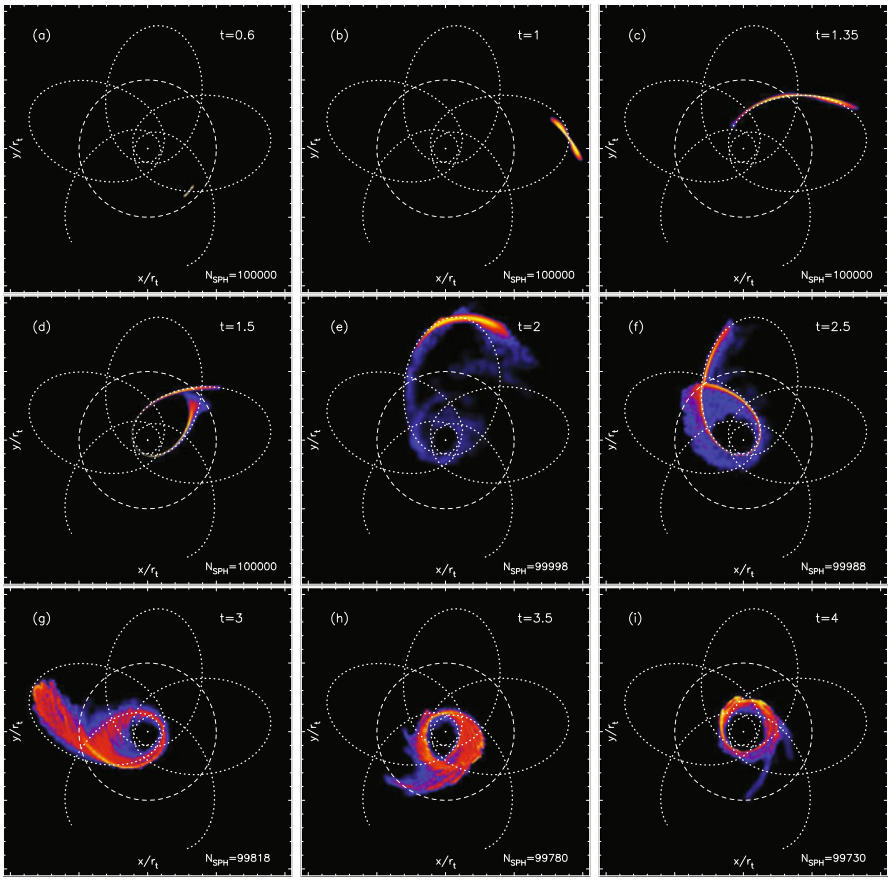

Fig. 6.5 Snapshots of the circularization process, for a TDE with $e = 0.8$ and $\beta = 5$. A $M_{\rm BH} = 10^6 M_\odot$ black hole is the small white dot at the center of each snapshot; the tidal radius is the dashed white circle, and the precessing point particle trajectory of the star's center of mass is the dotted white rosette. Projected gas density is indicated logarithmically with colors (*blue being dilute, yellow being dense*). Following the progression of snapshots (time t is shown in the top right, measured in units of $\sqrt{R_{\rm t}/GM_{\rm BH}}$), we see that circularization runs away quickly after the first stream self-intersection at $t = 2.5$

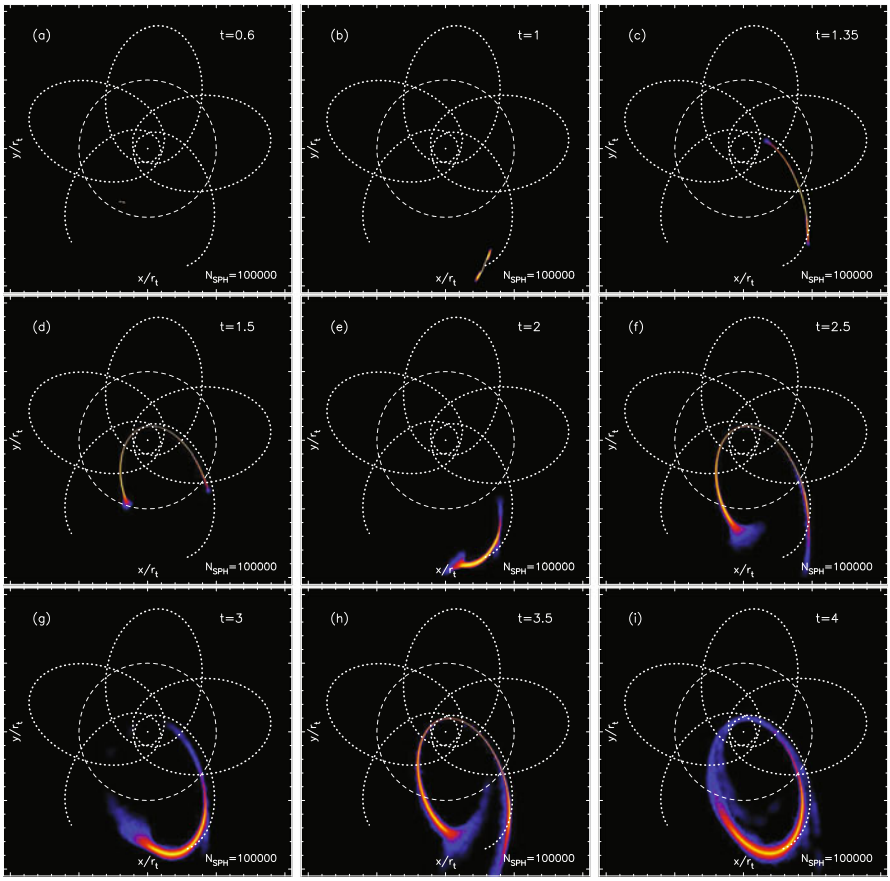

Fig. 6.6 The same as Fig. 6.5, but now for a simulation with purely Newtonian gravity. Almost no energy dissipation occurs over the course of the simulation, with debris streams "frozen in" to their initial trajectories. These results highlight the importance of GR-mediated precession for producing shocks in TDE debris

Chapter 7
Observing Lense-Thirring Precession in Tidal Disruption Flares

N. Stone & A. Loeb Physical Review Letters*, Vol. 108, id. 061302, 2012*

7.1 Introduction

Recent observations have established that a subset of TDEs launch collimated, relativistic jets. Two such relativistic TDEs have been detected with the *Swift* satellite: Swift J164449.3+573451 (Bloom et al. 2011; Burrows et al. 2011; Levan et al. 2011; Zauderer et al. 2011, hereafter Swift J1644+57), and Swift J2058.4+0516 (Cenko et al. 2012b). Both events are generally interpreted as the tidal disruption of a main sequence star by a SMBH, with a relativistic jet pointed down our line of sight; however, alternate explanations do exist (Krolik and Piran 2011; Quataert and Kasen 2012). These discoveries were not widely anticipated by theoretical work on TDEs, with the notable exception of Giannios and Metzger (2011). Subsequent searches for radio afterglows from off-axis jets have generally returned negative results (van Velzen et al. 2011a), with one to two detections of afterglows around X-ray selected TDEs that may reflect contamination from AGN (Bower et al. 2013).

In this paper we consider the following question: when an accretion disk misaligned with its black hole's equatorial plane launches a jet, in which direction will the jet point? Although much analytic literature exists on tilted accretion disks, almost none of it concerns the production of jets. Numerical simulations of jet production in tilted accretion systems are almost as rare; it was only after the publication of this paper that the first such simulation appeared in the literature. As of now, it is unclear whether jets launched from tilted accretion disks will align with the black hole spin vector, with the disk angular momentum vector, or in some other direction associated with the magnetic field geometry (Fragile 2008).

These concerns are generally academic, as most observed accretion disks are in fact aligned with the equatorial plane of their black hole. However, stars destroyed in TDEs are scattered in from $\sim$pc scales via processes that have no knowledge of the SMBH spin direction. The transient accretion disk that results from circularization will in general possess a significant tilt. The subset of TDEs which do power relativistic jets therefore offer a unique laboratory to test open questions about accretion and jet launching physics in tilted accretion flows. In the following sections, we show that any jet that aligns with the disk angular momentum vector will precess

N. C. Stone, *The Tidal Disruption of Stars by Supermassive Black Holes,*
Springer Theses, DOI 10.1007/978-3-319-12676-0_7

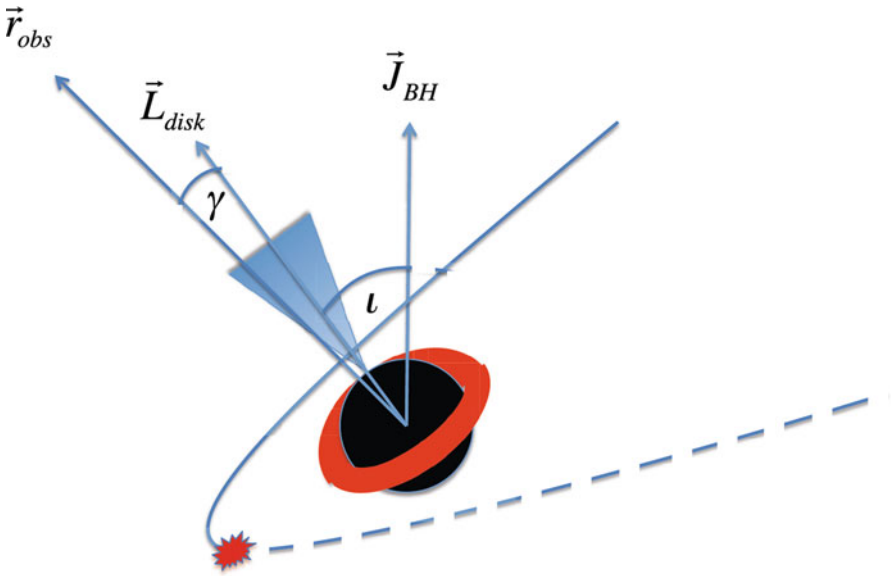

Fig. 7.1 Cartoon picture of misaligned stellar tidal disruption. The star, initially on a parabolic orbit, is disrupted near pericenter. The star's initial orbit is misaligned by an angle ι_* from the star; we assume that the circularized disk forms with the same tilt angle, $\iota = \iota_*$. The disk angular momentum vector $\vec{L}_{\rm disk}$ is misaligned from the SMBH spin vector $\vec{J}_{\rm BH}$ by the angle ι; this can cause an associated jet to change its offset angle ψ from a fixed line-of-sight direction

significantly. We then apply our jet precession model to Swift J1644+57 to argue that the jet launched in this event likely aligned with the (steady) SMBH spin vector. Even in TDEs that lack associated jets, relativistic precession of the accretion disk may produce observable consequences sensitive to the value of SMBH spin.

7.2 Spin Evolution of a Tilted Disk

The orbits of particles inclined out of the equatorial plane of a spinning SMBH can be strongly affected by torques due to black hole spin; Lense-Thirring torques generally dominate (and diminish $\propto r^{-3}$), but torques from the quadrupole ($\propto r^{-4}$) and higher multipole moments contribute at a subdominant level. We present a cartoon in Fig. 7.1; here the disk is tilted by an angle ι that is assumed to equal the tilt of the pre-disruption stellar orbit, ι_*.

The response of an inclined disk to external torques depends critically on the interplay between viscosity (parametrized with the Shakura-Sunyaev coefficient α) and disk scale height H/R. For thin disks ($H/R \lesssim \alpha$), small perturbations due to differential precession propagate in a diffusive way (Kumar and Pringle 1985), and the Bardeen-Petterson effect will align the inner region of the disk with the black

hole equatorial plane. This creates a larger-scale warp in the disk structure (Bardeen and Petterson 1975; Papaloizou and Pringle 1983). However, the response of a thick disk ($H/R \gtrsim \alpha$) is qualitatively different: small perturbations from differential precession propagate as bending waves through the disk, causing (to first order) rigid body precession of the accretion disk (Fragile et al. 2007; Dexter and Fragile 2011). The precession period of a solid-body rotator is

$$T_{\rm prec} = 2\pi \sin\iota \frac{J}{\tau}, \tag{7.1}$$

where we have defined J as the total angular momentum of the disk, and τ is the total integrated torque acting on it. The transient accretion flows produced in TDEs are, initially, expected to be significantly super-Eddington and geometrically thick (Ulmer 1999; Strubbe and Quataert 2009). Combining this with the fact that tidally disrupted stars should arrive from arbitrary inclinations, we therefore expect most TDE disks to initially precess like solid-body rotators.

If we parametrize the disk surface density as a power law $\Sigma(R) = \Sigma_{\rm i} \times (R/R_{\rm i})^{-\zeta}$, then we can analytically calculate the precession timescale (Fragile et al. 2007) to be

$$T_{\rm prec} = \frac{8\pi G M_{\rm BH}(1+2\zeta)}{c^3(5-2\zeta)} \frac{r_{\rm o}^{5/2-\zeta} r_{\rm i}^{1/2+\zeta}(1-(r_{\rm i}/r_{\rm o})^{5/2-\zeta})}{a_{\rm BH}(1-(r_{\rm i}/r_{\rm o})^{1/2+\zeta})}. \tag{7.2}$$

We have defined here the disk inner ($R_{\rm i}$) and outer ($R_{\rm o}$) edges, with normalizations in units of the Schwarzschild radius $R_{\rm S}$: $r_{\rm i} = R_{\rm i}/R_{\rm S}$, and $r_{\rm o} = R_{\rm o}/R_{\rm S}$. We have also used the dimensionless black hole spin parameter, $0 < a_{\rm BH} < 1$. In this paper, we approximate the disk inner and outer edges as constant; if this assumption were to hold, disk precession would be nearly periodic, but in reality viscous spreading of the disk outer-edge will grow the precession period with time. Follow-up work to this paper provided a detailed discussion of quasi-periodicity in viscously spreading, precessing TDE disks (Shen and Matzner 2014).

A power law parametrization is of course an approximation to the more complicated reality of TDE disk accretion. Using analytic (Strubbe and Quataert 2009) and numerical (Montesinos Armijo and de Freitas Pacheco 2011) TDE disk solutions as motivation, we will use $\zeta = \{-3/2, 0, 1\}$ in this paper. Going from $\zeta = -3/2$ to $\zeta = 1$ decreases $T_{\rm prec}$ by a factor ≈ 7. Throughout this paper we assume that

1. Circularization processes are able to quickly establish a small-scale accretion disk.
2. The accretion disk precesses as a solid body rotator (equivalently, $H/R \gtrsim \alpha$).

Assumption 1 holds after a timescale $t_{\rm circ} = n_{\rm circ} t_{\rm fall}$; as discussed previously, the exact value of $n_{\rm circ}$ is quite uncertain and may depend on β and $a_{\rm BH}$. Assumption 2 typically breaks down once the mass fallback rate $\dot{M}$ becomes sub-Eddington; at this point a Bardeen-Petterson warp will develop in the geometrically thin disk, and solid body precession will cease.

To determine a more precise timescale for the disk to become geometrically thin, we adopt Eq. (1.32), the expression for H/R given in Strubbe & Quataert (2009).

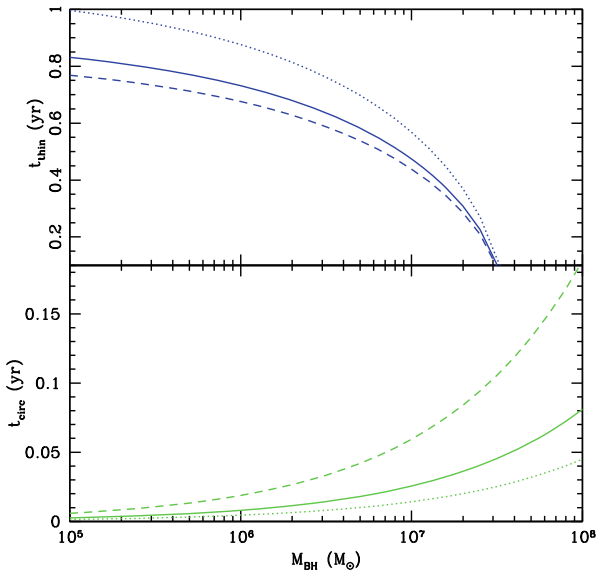

Fig. 7.2 Relevant timescales that bracket the duration of solid-body precession. The *blue lines* in the top panel show the time required for the disk outer edge to become geometrically thin and susceptible to Bardeen-Petterson warps; the *green lines* in the bottom panel show approximate circularization timescales (both panels are functions of black hole mass $M_{\rm BH}$). In each panel, the *dotted, solid, and dashed lines* are for stars of mass $2M_\odot$, $1M_\odot$, and $0.5M_\odot$, respectively. The stellar mass-radius relationship is taken from Kippenhahn & Weigert (1994), p. 208. The top panel assumes $n_{\rm circ} = 3$, while the bottom takes a disk outer edge of $R_{\rm o} = R_{\rm t}$

The disk height $H/R < \alpha$ after a time

$$t_{\rm thin} = t_{\rm fall}\left(\frac{5}{2}\frac{f}{X}\frac{M_*/t_{\rm fall}}{\dot{M}_{\rm Edd}}\frac{R_{\rm S}}{R}\right)^{3/5} \approx 0.3\, M_6^{2/5} r_{\rm p}^{6/5} m_*^{3/5} r_*^{-3/5}\left(\frac{f}{X_{-1}}\frac{R_{\rm S}}{R}\right)^{3/5} \text{ yr}. \tag{7.3}$$

We have defined $X = \alpha/(1 - 8\alpha^2/3f)$, and normalized $X_{-1} = X/0.1$. Fig. 7.2 illustrates the range of times $t_{\rm circ} < t < t_{\rm thin}$ during which solid body precession is feasible. Generally speaking, such precession can persist for times $\lesssim$1 yr.

7.3 Differential Stream Precession

A second effect that can modulate the angular momentum vector of the accretion disk is the time-varying orientation of returning debris streams. The streams themselves experience differential Lense-Thirring torques, implying that the supply of gas into

the accretion disk is not itself coming from a fixed orbital plane. This differential stream precession (DSP) can potentially alter the direction of $\vec{L}_{\rm disk}$; in this section we compute both leading order estimates and exact geodesic values for the magnitude of DSP.

The leading order, single-orbit angular shift in the angular momentum vector of a returning debris stream with orbital period T is given by $\phi_{\rm orb} \approx \Delta\Omega \sin\iota = 2\pi \sin\iota (T/T_{\rm LT})$. Here $\Delta\Omega$ is the per-orbit nodal precession, and the related Lense-Thirring precession period (Merritt et al. 2010)

$$t_{\rm LT} = \frac{T}{2a_{\rm BH}} \left(\frac{c^2 a(1-e^2)}{GM_{\rm BH}} \right)^{3/2} . \tag{7.4}$$

We have considered a debris stream with semimajor axis a and eccentricity e. Of course, what matters more is the differential precession between the currently returning stream at time t, and more loosely bound streams returning at a later time ∞. This differential precession is $\Delta\phi_{\rm orb} = \phi_{\rm orb}(T) - \phi_{\rm orb}(\infty)$, or, to leading order,

$$\Delta\phi_{\rm orb} = 4\pi a_{\rm BH} \sin(\iota) (2r_{\rm p})^{3/2} \left((1+e)^{-3/2} - 2^{-3/2} \right) . \tag{7.5}$$

Making the further (accurate) approximation that $r_{\rm p}/a \ll 1$, $\Delta\phi_{\rm orb} \approx 1.7 \sin(\iota)$ $a r_{\rm p}^{-5/2} \times r_* M_6^{-1} (t/t_{\rm fall})^{-2/3}$.

Qualitatively, the DSP is largest for rapidly spinning SMBHs that tidally disrupt stars near the ISCO. Eq. (7.5) is an upper limit on the modulation of $\vec{L}_{\rm disk}$ by the DSP: even though the mass in a TDE disk is, at early times, dominated by material that has just returned (as the disk viscous timescale $t_{\rm visc} \ll t_{\rm fall}$, initially), the instantaneous angular momentum in the disk is approximately the integrated history of angular momentum return. Even this upper limit is quite modest; $\Delta\phi_{\rm orb} < 1^\circ$ for realistic circularization timescales ($t > 3t_{\rm fall}$) and tidal disruptions of solar-type stars by SMBHs.

We check our leading order calculation by using the formalism of Drasco & Hughes (2004) to numerically integrate the Kerr geodesic equations. Specifically, we take a spread of debris streams with Newtonian specific energy, pericenter, and inclination given by ϵ, $r_{\rm p}$, and ι, and transform these to geodesic constants of motion: specific energy E, vertical component of angular momentum $L_{\rm z}$, and Carter constant Q. Good agreement with our leading order approximation in Eq. (7.5) is demonstrated in Fig. 7.3. In general, the DSP is highly subdominant to direct precession of the accretion disk, which we focus on in the remainder of this paper. The estimates presented in Fig. 7.3 are also overestimates of the true value of $\Delta\phi_{\rm orb}$, in that they assume the larger Newtonian spread in debris specific energy $\Delta\epsilon = 3GM_{\rm BH}R_*/R_{\rm p}^2$ that was current at the time this paper was written; as was seen in §5, this is a significant overestimate of the true energy spread when $R_{\rm p} < R_{\rm t}$, and therefore overestimates the effect of DSP as well.

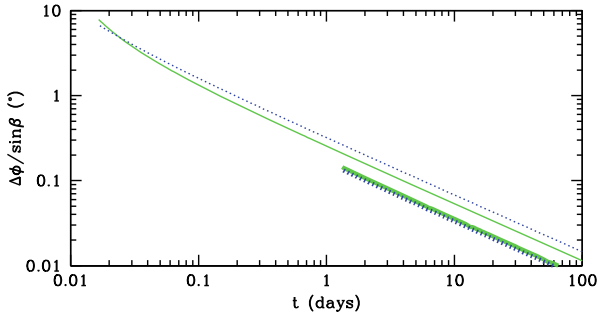

Fig. 7.3 Differential stream precession, as approximated by the angular shift $\Delta\phi_{\rm orb}$. *Thick curves* show tidal disruption of a solar-type star with $M_6 = 1$, $a_{\rm BH} = 0.8$, $R_{\rm p} = 26R_{\rm g}$. *Thin curves* show an alternate case with $R_{\rm p} = 6R_{\rm g}$; however, the *thin curves* seriously overestimate the magnitude of DSP due to their use of the older, inaccurate expression for the Newtonian specific energy spread $\Delta\epsilon$. *Green solid lines* are calculated numerically from the Kerr geodesic equations; *blue dotted lines* use our leading order expression in Eq. (7.5) and show excellent agreement

7.4 Observational Implications

Lense-Thirring torques will cause direct, quasi-periodic precession of the transient accretion disks formed in misaligned TDEs. Nodal precession of the debris streams will affect the disk angular momentum vector more subtly through the DSP; however, we neglect this subdominant effect for the remainder of the paper. A precessing accretion disk will present different portions of itself to an observer at fixed viewing angle, and its observed luminosity will be modulated by a factor $\sim \cos\psi$. This quasi-periodic modulation of thermal disk emission will leave an observable imprint on the power spectrum of TDE light curves. In a subset of TDEs, a much more dramatic signal will exist: if the disk precesses into an edge-on configuration, cutting off the observer's line of sight to the hottest parts of the inner disk, the SED will redden and the observed disk luminosity will temporarily drop by up to $\sim$2 orders of magnitude (Ulmer 1999). Well-sampled TDE light curves may reveal this type of "blinking" in a subset of flares, allowing constraints to be placed on $a_{\rm BH}$.

Even more exciting observational consequences of disk precession will exist for the subset of TDEs that launch relativistic jets. If jets powered by tilted accretion disks align with $\vec{L}_{\rm disk}$, then the jets will precess along with the disk, and a jet pointed down an observer's line of sight with opening angle $\theta_{\rm jet}$ will precess away on a characteristic time

$$t_{\rm jet} = \frac{T_{\rm prec}\theta_{\rm jet}}{2\pi\,\sin\iota}. \tag{7.6}$$

The jet could precess away from the line of sight faster or slower if it is not perfectly aligned with the observer's viewing angle; the maximum amount of time it can remain visible is $2t_{\rm jet}$. Under the assumption that the jet aligns itself with $\vec{L}_{\rm disk}$, even brief observations of continuous beamed emission from a TDE can place very strong

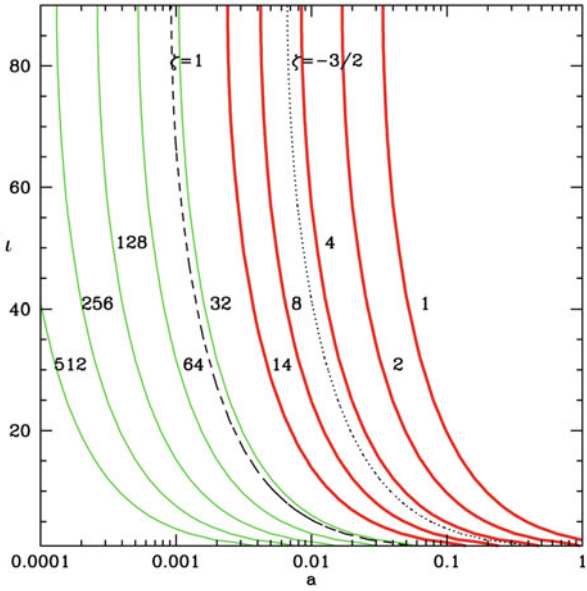

Fig. 7.4 The joint parameter space of black hole spin $a_{\rm BH}$ and disk inclination angle ι. Solid contours show the maximum number of days $2t_{\rm obs}$ that the Swift J1644+57 jet, with parameters inferred from Zauderer et al. (2011), could stay on-axis with respect to an observer. In our calculation of $T_{\rm prec}$ we assume $\zeta = 0$, $R_{\rm o} = 2R_{\rm p}$ and $R_{\rm i} = 6R_{\rm g}$. All regions of parameter space to the right of the thick red curves are excluded by the $\gtrsim$2 weeks a relativistic jet was observed for. Equivalent 14 day contours are shown as black dotted and dashed lines for $\zeta = -3/2$ and $\zeta = 1$, respectively

constraints on the joint parameter space of $a_{\rm BH}$ and ι_* (we also assume that $\iota = \iota_*$). Likewise, observation of a small sample of TDE jets would resolve the question of jet alignment in (this subset of) tilted accretion systems: while a single nondetection of jet precession could be attributed to a slowly spinning SMBH or an event with $\iota \approx 0$, nondetection of jet precession in a large TDE sample would indicate that these jets align with $\vec{J}_{\rm BH}$.

These considerations can be made more concrete by considering the relativistic tidal disruption event Swift J1644+57, which was found by Zauderer et al. (2011) to possess $M_{\rm BH} \sim 10^{5-6} M_\odot$ and $\theta_{\rm jet} \sim 10^{-1.5}$ (the jet opening angle was roughly estimated from both rate and Eddington limit considerations). We show constraints on the joint parameter space of $\{a_{\rm BH}, \iota\}$ in Fig. 7.4, assuming $M_6 = 1$. Observed relativistic emission from Swift J1644+57 lasted for at least two weeks, which rules out those (significant!) portions of parameter space marked with red curves. For Swift J1644+57, we are therefore presented with a trichotomy: at least one of the three following statements must be true.

1. The SMBH that produced this TDE was spinning extremely slowly, with $a_{\rm BH} \lesssim 10^{-2}$ (or 10^{-1} if $\zeta = -3/2$).
2. The orbit of the tidally disrupted star was closely aligned with the SMBH equatorial plane ($\iota_* \lesssim \theta_{\rm jet}$).
3. In this event, the relativistic event did *not* align with the disk angular momentum vector, but instead with a direction fixed in space (e.g. the SMBH spin axis).

Possibility (1) requires a low but not impossible value of SMBH spin (Berti & Volonteri, 2008); however, it may be inconsistent on theoretical grounds with the launching of a jet powered by the Blandford-Znajek mechanism (Lei and Zhang 2011). Possibility (2) is statistically improbable and also implies that the *Swift* satellite should have seen many more (precessing) relativistic TDEs of shorter duration. Because both of these options seem unlikely, our tentative conclusion is that the persistent X-ray emission observed from Swift J1644+57 points to a jet aligned with the constant spin axis of the SMBH, and not with the angular momentum vector of a precessing disk. Future nondetections of precession in relativistic TDEs would greatly strengthen this conclusion; conversely, detection of precessing TDE jets would indicate alignment with $\vec{L}_{\rm disk}$ and suggest that one of the unlikely alternate possibilities (small $a_{\rm BH}$, or $\iota \lesssim \theta_{\rm jet}$) explains the lack of precession in Swift J1644+57. Regardless, relativistic tidal disruption flares have great potential to probe open questions in jet launching physics.

Chapter 8
Conclusions and Future Directions

The tidal disruption of stars by supermassive black holes (SMBHs) is an exciting research frontier in both theoretical and observational astronomy. In this thesis, we have studied these dramatic events from a theoretical perspective and found that they hold great promise: as measures of SMBH demography; as probes to study general relativity; and as laboratories for high energy accretion physics. For many decades tidal disruption events (TDEs) were a theory-dominated subject with no substantiating observations. Fortunately, we now live in an era where exciting new TDE detections are reported every year, and, increasingly, theorists' models are challenged by unexpected observations. In this concluding chapter, we summarize recent developments in TDE research, with a focus on papers relevant to the work in this thesis. Finally, we offer brief remarks about future avenues of research.

In Chapt. 2, we reviewed the simplest standard formalism for calculating TDE rates due to two-body relaxation in galactic nuclei. Although the theory of two-body relaxation is well-developed, many theoretical works have suggested alternative mechanisms for funneling stars to hungry SMBHs. Examples of these include binary SMBHs, axisymmetric or triaxial stellar density profiles, tidal separation of binary stars, and infalling massive perturbers. It is currently unclear if any of these alternative mechanisms can compete with standard two-body relaxation, and resolving this question will require both observational and theoretical progress on topics as disparate as the final parsec problem, equilibrium stellar density profiles, and extragalactic molecular clouds. Fortunately, the observational sample of TDEs continues to expand: just in the last year, roughly half a dozen new TDE candidates have been announced (Arcavi et al. 2014; Chornock et al. 2014; Holoien et al. 2014; Maksym et al. 2014). On the theoretical side, the continued progress of computational astrophysics has recently allowed N-body simulations of two-body scattering sufficient run time to estimate TDE rates (Zhong et al. 2014). Even though these simulations do not yet have the same number of stars as a realistic galactic nucleus, they can be coupled to scaling relations as a valuable check on the traditional analytic estimates presented in Chapter 2. Complicating this picture, however, is a persistent tension between theoretical rate calculations and observed samples of TDEs: even conservative, two-body relaxation rate estimates generally predict $\dot{N}_{\rm TDE} \sim 10^{-4}$ yr^{-1} (Wang

N. C. Stone, *The Tidal Disruption of Stars by Supermassive Black Holes,*
Springer Theses, DOI 10.1007/978-3-319-12676-0_8

and Merritt 2004), roughly an order of magnitude higher than observationally inferred rates (Donley et al. 2002). More recent estimates of the observed TDE rate have not budged (van Velzen and Farrar 2014), and it is unclear whether the errors are due to observations (e.g. unmodeled selection effects), due to stellar dynamical uncertainties (e.g. assumptions of dynamical equilibrium or near-isotropy in rate calculations), or due to something else entirely (e.g. dust obscuration). It is worth noting that these alternate mechanisms are of interest not just as sources of TDEs, but also as sources of the "extreme mass ratio inspirals" which form a major scientific motivation for space-based gravitational wave observatories.

In Chapts. 3 and 4, we investigated how TDEs can be used as indicators of SMBH recoil, a prediction of relatively recent numerical relativity breakthroughs. Immediately following the coalescence of a SMBH binary, there will be a burst of TDEs as the host galaxy's "loss cone" refills due to gravitational wave recoil. In a relatively conservative dry merger scenario, this burst produces one TDE every few decades for typical recoils among *LISA*-band ($\sim 10^6 M_\odot$) black holes. However, this rate could be enhanced by resonant migration of stars in dry mergers, or viscous migration of stars in wet mergers. Since publication of Stone and Loeb (2011), the first of these possibilities has been studied analytically by Seto and Muto (2011), who conducted three-body integrations and found that stars could indeed be captured into resonant migration around inspiraling SMBH binaries. Post-Newtonian corrections eventually break these stars out of their mean motion resonances at $\sim$ tens of R_g, which is a very promising distance for providing EM counterparts: these stars would be disrupted not decades but *weeks* after GW recoil! Stellar migration through circumbinary disks remains less well understood. If either mechanism proves viable, it would provide a strong electromagnetic counterpart for future low-frequency gravitational wave astronomy. In the nearer term, the *LSST* will go online within a decade, and should be able to detect spatially offset tidal disruption flares at a rate of $\sim 1 - 10\ \mathrm{yr}^{-1}$. Following publication of Stone and Loeb (2012b), two subsequent papers have examined the rate at which recoiling SMBHs will produce TDEs. The N-body simulations of Li et al. (2012) found, in contrast to our work, that the total number of TDEs is dominated by unbound stars disrupted during the SMBH's pericenter passages through its host galaxy's nucleus. Such a result is plausible: our estimates of the unbound disruption rate were most unreliable in the rapidly relaxing, out of equilibrium environment of the galactic nucleus. The observable consequences of this may be minimal, however: such TDEs will not have observable spatial offsets, and the detectability of kinematic offsets remains uncertain at best. A subsequent analytic study (Liu and Chen 2013) found that TDEs from widely separated SMBH pairs (during early stages of a galaxy merger) should dominate the TDE rate from recoiling SMBHs, highlighting the need for careful followup (e.g. searching for a second centroid of light) of spatially offset tidal disruption flares. Although a small minority of the total TDE population, such offset flares would serve as valuable tracers of SMBH recoil.

In Chapt. 5, we argued that traditional estimates for TDE mass fallback timescales were only correct for grazing, marginal disruptions, and are in fact enormously incorrect for deeply plunging disruptions. We reached this conclusion through analytic

considerations; our approach is complementary to the numerical simulations of Guillochon and Ramirez-Ruiz (2013), which covered $\beta \leq 4$ TDEs. These simulations were performed while our paper was being written (and, it should be noted, were published shortly before our own work), and reached similar conclusions on the β independence of the fallback timescale and energy spread. These conclusions were further verified by our own subsequent hydrodynamic simulations of tidal disruption, which found similar energy spreads for $\beta = 1$ and $\beta = 5$ events (Hayasaki et al. 2013). Midplane resolution limitations prevent numerical simulations from accurately estimating the energy spread for high β events (Guillochon et al. 2009), but our analytic estimates apply to arbitrarily large β, and found that the vertical collapse and bounce of a tidally disrupting star, general relativity, and stellar spin are all inadequate on their own to alter the β-independence of $\Delta\epsilon$. It is possible, however, that a combination of these factors might restore some β dependence to the dynamical outcome of a TDE. Future work should address whether misaligned SMBH spin is capable of desynchronizing a bounce strongly enough to change the spread in debris energy. The new picture of energy freeze-in we have proposed eliminates a high-β tail of TDEs that was once thought to produce enormous peak fallback rates; this limits the observability of super-Eddington outflows (Strubbe and Quataert 2009) and largely eliminates a free parameter that could once be used to explain extreme events (Cannizzo et al. 2011). However, the distribution of β within a sample of TDEs carries valuable information about stellar dynamical processes, and the onus is now on theorists to discover novel ways to measure it. One speculative possibility that we have raised for the first time is high frequency gravitational wave emission, which can be generated by the rapidly changing internal quadrupole moment of a tidally "bouncing" star. This is a scenario that can be studied in more detail with full numerical simulations, or analytically with the parabolic free solutions we have used here.

In Chapt. 6, we surveyed the different ways in which TDE rates, dynamics, and flares can be affected by general relativistic effects. This is a topic certain to be of much future interest, as SMBH spin sets the maximum black hole mass capable of disrupting a main sequence star, and may well play an important role in the bounce dynamics as well. It also appears increasingly likely that debris circularization is mediated by GR precession; Guillochon et al. (2014) have found that purely hydrodynamic dissipation at the pericentric "nozzle" (Ramirez-Ruiz and Rosswog 2009) is unlikely to effectively circularize TDE debris around SMBHs. The pseudo-Newtonian simulations we presented in Chap. 6 (Hayasaki et al. 2013) offer an exploratory realization of relativistic circularization; however, this work needs to be extended to realistic eccentricities, higher particle resolutions, and spinning SMBHs before GR can be definitively said to explain debris circularization. Until then, consideration of alternatives, such as the magnetic dissipation proposed in Guillochon et al. (2014), offers another intriguing avenue of research.

In Chapt. 7, we argued that TDE flares offer a more direct way to measure SMBH spin: direct precession of the accretion disk, driven by Lense-Thirring torques. A precessing TDE disk will exhibit quasiperiodic oscillations in its light curve and spectrum as different portions of the disk are presented to the observer, potentially

enabling a direct SMBH spin measurement. Since the publication of Stone and Loeb (2012a), Shen and Matzner (2014) have coupled our picture of disk precession to a much more accurate, semi-analytic model of a viscously spreading disk. They consequently find a precession period that grows in time, which will complicate observational searches for precessing disks[1]. A very exciting TDE candidate was recently found to have quasiperiodic breaks in its light curve (Liu et al. 2014); the authors interpreted this as evidence for a SMBH binary periodically interrupting the return flow of loosely bound debris streams. However, the observations are also qualitatively similar to our proposal of TDE "blinking," when a precessing disk moves into an edge-on configuration with respect to the observer's line of sight. It will be very interesting to see if similar dips are seen in the light curves of future TDEs. We have tentatively used our model to address an open question in accretion physics (alignment of jets in tilted accretion flows), and argued that in the Swift J1644+57 flare, the jet likely aligned with the SMBH spin vector. Other "one-off" possibilities are improbable but viable, however, and a larger sample of relativistic TDE flares will be needed to settle the question of jet alignment. Jet precession has subsequently been studied by other authors in the context of the Swift J1644+57 TDE; for example, power spectrum analysis of the X-ray light curve in this event has detected multiple peaks, which have been interpreted as evidence for a weakly precessing jet (Saxton et al. 2012a). More complicated precession models involving disk warps have been invoked to explain this behavior (Lei et al. 2013; Wang et al. 2014), although the small inferred amplitude of precession in Saxton et al. (2012a) raises a troubling question (Stone and Loeb, 2012a): if TDE jets can precess, why have we not seen a much larger number of wildly precessing ones? Recently, McKinney et al. (2013) published the first GRMHD simulations of jet launching in tilted accretion systems, and found mixed evidence for precession: at small radii, their jets aligned with the BH spin vector, but at larger radii $\gtrsim 100 R_{\rm g}$, the jet bent to realign with the disk angular momentum vector. If this result applies to generic initial conditions (and not just to the large net magnetic flux scenario simulated), it implies that TDE jets can precess along with their disk if significant emission comes from a large enough distance in the jet. These numerical results have also motivated a more complex analytic model, in which disk precession is eventually quenched by electromagnetic alignment (Tchekhovskoy et al. 2014).

Many open questions still exist concerning TDEs. Does two-body relaxation dominate the event rate, or is this rate significantly enhanced by more exotic dynamical processes? Why do TDE rates inferred from observations consistently fall an order of magnitude below the conservative event rates calculated from two body relaxation? Is there a practical way to measure the pericenter of disruption from TDE light curves or SEDs? Can the high frequency gravitational wave emission proposed in this thesis be physically realized if symmetry above and below the orbital plane is broken by misaligned SMBH spin? Are there interesting observational consequences of stellar

[1] This is similar to the conclusion we reached in the analogous problem of precessing disks in short gamma ray bursts following the merger of a neutron star and a black hole (Stone et al. 2013a).

"pancaking" during pericenter passage? What physical mechanism drives circularization in realistic TDEs? Why do observed optical light curves approximate $t^{-5/3}$ behavior so well, contrary to simple predictions? What unique electromagnetic signatures can observers use to separate TDEs from contaminating transients (e.g. core collapse supernovae)? In what direction will a relativistic jet launched from a tilted TDE disk point?

Clearly, in conducting the research outlined here, we have often come across as many new questions as we have answered old ones. Progress will come from many different avenues. The advent of time domain optical astronomy has already revolutionized many fields, and it may do the same for TDE physics. Expanding the observational sample of TDEs and better accounting for observational selection effects should help address open questions about event rates. Some of the theoretical questions outlined above most likely require numerical simulations to address (e.g. any scenario with misaligned SMBH spin), but others are notoriously intractable to numerical computations and may require an analytic or hybrid approach (e.g. circularization). Ultimately, realizing the full scientific promise of TDEs requires a combination of observational and theoretical progress, so that we can extract the wealth of information these events carry on SMBH demographics, general relativity, and extreme accretion environments.

Appendices

Appendix A

The Parabolic Hill Equations

Consider the parabolic restricted three body problem, where the central mass $M_{\rm BH} \gg M_*$ and $M_* = m_1 + m_2$. Here the smaller bodies of masses m_1 and m_2 represent pieces of the star undergoing tidal disruption. The equations of motion for this system are derived in § 2 of SKR10; we present the derivation here for completeness. These differential equations do not make assumptions about the relative masses of m_1 and m_2.

If we center our coordinate system on the SMBH, and define position vectors $\vec{r}_1$ and $\vec{r}_2$ for the smaller particles, we can write the Newtonian equations of motion:

$$\ddot{\vec{r}}_1 = -\frac{GM_{\rm BH}}{r_1^3}\vec{r}_1 + \frac{Gm_2}{|\vec{r}_1 - \vec{r}_2|^3}(\vec{r}_2 - \vec{r}_1) \tag{A.1}$$

$$\ddot{\vec{r}}_2 = -\frac{GM_{\rm BH}}{r_2^3}\vec{r}_2 - \frac{Gm_1}{|\vec{r}_1 - \vec{r}_2|^3}(\vec{r}_2 - \vec{r}_1). \tag{A.2}$$

Defining $\vec{r} = \vec{r}_2 - \vec{r}_1$, we can then write

$$\ddot{\vec{r}} = -\frac{GM_{\rm BH}}{r_2^3}\vec{r}_2 + \frac{GM_{\rm BH}}{r_1^3}\vec{r}_1 - \frac{GM_*}{r^3}\vec{r}. \tag{A.3}$$

Next, we assume that both of the smaller bodies are roughly following a parabolic center of mass trajectory,

$$\vec{R} = \frac{2R_{\rm p}}{1+\cos f}(\cos f, \sin f, 0), \tag{A.4}$$

so we can linearize Eqs. A.1, A.2 as $\vec{r}_1 \approx \vec{R} + \delta\vec{r}_1$, $\vec{r}_2 \approx \vec{R} + \delta\vec{r}_2$ (assuming $\delta r_{1,2} \ll R$) to find

$$\ddot{\vec{r}} = \frac{GM_{\rm BH}}{R^3}\left(-\vec{r} + \frac{3\vec{r}\cdot\vec{R}}{R^2}\vec{R}\right) - \frac{GM_*}{r^3}\vec{r}. \tag{A.5}$$

N. C. Stone, *The Tidal Disruption of Stars by Supermassive Black Holes*,
Springer Theses, DOI 10.1007/978-3-319-12676-0

Here we have discarded all terms quadratic or higher in $\delta r_{1,2}$. Separating this equation of motion into components gives us three ordinary differential equations for the coordinate motion of each small body. Following the unit convention of § 3, where tildes denote distances normalized by R_* and times normalized by $\sqrt{R_*^3/(GM_*)}$, these parabolic Hill equations are

$$\ddot{\tilde{x}} = \beta^3 \frac{(1+\cos f)^3}{8}[-\tilde{x} + 3(\tilde{x}\cos f + \tilde{y}\sin f)\cos f] - \frac{\tilde{x}}{(\tilde{x}^2+\tilde{y}^2+\tilde{z}^2)^{3/2}} \tag{A.6}$$

$$\ddot{\tilde{y}} = \beta^3 \frac{(1+\cos f)^3}{8}[-\tilde{y} + 3(\tilde{x}\cos f + \tilde{y}\sin f)\sin f] - \frac{\tilde{y}}{(\tilde{x}^2+\tilde{y}^2+\tilde{z}^2)^{3/2}} \tag{A.7}$$

$$\ddot{\tilde{z}} = -\beta^3 \frac{(1+\cos f)^3}{8}\tilde{z} - \frac{\tilde{z}}{(\tilde{x}^2+\tilde{y}^2+\tilde{z}^2)^{3/2}}. \tag{A.8}$$

Dropping the last term (which gives the interaction between the masses m_1 and m_2) in each of these three equations allows the six "free solutions" to the parabolic Hill equations to be found analytically. These solutions are given in Eqs. 5.7 and 5.1, and represent the motion of a cloud of test particles in tidal free fall, if m_1 is taken to be a particle located at $\tilde{x} = \tilde{y} = \tilde{z} = 0$, and m_2 is a particle located anywhere else in the cloud.

Each of the six free solutions can be thought of as the perturbation to a single orbital element of the parabolic center of mass trajectory. Specifically, the in-plane solutions vary longitude of pericenter (A), time of pericenter (B), variation in the pericenter distance (C), and variation in eccentricity given a fixed pericenter (D). The out of plane solutions represent rotations around the apsidal line (E) and latus rectum (F).

Appendix B

Principal Axes of Free Solutions

Using the in-plane free solutions, we find that the initial phases of the principal axes at $f = f_c$ are given by

$$\cos\theta_{ex} = \pm\sqrt{\frac{1}{2} \pm \frac{j}{2\sqrt{j^2+4k^2}}} \tag{B.1}$$

where

$$
\begin{aligned}
j =& -\frac{16}{25}\beta + \frac{148}{25} + \frac{1312}{25\beta} - \frac{352}{5\beta^2} \\
&+ \sqrt{1-\beta^{-1}}\left(-\frac{16}{25}\beta + \frac{788}{25} - \frac{2208}{25\beta} + \frac{32}{5\beta^2}\right) \\
k =& \sqrt{\beta}\left(\frac{72}{25} - \frac{936}{25\beta} + \frac{1144}{25\beta^2} - \frac{16}{5\beta^3}\right) \\
&+ \sqrt{\beta-1}\left(\frac{72}{25} + \frac{216}{25\beta} - \frac{176}{5\beta^2}\right)
\end{aligned}
\tag{B.2}
$$

are exact expressions. Note that this gives us 8 possible solutions for θ_{ex}. While 4 are spurious, the other 4 of these are valid, with each minimum (maximum) in r_{H} possessing an equal minimum (maximum) 180° around the star's center of mass. In particular, for $\sin\theta_0 > 0$,

$$
\cos\theta_{\min} = (-1)^p\sqrt{\frac{1}{2} + (-1)^q\frac{j}{2\sqrt{j^2+4k^2}}} \tag{B.3}
$$

and

$$
\cos\theta_{\max} = (-1)^P\sqrt{\frac{1}{2} + (-1)^Q\frac{j}{2\sqrt{j^2+4k^2}}}. \tag{B.4}
$$

Here the behavior of $\theta_{\min}$ and $\theta_{\max}$ is piecewise with respect to β, due to zeros of j and k. We can describe this behavior for all $\beta > 1$ by setting

$$
\{p,q,P,Q\} = \begin{cases} \{1,2,2,1\}, \beta < 1.073 \\ \{2,1,1,2\}, 1.073 \le \beta < 4.944 \\ \{1,2,2,1\}, 4.944 \le \beta. \end{cases} \tag{B.5}
$$

To gain better intuition for the geometry of these principal axes, we can Taylor expand $r_{\mathrm{long}} = r_{\mathrm{H}}(\theta_{\max})$ and $r_{\mathrm{short}} = r_{\mathrm{H}}(\theta_{\min})$ in the limit of large β:

$$
r_{\mathrm{long}} = \frac{4}{5}\beta^{1/2} + \frac{22}{5}\beta^{-1/2} + O(\beta^{-3/2}) \tag{B.6}
$$

$$
r_{\mathrm{short}} = 2\beta^{-1/2} - \frac{23}{2}\beta^{-3/2} + O(\beta^{-5/2}). \tag{B.7}
$$

These results are poorly convergent for $\beta < 10$, but describe the exact solutions well above this threshold. We are now in a position to derive approximate formulae for the angles presented in Fig. 5.3. By expanding the numerator and denominator of $\tan\psi_{\mathrm{c}} = -y_{\mathrm{H}}(\theta_{\max})/x_{\mathrm{H}}(\theta_{\max})$ we find

$$
\tan\psi_{\mathrm{c}} \approx \frac{16\beta^{1/2} + 86\beta^{-1/2}}{8 + 185\beta^{-1}}. \tag{B.8}
$$

Using trigonometric identities and the Keplerian expression $\tan \Upsilon_c = \sqrt{\beta} + \sqrt{\beta - 1} \approx 2\beta^{1/2}$ (Υ_c is the angle between the $\hat{x}$ and a parabolic orbit's velocity vector at $f = f_c$), we find the misalignment angle

$$\tan \nu_c \approx \frac{284}{32\beta^{3/2} + 180\beta^{1/2} + 185\beta^{-1/2}}. \tag{B.9}$$

We have defined ν_c as the (positive) angle between the center of mass velocity and the long principal axis at $f = f_c$. It asymptotes to 0° as β goes to ∞.

References

1. Alexander, T., Morris, M.: Astrophys. J. **590**, L25 (2003)
2. Alexander, T., Natarajan, P.: Rapid growth of seed black holes in the early universe by supra-exponential accretion. Science **345**(6202), 1330–1333. (2014). (ArXiv e-prints)
3. Alexander, R.D., Armitage, P.J., Cuadra, J.: Binary formation and mass function variations in fragmenting disks with short cooling times. Mon. Not. R. Astron. Soc. **389**, 1655 (2008)
4. Amaro-Seoane, P., Gair, J.R., Freitag, M., Miller, M.C., Mandel, I., Cutler, C.J., Babak, S.: Intermediate and extreme mass-ratio inspirals—astrophysics, science applications and detection using LISA. Class. Quantum Gravity **24**(17), 113 (2007)
5. Amaro-Seoane, P., Miller, M.C., Kennedy, G.F.: Tidal disruptions of separated binaries in galactic nuclei. Mon. Not. R. Astron. Soc. **425**, 2401–2406 (2012a)
6. Amaro-Seoane, P., et al.: Intermediate and extreme mass-ratio inspirals—astrophysics, science applications and detection using LISA. Class. Quantum Gravity **29**(17), 124016 (2012b)
7. Amaro-Seoane, P., Sopuerta, C.F., Freitag, M.D.: The role of the supermassive black hole spin in the estimation of the EMRI event rate. Mon. Not. R. Astron. Soc. **429**(4), 3155–3165 (2013)
8. Arcavi, I., et al.: ArXiv e-prints (2014)
9. Arun, K.G., et al.: Massive black-hole binary inspirals: Results from the LISA parameter estimation taskforce. Class. Quantum Gravity **26**, 094027 (2009)
10. Ayal, S., Livio, M., Piran, T.: Astrophys. J. **545**, 772 (2000)
11. Bade, N., Komossa, S., Dahlem, M.: Detection of an extremely soft X-ray outburst in the HII-like nucleus of NGC 5905. Astron. Astrophys. **309**, L35 (1996)
12. Baganoff, F.K., et al.: Astrophys. J. **591**, 891 (2003)
13. Bahcall, J.N., Wolf, R.A.: Star distribution around a massive black hole in a globular cluster. Astrophys. J. **209**, 214 (1976)
14. Baker, J.G., Centrella, J., Choi, D.-I., Koppitz, M., van Meter, J.: Phys. Rev. Lett. **96**, 111102 (2006)
15. Bandara, K., Crampton, D., Simard, L.: Astrophys. J. **704**, 1135 (2009)
16. Bardeen, J.M., Petterson, J.A.: The Lense-thirring effect and accretion disks around Kerr black holes. Astrophys. J. **195**, L65–L67 (1975)
17. Bardeen, J.M., Press, W.H., Teukolsky, S.A.: Rotating black holes: Locally nonrotating frames, energy extraction, and scalar synchrotron radiation. Astrophys. J. **178**, 347–370 (1972)
18. Bartko, H., et al.: An extremely top-heavy initial mass function in the galactic center stellar disks. Astrophys. J. **708**, 834–840 (2010)
19. Beckmann, V., Shrader, C.R.: Active Galactic Nuclei. Wiley, Berlin (2012)
20. Begelman, M.C., Blandford, R.D., Rees, M.J.: Massive black hole binaries in active galactic nuclei. Nature **287**, 307 (1980)
21. Begelman, M.C., Volonteri, M., Rees, M.J.: Mon. Not. R. Astron. Soc. **370**, 289 (2006)

N. C. Stone, *The Tidal Disruption of Stars by Supermassive Black Holes,*
Springer Theses, DOI 10.1007/978-3-319-12676-0

22. Begelman, M.C., Rossi, E.M., Armitage, P.J.: Mon. Not. R. Astron. Soc. **387**, 1649 (2008)
23. Beloborodov, A.M., Illarionov, A.F., Ivanov, P.B., Polnarev, A.G.: Mon. Not. R. Astron. Soc. **259**, 209 (1992)
24. Bentz, M.C., Peterson, B.M., Pogge, R.W., Vestergaard, M.: Astrophys. J. **694**, L166 (2009)
25. Berti, E., Volonteri, M.: Astrophys. J. **684**, 822 (2008)
26. Bicknell, G.V., Gingold, R.A.: Astrophys. J. **273**, 749 (1983)
27. Biermann, P.L., Strittmatter, P.A.: Astrophys. J. **322**, 643 (1987)
28. Binney, J., Tremaine, S.: Galactic Dynamics, 2nd edn. Princeton University Press, Princeton (2008)
29. Blanchet, L.: Gravitational radiation from post-newtonian sources and inspiralling compact binaries. Living Rev. Relativit. **9**, 4 (2006)
30. Blecha, L., Loeb, A.: Mon. Not. R. Astron. Soc. **390**, 1311 (2008)
31. Blecha, L., Cox, T.J., Loeb, A., Hernquist, L.: Mon. Not. R. Astron. Soc. **412**, 2154 (2011)
32. Bloom, J.S., et al.: Science **333**, 203 (2011)
33. Bode, T., Haas, R., Bogdanović, T., Laguna, P., Shoemaker, D.: Astrophys. J. **715**, 1117 (2010)
34. Bogdanović, T., Eracleous, M., Mahadevan, S., Sigurdsson, S., Laguna, P.: Astron. J. **610**, 707 (2004)
35. Bogdanović, T., Reynolds, C.S., Miller, M.C.: Astrophys. J. **661**, L147 (2007)
36. Bonning, E.W., Shields, G.A., Salviander, S.: Astrophys. J. **666**, L13 (2007)
37. Bogdanović, T., Eracleous, M., Sigurdsson, S.: Astrophys. J. **697**, 288 (2009)
38. Bower, G.C., Metzger, B.D., Cenko, S.B., Silverman, J.M., Bloom, J.S.: Astrophys. J. **763**, 84 (2013)
39. Brandt, W.N., Pounds, K.A., Fink, H.: Mon. Not. R. Astron. Soc. **273**, L47 (1995)
40. Brassart, M., Luminet, J.-P.: Shock waves in tidally compressed stars by massive black holes. Astron. Astrophys. **481**, 259 (2008)
41. Brassart, M., Luminet, J.-P.: Astron. Astrophys. **511**, A80 (2010)
42. Brem, P., Amaro-Seoane, P., Sopuerta, C.F.: ArXiv e-prints (2012)
43. Brenneman, L.W., Reynolds, C.S.: Astrophys. J. **652**, 1028 (2006)
44. Broderick, A.E., Loeb, A.: Mon. Not. R. Astron. Soc. **363**, 353 (2005)
45. Broderick, A.E., Loeb, A.: Astrophys. J. **697**, 1164 (2009a)
46. Broderick, A.E., Loeb, A., Narayan, R.: Astrophys. J. **701**, 1357 (2009b)
47. Bromley, B.C., Kenyon, S.J., Geller, M.J., Brown, W.R.: Astrophys. J. **749**, L42 (2012)
48. Bromm, V., Loeb, A.: Astrophys. J. **596**, 34 (2003)
49. Burkert, A., Tremaine, S.: Astrophys. J. **720**, 516 (2010)
50. Burrows, D.N., et al.: Nature **476**, 421 (2011)
51. Callegari, S., Mayer, L., Kazantzidis, S., Colpi, M., Governato, F., Quinn, T., Wadsley, J.: Astrophys. J. **696**, L89 (2009)
52. Campanelli, M., Lousto, C.O., Marronetti, P., Zlochower, Y.: Phys. Rev. Lett. **96**, 111101 (2006)
53. Campanelli, M., Lousto, C., Zlochower, Y., Merritt, D.: Astrophys. J. **659**, L5 (2007)
54. Cannizzo, J.K., Lee, H.M., Goodman, J.: Astrophys. J. **351**, 38 (1990)
55. Cannizzo, J.K., Troja, E., Lodato, G.: Astrophys. J. **742**, 32 (2011)
56. Carter, B., Luminet, J.P.: Nature **296**, 211 (1982)
57. Carter, B., Luminet, J.-P.: Astron. Astrophys. **121**, 97 (1983)
58. Carter, B., Luminet, J.P.: Mon. Not. R. Astron. Soc. **212**, 23 (1985)
59. Cenko, S.B., et al.: Mon. Not. R. Astron. Soc. **420**, 2684 (2012a)
60. Cenko, S.B., et al.: Astron. Astrophys. **753**, 77 (2012b)
61. Chen, X., Madau, P., Sesana, A., Liu, F.K.: Astrophys. J. **697**, L149 (2009)
62. Chen, X., Sesana, A., Madau, P., Liu, F.K.: Astrophys. J. **729**, 13 (2011)
63. Chornock, R., et al.: Astrophys. J. **780**, 44 (2014)
64. Civano, F., et al.: Astrophys. J. **717**, 209 (2010)
65. Cohn, H., Kulsrud, R.M.: Astrophys. J. **226**, 1087 (1978)

66. Colpi, M., Dotti, M.: ArXiv e-prints (2009)
67. Comerford, J.M., et al.: Astrophys. J. **698**, 956 (2009)
68. Dai, L., Blandford, R.D.: ArXiv e-prints (2011)
69. Davies, M.B., Miller, M.C., Bellovary, J.M.: Astrophys. J. **740**, L42 (2011)
70. De Colle, F., Guillochon, J., Naiman, J., Ramirez-Ruiz, E.: Astrophys. J. **760**, 103 (2012)
71. Devecchi, B., Volonteri, M.: Astrophys. J. **694**, 302 (2009)
72. Devecchi, B., Volonteri, M., Colpi, M., Haardt, F.: Mon. Not. R. Astron. Soc. **409**, 1057 (2010)
73. Devecchi, B., Volonteri, M., Rossi, E.M., Colpi, M., Portegies Zwart, S.: Mon. Not. R. Astron. Soc. **421**, 1465 (2012)
74. Dexter, J., Fragile, P.C.: Astrophys. J. 730, 36 (2011)
75. Di Matteo, T., Springel, V., Hernquist, L.: Nature **433**, 604 (2005)
76. Diener, P., Frolov, V.P., Khokhlov, A.M., Novikov, I.D., Pethick, C.J.: Astrophys. J. **479**, 164 (1997)
77. Doeleman, S.S., Fish, V.L., Broderick, A.E., Loeb, A., Rogers, A.E.E.: Astrophys. J. **695**, 59 (2009)
78. Donley, J.L., Brandt, W.N., Eracleous, M., Boller, T.: Astrophys. J. **124**, 1308 (2002)
79. Dotti, M., Volonteri, M., Perego, A., Colpi, M., Ruszkowski, M., Haardt, F.: Mon. Not. R. Astron. Soc. **402**, 682 (2010)
80. Drasco, S., Hughes, S.A.: Phys. Rev. D **69**, 044015 (2004)
81. Escala, A., Larson, R.B., Coppi, P.S., Mardones, D.: Astrophys. J. **607**, 765 (2004)
82. Escala, A., Larson, R.B., Coppi, P.S., Mardones, D.: Astrophys. J. **630**, 152 (2005)
83. Esquej, P., et al.: Astron. Astrophys. **489**, 543 (2008)
84. Evans, C.R., Kochanek, C.S.: Astron. J. **346**, L13 (1989)
85. Faber, S.M., et al.: Astron. J. **114**, 1771 (1997)
86. Fan, X., et al.: Astron. J. **125**, 1649 (2003)
87. Farrar, G.R., Gruzinov, A.: Astrophys. J. **693**, 329 (2009)
88. Ferrarese, L.: Astrophys. J. **578**, 90 (2002)
89. Ferrarese, L., Ford, H.: Space Sci. Rev. **116**, 523 (2005)
90. Ferrarese, L., Merritt, D.: Astrophys. J. **539**, L9 (2000)
91. Fragile, P.C.: Proceedings of Science. Microquasars and Beyond, Izmir (2008)
92. Fragile, P.C., Blaes, O.M., Anninos, P., Salmonson, J.D.: Astrophys. J. **668**, 417 (2007)
93. Franceschini, A., Vercellone, S., Fabian, A.C.: Mon. Not. R. Astron. Soc. **297**, 817 (1998)
94. Frank, J., Rees, M.J.: Mon. Not. R. Astron. Soc. **176**, 633 (1976)
95. Frolov, V.P., Khokhlov, A.M., Novikov, I.D., Pethick, C.J.: Astrophys. J. **432**, 680 (1994)
96. Fujita, R., Hikida, W.: Analytical solutions of bound timelike geodesic orbits in Kerr spacetime. Class. Quantum Gravity **26**, 135002 (2009)
97. Gebhardt, K., et al.: Astron. J. **119**, 1157 (2000)
98. Gezari, S., Halpern, J.P., Komossa, S., Grupe, D., Leighly, K.M.: Astrophys. J. **592**, 42 (2003)
99. Gezari, S., et al.: Astrophys. J. **653**, L25 (2006)
100. Gezari, S., et al.: Astrophys. J. **676**, 944 (2008)
101. Gezari, S., et al.: Astrophys. J. **698**, 1367 (2009)
102. Gezari, S., et al.: Nature **485**, 217 (2012)
103. Ghez, A.M., Salim, S., Hornstein, S.D., Tanner, A., Lu, J.R., Morris, M., Becklin, E.E., Duchêne, G.: Astrophys. J. **620**, 744 (2005)
104. Ghez, A.M., et al.: Astrophys. J. **689**, 1044 (2008)
105. Giannios, D., Metzger, B.D.: Mon. Not. R. Astron. Soc. **416**, 2102 (2011)
106. Gillessen, S., Eisenhauer, F., Trippe, S., Alexander, T., Genzel, R., Martins, F., Ott, T.: Astrophys. J. **692**, 1075 (2009)
107. Goodman, J., Tan, J.C.: Astrophys. J. **608**, 108 (2004)
108. Graham, A.W., Onken, C.A., Athanassoula, E., Combes, F.: Mon. Not. R. Astron. Soc. **412**, 2211 (2011)
109. Greene, J.E., Ho, L.C.: Astrophys. J. **667**, 131 (2007)

110. Greenhill, L.J., Moran, J.M., Herrnstein, J.R.: Astrophys. J. **481**, L23 (1997)
111. Grupe, D., Beuermann, K., Mannheim, K., Bade, N., Thomas, H.-C., de Martino, D., Schwope, A.: Astron. Astrophys. **299**, L5 (1995)
112. Gualandris, A., Merritt, D.: Astrophys. J. **678**, 780 (2008)
113. Guillochon, J., Ramirez-Ruiz, E.: Astrophys. J. **767**, 25 (2013)
114. Guillochon, J., Ramirez-Ruiz, E., Rosswog, S., Kasen, D.: Astrophys. J. **705**, 844 (2009)
115. Guillochon, J., Manukian, H., Ramirez-Ruiz, E.: Astrophys. J. **783**, 23 (2014)
116. Haas, R., Shcherbakov, R.V., Bode, T., Laguna, P.: Astrophys. J. **749**, 117 (2012)
117. Halpern, J.P., Gezari, S., Komossa, S.: Astrophys. J. **604**, 572 (2004)
118. Hayasaki, K., Stone, N., Loeb, A.: Mon. Not. R. Astron. Soc. **434**, 909 (2013)
119. Hazard, C., Mackey, M.B., Shimmins, A.J.: Nature **197**, 1037 (1963)
120. Herrnstein, J.R., et al.: Nature **400**, 539 (1999)
121. Hills, J.G.: Nature **254**, 295 (1975)
122. Hills, J.G.: Nature **331**, 687 (1988)
123. Hoffman, L., Loeb, A.: Mon. Not. R. Astron. Soc. **377**, 957 (2007)
124. Holoien, T.W.-S., et al.: ArXiv e-prints (2014)
125. Holz, D.E., Hughes, S.A.: Astrophys. J. **629**, 15 (2005)
126. Hopkins, P.F., Hernquist, L., Cox, T.J., Di Matteo, T., Robertson, B., Springel, V.: A Unified, Merger-driven Model of the Origin of Starbursts, Quasars, the Cosmic X-Ray Background, Supermassive Black Holes, and Galaxy Spheroids. Astrophys. J. Suppl. Ser. **163**, 1 (2006)
127. Hopkins, P.F., Richards, G.T., Hernquist, L.: Astrophys. J. **654**, 731 (2007)
128. Hopkins, P.F., et al.: Astrophys. J. **715**, 202 (2010)
129. Hopman, C., Alexander, T.: Astrophys. J. **645**, 1152 (2006)
130. Hoyle, F., Fowler, W.A.: Mon. Not. R. Astron. Soc. **125**, 169 (1963)
131. Hunter, C., Qian, E.: Mon. Not. R. Astron. Soc. **262**, 401 (1993)
132. Ivanov, P.B., Novikov, I.D.: Astrophys. J. **549**, 467 (2001)
133. Ivanov, P.B., Chernyakova, M.A.: Astron. Astrophys. **448**, 843 (2006)
134. Ivanov, P.B., Chernyakova, M.A., Novikov, I.D.: Mon. Not. R. Astron. Soc. **338**, 147 (2003)
135. Ivanov, P.B., Polnarev, A.G., Saha, P.: Mon. Not. R. Astron. Soc. **358**, 1361 (2005)
136. Jahnke, K., Macciò, A.V.: Astrophys. J. **734**, 92 (2011)
137. Jenet, F.A., Lommen, A., Larson, S.L., Wen, L.: Astrophys. J. **606**, 799 (2004)
138. Jennrich, O.: LISA technology and instrumentation. Class. Quantum Gravity **26**(15), 153001 (2009)
139. Johannsen, T., Psaltis, D.: Astrophys. J. **716**, 187 (2010)
140. Johannsen, T., Psaltis, D.: ArXiv e-prints (2012)
141. Kasen, D., Ramirez-Ruiz, E.: Astrophys. J. **714**, 155 (2010)
142. Kaspi, S., Smith, P.S., Netzer, H., Maoz, D., Jannuzi, B.T., Giveon, U.: Astrophys. J. **533**, 631 (2000)
143. Kesden, M.: Phys. Rev. D. **86**, 064026 (2012a)
144. Kesden, M.: Phys. Rev. D. **85**, 024037 (2012b)
145. Kesden, M., Sperhake, U., Berti, E.: Astrophys. J. **715**, 1006 (2010)
146. Khan, F.M., Holley-Bockelmann, K., Berczik, P., Just, A.: Astrophys. J. **773**, 100 (2013)
147. Khokhlov, A., Novikov, I.D., Pethick, C.J.: Astrophys. J. **418**, 181 (1993a)
148. Khokhlov, A., Novikov, I.D., Pethick, C.J.: Astrophys. J. **418**, 163 (1993b)
149. King, A.R., Lubow, S.H., Ogilvie, G.I., Pringle, J.E.: Mon. Not. R. Astron. Soc. **363**, 49 (2005)
150. Kippenhahn, R., Weigert, A.: Stellar Structure and Evolution. Springer (1994)
151. Klein, A., Jetzer, P., Sereno, M.: Phys. Rev. D **80**, 064027 (2009)
152. Kobayashi, S., Laguna, P., Phinney, E.S., Mészáros, P.: Astrophys. J. **615**, 855 (2004)
153. Kochanek, C.S.: Astrophys. J. **422**, 508 (1994)
154. Kocsis, B., Loeb, A.: Phys. Rev. Lett. **101**, 041101 (2008)
155. Komossa, S., Bade, N.: Astron. Astrophys. **343**, 775 (1999)
156. Komossa, S., Greiner, J.: Astron. Astrophys. **349**, L45 (1999)

157. Komossa, S., Halpern, J., Schartel, N., Hasinger, G., Santos-Lleo, M., Predehl, P.: Astrophys. J. **603**, L17 (2004)
158. Komossa, S., Merritt, D.: Astrophys. J. **683**, L21 (2008)
159. Komossa, S., Zhou, H., Lu, H.: Astrophys. J. **678**, L81 (2008)
160. Komossa, S., et al.: Astrophys. J. **701**, 105 (2009)
161. Kormendy, J., Bender, R.: Nature **469**, 377 (2011)
162. Kormendy, J., Richstone, D.: Annu Rev Astron Astrophys **33**, 581 (1995)
163. Kormendy, J., Fisher, D.B., Cornell, M.E., Bender, R.: Astrophys. J. Suppl. Ser. **182**, 216 (2009)
164. Kouwenhoven, M.B.N., Brown, A.G.A., Portegies Zwart, S.F., Kaper, L.: Astron. Astrophys. **474**, 77 (2007)
165. Krolik, J.H.: Active galactic nuclei: From the central black hole to the galactic environment (1999)
166. Krolik, J.H., Piran, T.: Astrophys. J. **743**, 134 (2011)
167. Kumar, S., Pringle, J.E.: Mon. Not. R. Astron. Soc. **213**, 435 (1985)
168. Laguna, P., Miller, W.A., Zurek, W.H., Davies, M.B.: Astrophys. J. **410**, L83 (1993)
169. Lauer, T.R., et al.: Astron. J. **110**, 2622 (1995)
170. Lauer, T.R., et al.: Astron. J. **129**, 2138 (2005)
171. Lauer, T.R., et al.: Astrophys. J. **664**, 226 (2007)
172. Lei, W.-H., Zhang, B.: Astrophys. J. **740**, L27 (2011)
173. Lei, W.-H., Zhang, B., Gao, H.: Astrophys. J. **762**, 98 (2013)
174. Levan, A.J., et al.: Science **333**, 199 (2011)
175. Li, G., Loeb, A.: Mon. Not. R. Astron. Soc. **429**, 3040 (2013)
176. Li, S., Liu, F.K., Berczik, P., Chen, X., Spurzem, R.: Astrophys. J. **748**, 65 (2012)
177. Lidskii, V.V., Ozernoi, L.M.: Sov. Astron. Lett. **5**, 16 (1979)
178. Lightman, A.P., Shapiro, S.L.: Astrophys. J. **211**, 244 (1977)
179. Lippai, Z., Frei, Z., Haiman, Z.: Astrophys. J. **676**, L5 (2008)
180. Liu, F.K., Chen, X.: Astrophys. J. **767**, 18 (2013)
181. Liu, F.K., Li, S., Komossa, S.: Astrophys. J. **786**, 103 (2014)
182. Lodato, G., Pringle, J.E.: Mon. Not. R. Astron. Soc. **368**, 1196 (2006)
183. Lodato, G., King, A.R., Pringle, J.E.: Mon. Not. R. Astron. Soc. **392**, 332 (2009)
184. Lodato, G., Rossi, E.M.: Mon. Not. R. Astron. Soc. **410**, 359 (2011)
185. Loeb, A.: Phys. Rev. Lett. **99**, 041103 (2007)
186. Loeb, A., Rasio, F.A.: Astrophys. J. **432**, 52 (1994)
187. Loeb, A., Ulmer, A.: Astrophys. J. **489**, 573 (1997)
188. Lousto, C.O., Campanelli, M., Zlochower, Y., Nakano, H.: Class. Quantum Gravity **27**, 114006 (2010a)
189. Lousto, C.O., Nakano, H., Zlochower, Y., Campanelli, M.: Phys. Rev. D **81**, 084023 (2010b)
190. Lousto, C.O., Zlochower, Y.: Phys. Rev. Lett. **107**, 231102 (2011)
191. Lousto, C.O., Zlochower, Y.: ArXiv e-prints (2012)
192. LSST Science Collaboration et al.: ArXiv e-prints (2009)
193. Lucy, L.B.: Astrophys. J. **82**, 1013 (1977)
194. Luminet, J.-P., Carter, B.: Astrophys. J. Suppl. Ser. **61**, 219 (1986)
195. Luminet, J.-P., Marck, J.-A.: Mon. Not. R. Astron. Soc. **212**, 57 (1985)
196. Luminet, J.-P., Pichon, B.: Astron. Astrophys. **209**, 85 (1989)
197. Lynden-Bell, D.: Nature **223**, 690 (1969)
198. Madau, P., Quataert, E.: Astrophys. J. **606**, L17 (2004)
199. Madau, P., Rees, M.J.: Astrophys. J. **551**, L27 (2001)
200. Madigan, A.-M., Hopman, C., Levin, Y.: Astrophys. J. **738**, 99 (2011)
201. Magorrian, J., Tremaine, S.: Mon. Not. R. Astron. Soc. **309**, 447 (1999)
202. Maksym, W.P., Ulmer, M.P., Roth, K.C., Irwin, J.A., Dupke, R., Ho, L.C., Keel, W.C., Adami, C.: Mon. Not. R. Astron. Soc. **444**, 866 (2014)
203. Marck, J.-A.: Phys. Lett. A. **97**, 140 (1983a)

204. Marck, J.-A.: R. Soc. Lond. Proc. Ser. A, **385**, 431 (1983b)
205. Marconi, A., Hunt, L.K.: Astrophys. J. **589**, L21 (2003)
206. Mayer, L., Kazantzidis, S., Madau, P., Colpi, M., Quinn, T., Wadsley, J.: Science. **316**, 1874 (2007)
207. Mayer, L., Kazantzidis, S., Escala, A., Callegari, S.: Nature. **466**, 1082 (2010)
208. McKinney, J.C., Tchekhovskoy, A., Blandford, R.D.: Science **339**, 49 (2013)
209. Merritt, D.: Astrophys. J. **648**, 976 (2006)
210. Merritt, D., Alexander, T., Mikkola, S., Will, C.M.: Phys. Rev. D. **81**, 062002 (2010)
211. Merritt, D., Alexander, T., Mikkola, S., Will, C.M.: Phys. Rev. D. **84**, 044024 (2011)
212. Merritt, D., Mikkola, S., Szell, A.: Astrophys. J. **671**, 53 (2007)
213. Merritt, D., Milosavljević, M.: 2005, Living Rev. Relativ. **8**, 8 (2005)
214. Merritt, D., Poon, M.Y.: Astrophys. J. **606**, 788 (2004)
215. Merritt, D., Schnittman, J.D., Komossa, S.: Astrophys. J. **699**, 1690 (2009)
216. Merritt, D., Wang, J.: Astrophys. J. **621**, L101 (2005)
217. Metzger, B.D., Giannios, D., Mimica, P.: Mon. Not. R. Astron. Soc. **420**, 3528 (2012)
218. Meyer, L., et al.: Science **338**, 84 (2012)
219. Mihos, J.C., Hernquist, L.: Astrophys. J. **464**, 641 (1996)
220. Milosavljević, M., Merritt, D.: Astrophys. J. **563**, 34 (2001)
221. Milosavljević, M., Phinney, E.S.: Astrophys. J. **622**, L93 (2005)
222. Montesinos Armijo, M., de Freitas Pacheco, J.A.: Astrophys. J. **736**, 126 (2011)
223. Mortlock, D. J., et al.: Nature **474**, 616 (2011)
224. Navarro, J.F., Frenk, C.S., White, S.D.M.: Astrophys. J. **490**, 493 (1997)
225. Nolthenius, R.A., Katz, J.I.: Astrophys. J. **263**, 377 (1982)
226. Novikov, I.D., Pethick, C.J., Polnarev, A.G.: Mon. Not. R. Astron. Soc. **255**, 276 (1992)
227. Oesch, P.A., et al.: Astrophys. J. **709**, L21 (2010)
228. Ohsuga, K., Mineshige, S.: Astrophys. J. **736**, 2 (2011)
229. Ohsuga, K., Mori, M., Nakamoto, T., Mineshige, S.: Astrophys. J. **628**, 368 (2005)
230. Okazaki, A.T., Bate, M.R., Ogilvie, G.I., Pringle, J.E.: Mon. Not. R. Astron. Soc. **337**, 967 (2002)
231. O'Leary, R.M., Loeb, A.: Mon. Not. R. Astron. Soc. **395**, 781 (2009)
232. O'Leary, R.M., Loeb, A.: Mon. Not. R. Astron. Soc. **421**, 2737 (2012)
233. Öpik, E.: Publ. Tartu Astrofizica Observatory **25**, 1 (1924)
234. Ostriker, E.C.: Astrophys. J. **513**, 252 (1999)
235. Paczyński, B., Wiita, P.J.: Astron. Astrophys. **88**, 23 (1980)
236. Pani, P., Cardoso, V., Gualtieri, L., Berti, E., Ishibashi, A.: Phys. Rev. Lett. **109**, 131102 (2012)
237. Papaloizou, J.C.B., Pringle, J.E.: Mon. Not. R. Astron. Soc. **202**, 1181 (1983)
238. Peng, C.Y.: Astrophys. J. **671**, 1098 (2007)
239. Perets, H.B., Hopman, C., Alexander, T. 2007, Astrophys. J. **656**, 709 (2007)
240. Pfahl, E., Loeb, A.: Astrophys. J. **615**, 253 (2004)
241. Phinney, E.S.: In: Morris, M. (ed.) IAU Symposium, Vol. 136, The Center of the Galaxy, p. 543 (1989)
242. Pierre Auger Collaboration et al. Astropart. Phys. **29**, 188 (2008)
243. Poon, M.Y., Merritt, D.: Astrophys. J. **606**, 774 (2004)
244. Press, W.H., Teukolsky, S.A.: Astrophys. J. **213**, 183 (1977)
245. Press, W.H., Teukolsky, S.A., Vetterling, W.T., Flannery, B.P. Numerical Recipes in C++ : The Art of Scientific Computing. Cambridge University Press, Cambridge (2002)
246. Pretorius, F.: Phys. Rev. Lett. **95**, 121101 (2005)
247. Quataert, E., Kasen, D.: Mon. Not. R. Astron. Soc. **419**, L1 (2012)
248. Ramirez-Ruiz, E., Rosswog, S.: Astrophys. J. **697**, L77 (2009)
249. Rauch, K.P., Tremaine, S. New Astron. **1**, 149 (1996)
250. Rauch, K.P., Ingalls, B. Mon. Not. R. Astron. Soc. **299**, 1231 (1998)
251. Rees, M.J.: Nature **333**, 523 (1988)

252. Reynolds, C.S.: ArXiv e-prints (2013.)
253. Reynolds, C.S., Young, A.J., Begelman, M.C., Fabian, A.C.: Astrophys. J. **514**, 164 (1999)
254. Rosswog, S., Ramirez-Ruiz, E., Hix, W.R.: Astrophys. J. **695**, 404 (2009)
255. Ryan, F. D. 1995, Phys. Rev. D, 52, 5707
256. Sadowski, A., Narayan, R., Tchekhovskoy, A., Abarca, D., Zhu, Y., McKinney, J.C.: ArXiv e-prints (2014)
257. Salpeter, E.E.: Astrophys. J. **140**, 796 (1964)
258. Sari, R., Kobayashi, S., Rossi, E.M.: Astrophys. J. **708**, 605, (2010)
259. Saxton, C.J., Soria, R., Wu, K., Kuin, N.P.M.: Mon. Not. R. Astron. Soc. **422**, 1625 (2012a,)
260. Saxton, R.D., Read, A.M., Esquej, P., Komossa, S., Dougherty, S., Rodriguez-Pascual, P., Barrado, D.: Astron. Astrophys. **541**, A106 (2012b)
261. Sazhin, M.V.: Soviet Ast. **22**, 36 (1978)
262. Schmidt, M.: Nature **197**, 1040 (1963)
263. Schnittman, J.D.: Astrophys. J. **667**, L133 (2007)
264. Schnittman, J.D.: Astrophys. J. **724**, 39 (2010)
265. Schnittman, J.D.: Class. Quantum Gravity **28**, 094021 (2011)
266. Schnittman, J.D., Buonanno, A.: Astrophys. J. **662**, L63 (2007)
267. Schnittman, J.D., Krolik, J.H.: Astrophys. J. **684**, 835 (2008)
268. Schödel, R., et al.: Nature **419**, 694 (2002)
269. Schutz, B.F.: Nature **323**, 310 (1986)
270. Schutz, B.F.: Class. Quantum Gravity **26**, 094020 (2009)
271. Schwarzschild, M.: Astrophys. J. **232**, 236 (1979)
272. Sesana, A.: Advances in Astronomy (2012)
273. Sesana, A., Vecchio, A.: Phys. Rev. D **81**, 104008 (2010)
274. Sesana, A., Vecchio, A., Volonteri, M.: Mon. Not. R. Astron. Soc. **394**, 2255 (2009)
275. Seto, N., Muto, T.: Phys. Rev. D **81**, 103004 (2010)
276. Seto, N., Muto, T.: Mon. Not. R. Astron. Soc. **415**, 3824 (2011)
277. Shakura, N.I., Sunyaev, R.A.: Astron. Astrophys. **24**, 337 (1973)
278. Shankar, F., Salucci, P., Granato, G.L., De Zotti, G., Danese, L.: Mon. Not. R. Astron. Soc. **354**, 1020 (2004)
279. Shen, R.-F., Matzner, C.D.: Astrophys. J. **784**, 87 (2014)
280. Shields, G.A., Bonning, E.W.: Astrophys. J. **682**, 758 (2008)
281. Shields, G.A., et al.: Astrophys. J. **707**, 936 (2009)
282. Shlosman, I., Begelman, M.C.: Nature **329**, 810 (1987)
283. Sijacki, D., Springel, V., Haehnelt, M. G.: Mon. Not. R. Astron. Soc. **414**, 3656 (2011)
284. Silk, J., Rees, M.J.: Astron. Astrophys. **331**, L1 (1998)
285. Soltan, A.: Mon. Not. R. Astron. Soc. **200**, 115 (1982)
286. Sopuerta, C.F.: GW Notes, Vol. 4, p. 3–47, 4, 3 (2010)
287. Spergel, D.N.: et al.: Astrophys. J. Suppl. Ser. **170**, 377 (2007)
288. Spitzer, L.: Dynamical evolution of globular clusters (1987)
289. Stacy, A., Greif, T.H., Bromm, V.: Mon. Not. R. Astron. Soc. **403**, 45 (2010)
290. Stewart, G.R., Ida, S.: Icarus, **143**, 28 (2000)
291. Stone, N., Loeb, A.: Mon. Not. R. Astron. Soc. **412**, 75 (2011)
292. Stone, N., Loeb, A.: Phys. Rev. Lett. **108**, 061302 (2012a)
293. Stone, N., Loeb, A.: Mon. Not. R. Astron. Soc. **422**, 1933 (2012b)
294. Stone, N., Loeb, A., Berger, E.: Phys. Rev. D **87**, 084053 (2013a)
295. Stone, N., Sari, R., Loeb, A.: Mon. Not. R. Astron. Soc. **435**, 1809 (2013b)
296. Strubbe, L.E., Quataert, E.: Mon. Not. R. Astron. Soc. **400**, 2070 (2009)
297. Strubbe, L.E., Quataert, E.: Mon. Not. R. Astron. Soc. **415**, 168 (2011)
298. Syer, D., Clarke, C.J., Rees, M.J.: Mon. Not. R. Astron. Soc. **250**, 505 (1991)
299. Syer, D., Ulmer, A.: Mon. Not. R. Astron. Soc. **306**, 35 (1999)

300. Takahashi, T. et al.: in Society of Photo-Optical Instrumentation Engineers (SPIE) Conference Series, Vol. 7732, Society of Photo-Optical Instrumentation Engineers (SPIE) Conference Series (2010)
301. Tchekhovskoy, A., Metzger, B.D., Giannios, D., Kelley, L.Z.: Mon. Not. R. Astron. Soc. **437**, 2744 (2014)
302. Thompson, T.A., Quataert, E., Murray, N.: Astrophys. J. **630**, 167 (2005)
303. Toomre, A.: Astrophys. J. **139**, 1217 (1964)
304. Tremaine, S., et al.: Astrophys. J. **574**, 740 (2002)
305. Ulmer, A.: Astrophys. J. **514**, 180 (1999)
306. Ulmer, A., Paczynski, B., Goodman, J.: Astron. Astrophys. **333**, 379 (1998)
307. van Velzen, S., Farrar, G.R.: Astrophys. J. **792**, 53 (2014)
308. van Velzen, S., Frail, D.A., Körding, E., Falcke, H.: Astron. Astrophys. **552**, A5 (2013)
309. van Velzen, S., Körding, E., Falcke, H.: Mon. Not. R. Astron. Soc. **417**, L51 (2011a)
310. van Velzen, S., et al.: Astrophys. J. **741**, 73 (2011b)
311. Vasiliev, E., Merritt, D.: ArXiv e-prints. (2013)
312. Vereshchagin, S., Tutukov, A., Iungelson, L., Kraicheva, Z., Popova, E.: Ap&SS, **142**, 245 (1988)
313. Volonteri, M., Haardt, F., Madau, P.: Astrophys. J. **582**, 559 (2003)
314. Volonteri, M., Rees, M.J.: Astrophys. J. **650**, 669 (2006)
315. Volonteri, M., Madau, P., Quataert, E., Rees, M.J.: Astrophys. J. **620**, 69 (2005)
316. Volonteri, M., Lodato, G., Natarajan, P.: Mon. Not. R. Astron. Soc. **383**, 1079 (2008)
317. Wald, R.M.: General relativity (1984)
318. Wandel, A., Peterson, B.M., Malkan, M.A.: Astrophys. J. **526**, 579 (1999)
319. Wang, J., Merritt, D. 2004, Astrophys. J. **600**, 149
320. Wang, J.-Z., Lei, W.-H., Wang, D.-X., Zou, Y.-C., Zhang, B., Gao, H., Huang, C.-Y.: Astrophys. J. **788**, 32 2014
321. Wang, T.-G., Zhou, H.-Y., Wang, L.-F., Lu, H.-L., Xu, D.: Astrophys. J. **740**, 85 (2011)
322. Wang, T.-G., Zhou, H.-Y., Komossa, S., Wang, H.-Y., Yuan, W., Yang, C.: Astrophys. J. **749**, 115 (2012)
323. Wegg, C.: Astrophys. J. **749**, 183 (2012)
324. Wegg, C., Bode, J.: Astrophys. J. **738**, L8 (2011)
325. Wetzel, A.R., White, M.: Mon. Not. R. Astron. Soc. **403**, 1072 (2010)
326. Wheeler, J.: in Study Week on Nuclei of Galaxies, ed. D. J. K. O'Connell, 539, (1971)
327. Wyithe, J.S.B., Loeb, A.: Astrophys. J. **595**, 614 (2003)
328. Yu, Q., Tremaine, S.: Astrophys. J. **121**, 1736 (2001)
329. Yu, Q., Tremaine, S.: Mon. Not. R. Astron. Soc. **335**, 965 (2002)
330. Yu, Q., Tremaine, S.: ApJAstrophys. J.refvol**599**, 1129 (2003)
331. Zalamea, I., Menou, K., Beloborodov, A.M.: Mon. Not. R. Astron. Soc. **409**, L25 (2010)
332. Zauderer, B.A., et al.: Birth of a relativistic outflow in the unusual γ-ray transient Swift J164449.3+573451. Nature **476**, 425 (2011)
333. Zauderer, B.A., Berger, E., Margutti, R., Pooley, G.G., Sari, R., Soderberg, A.M., Brunthaler, A., Bietenholz, M.F.: Astrophys. J. **767**, 152 2013
334. Zhong, S., Berczik, P., Spurzem, R.: Astrophys. J. **792**, 137 (2014)